



Durham E-Theses

Strategies for Cobalt Nanoparticle Synthesis Using Surface Organometallic Chemistry

SMITH, ALANA

How to cite:

SMITH, ALANA (2024) *Strategies for Cobalt Nanoparticle Synthesis Using Surface Organometallic Chemistry*, Durham theses, Durham University. Available at Durham E-Theses Online:
<http://etheses.dur.ac.uk/15451/>

Use policy

The full-text may be used and/or reproduced, and given to third parties in any format or medium, without prior permission or charge, for personal research or study, educational, or not-for-profit purposes provided that:

- a full bibliographic reference is made to the original source
- a [link](#) is made to the metadata record in Durham E-Theses
- the full-text is not changed in any way

The full-text must not be sold in any format or medium without the formal permission of the copyright holders.

Please consult the [full Durham E-Theses policy](#) for further details.

Strategies for Cobalt Nanoparticle Synthesis Using Surface Organometallic Chemistry



Durham
University

Thesis submitted for the degree of Doctor of Philosophy

By

Alana Smith

Department of Chemistry

Durham University

March 2023

Statement of Originality

This thesis is based on work conducted in the department of Chemistry at Durham University between October 2017 and December 2021. All work was carried out by the author, unless otherwise stated, and has not been submitted for another degree at this, or any other university.

The copyright of this thesis rests with the author. No quotation from it should be published without the author's prior written consent and information derived from it should be acknowledged.

Signed: _____

Alana Smith

Date: _____

Abstract

Title: Strategies for Cobalt Nanoparticle Synthesis Using Surface Organometallic Chemistry

This project explores a route for controlling the size of nanoparticles without capping agents with the aim of targeting sub-nanosized particles. A cobalt organometallic compound is tethered to a dehydroxylated silica support to produce a supported cobalt precursor. Reduction of this precursor leads to silica-supported cobalt nanoparticles without the use of capping agents.

The silica support is prepared for the tethering of the cobalt organometallic compound through calcination. The hydroxyl density of three silica supports (Aeroperl 300/30, SBA-15, and KIT-6) are determined at different calcination temperatures through ^{29}Si and ^1H solid-state NMR spectroscopy and chemical titration of the OH surface species. The surface area of the silica supports is also probed through BET analysis to determine if any pore structure collapse occurs during the calcination. Studies showed Aeroperl 300/30 calcined at 600 °C to be the most appropriate potential nanoparticle support for this project due to its relatively low hydroxyl density (0.8 mmol g^{-1}) and stable pore structure. Chapter 3 describes attempts to tether various cobalt organometallic and amide species to the SiO_{2-600} support. Here, $[\text{Co}(\text{N}(\text{TMS})_2)_2\text{THF}]$ was found to demonstrate significant promise as a precursor for SiO_{2-600} -supported cobalt nanoparticle formation. The composition of the cobalt-decorated silica material obtained following reaction of $[\text{Co}(\text{N}(\text{TMS})_2)_2\text{THF}]$ with SiO_{2-600} was probed using SS-NMR spectroscopy, ICP-OES, BET, and CHN analyses. The surface species of $[\text{Co}(\text{N}(\text{TMS})_2)_2(\text{THF})]/\text{SiO}_2$ was found to be a monografted $-\text{Si}-\text{O}-\text{Co}-\text{N}(\text{TMS})_2\cdot\text{THF}$ species. In Chapter 4, with a view to the generation of silica-supported cobalt nanoparticles, the thermal treatment and/or reduction under hydrogen at elevated temperature of the silica-grafted cobalt species was explored. The analysis of the magnetic properties of the thermally treated-/reduced-cobalt materials with a Guoy balance was inconclusive, the cobalt surface species could not be determined as either Co^{2+} or Co^0 . TEM imaging suggests the presence of cobalt particles, and it was concluded that heating $[\text{Co}(\text{N}(\text{TMS})_2)_2(\text{THF})]/\text{SiO}_2$ under hydrogen likely afforded cobalt nanoparticles (0.5 – 3 nm), while heating $[\text{Co}(\text{N}(\text{TMS})_2)_2(\text{THF})]/\text{SiO}_2$ under nitrogen produced cobalt nanoparticles (2 - 3 nm). However, the exact nature of the cobalt surface species has been difficult to characterise due to their air-sensitivity.

Following synthesis of these small cobalt/cobalt-oxide particles, the use of these materials in catalytic hydrogenation of cinnamaldehyde was examined. While the catalysts containing cobalt nanoparticles were found to be mostly selective towards hydrocinnamaldehyde (11 – 24%), the formation of side-products, including (1E,2E)-3-Phenyl-N-(trimethylsilyl)-2-propen-1-imine (6%), was also observed during the reaction. It was determined that the cause of the formation of the unwanted side-product was due to traces of $\text{H}-\text{N}(\text{TMS})_2$ physisorbed to the silica surface.

Acknowledgements

I want to start this off by thanking my supervisors Phil Dyer and Simon Beaumont for being amazing. Phil has given me 5 years' worth of encouraging words, endless patience, and tireless guidance. He always made me smile with his many famous sayings (*how long is a piece of string?*). Simon gifted me with his amazing knowledge, his brilliant insight, and his feedback. Whenever I was unsure of the next step, he always had another idea to try. I am so thankful to the both of them for making me feel so welcomed at Durham. Their combined guidance is what has led me to finishing this thesis. Every time I think of badgers, I think of Durham University and Phil's lab.

I must also thank Leon Van de Water and Xavier Baucherel, who were both kind to me and listened to me. I always enjoyed visiting the Billingham JM site and being able to meet them and discuss my work. They gave me the confidence to present my work at the annual Johnson Matthey academic conferences. They were a great help, offering JM's services to me, like BET analysis and mercury porosimetry.

I thank Johnson Matthey and the EPSRC for their funding and contributions that allowed me to do this project. I also thank Durham University and the staff of the Chemistry Department for their services and advice.

Next I want to thank the Dyer and Beaumont groups: Richard and Eder were always great office conversation partners; Sherry was always there to help keep the GC running and also share our mutual love of different foods and instant noodles; Kathryn and Nargiz were both so kind and we would always stop and talk in the hallways, and I also owe them both for doing my TEM imaging for me; Adam and Jake were the great providers of lab hijinks and jokes (both Schlenk and non-Schlenk related); and Stephen, Claire, and the rest were all supportive and encouraging when I first joined.

Of course, I want to thank my friends Sophie, Jacob, and Luke. They were the suppliers of memes and moral support. If I was ever stressed and on the verge of tears, they would always make me laugh and bring some joy to my situation. Their insanity became my sanity check in the best way possible. I could never thank them enough for sticking with me through the last 5 years.

And finally, I want to thank my parents, Susan and David, for all their love, empathy, and amazing emotional support. They kept me upright when I felt like I was going to be crushed under the weight of my stress. Even if I called them at 3 am in the morning, they would always answer and make time for me. Words cannot express my full gratitude but hopefully this is a good start. This PhD would not have been possible without them.

Contents

Chapter 1: Introduction

1.0	Literature Review.....	1
1.0.1	Project Outline	1
1.0.2	Heterogeneous Catalysis.....	1
1.0.2.1	Nanoparticles in Catalysis	3
1.0.3	Nanoparticle Synthesis	5
1.0.3.1	History of Nanoparticle Synthesis.....	5
1.0.3.2	History of Preventing Sintering of Nanoparticles during Synthesis.....	7
1.0.4	Oxide Supports as Supports for Nanoparticles in Catalysis	9
1.0.4.1	Silica as a Support for Nanoparticles in Catalysis	13
1.0.5	Current Conventional Methods for Synthesising Nanoparticles on a Solid Support.....	15
1.0.5.1	The Synthesis of Sub-nanosized Particles (Sub-NPs)	17
1.0.6	Impregnation of Organometallic Species onto Silica Surfaces <i>via</i> Surface Organometallic Chemistry (SOMC).....	18
1.0.6.1	Organyl Metal Complexes Grafted on Silica	20
1.0.6.2	Silica-bound Metal Amide Complexes	24
1.0.7	Reduction of Organometallic Precursors Grafted Oxide Support Surfaces	31
1.0.7.1	Reduction of Organometallic Precursors on Oxide Supports under Hydrogen	32
1.0.7.2	Calcination of Organometallic Precursors on Oxide Supports under Inert Gas or Vacuum	34
1.0.8	Hydrogenation Catalysis	37
1.0.8.1	Hydrogenation Catalysis using Cobalt Nanoparticles	38
1.1.0	Project Aims	40
1.1.1	Developing Methods for Synthesising Sub-nanosized Cobalt Nanoparticles	41
1.1.1.1	Step 1: Preparation of Oxide Supports	41
1.1.1.2	Step 2: Target Metal-organyl Complexes.....	42
1.1.1.3	Step 3: Impregnation of Cobalt Precursors onto the Oxide Supports	43
1.1.1.4	Step 4: Reduction of Organometallic Precursors to Sub-nanosized Particles	44
1.1.2	Target Outcomes of the Proposed Synthetic Method.....	44
1.1.3	Catalytic Testing of Synthesised Sub-NPs: Choosing the Hydrogenation of Cinnamaldehyde (CNA) over the Hydrogenation of Nitrobenzene	44
1.2	References	45

Chapter 2: Silica-based Catalyst Supports

2.0 Introduction to Silica-based Catalyst Supports.....	55
2.0.1 Silica as a Catalyst Support for the Synthesis of Nanoparticles.....	55
2.0.1.1 Properties of Aeroperl® 300/30 Silica.....	55
2.0.1.2 Properties of SBA-15 Silica.....	55
2.0.1.3 Properties of KIT-6.....	57
2.1 Preparation of Silica for Tethering Organometallic Precursors by Controlling the Hydroxyl Density.....	58
2.1.1 Calcination of Silica to Reduce the Surface Hydroxyl Density.....	59
2.2 Analysis of Calcined Silica to Determine the Hydroxyl Density.....	59
2.2.1 Brunauer-Emmett-Teller (BET) Analysis of Prepared Oxide Supports.....	60
2.2.1.1 BET Analysis of Aeroperl 300/30 Silica.....	60
2.2.1.2 BET Analysis of SBA-15.....	62
2.2.1.3 BET Analysis of KIT-6.....	63
2.2.1.4 Summary of BET Analysis of Variously Calcined Silica Supports.....	64
2.2.2 Determination of Hydroxyl Density by Titration with <i>o</i> -Tolyl Magnesium Bromide.....	64
2.2.3 Solid State Nuclear Magnetic Resonance (SS-NMR) Spectroscopic Studies of Prepared Oxide Supports.....	68
2.2.3.1 ²⁹ Si CP MAS NMR (Cross Polarisation-Magic Angle Spinning-Nuclear Magnetic Resonance) Spectroscopy For Surface Specific Characterisation of Silanols.....	69
2.2.3.2 ²⁹ Si SS-NMR Analysis of Silica Supports.....	69
2.2.3.3 ¹ H SS-NMR Spectroscopic Analysis of Silica Supports.....	85
2.3 Conclusions.....	89
2.4 References.....	90

Chapter 3: Tethering of Co-Precursors to Pre-treated Silica Supports

3.0 Introduction to Cobalt Organometallic Compounds Tethered To Silica.....	93
3.1 [Co(N(TMS) ₂) ₂ (THF)] (2) + Silica Support.....	95
3.1.1 Synthesis of [Co(N(TMS) ₂) ₂ (THF)] (2) + Silica Support.....	96
3.1.1.1 Synthesis of Complex 2 for Impregnation onto Silica Support.....	96
3.1.1.2 Impregnation of [Co(N(TMS) ₂) ₂ (THF)] (2) onto Silica Supports.....	96
3.1.2 Analysis of the Cobalt Surface Structure of [Co(N(TMS) ₂) ₂ (THF)] Tethered onto the Surface of Aeroperl 300/30 Silica ((2)/A-SiO _{2-x}).....	97

3.1.2.1 Cobalt-loading on Aeroperl 300/30 Silica Determined by ICP-OES	97
3.1.2.2 ²⁹ Si SS-NMR Spectroscopic Analysis of (2)/A-SiO ₂₋₆₀₀	98
3.1.2.3 ¹ H SS-NMR Spectroscopy of (2)/A-SiO ₂₋₆₀₀	99
3.1.2.4 Determining the Degree of Surface Silylation through Analysis of the amount of HN(TMS) ₂ Ligand Present after the Synthesis of (2)/A-SiO ₂₋₆₀₀	101
3.1.2.5 Surface Area Analysis of (2)/A-SiO ₂₋₆₀₀ to Determine Degree of Surface Functionalisation	102
3.1.2.6 CHN Elemental Analysis of (2)/A-SiO ₂₋₆₀₀	104
3.1.3 Analysis of product from reaction of [Co(N(TMS) ₂) ₂ (THF)] with KIT-6 ((2)/K-SiO _{2-x})	105
3.1.3.1 Cobalt loading of on KIT-6 Silica Determined by ICP-OES.....	105
3.1.4 Analysis of material from reaction of [Co(N(TMS) ₂) ₂ (THF)] with SBA-15 ((2)/S-SiO _{2-x}).....	106
3.1.4.1 Cobalt loading on SBA-15 Silica Determined by ICP-OES.....	106
3.1.5 Conclusions for Reactions of [Co(N(TMS) ₂) ₂ (THF)] with Silica Supports.....	106
3.2 Reactions of Cobalt Precursors Complexes 3 - 8 with Calcined Silica Support.....	107
3.2.1 CoCp ₂ + Aeroperl 300/30 Silica ((3)/A-SiO _{2-x}).....	107
3.2.1.1 Analysis of (3)/A-SiO _{2-x}	109
3.2.2 Co(dmp) ₂ + Aeroperl 300/30 Silica ((4)/A-SiO _{2-x})	115
3.2.2.1 Analysis of (4)/A-SiO _{2-x}	117
3.2.3 CoCp(CO) ₂ + Aeroperl 300/30 Silica ((5)/A-SiO ₂₋₆₀₀)	119
3.2.3.1 Analysis of (5)/A-SiO ₂₋₆₀₀	121
3.2.4 Co ₂ (CO) ₈ + Aeroperl 300/30 Silica ((6)/A-SiO ₂₋₆₀₀).....	123
3.2.4.1 Analysis of (6)/A-SiO ₂₋₆₀₀	123
3.2.5 Co(C ₈ H ₁₂)(C ₈ H ₁₃) + Aeroperl 300/30 Silica ((7)/A-SiO ₂₋₆₀₀).....	127
3.2.5.1 Analysis of (7)/A-SiO ₂₋₆₀₀	128
3.2.6 CoCpCOD + Aeroperl 300/30 Silica ((8)/A-SiO ₂₋₆₀₀)	130
3.2.6.1 Analysis of (8)/A-SiO ₂₋₆₀₀	132
3.2.7 Conclusions for Cobalt Precursors for the Formation of Silica-immobilised Cobalt Nanoparticles.....	133
3.3 References	134

Chapter 4: Reduction of Silica-Grafted Organometallic Cobalt Species

4.0 Introduction to the Reduction of Cobalt Precursors on the Surface of (2)/A-SiO ₂₋₆₀₀ and (3)/A-SiO ₂₋₆₀₀	137
4.1 The Reduction of (2)/A-SiO ₂₋₆₀₀	138

4.1.1 Determining the Reduction Temperature of (2)/A-SiO ₂₋₆₀₀ using Temperature Programmed Reduction	138
4.1.1.1 TPR Analysis of (2)/A-SiO ₂₋₆₀₀	139
4.1.1.2 TPR Analysis of air-exposed (2)/A-SiO ₂₋₆₀₀	141
4.1.2 Methodology for Reducing (2)/A-SiO ₂₋₆₀₀ <i>via</i> Heating Under a Gas Flow.....	142
4.1.2.1 Reduction of (2)/A-SiO ₂₋₆₀₀ under H ₂ /N ₂ at 150 °C	143
4.1.2.2 Reduction of (2)/A-SiO ₂₋₆₀₀ at Different Temperatures	144
4.1.2.4 Thermal Treatment of (2)/A-SiO ₂₋₆₀₀ under N ₂	145
4.1.2.5 Reduction of air-exposed (2)/A-SiO ₂₋₆₀₀ under H ₂ /N ₂ at 150 °C	146
4.1.3 Analysis and Characterisation of (2)/A-SiO ₂₋₆₀₀ after Reduction	146
4.1.3.1 Determining Cobalt Loading after Thermal Treatments of (2)/A-SiO ₂₋₆₀₀ by ICP-EOS.....	146
4.1.3.2 SS-NMR Spectroscopic Analysis of (2)/A-SiO ₂₋₆₀₀ after Thermal Treatments	147
4.1.3.3 BET Analysis of (2)/SiO ₂₋₆₀₀ to Determine Further Silylation of the Surface After Reduction	152
4.1.3.4 Analysing the Change of Magnetic Properties of Reduced (2)/SiO ₂₋₆₀₀ using a Gouy Balance	153
4.1.3.5 PXRD of (2)/A-SiO ₂₋₆₀₀ (150 °C, H ₂ /N ₂), (2)/A-SiO ₂₋₆₀₀ (150 °C, N ₂), and (2)/A-SiO ₂₋₆₀₀ (air-exposed, 150 °C, H ₂ /N ₂).....	156
4.1.3.6 TEM Imaging of (2)/A-SiO ₂₋₆₀₀ after Heating under Hydrogen	158
4.2 The Reduction of (3)/A-SiO ₂₋₆₀₀	163
4.2.1 Determining the Reduction Temperature of (3)/A-SiO ₂₋₆₀₀ using Temperature Probe Reduction	164
4.2.1.1 Investigating the Sublimation of Complex (3) from (3)/A-SiO ₂₋₆₀₀	165
4.3 Conclusions	166
4.4 References	167
Chapter 5: Catalytic Hydrogenation of Cinnamaldehyde with Supported Cobalt Catalysts	
5.0 Introduction to Catalytic Hydrogenation Using Cobalt Nanoparticles.....	169
5.0.1 Catalytic Hydrogenation of Cinnamaldehyde (CNA).....	169
5.1 Results and Discussion.....	170
5.1.1 Catalyst Selection	170
5.1.1.1 The Catalytic Performance for Hydrogenation of CNA Using (2)/A-SiO ₂₋₆₀₀ Reduced at T = 150, 200, and 250 °C	171
5.1.2.1 Formation and Characterisation of Side-products Formed During Hydrogenation of CNA	174

5.1.1.3 Reducing the Amount of Surface Amine on Catalysts <i>via</i> Heating Under Vacuum or Pentane Wash	178
5.1.1.4 Thermal Treatment of (2)/A-SiO ₂₋₆₀₀ In Absence of Hydrogen.....	180
5.1.1.5 Thermal Treatment of (2)/A-SiO ₂₋₆₀₀ Prior to Reduction Under Hydrogen	181
5.1.1.6 Probing the Effects of Air Exposure on Reduced (2)/A-SiO ₂₋₆₀₀ Catalysts.....	183
5.1.2 Analysis of the Activity and Selectivity of (2)/A-SiO ₂₋₆₀₀ (150 °C, N ₂ , then H ₂ , vacuum) For Hydrogenation of CNA.....	185
5.1.3 Summary and Discussion of Catalysts Synthesised from Precursor (2)/A-SiO ₂₋₆₀₀ and their Catalytic Selectivity for the Reaction of CNA	188
5.2 Conclusions	194
5.3 References.....	194

Chapter 6: Experimental

6.0 Experimental	196
6.0.1 General Considerations.....	196
6.0.2 Methodology of Analytical Techniques	197
6.0.2.1 BET and Hg intrusion Analyses.....	197
6.0.2.2 Oxide Support Hydroxyl Density Determination <i>via</i> Grignard Titration.....	197
6.0.2.3 Solid State NMR Spectroscopy.....	197
6.0.2.4 ICP-OES Analysis: Sample Preparation.....	198
6.0.2.5 GC Analysis of Reaction Solvent to Quantify Ligand Released during Impregnation	198
6.0.2.6 PXRD Sample Preparation	198
6.0.2.7 CHN Sample Preparation	199
6.0.2.8 Temperature Programmed Reduction (TPR)	200
6.0.2.9 Magnetic Moment Measurement using a Gouy (JME) Balance	201
6.0.2.10 Transmission Electron Microscopy (TEM) Imaging	201
6.0.2.11 Approximation of the Diameter of Complex 2, 4, and 7.....	202
6.0.3 Synthetic Methods.....	202
6.0.3.1 Synthesis of SBA-15.....	202
6.0.3.2 Synthesis of KIT-6.....	202
6.0.3.3 Calcination of Aeroperl 300/30 Silica (A-SiO _{2-700/600/400/200})	203
6.0.3.4 Synthesis of Li(N(TMS) ₂)(THF)	203
6.0.3.5 Synthesis of [Co(N(TMS) ₂) ₂ (THF)] (2)	204
6.0.3.6 Synthesis of dimesitylphenyl iodine (dmp-I).....	204
6.0.3.7 Synthesis of dimesitylphenyl lithium (dmp-Li).....	205

6.0.3.8 Synthesis of Co(dmp)_2 (4).....	205
6.0.3.9 Synthesis of CoCp(CO)_2 (5).....	205
6.0.3.10 Synthesis of $\text{Co(C}_8\text{H}_{12}\text{)(C}_8\text{H}_{13}\text{)}$ (7).....	206
6.0.3.11 Tethering Cobalt Complexes 2-5, 7, and 8 to Silica	206
6.0.3.12 Addition of $\text{Co}_2(\text{CO})_8$ (6) to Silica.....	206
6.0.3.13 Reduction of (2)/A-SiO ₂₋₆₀₀	206
6.0.3.14 Sublimation of Residual Complex 3 from (3)/A-SiO ₂₋₆₀₀	207
6.0.3.15 Synthesis of $\text{Co(NO}_3\text{)}_2/\text{SiO}_2$	207
6.0.3.16 Catalytic Hydrogenation of CNA	208
6.1 References	209
Chapter 7: Summary and Future Work	
7.0 Summary	210
7.1 Future Work	213
7.2 References	215
Appendices	
Appendix A: Calibration of Nonane against Toluene.....	217
Appendix B: Brunauer-Emmett-Teller (BET) Analysis.....	218
Appendix C: ¹ H SS-NMR Spectroscopy of Complex 2.....	219
Appendix D: REAPDOR SS-NMR Spectroscopy of (3)/A-SiO ₂₋₆₀₀	221
Appendix E: Initial Attempts at TPR Analysis of (2)/A-SiO ₂₋₆₀₀	222
Deconvolution of the Initial Attempts at TPR of (2)/A-SiO ₂₋₆₀₀	224
Appendix F: Scherrer Equation for PXRD analysis of	226
Appendix G: Testing for Cobalt in CNA Catalysis Reaction Mixture	227
Appendix H: Calibration Curves For CNA, CNOL, HCNA, HCNOL in the Hydrogenation of CNA.....	228
Appendix References	230

List of Abbreviations

POCOP	1,3-bis((di-<i>tert</i>-butylphosphino)oxy)benzene
dmp	2,6-dimesitylphenyl
atm	atmosphere
BET	Brunauer–Emmett–Teller
CHN	carbon, hydrogen, and nitrogen elemental
cm	centimetre
CNA	cinnamaldehyde
CNOL	cinnamyl alcohol
CDP	cross depolarisation
CP	cross-polarisation
CD	cyclodextrin
COD	cyclooctene
Cp	cyclopentadienyl
°C	degrees Celsius
DEN	dendrimer-encapsulated nanoparticle
DE	direct excitation
DQ	double quantum
μ_{eff}	effective magnetic moment
EO	ethylene unit
FT	Fischer Tropsch
FTIR	Fourier-transform infrared
GC	gas chromatography
GC-MS	gas chromatography–mass spectrometry
g	gram
h	hours
HCNA	hydrocinnamaldehyde
HCNOL	hydrocinnamyl alcohol
ICP-OES	inductively coupled plasma-optical emission spectroscopy
IR	infrared
K	kelvin
kHz	kilohertz
MAS	Magic Angle Spinning
χ_{g}	magnetic susceptibility
Mes	mesityl
mbar	millibar
mg	milligram
mL	millilitre
min	minutes
χ_{M}	molar magnetic susceptibility
nm	nanometre
NP	nanoparticle

ⁿ Bu	<i>n</i> -butyl
I	nuclei spin
ppm	parts per million
PVP	<i>poly</i> (<i>N</i> -vinyl-2-pyrrolidione)
POM	polyoxometallate
PVA	polyvinylalcohol
PXRD	powder X-ray diffraction
PO	propylene unit
QCP	quantitative cross-polarisation
REAPDOR	Rotational-Echo Adiabatic-Passage Double-Resonance
s	seconds
SF	silica foam
SQ	single-quantum
SDS	sodium dodecylsulfate
(SS-)NMR	(solid-state) nuclear magnetic resonance
SMSI	strong metal-support interaction
Sub-NP	Sub-nanosized particle
SCFD	super critical fluid deposition
SOMC	surface organometallic chemistry
T	temperature
TPR	temperature-programmed reduction
^t Bu	<i>tert</i> -butyl
TEOS	tetraethyl orthosilicate
THF	tetrahydrofuran
TGA	thermogravimetric Analysis
TEM	transmission electron microscopy
TMS	trimethylsilyl
TQ	triple quantum
cm ⁻¹	wavenumber

Chapter 1: Introduction

1.0 Literature Review

1.0.1 Project Outline

This PhD thesis describes attempts to develop a synthetic method for the preparation of sub-nanosized cobalt particles (<1 nm). The method targets preparation of nanoparticles synthesised free from the use of capping agents on the surface of a solid oxide support, through reduction of organometallic species tethered to the support's surface. This project explores the pre-treatment of the silica support; the tethering of selected organometallics to the support; and the reduction of the organometallic surface species to silica-bound nanoparticles. The resulting particles will be studied for activity and selectivity in catalytic hydrogenation.

1.0.2 Heterogeneous Catalysis

Catalysis is an essential branch of chemistry, important in both research and industry, providing lower energy methods for common chemical processes to be achieved in a sustainable manner (*i.e.* with high reaction selectivity and hence lower raw material usage). Today, over 90% of industrial chemical processes for the manufacturing of essential chemicals use catalysis in at least one step of their production.¹

Catalysts can be classified as *heterogeneous* or *homogeneous*, each class with its own benefits (Table 1.1). This project will focus on heterogeneous catalysts due to their greater suitability and hence prevalence in industry, with over 90% of industrial reactions involving a heterogeneous catalyst.² Heterogeneous catalysts used industrially are typically solid-phase systems that mediate reactions with gas- or liquid-phase reactants, and are usually preferable to homogeneous catalysts due to the greater ease with which they can be separated from reactions and the generally straightforward methods of regeneration.

Table 1.1. Traits of homogeneous and heterogeneous catalysts (Modified from Bowker³)

	Homogeneous Catalysis	Heterogeneous Catalysis
Selectivity	Highly selective	Comparably poor selectivity
Activity	Typically, greater activity at lower temperatures and milder conditions	Activity can be limited and sometimes requires harsher conditions and high temperatures
Ease of separation	Often requires complex procedures to separate catalyst and reaction mixture	Simple processes to remove catalyst
Ease of regeneration	Typically, harder to regenerate and easily contaminated/deactivated	Easily treated and regenerated, often just requiring thermal treatment
Stability	Discrete molecules that are not as stable and can decompose or undergo bimolecular pathways	Stable and robust materials that can withstand high temperatures and pressure
Risk of Contamination	Typically, discrete organometallic molecules that may contaminate product with heavy metals, making them unsuitable for some pharmaceutical processes	Supported catalysts tend to be strongly bonded to support so risk of catalyst contaminating product is significantly lower

The mode of action of heterogeneous catalysts is often regarded as being less well understood than that of homogeneous systems. A contributing factor here is that it is harder to probe reactions at a solid surface at a molecular level than it is to probe the reactivity of well-defined molecular species in solution. The resulting lack of deep understanding of the mode of action of heterogeneous catalysts can make their rational modification and improvement difficult. As a result of this perceived inability to fine tune heterogeneous catalysts with the same ease as homogeneous catalysts, the former frequently show poorer selectivity compared to their homogeneous counterparts.⁴ Therefore, analysing and developing a detailed understanding of mechanism is a key component of rational optimisation. With the idea of developing an understanding of the mode of action of heterogeneous catalysts in mind, nanoparticle catalysts are often regarded as bridging this homo-/hetero-geneous gap and have previously been referred to as “semi-heterogeneous” systems. Nanoparticle catalysts are considered applicable in both homogeneous and heterogeneous catalysis, with many characterisation techniques being amenable for their study including UV-vis, infrared, and Raman spectroscopies, microscopy and cyclic voltammetry.⁵ However, there is a new layer of difficulty in understanding the catalytic mechanisms associated with nanoparticle systems compared to other catalysts, as the shape and size of the nanoparticles will impact directly on their reactivity and catalytic performance. Nevertheless, the ability to prepare nanoparticles of uniform size, chemical

composition, shape or structure makes them much simpler to characterise, compared to conventional heterogeneous catalysts.⁶

1.0.2.1 Nanoparticles in Catalysis

A type of catalysis that has increased in popularity in recent years is that employing well-defined transition metal nanoparticles. In general terms, transition metal nanoparticles can be regarded as clusters of metal atoms with a highly reactive surface and a size that can range from a couple of dozen to hundreds of thousands of metal atoms, or from one nanometre to around a hundred nanometres.⁷ The chemistry of these clusters has been shown to have advantages in catalysis compared to conventional bulk materials.^{7, 8}

In contrast to bulk metals, metal nanoparticles have a large volume-to-surface-area ratio, creating many coordinatively unsaturated (and therefore reactive) atoms on their surface, which are available for reaction. As would then be expected, the size of nanoparticles is known to significantly affect their catalytic performance. Generally, smaller sized nanoparticle catalysts, typically tens to hundreds of atoms, show higher catalytic activity, something resulting from the unsaturated surface atoms having a low coordination number. This drives complexation or binding of reactants or substrates in order to increase their coordination number and hence lower their energy.⁸ These low coordinate atoms in nanoparticles, particularly those at steps, corners and edges of the particle, can exhibit very high catalytic activity.⁸

However, a drawback to the highly reactive surfaces of metal nanoparticles is that the nanoparticles tend to sinter, joining together and increasing their size and therefore decreasing their reactivity, as a result of the decreased volume-to-surface-area ratio.⁷ To prevent this unwanted amalgamation of the nanoparticles, their reactive surface must be stabilised, something that is conventionally done by using either electrostatic or steric effects.⁷⁻¹⁰ Examples of steric protection from sintering include the use of ligands, surfactants, polymers, and dendrimers. Each of which prevent the close approach of one nanoparticle to another. An example of electro-steric stabilisation (combining both options) is illustrated in Figure 1.1.⁹ The electrostatic stabilisation is provided by negatively charged halide ions located between the positively charged nanoparticle surface and the *tert*-N-butyl ammonium cations, while the bulky *tert*-N-butyl ammonium cations provide steric stabilisation. Both electrostatic and steric stabilisation contribute to the stabilisation of the core metal nanoparticle.

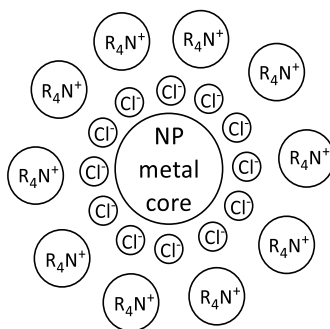
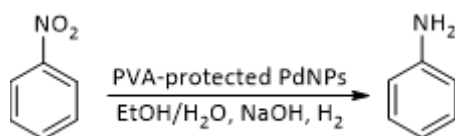


Figure 1.1. Electrosteric (a mix of electrostatic and steric) interactions protecting the nanoparticle core⁷

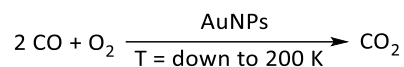
The use of nanoparticles as catalysts was first reported in the 1941 by Nord *et al.*, who were studying the reduction of nitrobenzene with polyvinylalcohol (PVA)-protected palladium nanoparticles (Scheme 1.1). Nord *et al.* stated that the PVA-palladium nanoparticles were highly efficient for this reduction, as well as the reduction of compounds that were previously considered impossible to reduce, such as quinone in acid solution.¹¹⁻¹³ The use of nanoparticle catalysts was reported again, in the 1970 by Parravano, who was studying hydrogen atom transfer reactions between benzene and cyclohexane and oxygen atom transfer between CO and CO₂ using Au nanoparticles.¹⁴ Subsequently, Au nanoparticles have become amongst the most studied/important metallic nanoparticles used in catalytic applications among all the examples of catalytically-active metal nanoparticles reported.



Scheme 1.1. Nord *et al.*'s reduction of nitrobenzene with PVA-protected Pd nanoparticles¹¹⁻¹³

A particularly good example of catalysis mediated by Au nanoparticles is the oxidation of CO with O₂ at low temperatures as developed by Haruta (Scheme 1.2)¹⁵. The Au nanoparticles were supported on solid supports, such as metal oxides, to stabilise the particles and prevent sintering. This catalytic reaction was recognised as a major step towards the recognition of nanoparticles as an important class of catalysts in their own right, as it demonstrated the potential for nanoparticles to have high activity at ambient temperatures, which is desirable in industry. Haruta also reported how the catalytic activity of the Au-nanoparticles was affected by the catalyst support and that the oxidation of CO was especially active on Group 8 oxides and alkaline earth metal hydroxides, evidencing the link between catalytic activity and the nature of the support. The size influence of the Au-nanoparticles was also studied, and revealed how influential the nanoparticle size was for catalysis, reporting that 5 nm gold particles showed the highest activity for CO oxidation at 0 °C compared to particles >5 nm, which showed a decrease in activity as the nanoparticle size increased. Haruta's study into these catalytically

active Au nanoparticles led to further research into nanoparticles, the significance of the particle size and solid support, and their potential for catalysis.¹⁵⁻¹⁸

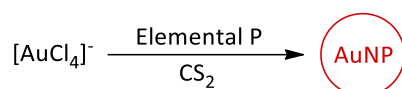


Scheme 1.2. Haruta *et al.*'s CO oxidation mediated by Au nanoparticles can be performed down to temperatures of 200 K.¹⁵

1.0.3 Nanoparticle Synthesis

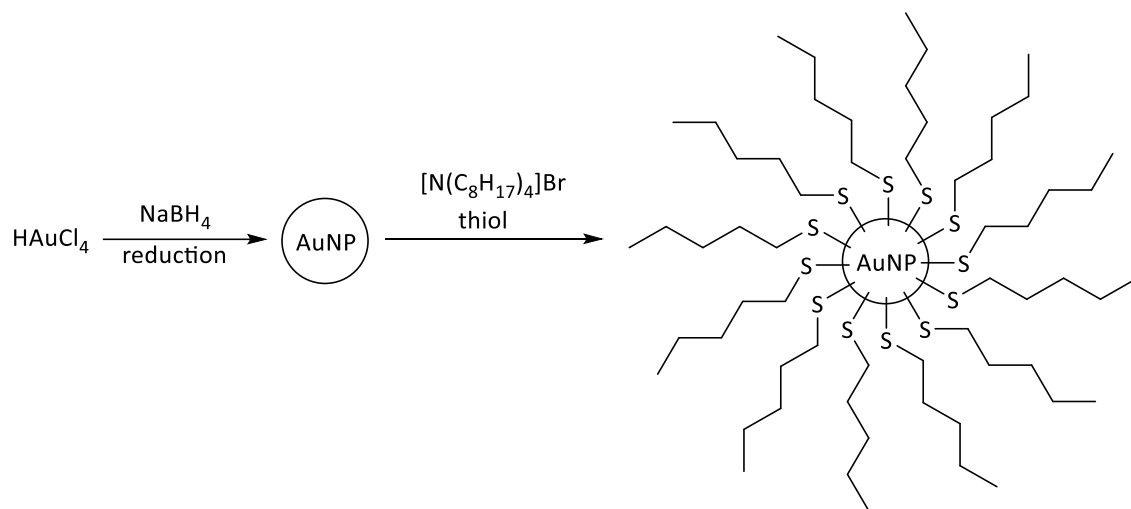
1.0.3.1 History of Nanoparticle Synthesis

Nanoparticles have been shown to be effective in both heterogeneous and homogeneous catalysis applications and have previously been referred to as “semi-heterogeneous” systems.⁷ Despite the attractive characteristic of being considered “semi-heterogeneous”, there is no getting away from one of the major drawbacks in using homogeneous nanoparticles, namely their tendency to sinter. As discussed in Section 1.0.2.1, this sintering can be prevented during synthesis by employing capping agents or surfactants. In general, today’s syntheses of stabilised nanoparticles can be said to be inspired by Faraday’s synthesis of Au nanoparticles (Scheme 1.3) during work involving the reduction of $[\text{AuCl}_4]^-$ by phosphorous, which led to formation of a red solution of soluble gold nanoparticles.^{19, 20} A similar reaction forming Au nanoparticles was performed by Schriffin *et al.* (Scheme 1.4) using NaBH_4 to reduce a HAuCl_4 solution.^{19, 21} In Schriffin’s synthesis, thiol was added as a stabilising agent, creating Au nanoparticles stabilised with thiolate ligands, popularising the method of using ligand stabilisation to prepare well-defined Au-nanoparticles.



Scheme 1.3. Faraday's general synthesis of soluble Au nanoparticles²⁰

A variety of different nanoparticles can also be produced by thermal decomposition of metal(0) precursors such as metal carbonyls as summarised in Figure 1.2. In this method, the carbonyl precursors are decomposed in the presence of a “steric” stabilising agent, such as a suitably functionalised polymer, to prevent amalgamation of the nanoparticles – catalytically active nanoparticles have been produced by this route.²²⁻²⁵ Using this approach, Reetz *et al.* developed a size-selective synthesis route to metal nanoparticles with electrochemistry, illustrated in Figure 1.3.²⁶⁻²⁹ In each of these synthetic routes (Scheme 1.3, Scheme 1.4, Figure 1.2 and Figure 1.3), the nanoparticles are stabilised during and after synthesis to prevent unwanted sintering.



Scheme 1.4. Synthesis of Au nanoparticles stabilised by thiolate ligands reported by Schriffin et al.¹⁹

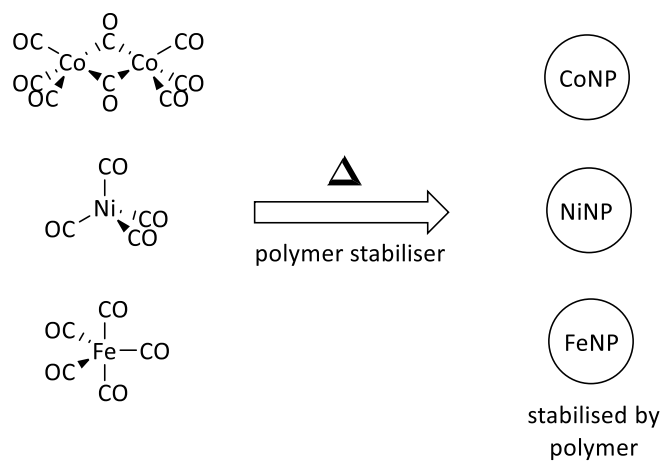


Figure 1.2. Thermal decomposition of the metal(0) carbonyls $\text{Co}_2(\text{CO})_8$, $\text{Ni}(\text{CO})_4$, $\text{Fe}(\text{CO})_5$ to their respective nanoparticles. The decomposition is performed in the presence of polymer stabilisers to prevent sintering

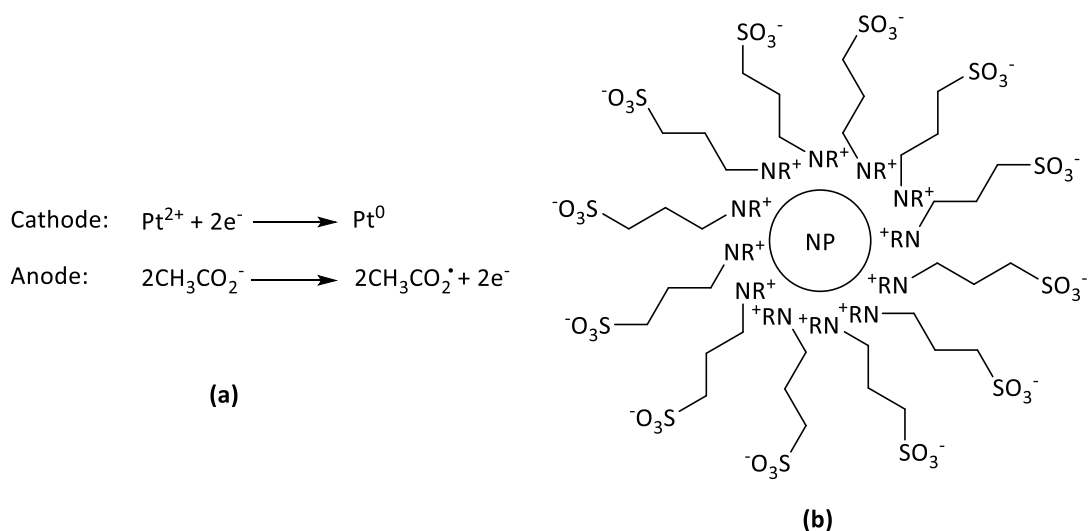


Figure 1.3. An example of electrochemical synthesis of nanoparticles from Reetz et al.,²⁷ which can be used for metals that are easily oxidised such as Pd, Ni, Cu, Au, etc. The electrodes are platinum metal and the electrolyte solution is a mixture of PtCl_2 and tetraalkylammonium salts $-(\text{NR}_4)\text{OAc}$ - in acetonitrile/THF (a) The cathode and anode reactions – the bulk metal was oxidised at the anode and the reduction at the cathode forms metal(0). The size of the resulting nanoparticles can be controlled by the current density through the electrodes. (b) The resulting nanoparticles stabilised by betain – the tetraalkylammonium salts in the electrolyte solution

1.0.3.2 History of Preventing Sintering of Nanoparticles during Synthesis

To prevent nanoparticle sintering, common surfactants are often used as nanoparticle stabilisers, such as sodium dodecylsulfate (SDS), Figure 1.4.³⁰ Nanoparticles stabilised by ligands are generally highly defined at the molecular level, as discrete ligands are well-defined.³¹ Polyoxometallates³² (POMs) and cyclodextrins³³ (CDs) are used as capping agents for Pd-nanoparticles, with the resulting materials being active catalysts for Heck, Suzuki, and Stille reactions, as well as the hydrogenation of unsaturated organic substrates. Examples of the use of CD-stabilised Pd-nanoparticles in catalysis are shown in Figure 1.5.

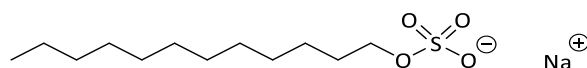


Figure 1.4. Structure of sodium dodecylsulfate (SDS)

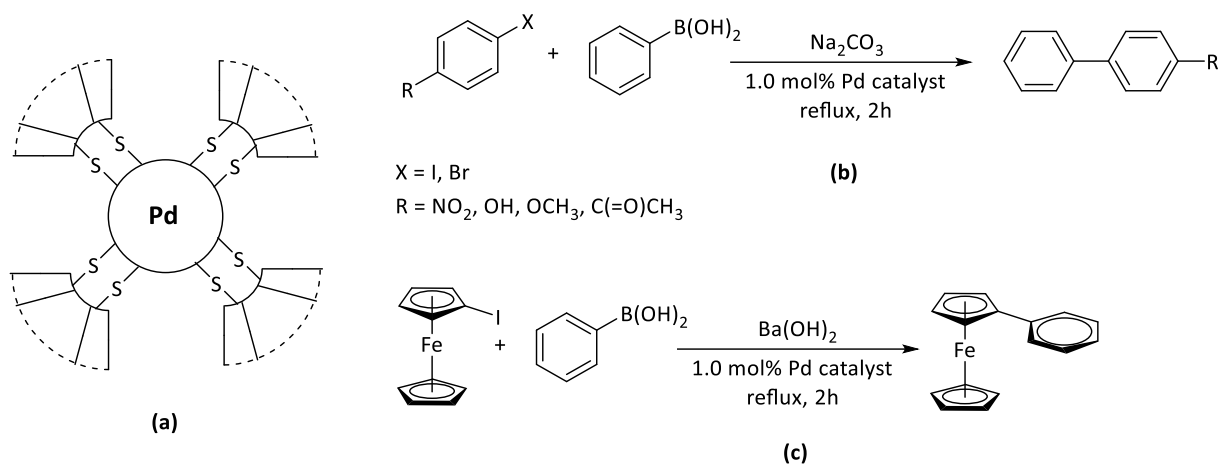


Figure 1.5. (a) An idealised nanoparticle stabilised by cyclodextrins (CDs); (b) Suzuki reaction and conditions catalysed by CD-stabilised Pd-nanoparticles; (c) Suzuki cross-coupling between iodoferrocene and phenylboronic acid by Pd-nanoparticles.³³

1.0.2.2.1 History of Nanoparticle Synthesis Stabilised by Polymers and Dendrimers

Polymers are also commonly used as stabilisers for catalytically active nanoparticles. When polymers are used in such a role, stabilisation results from not only steric factors, but also from weak surface coordination of heteroatoms from within the appropriately functionalised polymer. For example, *poly(N-vinyl-2-pyrrolidone)* (PVP), Figure 1.6, is a commonly employed stabiliser since it fulfils both “steric” and “nanoparticle-binding” requirements.³⁴ Indeed, Pt-, Pd-, and Rh-nanoparticles stabilised by PVP have been shown to be able to catalyse many different reactions including the hydrogenation of olefins and benzene.^{35,36} Additionally, a range of other polymers, such as polyurea, polyacrylonitrile, polyacrylic acid, oligosaccharides and poly(sodium acrylate), have also been reported as nanoparticle-stabilising polymers.^{7,37}

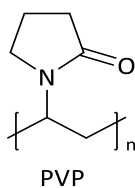


Figure 1.6. Structure of PVP

Dendrimers have also been used for the stabilisation of nanoparticles, first published as nanoparticle stabilisers in 1998 by Crooks *et al.*,³⁸ Tomalia *et al.*,³⁹ and Esumi *et al.*⁴⁰ Compared to conventional polymers, which are ill-defined, dendrimers have the advantage of being well-defined at the molecular level. This comes about as dendrimers are highly-branched globular macromolecules, which can trap and stabilise nanoparticles, as exemplified schematically in Figure 1.7, as well as providing solubility.⁴¹

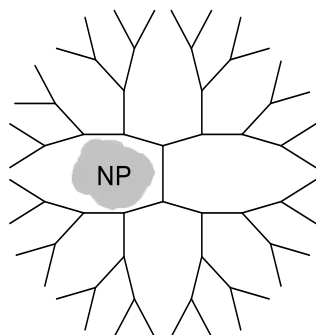


Figure 1.7. A simplified drawing of a nanoparticle stabilised inside a dendrimer

Though the use of groups such as ligands (e.g thiols), polymers (e.g PVP), and dendrimers as stabilisers in nanoparticle synthesis is common, the presence of these groups on the nanoparticle's surface will decrease available reaction sites and therefore reactivity.³⁶ One method of avoiding this unwanted decrease of surface sites is through binding the nanoparticles to a solid support (such as silica and alumina⁴²). Here, the rigid support will hold the nanoparticles in place and prevent amalgamation, thus acting as a stabiliser.

1.0.4 Oxide Supports as Supports for Nanoparticles in Catalysis

Oxide supports, such as silica and alumina, are commonly utilised to support nanoparticles during catalysis. Nanoparticles are often immobilised on the surface of the oxide support and provide stability to the nanoparticles during catalysis.⁴³ The support's role in a nanoparticle-based catalyst's behaviour (such as activity, selectivity, and lifetime) is often questioned, despite evidence that certain catalyst-support pairings show enhanced catalytic activity and selectivity over other catalyst-supports pairs.⁴⁴⁻⁴⁶ These effects of the support on the behaviour of the catalyst can be assumed to be due to properties of the support and are referred to as 'support effects'. Examples of metal oxide properties that may affect catalytic activity include the presence of potential Lewis acid and base sites on the surface,⁴⁷ the potential for charge transfer between the support and metal centre,⁴⁶ the shape/size of the pores,^{44, 48} and ease of metal loading onto the support.⁴⁴

An example that highlights the operation and importance of 'support effects' for catalytic reactions is a study into cobalt-nanoparticle-catalysed Fischer-Tropsch reactions, which compares use of silica, alumina and titania as supports.⁴⁸ In each case, the cobalt was loaded onto the oxide support using incipient wetness impregnation methods starting with $\text{Co}(\text{NO}_3)_2 \cdot 6\text{H}_2\text{O}$, with the resulting impregnated material then being calcined to generate Co particles on the surface of each oxide. These resulting Co-containing particles were found to exist in different forms on different supports: as Co_3O_4 clusters on SiO_2 and $\gamma\text{-Al}_2\text{O}_3$ and as single crystal Co_3O_4 on TiO_2 and $\alpha\text{-Al}_2\text{O}_3$. Furthermore, the size of the Co clusters was dependent on the pore size of the oxide support, agglomerating on the supports that had a larger pore size. The reducibility of the Co_3O_4 clusters to Co^0 also increases with pore diameter. The

study concluded that the pore structure has a significant effect on the size, location, shape, and appearance of the cobalt particles, which in turn affected the catalytic behaviour of each catalyst; the smaller cobalt particles of the γ -alumina- and silica-supported catalysts deactivated in the presence of water, while the larger particles on titania have a higher stability against water deactivation.

Similarly, in a study by Somorjai *et al.* the effects of several different oxide supports (SiO_2 , Al_2O_3 , TiO_2 , Nb_2O_5 , Ta_2O_5 , and ZrO_2) on the catalytic behaviour of Pt nanoparticles for the isomerisation of *n*-hexane to branched isomers has been examined.⁴² Here, the isomerisation of *n*-hexane was chosen as a model transformation since it provides an excellent model for exploring catalytic selectivity since there are five competing reaction routes that are available, namely cracking, isomerisation, cyclisation, aromatisation and dehydrogenation (Figure 1.8). Somorjai and co-workers demonstrated that the Pt/ Nb_2O_5 and Pt/ Ta_2O_5 systems both gave high selectivity towards isomerisation, forming 2-/3-methylpentane and 2,2-/2,3-dimethylbutane. In contrast, Pt/ ZrO_2 showed the poorest selectivity, giving a mixture of products resulting from isomerisation, cyclisation, cracking, and aromatisation. The bound Pt nanoparticles were also compared to blank supports to confirm that both the catalyst and the support act synergistically and are both required for the preferred selectivity towards isomerisation. Blank supports typically showed a preference for cracking with the exceptions of TiO_2 and ZrO_2 , which showed preferences for isomerisation and cyclisation, respectively. This study highlights how support effects can increase the selectivity and operation of certain reactions in an environment with potential competing reactions.

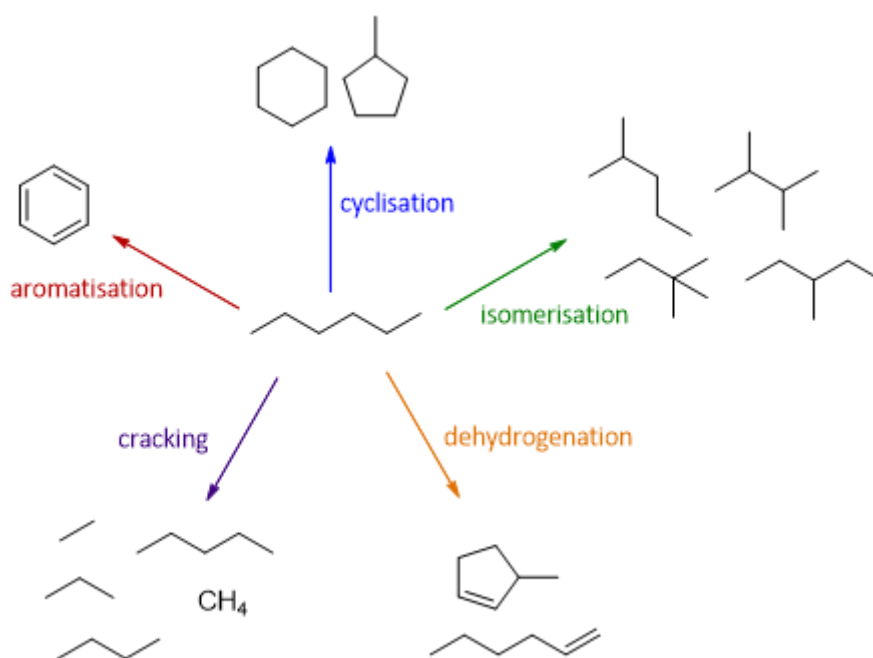
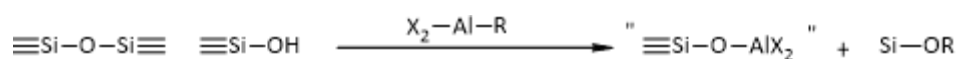


Figure 1.8. Five competing reaction pathways for the reactions of *n*-hexane over supported platinum catalysts: cyclisation, isomerisation, dehydrogenation, cracking, and aromatisation.⁴⁹

Metal oxide supports can also be modified prior to the impregnation of nanoparticles. The ability to modify the oxide support introduces the ability to tailor the support. The surface of the oxide support can be modified to increase activity or control selectivity by the addition of different surface species (e.g. silylation).⁵⁰ Similarly, modification through the removal of already present surface species may be employed.⁵¹ A commonly encountered example of the modification of silica is with aluminium (in the form of alkyl-aluminium compounds), an approach that introduces Lewis acid sites to the surface in a controlled manner (Scheme 1.5 and Figure 1.9).^{52, 53} An instance of the use of this approach is the chemical modification of the surface of the well-defined silica material MCF-17 with aluminium.



Scheme 1.5. A simplified scheme of the addition of alkyl-aluminium compounds to species on the surface of MCF-17 silica
 "≡Si-O-Si≡" denotes a surface siloxane species; "≡Si-O-H" denotes a silanol species

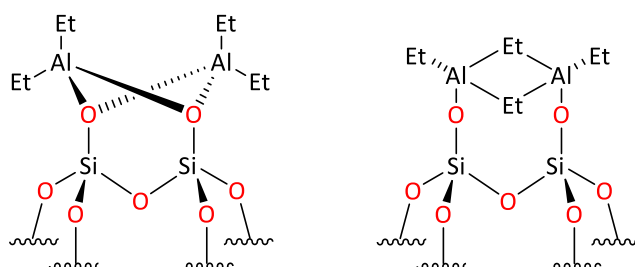


Figure 1.9. Two possible structures of silica modified by alkyl-aluminium creating Lewis acid Al-sites on the surface.^{52, 53}

A study by Musselwhite *et al.* found that Pt-nanoparticles supported on Al-modified MCF-17 show catalytic activity in the reformation of linear to branched hydrocarbons, whereas the parent MCF-17 system does not.⁴⁹ This difference in catalytic activity is thought to be due to the creation of Lewis acidic aluminium sites on the surface of the modified silica (similar to the Lewis acidic sites on alumina) that work in tandem with the Pt-nanoparticles (Figure 1.10), as proved by also testing blank Al-modified MCF-17, which was found to be inactive the reformation of linear hexane to branched isomers.⁴⁹ Selectivity towards isomerisation into branched isomers is also be greatly increased as evidenced by the Al-modified MCF-17/Pt showing high selectivity (>90 %) for isomerisation towards 2-methylpentane.⁴⁹

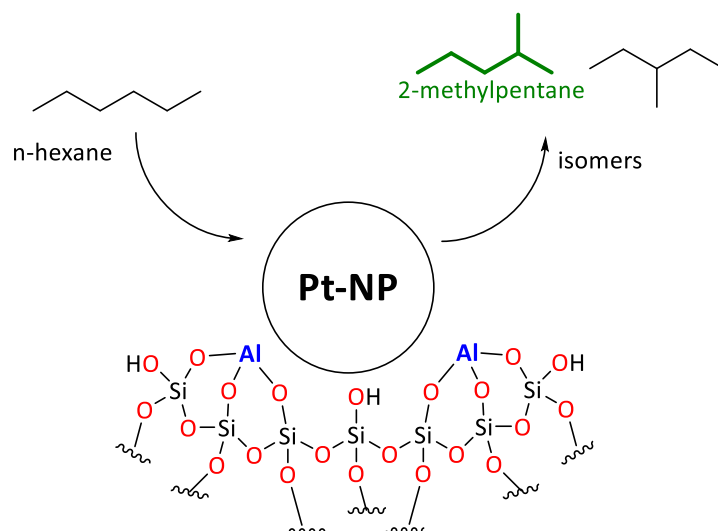
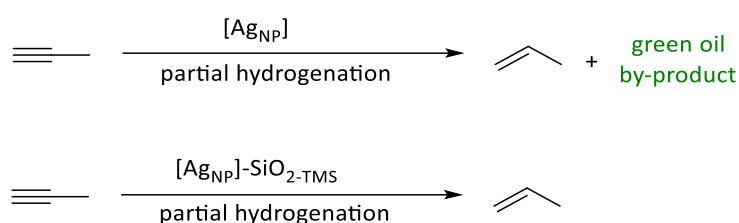


Figure 1.10. Pt-nanoparticle on an Al-modified silica surface used in the catalysis of the isomerisation of n-hexane. The reaction shows a >90 % selectivity towards 2-methylpentane (highlighted in green).⁴⁹

Silica when used to support metal nanoparticles is widely assumed to be relatively inert compared to other supports,⁵⁴ with most catalytic reactions thought to occur solely at the silica-bound metal species. This is in contrast to supports that contain strong acidic or basic sites (Al_2O_3 , La_2O_3),⁴⁸ or those that are reducible oxides and may mediate oxygen transfer processes (e.g. CeO_2 , TiO_2).⁵⁵ However, research by Sápi *et al.* suggests that the structure of the silica support can affect the catalytic activity of supported nanoparticle catalysts.⁵⁶ Sápi and co-workers found that ethanol decomposition to acetaldehyde mediated by silica-supported Pt nanoparticles at 300 °C was ~2 times faster on SBA-15 silica (0.073 molecules·site⁻¹·s⁻¹) than on MCF-17 (0.042 molecules·site⁻¹·s⁻¹) and silica foam (SF) (0.040 molecule site⁻¹·s⁻¹). The selectivity towards the formation of acetaldehyde was ~2 times higher for SF silica (55%) than MCF-17- (29%) or SBA-15- (25%) supported Pt-nanoparticles.⁵⁶ Following their study, Sápi proposed that the dissimilarity of activity may be due to differences in the surface smoothness, porosity, mesostructure, and therefore the Pt-SiO₂ interactions. This conclusion was reached as the well-defined silicas SBA-15, MCF-17, and SF are all chemically similar but differ in pore structure and shape, surface area, and extent of disorder. They concluded that SBA-15's high activity may be derived from the highly mesostructured and "rough" (small scattering centres and sharp electron density fluctuations) support, while SF's selectivity may be due to diffuse phase boundaries (the junction of two different phases) in the foam. However, these conclusions found by Sápi *et al.* may be flawed, as the polymer stabiliser was not removed prior to catalysis testing. Consequently, the formed nanoparticles may not have dispersed evenly throughout the silica structures as the channel sizes of the silica is narrower than the average diameter of the nanoparticle, without considering the added size of the polymer stabiliser.

Another demonstration of the effects of the support on catalytic behaviour of supported NPs was made by Oakton *et al.*,⁵⁷ who showed that the formation of stable silver nanoparticles (2.1±0.5 nm) on silica can decrease the formation of a green oligomeric oil side-product in the partial hydrogenation of alkynes, compared to free silver nanoparticle catalysts (Scheme 1.6). Silver nanoparticles on silica have also been shown to have a high selectivity for the partial hydrogenation of propyne to propene. However, this occurs with very low activity - 3-13% conversion depending on the size of the silver cluster formed.⁵⁷ Thus, it is clear that support effects can have a profound impact on a catalytic performance from activity to selectivity. It is therefore imperative to have an understanding of silica and its surface and potential support effects.



Scheme 1.6. The partial hydrogenation of propyne by silica-bound and unbound Ag nanoparticles.⁵⁷

1.0.4.1 Silica as a Support for Nanoparticles in Catalysis

Silica is a very commonly used and hence well studied oxide support for catalysts. Silica is known to be chemical and thermally stable;⁵⁸ typically has an uniform pore size and pore distribution,⁵⁹ which can be adjusted during synthesis by changing preparation parameters such as reaction temperature, reaction time, silica source, and templating agents;⁵⁸ and can be prepared with high surface area.⁶⁰ Silica is formed from tetrahedral $[\text{SiO}_4]$ units and, depending on its method of preparation, can have a very high surface area and high porosity, with silanol groups and siloxane bridges making up the surface.⁶¹ These silanols can be classified as isolated, vicinal and geminal (as shown in Figure 1.11).

Silanols are the necessary functionality used to graft compounds to the surface of silica. Surface Organometallic Chemistry (SOMC) is a specific example of a tool that uses silanols to bind a metal organometallic precursor to the silica surface through the reaction of an organometallic complex and a Si-OH to form a Si-O-M species. The relative densities and the distance between the silanol groups are proposed to control the grafting of organometallic precursor molecules during SOMC (a topic of importance to this project) according to studies by Copéret *et al.*⁶²⁻⁶⁴ Silica has been noted as being highly suited for the support of single site catalysts.⁶⁵ The reasoning behind this is due to silica's comparatively simple surface chemistry with its straightforward reactivity, the ease of dehydroxylation (removal of silanol groups), and the strength of the Si-O-M bonds, which ensure stable supported catalysts.

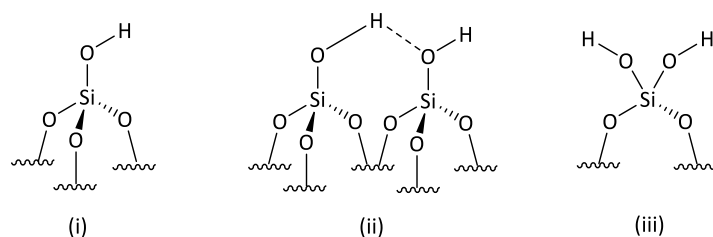
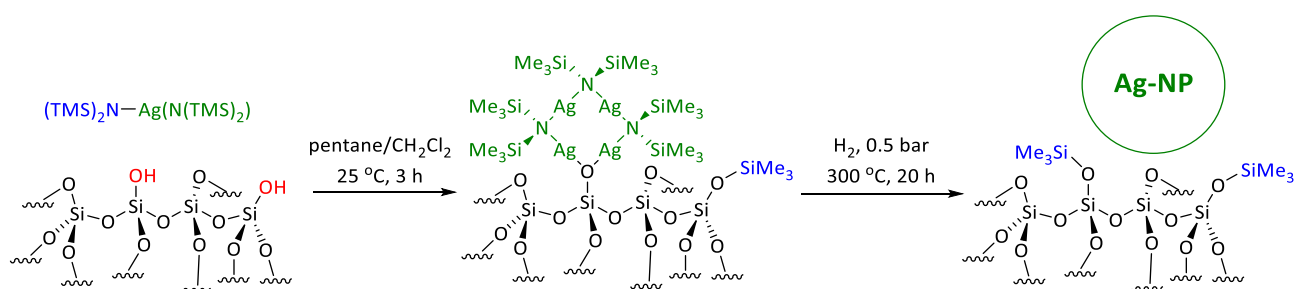


Figure 1.11. Types of silanol: i) isolated ii) vicinal iii) geminal.

The surface of silica is comprised predominantly of hydroxyl groups and siloxane bridges, with the ratio between these two functionalities being dependent on the thermal history of the silica sample in question.⁶⁶ Unlike other supports, such as aluminas or titanias, silica does not typically contain species such as Lewis acid/base sites, with silica's surface hydroxyl groups also being less reactive than other metal oxide surfaces such as those of alumina and zirconia. It is proposed that this decreased reactivity of silica is a result of the absence of Brønsted acid sites on the surface, which other metal oxide supports like alumina possess.⁶⁷ Due to the decreased reactivity, silica supports a lower density of grafted metal particles with a weaker bond.⁶⁸

Studies have shown that silica's surface can be easily modified and can be passivated prior to depositing metal clusters. For example - treatment to form trimethylsilyl groups in the place of the hydroxyl groups,⁵⁷ which affects the efficiency of formation of silver metal nanoparticles and the material's resultant catalytic behaviour. The passivation of the surface with trimethylsilyl groups allowed the formation of more particles per gram of material – however, this route, outlined in Scheme 1.7, also deactivates the catalyst.

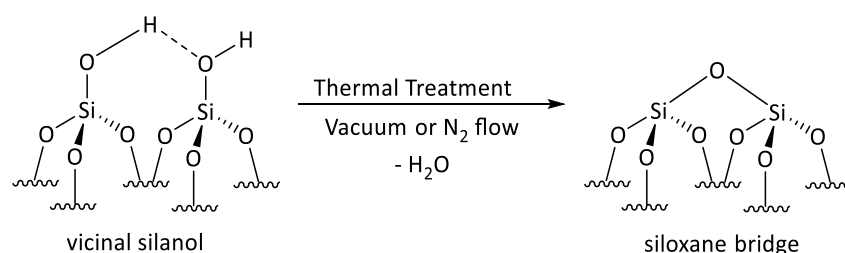


Scheme 1.7. The formation of Ag-nanoparticles on the surface of silica, alongside the formation of surface trimethylsilyl groups.⁵⁷

The surface of silica can also be modified by dehydroxylation, which can be used to remove and control the density of the silanols on the surface. Silica undergoes dehydroxylation when heated (200 - 1500 °C) under either a flow of nitrogen or under a vacuum (up to 10^{-9} mbar/ultra-high vacuum), Scheme 1.8.⁶⁹ However, the temperature at which dehydration (loss of physically adsorbed water) or

dehydroxylation (loss of silanols species) occurs is not a fixed parameter between different silicas since both these processes depend on the porosity and the size and shape of the pores within the silica matrix.⁷⁰ Zhuravlev states that for all silicas the total silanol number per unit surface area (α_{OH}) is constant when hydroxylated to its maximum degree, a physio-chemical constant known as the Zhuravlev constant, with the exception of silicas with very fine pores (as defined by Zhuravlev).⁶⁶ Additionally, Zhuravlev found that the ratio of isolated and vicinal silanols may be inconsistent between different batches of silica and is also dependent on the porosity and particle size of the silica being studied. When fully hydroxylated, independent of porosity, structure and surface area, silica has a range of OH group surface densities of 4.2-5.7 nm⁻², with an average of $\alpha_{\text{OH}} = 4.9$ OH groups nm⁻² over 100 amorphous silica samples.⁷¹

Most research groups agree that prolonged heating at 373 K will lead to complete dehydration, without causing any dehydroxylation for non-porous silica, while heating above 473 K may be necessary for silica with micro pores due to the small size of the pores slowing the removal of water.⁷² At low temperatures, below 473 K, a silica surface will be covered principally with vicinal hydroxyl groups, which comprise bridging hydrogen interactions. Typically, silica will lose the majority of these vicinal hydroxyls at temperatures between 473-673 K under vacuum, forming predominantly isolated silanols and siloxane bridges (Scheme 1.8). Under ambient conditions, where air humidity is a factor, vicinal silanols can remain on the surface even at temperatures of 873 K.⁷³ At temperatures above 673 K, isolated silanols will slowly begin to condense, albeit with increasing difficulty as their density decreases. Full dehydroxylation (removal of all silanol groups) will normally occur in most forms of porous silica at temperatures above 1473 K, a process that also leads to a decrease in surface area of the silica as a result of pore collapse.⁷³ This is due to interparticle condensation between silanols on different areas of the surface, forming siloxane bridges across pores.



Scheme 1.8. Dehydroxylation of a silica surface to form siloxane bridges from vicinal silanols with release of water.

1.0.5 Current Conventional Methods for Synthesising Nanoparticles on a Solid Support

Though there are many reports and studies into what are described as highly active stabilised homogeneous nanoparticle catalysts, it is difficult to differentiate whether the capped nanoparticles are catalytically active themselves or whether it is a few “clean nanoparticles” (without external

surface groups) that are responsible for the activity.³⁶ Immobilising nanoparticles on a solid support can provide stabilisation without the use of capping agents.⁴³ However, typical methods for securing nanoparticles to solid supports are to synthesise the nanoparticles first, with the use of stabilisers, then to immobilise the stabilised nanoparticle on the support. The stabiliser is then removed from the surface of the nanoparticle, typically through heating at high temperatures, leaving the nanoparticle on the solid support without the stabiliser present. For example, dendrimer-stabilised Pt nanoparticles and bimetallic Pd-Au nanoparticles, stabilised by dendrimers, absorbed onto silica and used in oxidation and hydrogenation catalysis, respectively, have been studied by Chandler *et al.* (Figure 1.12).⁷⁴

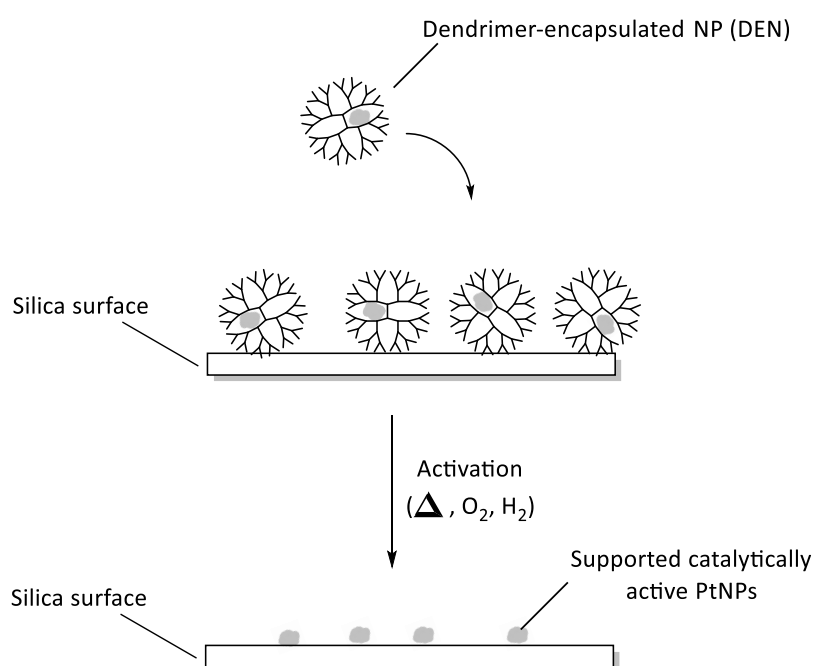


Figure 1.12. Chandler *et al.*'s synthesis of silica-bound nanoparticles prepared via attaching dendrimer-encapsulated nanoparticles (DENs) to silica then activating the catalyst by removal of the dendrimer⁷⁴

However, for the dendrimer-stabilised Pt nanoparticles to be catalytically active for CO oxidation at room temperature and the hydrogenation of toluene respectively, the dendrimer stabilisers must be removed thermally. Efficient catalysis was only achieved after the nanoparticle's surfaces were "cleaned" of stabilisers. Such "cleaning" or "activating" is often difficult to do or incomplete, and may result in sintering of the nanoparticles as a result of the temperatures used.⁷⁵ This protection, immobilisation, "activating" method of supporting nanoparticles on an oxide support is not ideal for catalysis as nanoparticles produced with this method undergo sintering during the "activating" step, decreasing their catalytic activity as their size increases. Preferably, to maximise catalytic performance, nanoparticles would be synthesised and immobilised on a solid support surface without the use of capping agents or stabilisers at any point during their preparation. With no capping agents

or stabilisers present, the nanoparticle surface will not need to be cleaned prior to catalysis, and potential sintering of the nanoparticles during the “activating” step is avoided.

1.0.5.1 The Synthesis of Sub-nanosized Particles (Sub-NPs)

As discussed in Section 1.0.2.1, nanoparticles are of interest in catalysis due to their high reactivity and selectivity, a combination that is not often achieved using bulk materials. As reactivity and selectivity are attributed to the small size of the nanoparticles (1 – 100 nm), there is an interest in even smaller metal particles – so-called sub-nanosized particles (Sub-NPs) that have a diameter of 1 nm or less.⁷⁶ Sub-NPs can be described by either their diameter (typically in nm) or by the number of atoms in the particle, also called atomicity. Sub-NPs can show changes in their characteristics with changes in their atomicity – such as higher catalytic activity with lower atomicity.⁷⁷

Such sub-nanosized particles will have constituent metal atoms that have very low coordination numbers and hence are exposed, and available for reaction.⁷⁸ Indeed, sub-NPs (<1 nm) have been predicted to have greater activity and selectivity than nanoparticles (1 – 100 nm) in catalysis; sub-NPs have already been shown to be capable of both reduction and oxidation, with high catalytic activity for the reduction of oxygen with Pt-Sub-NPs⁷⁷⁻⁷⁹ and the aerobic oxidation of hydrocarbons,⁸⁰⁻⁸² as well as catalytic hydrogenation of olefins.⁸³ Due to their predicted high activity, and the activity they have already shown to date, sub-NP are of great interest in the field of catalysis.⁷⁷

The preparation of Sub-NPs is considered significantly more difficult than that of their traditional nanoparticle counterparts, as finer size control is required to keep the particle on the sub-nano scale. Conventional nanoparticle synthesis methods are often considered lacking for the production of Sub-NPs since they do not provide enough control over the size and particle composition.⁸⁴ Consequently, a common synthetic method for preparation of Sub-NPs is the use of dendrimers, both as a stabiliser and also to restrict the particle size growth.^{77, 79, 81} For example, Kazume *et al.* studied tin oxide Sub-NPs produced with dendrimer templates and were able to demonstrate a correlation between particle size and activity towards CO oxidation.⁸⁵ They reported that their tin oxide Sub-NPS contained both stable Sn^{IV} and metastable Sn^{II}, with the fraction of the metastable Sn^{II} increasing as the particle size decreased. The catalytic activity of the CO oxidation by Sn oxide Sub-NPS increased as the size of the particles decreased, linearly correlating with the charge composition of the Sn atoms in the Sub-NPs.

Additionally, other research groups have demonstrated some success in synthesising not only mono-metal sub-NPS, but also bi- and tri-metallic sub-NPs using dendrimer templates. For example, Wakizaka *et al.* studied the composition of well-defined bimetallic Mo-Pt Sub-NPs. The particles demonstrated increased thermal stability as the size decreased, due to the interactions between the Mo and Pt.⁸⁶ Similarly, Takamasa *et al.* also found success in synthesising mono-, bi-, and tri-metallic

Sub-NPs, which have been studied as catalysts.⁷⁶ They found that their Sub-NPS showed higher activity and selectivity under milder conditions than the corresponding nanoparticles of size (~1 nm), with their Sub-NPS even being able to selectively synthesis hydroperoxide at low temperatures (80 °C) and under low pressure (atmospheric pressure), a high energy compound that is typically hard to produce due to its instability.⁷⁶

Despite the successes of Kazume and Wakizaka in synthesising Sub-NPs, there are still many difficulties associated with the synthesis of Sub-NPS. For example, as was found for the conventional method of synthesising nanoparticles on a solid support (as discussed in Section 1.0.3.2), there is the issue of the dendrimer blocking surface sites on the Sub-NP's surface. Blocked surface sites will not be able to take part in catalysis, reducing catalytic activity of the Sub-NPS. Any "activation" by heating to remove the dendrimer stabiliser, will also cause sintering and likely increase particle size outside of the sub-nanoscale regime. These challenges in the synthesis of sub-NPs, and the potential of Sub-NPs for greater activity than NPs, make the synthesis of Sub-NPs a subject of great interest for catalysis.

1.0.6 Impregnation of Organometallic Species onto Silica Surfaces *via* Surface Organometallic Chemistry (SOMC)

As a key part of this PhD project involves the tethering of an organometallic species to an oxide support, it is important to understand how the organometallic is grafted to the support surface. Two general methods have been identified for grafting and organometallic precursor to a solid support. The first method involves attaching a linker to the metal precursor and joining it to the support, something known as the *Supported Homogeneous Catalysis* method.⁸⁷ However, as a result of the metal being bound to the support through a linker, a possible shortcoming is that the metal centre can leach from the support. Due to possible metal leaching, the use of a capture bed may be required in order to remove the particles from the system since they may lead to unwanted side reactions or to fouling of the reactor system.⁸⁸ The second approach used to graft organometallic species to a solid support is *Surface Organometallic Chemistry* (SOMC), which involves the metal oxide support acting as a discrete rigid ligand to the metal centre. This means that the oxide support will have effects on the inorganic precursor's stability, selectivity and activity.⁸⁹ The difference between *Supported Homogeneous Catalysis* and SOMC is represented schematically in Figure 1.13.⁹⁰

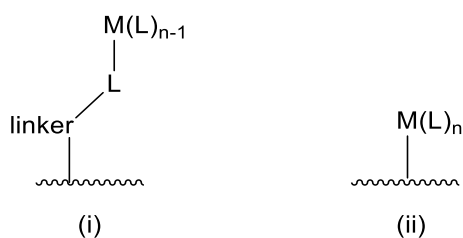
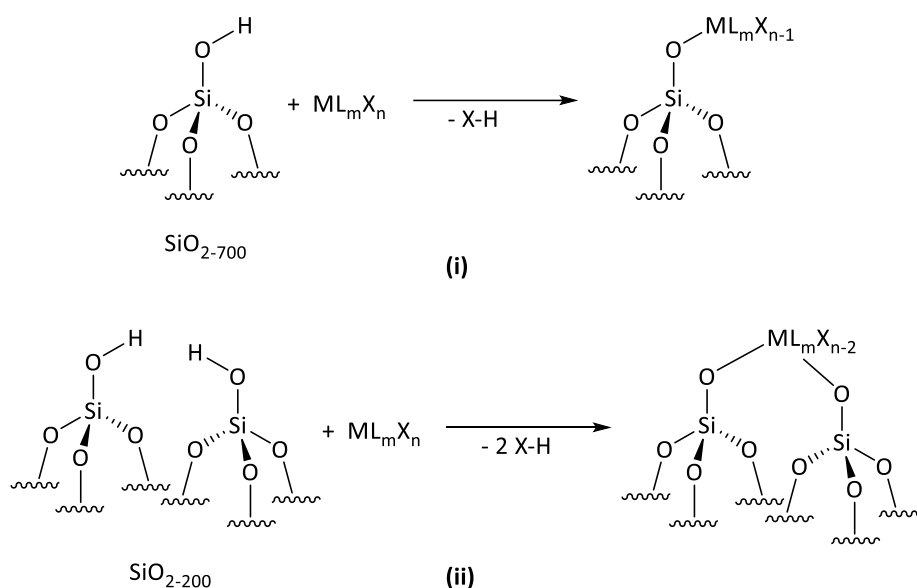


Figure 1.13. Schematic representation of i) Supported Homogeneous Catalyst and ii) Surface Organometallic Chemistry (SOMC).

In the context of SOMC, there has been research into studying how the oxide support controls the tethering of organometallic compounds, and in turn how this affects any catalytic behaviour of these tethered compounds – though control of such processes is still not fully understood. A general scheme showing the reaction of a $\equiv\text{Si-OH}$ group on the silica surface with a metal complex (ML_x) is given in Scheme 1.9. According to Copéret, in SOMC, a low density of isolated silanol groups is preferable for tethering well-defined organometallic species to oxide surface to generate single-site species on the oxide support. Since silica calcined at 700 °C contains mostly isolated silanols,⁹¹ this makes it an ideal surface upon which to graft metal surface species and to ensure that these remain spatially isolated from one another.⁶⁴

Generally, most silica-supported species follow this general reaction path in Scheme 1.9(i), with a proton transfer from the surface silanol to the ML_mX_n species, which results in loss of X-H following protonation. However, there are some exceptions to this, such as when grafting is attempted using silica that has been modified at a low temperatures (typically temperatures below 300 °C) and hence retains vicinal silanols on the surface.⁶⁴ Both neighbouring silanol groups may react with the metal centre, giving a bis-grafted complex.



Scheme 1.9. (i) The formation of a mono-grafted M species with a 1:1 OH:M reaction on the surface of silica calcined at 700 °C

(ii) The formation of a bis-grafted M species with a 2:1 OH:M reaction on the surface of silica calcined at 200 °C

The ability to attach such a wide variety of metal complexes to solid supports makes SOMC an attractive method to employ for the tethering/immobilisation of organometallic complexes. SOMC methods are also simple to employ, often only requiring stirring of a suspension of the appropriately prepared oxide support with a solution of the metal complex.⁶⁴ The surface-bound species are then simply isolated by filtration and washed with a solvent to remove excess metal complex and the released free ligand (X-H).

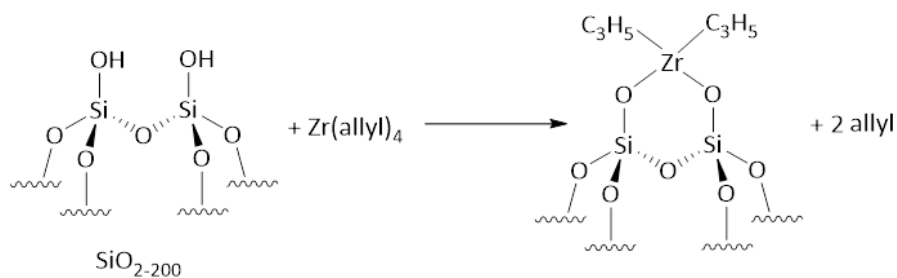
1.0.6.1 Organyl Metal Complexes Grafted on Silica

Organyl complexes, *i.e.* alkyl and aryl complexes,* are readily available for most metals. Both homoleptic and heteroleptic organyl complexes can be tethered to silica through SOMC-type approaches, though homoleptic compounds are more prevalent in the literature.⁶⁴ The silica surface grafting of such hydrocarbyl complexes exploits the release of the free hydrocarbon (R-H) *via* protonation as the main driving force for the reaction, something that is supplemented by the formation of a strong M-O bond.⁶⁴

The earliest examples of hydrocarbon complexes tethered to silica date from the 1970s, and were mainly allyl and methyl complexes of group 4 and 6 metals, which were studied as potential polymerisation and disproportionation catalysts.^{92, 93} For example, reaction of appropriately prepared silica with Zr(allyl)₄ (Scheme 1.10) results in the formation of a highly active alkene polymerisation

* Ligands on the metal centre contain only carbon and hydrogen

catalyst.^{92, 94} The structure of the surface Zr-allyl species was inferred from measuring the amount of propene released on reacting the zirconium allyl-functionalised silica with butanol.⁹⁵



Scheme 1.10. Reaction of $Zr(allyl)_4$ with silica calcined at 200 °C. The $Zr(allyl)_4$ reacts with two OH groups on the silica surface, releasing two propene groups.

A range of compounds with a combination of different hydrocarbyl ligands (*e.g.* aryl, allyl, *etc.*) and metals (*e.g.* Cr, Rh, Fe, *etc.*) can proceed *via* an SOMC style reaction. Figure 1.14 shows the structures of some examples of metal hydrocarbon complexes, such as $Cr(C_3H_6)_3$ (Figure 1.14(i)) and $Fe_2(Mes)_4$ (Figure 1.14(iv)), that can undergo SOMC and be tethered to the surface of silica before and after a SOMC reaction with the silanol groups on the silica surface.⁶⁴

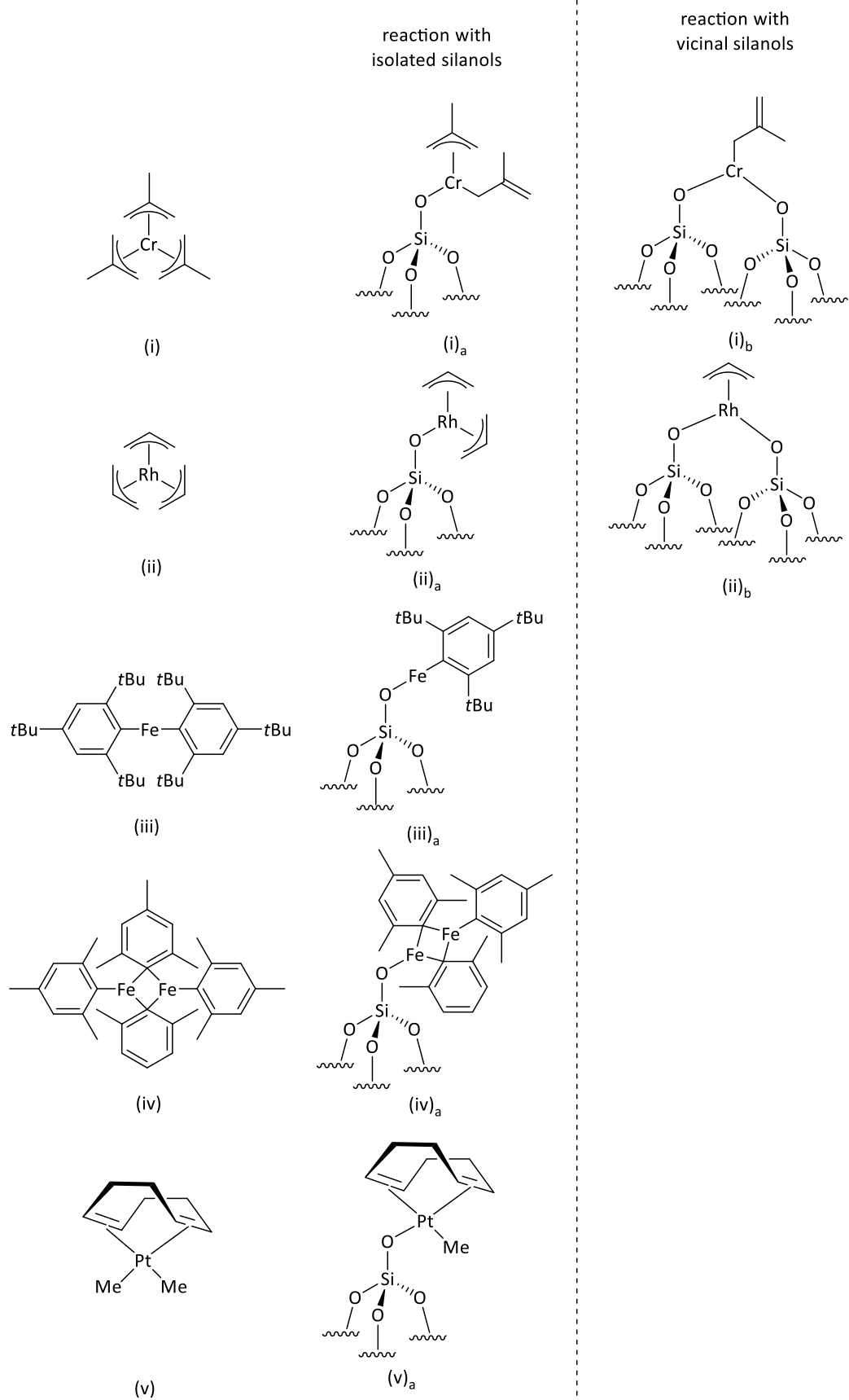


Figure 1.14. A selection of metal hydrocarbon complexes to highlight the wide variety of complexes that can undergo SOMC and be tethered to the surface of silica

Reaction of mixed alkyl/ η^5 -cyclopentadienyl complexes (*i.e.* η^5 -Cp_yML_mX_n, Cp = C₅H₅ or C₅Me₅) with silica generally results in the elimination of the alkyl rather than the η^5 -cyclopentadienyl ligand through protonation, as result of a combination of the greater volatility of the resulting alkane and the loss of aromaticity that would result in protonation of the cyclopentadienyl motif. Examples of the reaction of mixed alkyl/cyclopentadienyl complexes with silica are given in Figure 1.15(i),⁶⁴ emphasising the preference for the protonation and loss of the methyl over the cyclopentadiene ligands. However, it has been shown that the outcomes of reactions of mixed alkyl/ η^5 -cyclopentadienyl complexes are dependent on the nature of the dehydroxylated silica surface. For example, reaction of a mixed alkyl/ η^5 -cyclopentadienyl complex with highly dehydroxylated silica (calcined above 800 °C) can also lead to the ring opening of a siloxane bridge, leaving a ligand on the silica surface, Figure 1.15(ii).⁹⁶ This transfer of a ligand to the surface will only happen on highly dehydroxylated silicas, as the metal must be close to a highly strained and reactive [≡Si-O-Si≡] for the transfer to occur.⁹⁶ In the case where there is no ligand other than the Cp-ring on the metal centre, *i.e.* an homoleptic cyclopentadiene complex (MCp_y), a Cp-ring may be lost in the form of CpH, forming ≡SiO-MCp_{y-1} on the surface (Figure 1.15(iii)).⁹⁷ η^5 -Cyclopentadienyl complexes, such as MnCp₂ and FeCp₂,⁹⁸ tethered to oxide supports have been previously reported in the literature and have found application in catalysis. One such example is the Union Carbide ethene polymerisation system,⁹⁹ which comprises a chromocene-derived surface species supported on silica. The specific nature of the active catalytic site for polymerisation remains unknown, but it is well established that the Cr-Cp moiety is directly tethered to the silica surface.

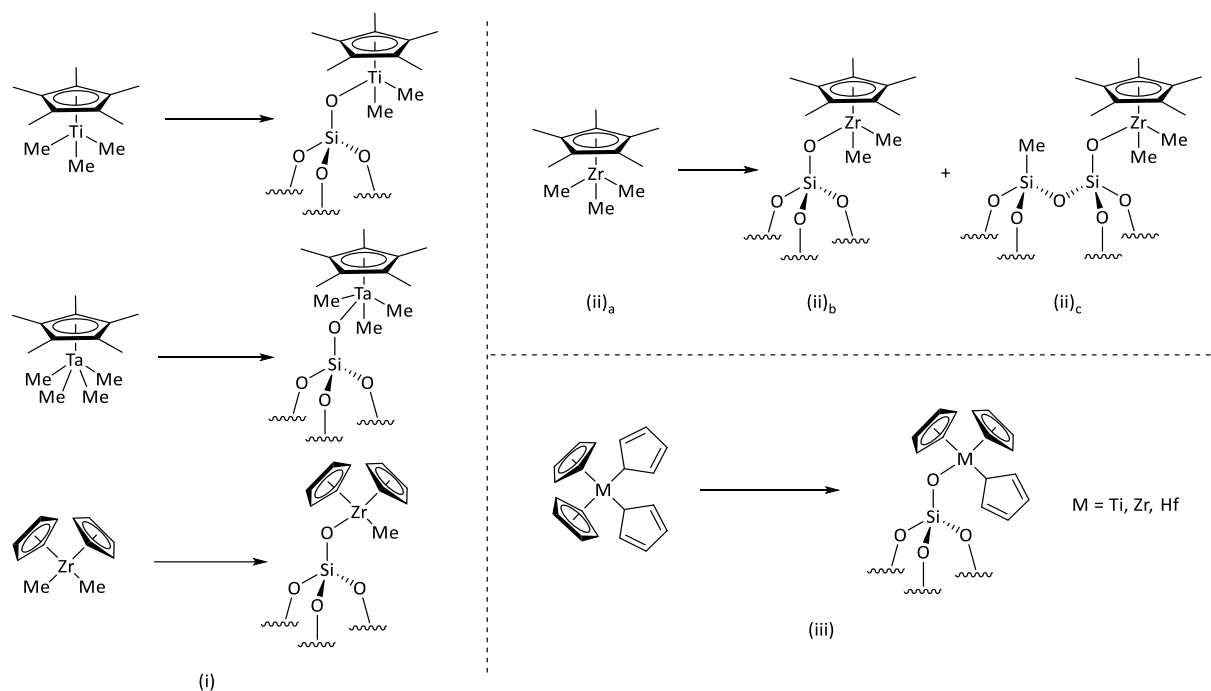
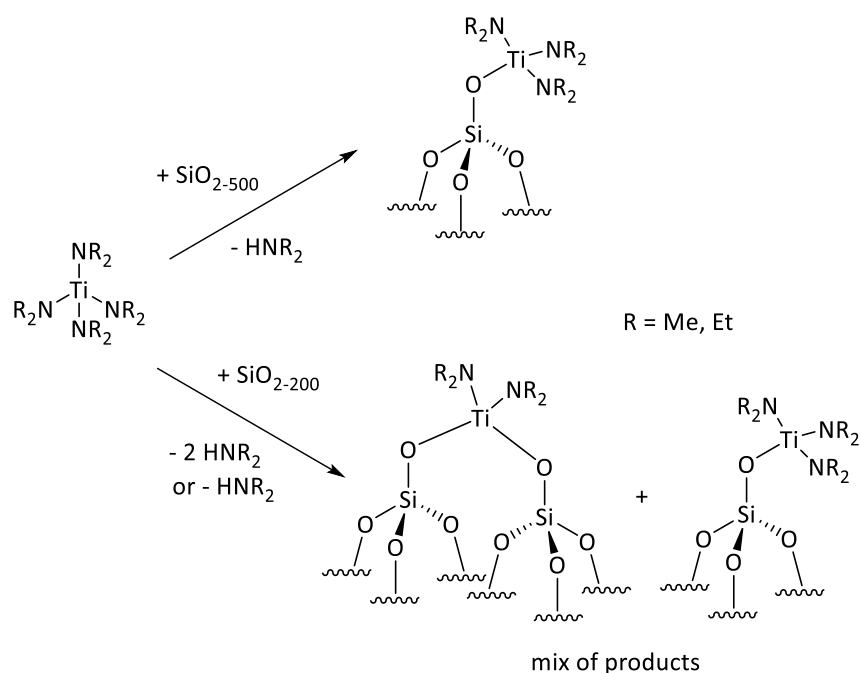


Figure 1.15. (i) Cyclopentadiene metal complexes reaction with hydroxyl groups on the surface of silica. The methyl ligand reacts preferentially over the cyclopentadiene ligand, leaving the cyclopentadiene attached to the metal centre; (ii) A highly dehydroxylated silica undergoing a siloxane ring opening after reaction with a cyclopentadiene complex, methylating the silica surface; (iii) a homoleptic cyclopentadiene complex reacting with a silica surface. When there are no other ligands, the Cp ligand will be protonated instead, and lost as CpH

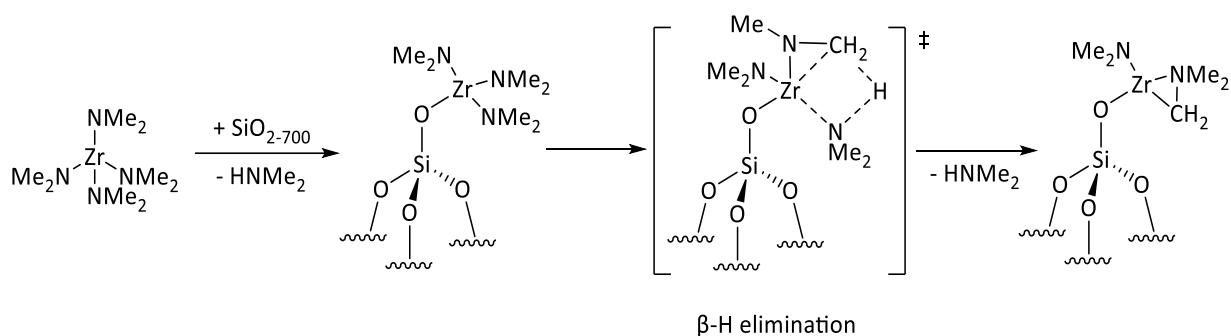
1.0.6.2 Silica-bound Metal Amide Complexes

Similar to the chemistry demonstrated by metal organyl complexes in their reactions with appropriately pre-treated silica, surface grafting of a wide range of transition metal amide complexes has also been investigated.¹⁰⁰ Homoleptic metal amide complexes are both prevalent and easy to prepare, with the amido motif offering significant scope for tuning structure and reactivity through a combination of steric and electronic effects. Silica grafting of metal amide complexes proceeds *via* protonation of the metal amide linkage liberating the corresponding amine; this is something that is generally regarded as more facile compared to the analogous reaction with a metal organyl complex as a result of the greater basicity of the amide ligand compared with that of a transition metal hydrocarbon. As with oxide surface immobilisation of metal hydrocarbon complexes, the mode of grafting of the transition metal amide complexes depends on the silica's pre-treatment, with silica calcined at lower temperatures giving mixtures of bis- and mono-grafted metal species. The lower the calcination temperature, and the lower the dehydroxylation of the silica surface, the more bis-grafted metal species will form on the surface. An example of this is shown in Scheme 1.11, which summarises the reactions of $\text{Ti}(\text{NET}_2)_4$ with silica calcined at 500 (SiO_{2-500}) and 200 °C (SiO_{2-200}), forming either predominantly the mono- or bis-grafted surface species, respectively.¹⁰¹



Scheme 1.11. Titanium amide reacting with silicas calcined at different temperatures and different degrees of dihydroxylation. The amide complex will form mostly mono-grafted surface species on silicas calcined at higher temperatures (>500 °C), and a mix of the mono- and bis-grafted species on silicas calcined at lower temperatures (<200 °C)¹⁰¹

Due to the greater reactivity of amide complexes compared to metal organyl complexes, there is a possibility of an amide complex undergoing further unintended chemistry after being tethered to the silica *via* SOMC. An example of an amide complex undergoing further chemistry after the initial tethering is Zr(NMe₂)₄. It was first postulated that the (≡SiO)Zr(NMe₂)₃ complex is an intermediate that will undergo β-H elimination to release another free HNMe₂ ligand, as seen in Scheme 1.12.¹⁰² However, further study into the SOMC reaction and the resulting surface species by Hamzaoui *et al.* has shown that a second dimethylamine is not released from the metal centre and that the true surface species is as shown in Figure 1.16.¹⁰³ The proton of the coordinated H-NMe₂ moiety originates from the hydroxyl groups on the silica surface and is liberated as part of the grafting process as the HNMe₂ generated temporarily interacts with a surface silanol, possibly by hydrogen bonding (Figure 16).¹⁰³



Scheme 1.12. The initial proposed mechanism of zirconium amide reacting with the silica surface¹⁰²

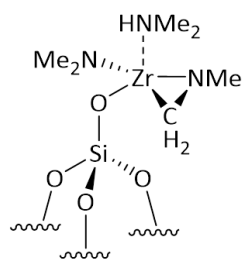
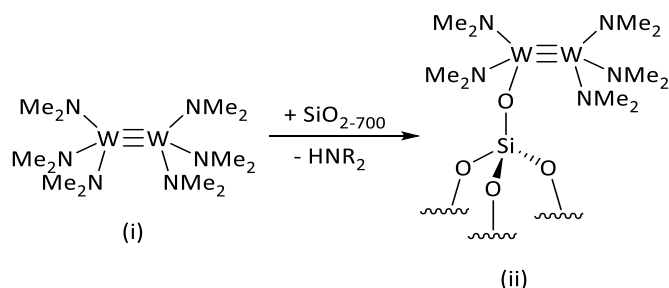


Figure 1.16. The current proposed final product of $Zr(NMe_2)_4$ tethered to silica¹⁰³

Metal amide complexes may also maintain their nuclearity upon immobilisation onto the silica surface. For example, $W_2(NMe_2)_6$, which contains a tungsten-tungsten triple bond and is known to be potentially useful in catalysis, has been shown to retain its nuclearity and triple bond after grafting onto silica, Scheme 1.13.¹⁰⁴ Further modification of the well-defined tungsten surface species (Scheme 1.13(ii)) produces a catalyst capable of alkyne metathesis. The preservation of the structure of the initial homogenous compound can be very useful in potentially maintaining the catalytic activity of a homogenous catalyst, while transforming it into an efficient and well-defined supported heterogeneous catalyst. Well-defined surface species also open up more possibilities for catalyst modification; a broad range of ligands can be introduced with greater control over the catalyst design than usually achieved with heterogeneous catalysts.

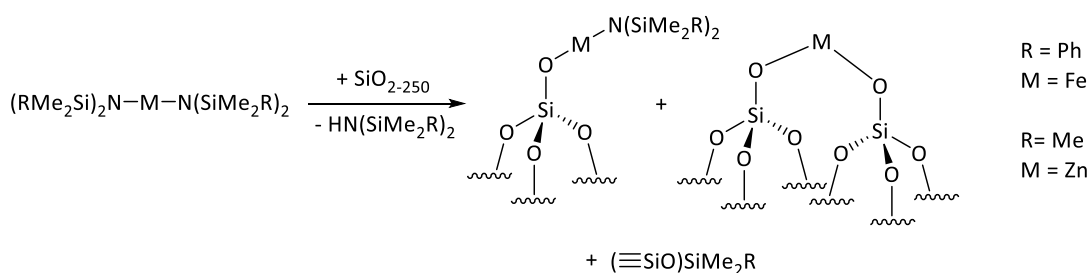


Scheme 1.13. A dinuclear tungsten complex, which maintains the $W=W$ bridge after grafting to the silica surface

1.0.6.2.1 Silica-grafted Silyl Amide Complexes

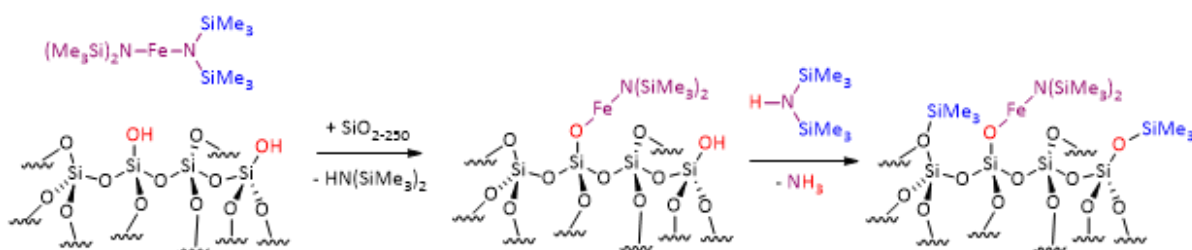
An important class of surface-grafted metal amides are the silyl amide derivatives $M(N(SiR_3)_2)_x$. As with alkyl metal and other metal alkyl/aryl amide species, silyl amide complexes react with a surface OH

group, protonating and losing a silyl amide ligand as the corresponding amine $\text{HN}(\text{SiR}_3)_2$. Similar to the SOMC-like tethering of hydrocarbon and other amide species onto silica (discussed in Section 1.0.6.1 and 1.0.5.2), the metal can form a mono- or bis-grafted surface species *via* SOMC (Scheme 1.14), with the ratio between the two species depending on the extent of dehydroxylation of the silica substrate.^{105, 106}



Scheme 1.14. Silyl amide complexes reacting with the silica surface, forming the mono- or bis-grafted complex depending on the pre-treatment of the silica surface^{105, 106}

For most silyl amide complexes, the released amine reacts further with the silica surface's silanols, forming silyl groups on the surface through silylation.¹⁰⁷ As both the metal centre and released amine react with the OH groups, the silylation of the silica surface becomes a competitive reaction that results in lower metal loadings than expected from the silanol density. For example, this type of competitive silylation of the silica surface is observed on reaction of $\text{Fe}(\text{N}(\text{SiMe}_3)_2)_2$ with silica (Scheme 1.15), a reaction that releases $\text{HN}(\text{SiMe}_3)_2$, which then goes on to react with another OH group, forming $(\equiv\text{SiO})\text{SiMe}_3$ and releasing ammonia.¹⁰⁸



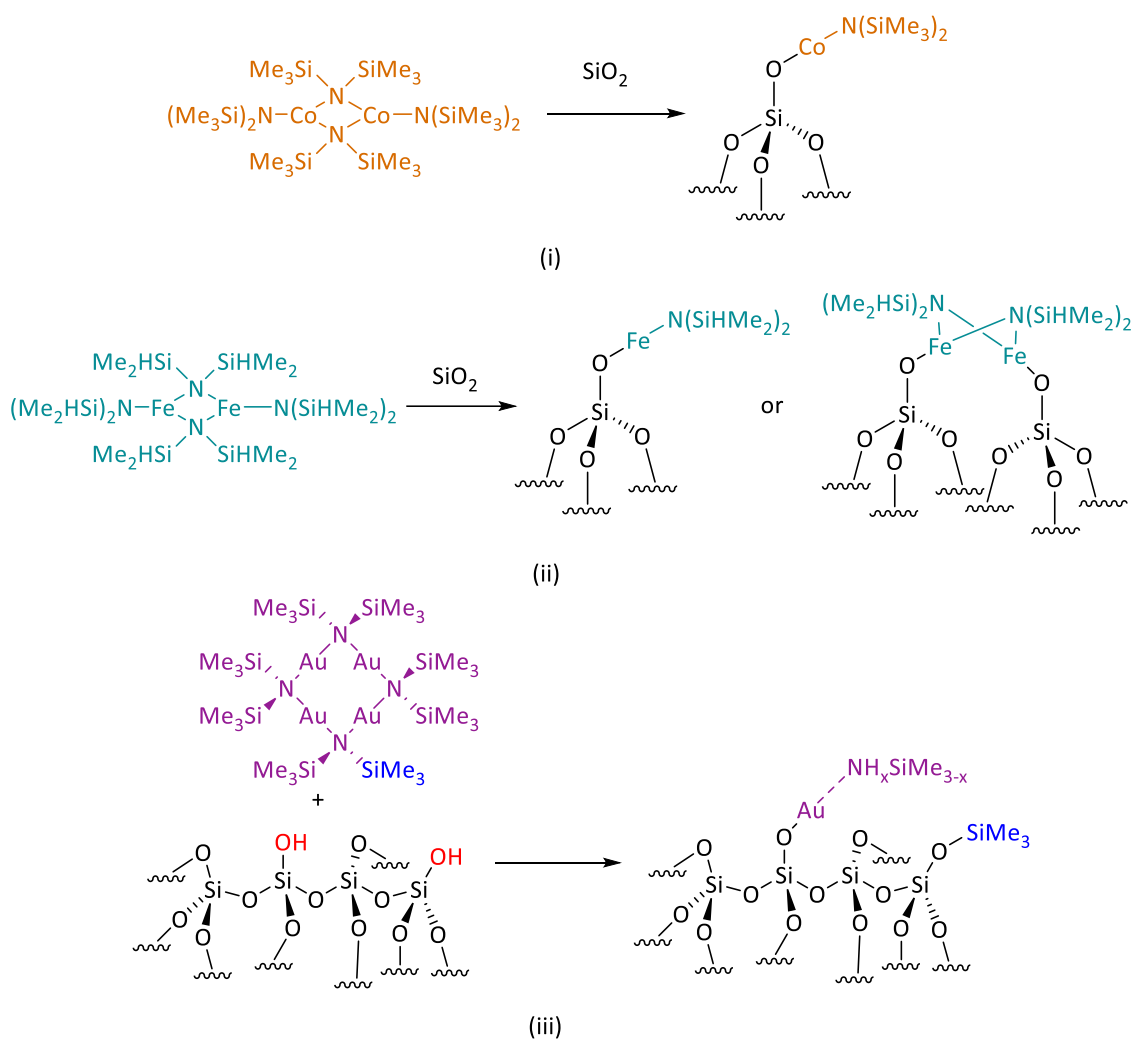
Scheme 1.15. The reaction of an iron silylamide complex reacting with silica. The released silylamine from the first step reacts further with a hydroxyl group on the silica surface, silylating the surface and releasing ammonia. This passivation of the silica surface is a competitive reaction with the initial SOMC-type grafting of the metal complex.¹⁰⁸

Bridging silyl amide complexes, such as those of cobalt¹⁰⁹ and iron¹⁰⁵ and gold silyl amide,¹¹⁰ typically form the corresponding mononuclear grafted complex from reaction with silica (Scheme 1.16). It is postulated that this happens as a result of steric constraints as the mononuclear species is less sterically demanding than the multinuclear species.¹⁰⁵ In all three cases of cobalt, iron, and gold silyl amide (Scheme 1.16), competitive silylation of the silica surface occurs.

As silylation and metalation of the surface occurs in the reactions between a metal silyl amide and a silica support in Scheme 1.16, it is expected that the surface area of the silica support will change, which Ahn *et al.* observe. The surface area of the silica supports summarised in Scheme 1.16(i) is reported by Ahn *et al.* to decrease, which is expected for silica that has undergone functionalisation of the surface. Since there was not a large change in the pore size, this led Ahn *et al.* to suggest that the degree of functionalisation and therefore silylation was minimal. Ahn *et al.* concluded that this limited extent of silylation is due to the short reaction times (<30 minutes).¹⁰⁹

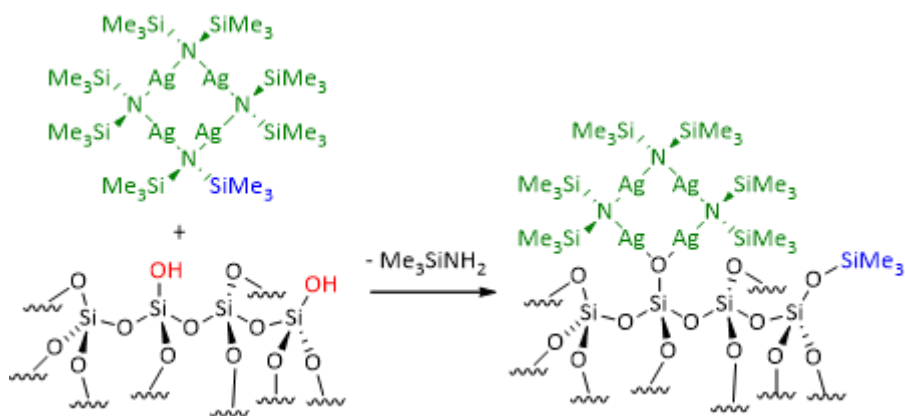
In contrast to the minimal silylation observed during the reaction of $\text{Co}_2[\text{N}(\text{TMS})_2]_4$ and silica by Ahn *et al.*, Deschner *et al.* reported significant silylation for the reaction of $\text{Fe}_2[\text{N}(\text{TMS})_2]_4$ and silica (Scheme 1.16(ii)), observed through the decrease of surface area and pore size of the silica. The surface area and pore size of the silica support (MCM-41) decreased on a scale comparable to chemical silylation by 1,1,3,3-tetramethyldisilazane, indicating that significant silylation occurred.¹⁰⁵ It should be noted that the reaction times reported by Ahn *et al.* and Deschner *et al.* are different; the reaction time of Scheme 1.16(ii) is longer than the reaction time of Scheme 1.16(i), 18 vs 0.5 h, respectively. Both research groups do conclude that the length of reaction time affects the degree of silylation, with longer reaction times showing a higher degree of silylation on the silica surface. This is consistent with the observation made by Deschner *et al.* who report a higher degree of silylation than Ahn *et al.* using analogous reactions.

Gajan *et al.* report that 50% of the available surface silanols reacted with a metal centre, with the Au-N bond being cleaved during the grafting process (Scheme 1.16(iii)). The product of Scheme 1.16(iii) is reported to be a good catalyst for liquid-phase epoxidation of trans-stilbene under aerobic conditions, showing that while the metal loading of silyl-amide complexes might be limited by the competing silylation reaction, highly active catalysts can still be obtained.¹¹⁰



Scheme 1.16. A series of reactions of silica with multinuclear silylamide complexes^{105, 109, 110}

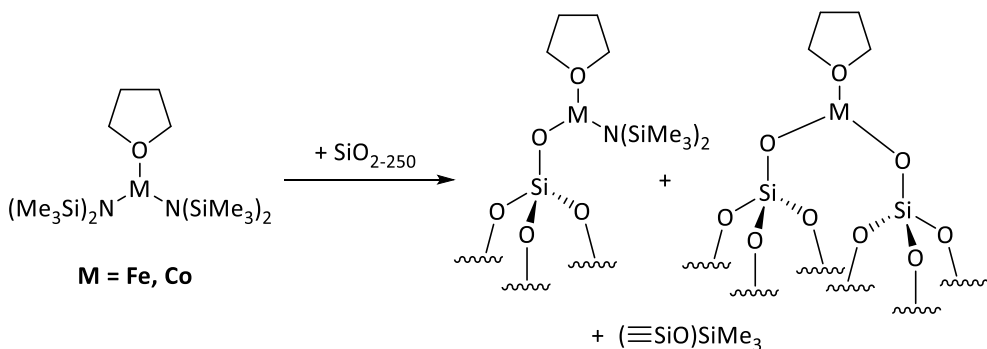
While metal-bridging silyl-amide complexes generally react with a silanol to form the mono-nuclear grafted complex, as shown in Scheme 1.16, there are some specific cases where the original nuclearity is maintained. The metal-metal bridges are preserved during the grafting process, resulting in the synthesis of a multinuclear surface metal-containing species. A specific case of this preservation of the initial nuclearity was obtained by Oakton *et al.*, who reacted a silver silyl-amide complex with silica (Scheme 1.17).⁵⁷



Scheme 1.17. A multinuclear gold silylamide complex that maintains its multinuclearity post-grafting⁵⁷

Silyl amide metal complexes with coordinated solvents (such as THF) will also undergo SOMC-type chemistry when grafting to a silica surface. The coordinated solvent typically remains coordinated to the metal centre, forming the corresponding solvent adduct on the surface (Scheme 1.18).¹⁰⁵ The THF remains coordinated, even if both silyl-amide ligands are lost, forming a metal THF adduct on the silica surface.¹⁰⁵

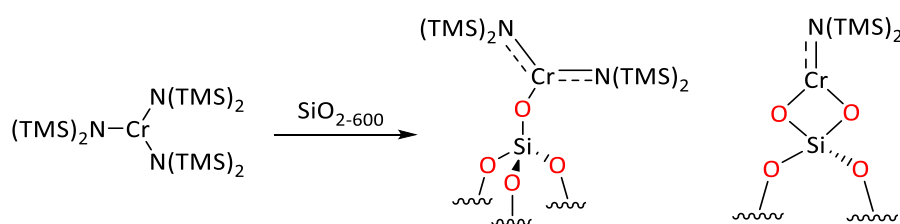
Liang *et al.* reported that the presence of the THF on the cobalt has a great effect on the resulting surface area of the silica support, with the pore parameters being significantly smaller when THF is present (a decrease in surface area of 60%). Some of the decrease in surface area will be due to metalation and silylation occurring, but Liang *et al.* suggests that the strongly coordinating THF occupies void space in the pores by coordinating to Lewis-acidic sites on the silica surface.¹⁰⁶



Scheme 1.18. Silylamide complexes with a coordinated THF solvent group.¹⁰⁵

While this thesis has discussed the grafting of an organometallic complex to isolated or vicinal silanols, it should be noted that silyl-amide metal complexes have also been reported to react with geminal silanols on the silica surface. An example of a metal silyl-amide complex reacting with a geminal silanol is found in Lamb *et al.*'s work on tethering chromium amide (Scheme 1.19) to the surface of silica for use as an olefin oligomerisation catalyst.¹¹¹ Lamb *et al.*'s work on the reaction of a chromium(III) amide with silica suggests that the Cr metal centres graft to both the isolated and geminal silanol surface

groups giving rise to two distinct structures.¹¹¹ However, it is difficult to determine whether the chromium is tethered to a geminal silanol as Lamb postulates, or whether a bis-grafted species is formed from reaction with vicinal silanols. The silica used has been calcined at 600 °C, suggesting that there should be no, or at least, very few vicinal silanols on the surface, supporting Lamb's claim that the chromium is bound to a geminal silanol through the loss of two free silyl amine molecules. Lamb reports that the paramagnetic nature of the surface-bound Cr^{III} species in combination with solid-state ²⁹Si NMR spectroscopy as a relaxation agent give a means of "mapping" where the chromium species reside on a silica surface; the silicon resonances that arise from the Si species that are in close proximity to the paramagnetic metal centre experience both a (small) change in chemical shift, but principally peak intensity.



Scheme 1.19. Two distinct structures of surface-bound Cr-amide species identified by Lamb et al. on the surface of Aeroperl 300/30 silica⁵⁷

Lamb's work on tethering chromium silyl amide species to silica,¹¹¹ along with other studies, such as work by Oakton's work on silver silyl amide⁵⁷ and Liang's study on cobalt and iron amides,¹⁰⁶ provides evidence that SOMC-like techniques can be applied to amide and silyl-amide species when tethering to a silica surface. The SOMC-like reactions of silyl amide organometallic species and silica have been reported to produce well-defined surface species on the silica, similar to the SOMC-methods used to synthesise well-defined surface-grafted metal hydrocarbon species (Section 1.0.6.1). The well-defined surface metal amide surface species produced in the SOMC-like reaction between a silyl amide complex and silica can undergo further chemistry, such as reduction.⁵⁷

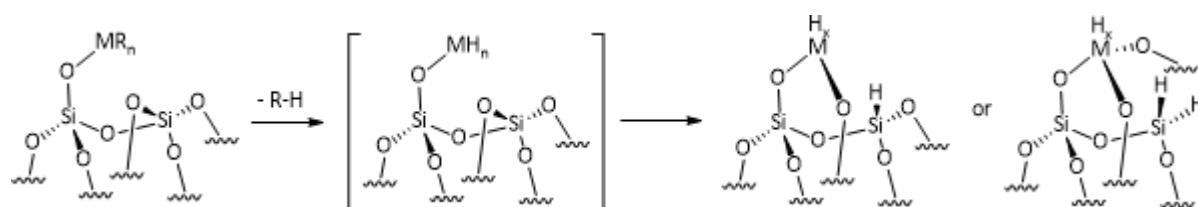
1.0.7 Reduction of Organometallic Precursors Grafted Oxide Support Surfaces

As discussed in Section 1.0.3, a common method for the preparation of metal nanoparticles is through the reduction of metal salts by chemical means such as the addition of NaBH_4 .^{19, 21} This has been extended to organometallic complexes, when free from a solid catalyst support, with their chemical reduction also giving rise to the formation of nanoparticles.¹⁹ However, in contrast, once a nanoparticle precursor (metal salt or organometallic complex) is tethered to a support, the most common means of reduction are quite different from those of non-supported nanoparticle precursors. For nanoparticle precursors bound to surfaces, the most widely used reduction method is reaction with hydrogen gas, usually at elevated temperatures.¹¹² This change from chemical- to thermal-based

methods is likely due to the difficulty of the chemical reducing agent being able to reach all of the precursor in deeper areas in the support, or even if the reducing agents reached the deeper pores of the support, it might be unable to reduce the precursor due to being constrained by the structure of the surrounding pore. The small size of hydrogen is advantageous since it readily diffuses into pores and can hence easily reduce metal species buried within pores, something which contrasts with the use of other chemical reductants such as NaBH_4 , which is larger and hence will not penetrate within the pores so readily. While there are some examples of chemical reduction of nanoparticle precursors on solid supports, they are rare compared to those describing thermal reduction of the precursor.¹¹³

1.0.7.1 Reduction of Organometallic Precursors on Oxide Supports under Hydrogen

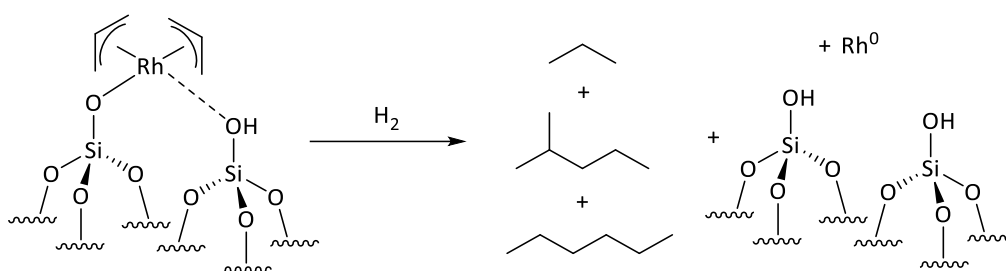
Heating under hydrogen gas is one of the most common chemical methods of reducing a supported metal species. Reduction by hydrogen gas can even occur at relatively low temperatures due to the unstable nature of some surface species. For example, a range of early transition metal organyl complexes, such as $-\equiv\text{SiO}-\text{Zr}(\text{Np})_3$ (Np = neopentyl), readily react with hydrogen at temperatures between 100 – 200 °C to form metal hydrides on the silica surface.¹¹⁴ As reaction temperature increases, the hydride is transferred to the silica surface and the metal is incorporated into the support (Scheme 1.20).¹¹⁴⁻¹¹⁶ It is thought that the formation of the surface hydride and incorporation of the metal happens *via* the loss of the hydrocarbon ligands (R) by protonation. The hydrocarbon ligand reacts with hydrogen, breaking the metal-carbon bond, and releasing R-H and forming a metal hydride on the surface. Subsequently, this highly reactive metal hydride species can react further with nearby siloxane bridges, transferring the hydride to the surface and forming an M-O bond (Scheme 1.20).¹¹⁵



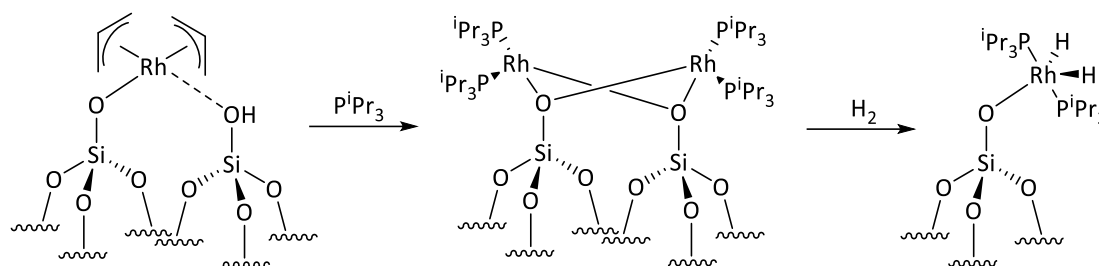
Scheme 1.20. Reduction of supported hydrocarbon complexes by thermal treatment under hydrogen, releasing a free R-H molecule and forming a metal hydride on the silica surface.¹¹⁵

The formation of a stable surface hydride species through reduction of a surface organometallic species under hydrogen typically occurs with early transition metals (such as Zr,¹¹⁷ Ti,¹¹⁸ Ta,¹¹⁹ and Hf¹²⁰), but there are some examples of late transition metals that can form stable surface hydride species. Reported examples of late transition metal hydride surface species formed through reduction under hydrogen are rare and often debated. For example, for $[\text{Rh}(\eta^3\text{-C}_3\text{H}_5)_3]$ grafted on silica (previously shown in Figure 1.14(ii)), which reportedly reacts with hydrogen to form a surface dihydride^{121, 122} that can catalyse the hydrogenation of alkenes¹²² and arenes.¹²³ However, there is debate on whether this species is a grafted metal hydride or not. A later paper by Gates *et al.*,¹²⁴ and

then further work by Basset and co-workers,^{125, 126} suggests that most of the allyl ligands of $[(\equiv\text{SiO})(\text{RhC}_3\text{H}_5)]$ are lost, forming propane and hexanes when heated under H_2 and leaving Rh^0 on the surface of the silica (Scheme 1.21). Further attempts to make the Rh-dihydride surface species were done by exposing $[(\equiv\text{SiO})(\text{RhC}_3\text{H}_5)]$ to PMe_3 , as phosphines can stabilise the metal coordination sphere, before heating under hydrogen. While a dihydride species was formed *via* the thermal treatment, it was not grafted to the silica surface, instead being surface-attached by ion pairing.¹²⁷ A rhodium surface hydride was eventually tentatively formulated with use of a bulkier phosphine ligand (P^iPr_3 instead of PMe_3), Scheme 1.22.¹²⁸



Scheme 1.21. Proposed products from the thermal treatment of grafted $[\text{Rh}(\eta^3\text{-C}_3\text{H}_5)_3]$ on silica under hydrogen.^{125, 126}

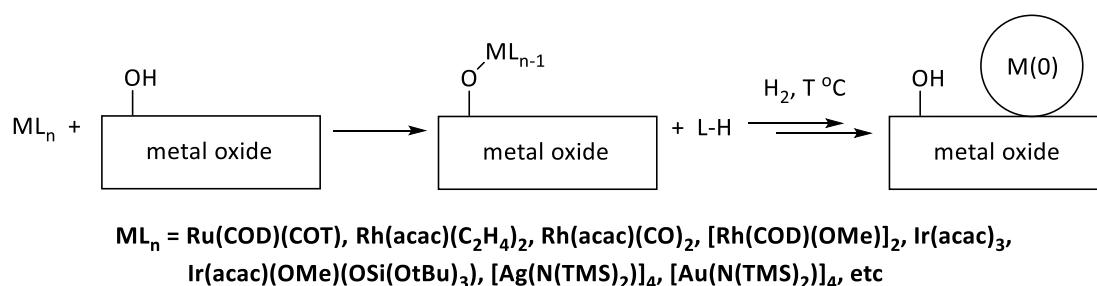


Scheme 1.22. A rhodium dihydride complex formed from grafted $[\text{Rh}(\eta^3\text{-C}_3\text{H}_5)_3]$ on silica undergoing thermal treatment under hydrogen¹²⁸

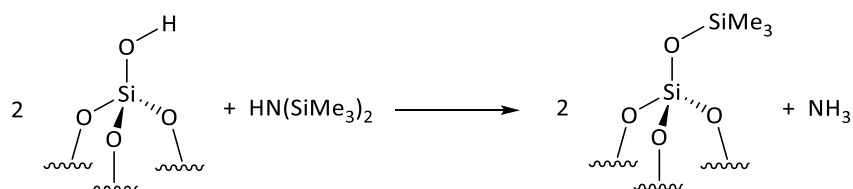
While early transition metal complexes tend to form surface hydride species when reduced under hydrogen, grafted late transition metal complexes on silica are more likely to form small nanoparticles, regenerating silanol groups (SiOH) on the silica surface (Scheme 1.23); the thermodynamic force behind the formation of a strong SiO-H bond drives the formation of nanoparticles.¹²⁹ This nanoparticle formation occurs with a wide range of late transition metals and ligands, forming nanoparticles with a “clean” surface.^{†69, 130-133} This difference of behaviour between late and early transition metals on reaction with hydrogen is postulated to be due to the larger predisposition of late transition metals to undergo reductive elimination.¹²⁹

† Nanoparticles with a “clean” surface is defined as nanoparticles without the presence of surfactants or capping agents.

Late transition metal silyl amide complexes form nanoparticles on the surface and also silylate the generated silanol groups formed through the reduction, producing an OH-free silica surface (Scheme 1.24).^{57, 110, 134} Trimethylsilylamide metal complexes with ‘coinage’ metals (copper, gold, or silver) have been shown to be particularly successful precursors for the formation of small nanoparticles that are capable of catalysis, such as Oakton *et al.*'s synthesis of silver nanoparticles,⁵⁷ which has been discussed previously in Section 1.0.4.



Scheme 1.23. The general reaction pathway of late transition metal surface species when heated under hydrogen.¹²⁹



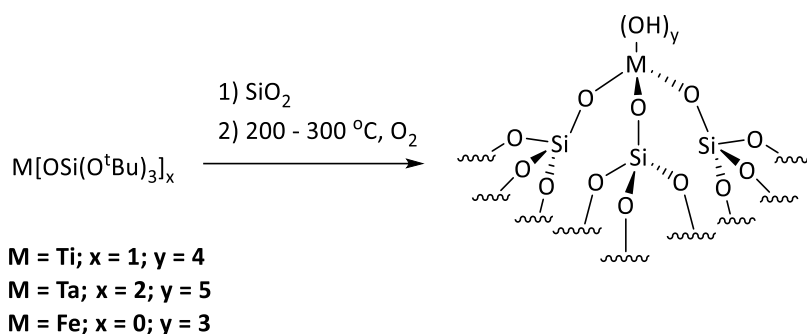
Scheme 1.24. The silylation of the silica surface by the reaction of SiOH and $\text{HN(SiMe}_3)_2$ ¹³⁵

To conclude, there is a difference in behaviour between early and late transition metals in surface-bound organometallic species when thermally treated under hydrogen gas.¹²⁹ Early transition metal surface species will react to form metal hydride species on the surface, which can react further with higher temperatures to incorporate the metal into the silica and form Si-H surface sites. Late transition metal systems, on the other hand, rarely form surface hydride species, except when phosphine ligands are present to stabilise the hydride, and these late transition metal hydride species are very rarely formed by thermal treatment under hydrogen gas, with one example being $[(\equiv\text{SiO})(\text{RhC}_3\text{H}_5)]$ pre-treated with bulky phosphine P^iPr_3 prior to heating under hydrogen.

1.0.7.2 Calcination of Organometallic Precursors on Oxide Supports under Inert Gas or Vacuum

Calcination usually refers to a treatment at a high temperature under air or oxygen (typically $>400^\circ\text{C}$). In this project, calcination of surface-bound organometallic species is used to describe the removal of carbon-containing species, including organic ligands, tethered to the grafted metal centre through thermal treatment under an inert gas or vacuum.^{136, 137} The metal surface sites can remain isolated upon heating and removal of the organic ligands, especially early or first-row transition metals or if the metal loading on the silica surface is low. For example, surface $\text{M}[\text{OSi}(\text{O}^t\text{Bu})_3]_x$ complexes can be

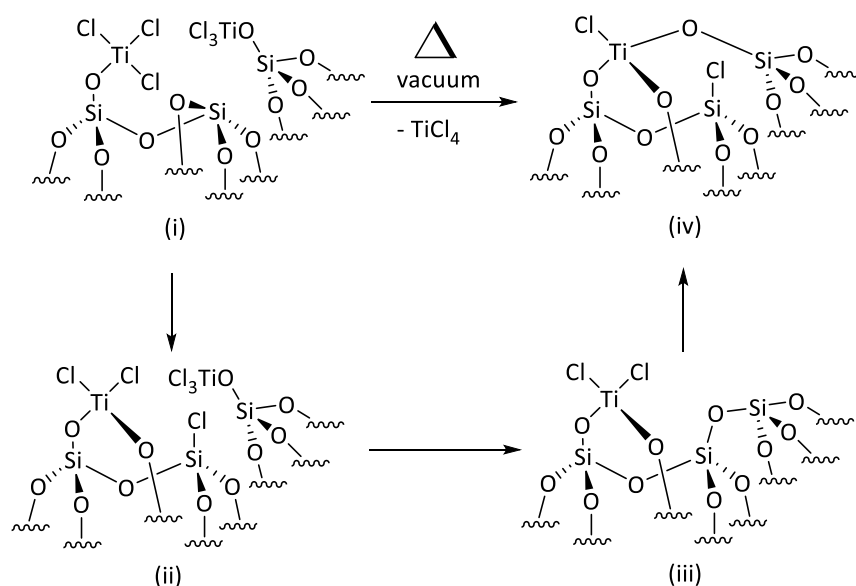
cleanly converted to carbon-free materials between 200 – 300 °C when heated under oxygen (Scheme 1.25).⁶⁴ At temperatures above 300-600 °C, the metal can start to be incorporated into the support matrix or sinter to form metal-oxide clusters on the surface.¹³⁸



Scheme 1.25. The formation of isolated surface sites via calcination of grafted metal -OSi(O^tBu)₃ complexes under a normal laboratory atmosphere.⁶⁴

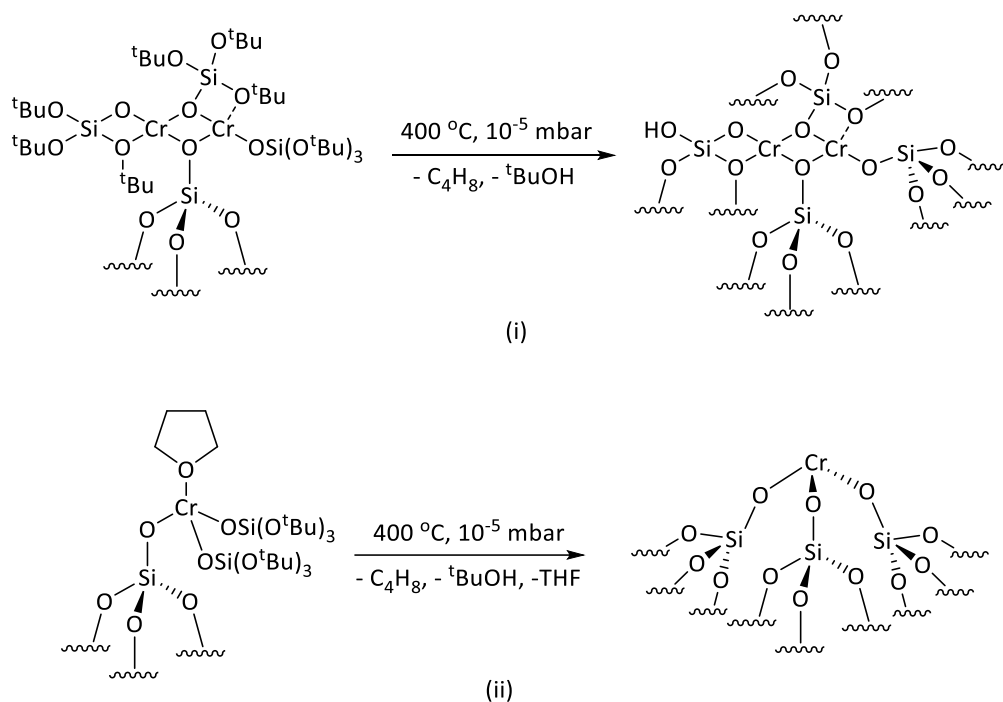
Calcination does not necessarily need to be achieved under oxygen or air, and it can be preferable to calcine silica-bound organometallics under an inert gas, such as nitrogen, or under vacuum. When heated under vacuum (>150-400 °C), -Cl, -O^tBu, OSi(O^tBu)₃, and -N(SiMe₃)₂ ligands can be easily removed from the metal centre to leave an isolated metal site. The loss of the ligands upon thermal treatment involves the metal reacting with nearby siloxane bridges, and forms stable silicate surface sites.^{139, 140}

Metal chlorides supported on silica, such as TiCl₄, CrO₂Cl₂, and VOCl₃, have been shown to form bis- and tris-grafted species when heated under vacuum (Scheme 1.26).^{139, 140} The degree of grafting of the metal chloride depends on the calcination temperature, with a higher temperature leading to a higher degree of grafting. TiCl₄ is a good example of this; TiCl₄ initially grafts to the silica surface *via* a hydroxyl group in a mono-grafted species (Scheme 1.26(i)). This grafted TiCl₄ species (Scheme 1.26(i)) is stable up to 50 °C, but further heating transfers a Cl ligand to a nearby siloxane bridge, become the bis-grafted species in Scheme 1.26(ii). Above 250 °C, TiCl₄ is eliminated from the silica surface, decreasing the metal loading; the proposed mechanism for this is believed to involve the reaction of surface Si-Cl with remaining TiCl₃ sites reforming a siloxane bridge, as illustrated in Scheme 1.26(iii). There is also further restructuring of the Ti-sites with a second transfer of a Cl ligand to the surface, leading to tris-grafted species (Scheme 1.26(iv)). Above 450 °C, there is no mono-grafted Ti-species remaining on the surface.¹³⁹ Similar mechanisms have been proposed for CrO₂Cl₂, and VOCl₃ surface species.¹⁴⁰



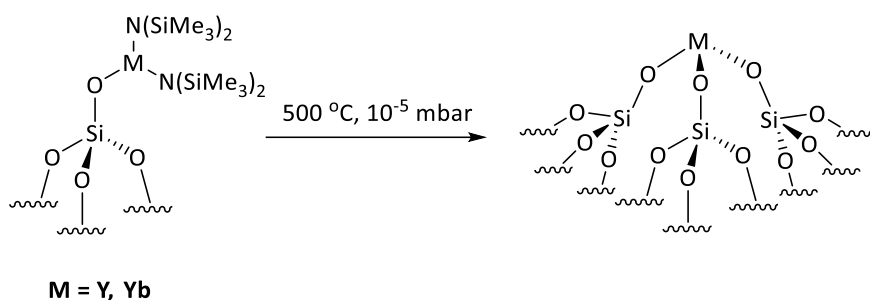
Scheme 1.26. The proposed mechanism of grafted TiCl_4 on silica forming bis- or tris-grafted surface species when heated under vacuum¹³⁹

For tethered organometallics with metal-bridging, the nuclearity of the surface species may be maintained throughout the air-free calcination, forming metal silicates with any pre-existing bridges remaining. An example of this maintained nuclearity is tri-*tert*-butoxysiloxy chromium, which is a dinuclear organometallic complex, and the corresponding monomeric THF-adduct species. As shown in Scheme 1.27(i), the Cr^{II} species remains a dimer under thermal treatment,¹⁴¹ releasing *iso*-butene, *tert*-butanol, and water as it decomposes to the metal silicate $[(\equiv\text{SiO})_4\text{Cr}_2]$. The corresponding monomeric chromium species will remain monomeric upon decomposition to an isolated chromium-silicate as seen in Scheme 1.27(ii).¹⁴² The dimer and monomeric chromium species both maintain their nuclearity throughout air-free calcination.



Scheme 1.27. Two chromium complexes that maintain their nuclearity when treated thermally under vacuum, forming either mono- or bi-metal silicate species^{141,142}

Lanthanide metal silylamides have also been shown to form isolated metal silicate sites on a silica surface under a thermal treatment under vacuum (Scheme 1.28). For example, the thermolysis of $[(\equiv\text{SiO})\text{M}(\text{N}(\text{SiMe}_3)_2)]$ produces a tripodal surface species, releasing silylamine, which reacts further to silylate the silica surface, producing surface SiMe_3 sites and releasing NH_3 (similar to silylation observed during the tethering of metal silyl amides to silica in Section 1.0.6.2.1).¹⁴³



Scheme 1.28. Lanthanide silyl amide complexes losing their silyl amide ligands when heated under vacuum, forming lanthanide metal silicate surface species.¹⁴³

1.0.8 Hydrogenation Catalysis

Hydrogenation is a broad reaction class that covers many reactions such as hydrogenation of carbon monoxide to methanol,¹⁴⁴ the transformation of hydrogen and nitrogen to ammonia,¹⁴⁵ the reduction of alkenes and alkynes to alkanes,¹⁴⁶ the reduction of aldehyde and ketones,¹⁴⁷ and asymmetric hydrogenation.^{148, 149} Hydrogenation is one of the most important catalytic reactions used in industry for the synthesis of both bulk and fine chemicals.¹⁵⁰ However, the reaction conditions needed for

practical catalytic heterogeneous hydrogenation can be difficult to achieve, often requiring both high temperatures and high hydrogen pressures.¹⁵¹ Improving the catalysts used for hydrogenation has the benefit of not only using milder conditions, but also higher selectivity towards desired products, reduction of reaction time, better conversion, and reduced formation of impurities and side-products.

The earliest example of catalysed hydrogenation used commercially was in 1823, which used platinum as a heterogeneous catalyst to mediate the addition of hydrogen to oxygen in Döbereiner's lamp.¹⁵² In 1897, Sabatier pioneered heterogeneous hydrogenation with his discovery of the Sabatier process, which used nickel to catalyse the addition of hydrogen to gaseous hydrocarbons.¹⁵³

As stated in Section 1.0.2, heterogeneous catalysis is more common in industry, and this is also true for catalytic hydrogenation. Industrial hydrogenation catalysts are often precious metals such as platinum, ruthenium, rhodium, iridium, or palladium deposited on a solid support such as silica, carbon, or alumina. However, these metals are often expensive, easily poisoned, and lost through leaching.¹⁵⁴ The development of cheaper alternatives that use more abundant metals such as iron, nickel or cobalt has been of great interest. However, there is often a trade-off with using non-precious metals in the catalysts, with the use of Raney Nickel catalyst for hydrogenation, which often requires higher pressures compared to other precious metal counterparts.¹⁵⁵

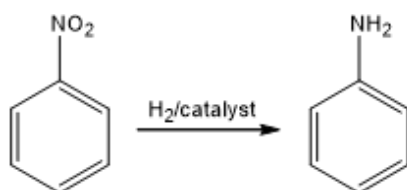
1.0.8.1 Hydrogenation Catalysis using Cobalt Nanoparticles

Cobalt is a non-precious metallic element that is capable of mediating hydrogenation catalysis. Compared to its precious counterparts, such as platinum¹⁵⁶ and ruthenium,¹⁵⁷ it shows lower activity and selectivity in reactions such as the heterogeneous hydrogenation of cinnamaldehyde (CNA)¹⁵⁸ and furfural¹⁵⁶ to their corresponding alcohols. However, despite its limitation cobalt-based hydrogenations are a more economic option due to its lower price and high abundance.¹⁵⁹ There has been interest in developing cobalt nanoparticles further for the use of hydrogenation due to the benefit of its lower cost. Cobalt nanoparticles have already shown much promise in the selective reduction of aldehydes; the hydrogenation of quinolones;^{160, 161} the hydrogenation of nitroarenes;¹⁶² and the asymmetric transfer hydrogenation of ketones.¹⁶³

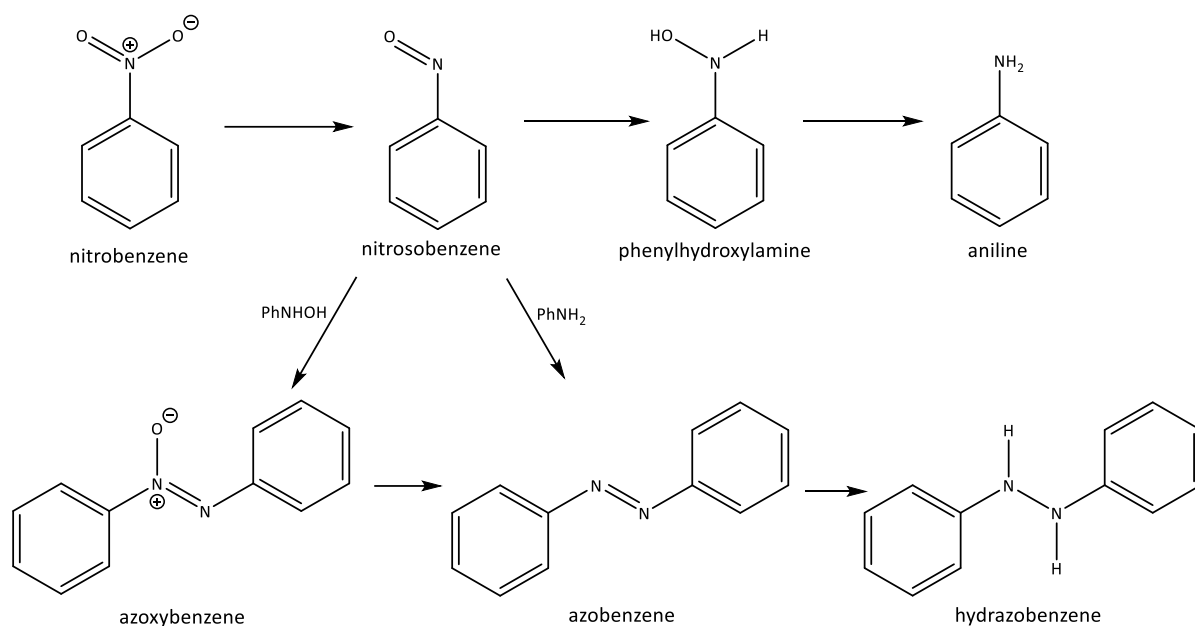
1.0.8.1.1 Hydrogenation of Nitrobenzene to Aniline by Cobalt NPs

A common model reaction for hydrogenation catalysis testing (catalyst synthesis/structure/property correlation) is the reduction of nitrobenzene to aniline, Scheme 1.29.¹⁶⁴ Additionally, aniline and its derivatives have significant commercial interest, hence there is continued drive to establish synthetic methods that operate under mild conditions.¹⁶² Although nitrobenzene has one likely site available for hydrogenation, the NO₂ group, the reaction has been shown to proceed through a complex reaction pathway, with several intermediates and possible side-products (proposed and simplified mechanism

shown in Scheme 1.30), making it potentially a useful transformation to probe catalyst selectivity.¹⁶⁵ However, in the literature, the best catalysts show high selectivity towards aniline (~99%),^{162, 166, 167} and hence this reduction is often explored in terms of catalytic activity rather than selectivity.¹⁶²



Scheme 1.29. Hydrogenation of nitrobenzene to aniline



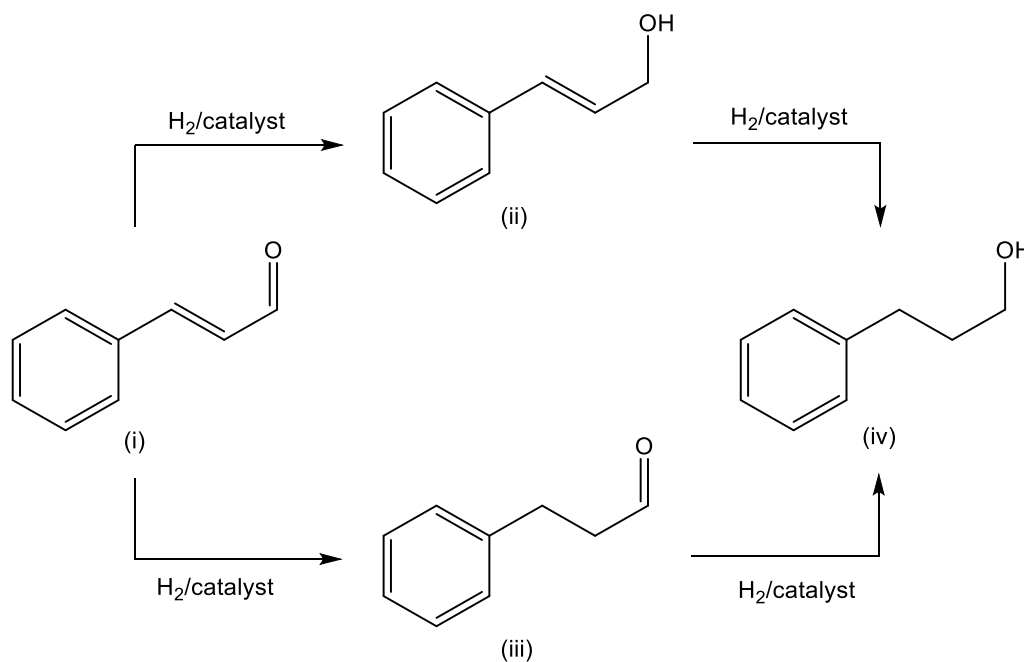
Scheme 1.30. Proposed mechanism of the hydrogenation of nitrobenzene and its intermediates and possible products¹⁶⁵

1.0.8.1.2 Hydrogenation of Cinnamaldehyde by Cobalt NPs

While the hydrogenation of nitrobenzene is a common model reaction for testing the activity of a hydrogenation catalyst, selectivity is often commonly tested by the hydrogenation of cinnamaldehyde (CNA). Unlike nitrobenzene, CNA has two available sites for hydrogenation (Scheme 1.31) the alkene group and the aldehyde group.¹⁶⁸ The hydrogenation of the aldehyde forms cinnamyl alcohol (CNOL), the hydrogenation of the alkene forms hydrocinnamaldehyde (HCNA), and the hydrogenation of both sites forms hydrocinnamyl alcohol (HCNOL). With two possible hydrogenation sites, the hydrogenation of CNA can be used to study selectivity and filter out catalysts with undesirable selectivity, as has been used as such by Dragoi *et al.*¹⁶⁹

For α,β -unsaturated aldehydes, such as CNA, the hydrogenation of the C=C bond is favoured thermodynamically over the hydrogenation of the C=O bond.¹⁷⁰ As the hydrogenation of the C=C bond is favoured thermodynamically over the hydrogenation of the C=O bond, there is more interest in targeting the reduction of the aldehyde. Therefore, the most preferable target reduction product of

CNA is CNOL.¹⁷¹ The transformation of CNA to the unsaturated alcohol is also of industrial significance since the CNOL product is a valuable compound used widely in pharmaceutical chemistry.¹⁷¹ It has been noted that cobalt catalysts are particularly suitable for selective hydrogenation to the unsaturated alcohol,^{172, 173} but it requires a higher hydrogen pressure or longer reaction time due to cobalt not being very active in this hydrogenation.¹⁷⁴



Scheme 1.31. Possible routes for the hydrogenation of cinnamaldehyde
 (i) Cinnamaldehyde (CNA) (ii) Cinnamyl alcohol (CNOL) (iii) Hydrocinnamaldehyde (HCNA) (iv) Hydrocinnamyl alcohol (HCNOL)¹⁶⁸

While both the hydrogenation of nitrobenzene and of CNA are well-established model reactions that are ideal for exploring different attributes of a catalyst's behaviour, activity and selectivity, respectively, the hydrogenation of CNA has the additional benefit of occurring at lower temperatures (150 °C) and pressures (1 atm). As part of this project includes the exploration of the activity and selectivity of very small nanoparticles, avoiding high temperatures that may cause sintering, and therefore increase the size of the particles, is important. The hydrogenation of CNA is a suitable reaction for this project due to being able to carry it out at lower temperatures.

1.1.0 Project Aims

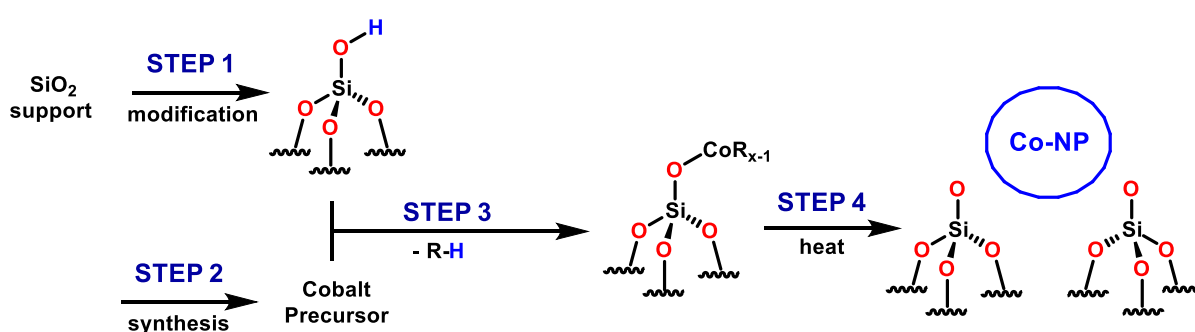
As described above, the synthesis of nanoparticles has a long history, dating back to the 1850s and Faraday's synthesis of Au nanoparticles (Scheme 1.3).^{19, 20} Since then, there has been a broad and varied range of different methods used to synthesise nanoparticles, such as the thermal decomposition of metal(0) precursors (Figure 1.2)²²⁻²⁵ and the chemical reduction of a precursor (*e.g.* HAuCl₄ precursor) using a reducing agent such as NaBH₄ (Scheme 1.4).^{19, 21} It has also been shown that

there is an interest in very small nanoparticles (<1 nm), *i.e.* sub-nanosized particles, due to the prediction of their greater activity and selectivity than nanoparticles in catalysis.⁷⁷ However, there are still many difficulties in synthesising and maintaining the small size of sub-nanosized particles, as discussed in Section 1.0.5.1, as well as keeping the surface of the resulting sub-nanosized particles “clean” enough from capping agents for the particles to be catalytically active.⁸⁴

This project explores routes for controlling the size of nanoparticles without capping agents, with the aim of targeting sub-nanosized particles. Each step of the method will be explored to determine how it affects the size of the resulting particles. Part of this project will involve testing the resulting particles for activity and selectivity in catalytic hydrogenation, to probe if the synthetic method is suitable for producing catalytically active sub-nanosized particles.

1.1.1 Developing Methods for Synthesising Sub-nanosized Cobalt Nanoparticles

A recent method introduced for the synthesis of nanoparticles involves attachment of a precursor complex to a solid support, followed by controlled reduction of the surface-bound species to form the target nanoparticles, which are in turn stabilised on the support’s surface.⁶² Consequently, developing an understanding of the mechanism and effectiveness of tethering well-defined cobalt-containing complexes to oxide supports (principally silica) and the subsequent transformation to oxide support-stabilised nano- or sub-nanosized particles will be a focus in this project. In this context, the silica support and the influence of the character of the cobalt-containing precursor will be of importance for the successful formation of the target nanoparticles, hence these two characteristics will also be studied. Thus, overall, this thesis will focus on the development of a four-step process for the preparation of the desired cobalt nanoparticles (in Scheme 1.32).



Scheme 1.32. The 4-step method simplified for the synthesis of bound nanoparticles.

1.1.1.1 Step 1: Preparation of Oxide Supports

As discussed in Section 1.0.4, support effects can have a significant impact on the stability and performance of oxide-supported catalysts. A large part of this project involves tethering highly reactive and unstable organometallic complexes to an oxide support surface. The project will focus on only using silicas as the oxide support. Silica was chosen as a catalyst support for this project due to

several factors, the most important being its uniform surface structure and comparatively simple surface chemistry, as discussed in Section 1.0.4.1. Indeed, silica is one of the most common and versatile oxide supports for used in heterogeneous catalysis, with its simple surface chemistry, large surface area and uniform pore structure. The silicas chosen for this project are as follows:

1. Aeroperl 300/30, a silica that is commercially available and has been previously studied in the group;
2. SBA-15, a common silica support with a well-defined structure and used in model studies;
3. KIT-6, another common silica support with a more interconnected pore network than SBA-15.

1.1.1.2 Step 2: Target Metal-organyl Complexes

Given the intended use of cobalt organometallic precursors to prepare the target nanoparticles, it is important to consider the different types/compositions of organometallic cobalt complex precursors.

Two key requirements in the context of using such complexes as nanoparticle precursors are:

- (1) the Co-containing precursor must be reactive enough to bind to the support surface – preferably through reaction with a hydroxyl group on the silica surface;
- (2) the precursor must be able to decompose cleanly into Co^0 nanoparticles under readily achievable conditions, with repeatable and reliable consistency.

In Figure 1.17, a potential series of cobalt complexes (complexes **1** – **8**) that could be used as precursors in this project are shown. These cobalt complexes were chosen as potential precursors as they are known structures and there are no heteroatoms such as phosphorus or sulfur in the structure of the ligands. The absence of potentially reactive heteroatoms was picked specifically to avoid side reactions between the ligand and the oxide surface and therefore avoid heteroatom poisoning of the nanoparticles' surfaces.

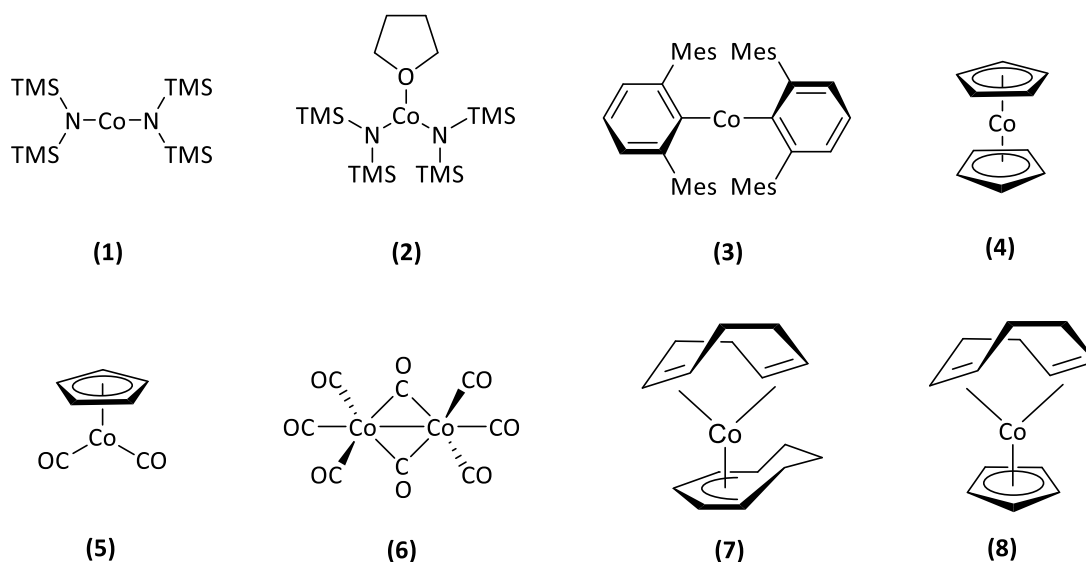


Figure 1.17. Co-containing precursors selected for this project

1.1.1.3 Step 3: Impregnation of Cobalt Precursors onto the Oxide Supports

The third step (Step 3 in Scheme 1.32) is the tethering of the organometallic precursors prepared in Step 2 onto the silica supports prepared in Step 1 using SOMC-like chemistry. Hence, the results of both Steps 1 and 2 are important for the results of Step 3. For example, the control of the density of organometallic complexes tethered to the surface of silica is determined by the number of reactive species (*i.e.* silanols) on the silica surface. The silanol density of the silicas will be determined by the treatment of the silicas in Step 1 (*e.g.* calcination to reduce the silanol density) and therefore Step 1 will affect the density of the organometallics tethered in Step 3. Similarly, the choice of organometallic species (complexes **1 – 8**) synthesised in Step 2 will affect the ease of tethering in Step 3; highly reactive cobalt species were chosen with the hopes that they would react easily with the surface silanols. The ligands of complexes **1 – 8** are easily removed during a SOMC-like reaction, assisted by steric constraints imposed by the bulk of the ligand or due to the ease of displacement of the carbonyl groups (complex **6**).

As stated in Section 1.0.6.1, tethering organometallic complexes to a silica surface *via* an SOMC-type approach can be done simply by adding a solution of the desired metal complex to the silica. It is hoped that these precursors (complexes **1 – 8**) will initially react with the surface hydroxyl groups and that the resulting organometallic fragments will then bind strongly to the oxide surface and undergo thermal decomposition or reduction (for example under a flow of hydrogen) without leaching from the supports' surface, and without translating along the surface freely to agglomerate with other Co nanoparticles.

1.1.1.4 Step 4: Reduction of Organometallic Precursors to Sub-nanosized Particles

Once a cobalt organometallic surface species on silica has been formed through SOMC-like chemistry, attempts to reduce the precursor to silica-bound cobalt nanoparticles under hydrogen gas will be explored. With the precursor bound to the silica support, the sintering of nanoparticles is prevented without the use of capping agents, creating nanoparticles with a “cleaner” surface (*i.e.* free of capping agents and hence potentially more reactive) available for reaction. In addition to nanoparticles with “cleaner” surfaces, another advantage of this four-step synthetic methodology is the potential to create very small nanoparticles (<1 nm) in a controlled manner, with the size of the nanoparticles potentially being controlled by the density of the loaded precursor.

1.1.2 Target Outcomes of the Proposed Synthetic Method

The target of developing the synthetic method proposed in Scheme 1.32, and indeed the overall target of the project, is to produce a reliable method for producing very small nanoparticles (preferably Sub-NPs, <1 nm) on the surface of silica without the use of capping agents. It is hoped that the four-step proposed method will have great control over the formation of the cobalt nanoparticles and their resulting size, by controlling the dispersion and loading of cobalt precursors on silica. Once the synthesis is optimised, it will be a quick method for the preparation of very small nanoparticles and potentially easy to scale up. It is hoped that without capping agents on the surface of the nanoparticles, they will be highly active in catalysis.

1.1.3 Catalytic Testing of Synthesised Sub-NPs: Choosing the Hydrogenation of Cinnamaldehyde (CNA) over the Hydrogenation of Nitrobenzene

A focus of this project is the synthesis of small cobalt nanoparticles in the absence of capping agents, to preserve the high reactivity of the nanoparticles. To evaluate the performance of the synthesised nanoparticles, catalysis testing will commence. Catalytic hydrogenation of CNA was chosen as the benchmark reaction over the hydrogenation of nitrobenzene to aniline. While the hydrogenation of nitrobenzene is one of the more common hydrogenation reactions for testing cobalt nanoparticles, it has only one easily hydrogenated site (the nitro-group on the benzene ring). An autoclave is also needed as high pressure and temperature is required. As heating the nanoparticles may cause sintering, increasing the size of the particles, the hydrogenation of nitrobenzene is inappropriate for this project. The hydrogenation of CNA can occur at lower temperatures (150 °C) and pressures (1 atm). There are also two possible sites for hydrogenation, with two competing possible reactions, allowing selectivity as well as activity to be explored.

The four-step synthetic method for silica-supported cobalt nanoparticles has been developed, and a catalysis test reaction has been chosen. The preparation of the silica supports is the first important step in this project and will be discussed in Chapter 2.

1.2 References

1. J. G. de Vries and S. D. Jackson, *Cata. Sci. Technol.*, 2012, **2**, 2009.
2. H. Toulhoat, in *Encyclopedia of Materials: Science and Technology*, New York, Second edn., 2010, pp. 1-7.
3. M. Bowker, *The Basis and Applications of Heterogeneous Catalysis*, Oxford Science Publications, Oxford, England, 1998.
4. Y. Imanishi and N. Naga, *Prog. Polym. Sci.*, 2001, **26**, 1147-1198.
5. S. Mourdikoudis, R. M. Pallares and N. T. K. Thanh, *Nanoscale*, 2018, **10**, 12871-12934.
6. G. A. Somorjai, A. M. Contreras, M. Montano and R. M. Rioux, *Proc. Natl. Acad. Sci. U. S. A.*, 2006, **103**, 10577-10583.
7. D. Astruc, *Nanoparticles and Catalysis*, Wiley-VCH, Weinheim, 2008.
8. K. J. Klabunde and R. M. Richards, *Nanoscale Materials in Chemistry*, Wiley, Hoboken, New Jersey, 2001.
9. G. Schmid, *Chem. Rev.*, 1992, 1709-1727.
10. J. A. Widegren and R. G. Finke, *J. Mol. Catal. A: Chem.*, 2003, **198**, 317-341.
11. L. D. Rampino and F. F. Nord, *J. Am. Chem. Soc.*, 1941, **63**, 2745-2749.
12. L. D. Rampino and F. F. Nord, *J. Am. Chem. Soc.*, 1941, **63**, 3268.
13. K. E. Kavanagh and F. F. Nord, *J. Am. Chem. Soc.*, 1943, **65**, 2121-2125.
14. G. Parravano, *J. Catal.*, 1970, **18**, 320-328.
15. M. Haruta, S. Tsubota, T. Kobayashi, H. Kageyama, M. J. Genet and B. Delmon, *J. Catal.*, 1993, **144**, 175-192.
16. M. Haruta, T. Kobayashi, H. Sano and N. Yamada, *Chem. Lett.*, 1987, **16**, 405-408.
17. M. Haruta, N. Yamada, T. Kobayashi and S. Iijima, *J. Catal.*, 1989, **115**, 301-309.
18. M. Haruta, *CATTECH*, 2002, **6**, 102-115.

19. M.-C. Daniel and D. Astruc, *Chem. Rev.*, 2004, **104**, 293-346.
20. M. Faraday, *Philos. Trans.*, 1857, **151**, 183.
21. M. Brust, M. Walker, D. Bethell, D. J. Schiffrin and R. Whyman, *J. Am. Chem. Soc. Commun.*, 1994, 801-802.
22. P. H. Hess and P. H. P. Jr., *J. Appl. Polym. Sci.*, 1966, **10**, 1915-1927.
23. S.R.Hoon, M.Kilner, G.J.Russell and B.K.Tanner, *J. Mag. Mater*, 1983, **39**, 107-110.
24. C. H. Griffiths, M. P. O'Horo and T. W. Smith, *J. Appl. Phys.*, 1979, **50**, 7108-7115.
25. J. R. Thomas, *J. Appl. Phys.*, 1966, **37**, 2914-1915.
26. M. T. Reetz and W. Helbig, *J. Am. Chem. Soc.*, 1994, **116**, 7401-7402.
27. M. T. Reetz and S. A. Quaiser, *Angew. Chem. Int. Ed.*, 1995, **34**, 2240-2241.
28. M. T. Reetz, R. Breinbauer and K. Wanninger, *Tetrahedron Lett.*, 1996, **37**, 4499-4502.
29. M. T. Reetz and G. Lohmer, *Chem. Commun.*, 1996, **16**, 1921-1922.
30. C.-C. Yang, C.-C. Wan and Y.-Y. Wang, *J. Colloid Interface Sci.*, 2004, **279**, 433-439.
31. J. Cookson, *Platinum Metals Rev.*, 2012, **56**, 83-98.
32. J. D. Aiken and R. G. Finke, *J. Am. Chem. Soc.*, 1999, **121**, 8803-8810.
33. L. Strimbu, J. Liu and A. E. Kaifer, *Langmuir*, 2003, **19**, 483-485.
34. Y. Shiraishi and N. Toshima, *J. Mol. Catal. A: Chem.*, 1999, **141**, 187-192.
35. N. Toshima and T. Yonezawa, *New J. Chem*, 1998, 1179-1201.
36. L. N. Lewis, *Chem. Rev.*, 1993, **93**, 2693-2730.
37. Y. Shiraishi and N. Toshima, *Colloid Surf. A*, 2000, **169**, 59-66.
38. M. Zhao, L. Sun and S. M. Crooks, *J. Am. Chem. Soc.*, 1998, **120**, 4877-4878.
39. L. Balogh and D. A. Tomalia, *J. Am. Chem. Soc.*, 1998, **120**, 7355-7356.
40. K. Esumi, A. Suzuki, N. Aihara, K. Usui and K. Torigoe, *Langmuir*, 1998, **14**, 3157-3159.
41. Y. Niu and R. M. Crooks, *C. R. Chimie*, 2003, **6**, 1049-1059.

42. K. An, S. Alayoglu, N. Musselwhite, K. Na and G. A. Somorjai, *J. Am. Chem. Soc.*, 2014, **136**, 6830-6833.
43. D. Astruc, *Inorg. Chem.*, 2007, **46**, 1884-1894.
44. F. Rascón, R. Wischert and C. Copéret, *Chem. Sci.*, 2011, **2**, 1449-1456.
45. P. Denton, A. Giroir-Fendler, H. Praliaud and M. Primet, *J. Catal.*, 2000, **189**, 410-420.
46. J. Handzlik, J. Ogonowski, J. Stoch, M. Mikołajczyk and P. Michorczyk, *Appl. Catal., A: General*, 2006, **312**, 213-219.
47. E. M. Moroz, D. A. Zyuzin, V. Y. Tregubenko, I. E. Udras, A. S. Belyi and V. A. Likholobov, *React Kinet Mech Cat*, 2013, **110**, 459-470.
48. S. Storsæter, B. Tøtdal, J. C. Walmsley, B. S. Tanem and A. Holmen, *J. Catal.*, 2005, **236**, 139-152.
49. N. Musselwhite, K. Na, S. Alayoglu and G. A. Somorjai, *J. Am. Chem. Soc.*, 2014, **136**, 16661-16665.
50. J. L. Castelbou, K. C. Szeto, W. Barakat, N. Merle, C. Godard, M. Taoufik and C. Claver, *Chem. Commun.*, 2017, **53**, 3261-3264.
51. I. E. Wachs, *Catal. Today*, 2005, **100**, 79-94.
52. R. N. Kerber, A. Kermagoret, E. Callens, P. Florian, D. Massiot, A. Lesage, C. Copéret, F. o. Delbecq, X. Rozanska and P. Sautet, *J. Am. Chem. Soc.*, 2012, **134**, 6767-6775.
53. A. Kermagoret, R. N. Kerber, M. P. Conley, E. Callens, P. Florian, D. Massiot, C. Copéret, F. Delbecq, X. Rozanska and P. Sautet, *Dalton Trans.*, 2013, **42**, 12681-12687.
54. T. Ueckert, R. Lamber, N. I. Jaeger and U. Schubert, *Appl. Catal., A: General*, 1997, **155**, 75-85.
55. A. Maeda, F. Yamakawa, K. Kunimori and T. Uchijima, *Catal. Lett.*, 1990, **4**, 107-112.
56. A. Sápi, D. G. Dobó, D. Sebők, G. Halasi, K. L. Juhász, Á. Szamosvölgyi, P. Pusztai, E. Varga, I. Kálomista, G. Galbács, Á. Kukovecz and Z. Kónya, *J. Phys. Chem. C*, 2017, **121**, 5130-5136.
57. E. Oakton, G. Vilé, D. S. Levine, E. Zocher, D. Baudouin, J. Pérez-Ramírez and C. Copéret, *Dalton Trans.*, 2014, **43**, 15138-15142.
58. C.-Y. Lai, *J. Thermodyn. Catal.*, 2013, **5**, 1-3.

59. Y. K. Priyanka Verma, Kohsuke Mori, Robert Raja, Hiromi Yamashita, *Nanoscale*, 2020, **12**, 11333-11363.
60. A. A. Christy, *Colloids and Surfaces A: Physicochem. Eng. Aspects*, 2008, **322**, 248-252.
61. A. P. Legrand, *The Surface Properties of Silicas*, John Wiley, Chichester, 1998.
62. M. P. Conley and C. Copéret, *Top Catal.*, 2014, **57**, 843-851.
63. M. P. Conley, C. Copéret and C. Thieuleux, *ACS Catal.* , 2014, **4**, 1458-1469.
64. C. Copéret, A. Comas-Vives, M. P. Conley, D. P. Estes, A. Fedorov, V. Mougel, H. Nagae, F. Núñez-Zarur and P. A. Zhizhko, *Chem. Rev.*, 2016, **116**, 324-421.
65. D. Gajan and C. Copéret, *New J. Chem*, 2011, **35**, 2403-2408.
66. L. T. Zhuravlev, *Colloids and Surfaces A: Physicochem. Eng. Aspects*, 2000, **173**, 1-38.
67. P. Euzen, P. Raybaud, X. Krokidis, H. Toulhoat, J.-L. L. Loarer, J.-P. Jolivet and C. Froidefond, *Handbook of porous materials*, Wiley-VCH, Weinheim, Germany, 2008.
68. I. E. Wachs, *Catal. Today*, 1996, **27**, 437-455.
69. C. Copéret, *Pure Appl. Chem.* , 2009, **81**, 585-596.
70. R. E. Richards and L. V. C. Rees, *Zeolites*, 1986, **6**, 17-25.
71. L. T. Zhuravlev, *Langmuir*, 1987, **3**, 316-318.
72. G. J. Young, *Colloid Sci.*, 1958, **13**, 67-85.
73. E. F. Vansant, P. V. D. Voort and K. C. Vrancken, *Characterisation and Chemical Modification of the Silica Surface*, Elsevier, Wilrijk, Belgium, 1995.
74. H. Lang, R. A. May, B. L. Iversen and B. D. Chandler, *J. Am. Chem. Soc*, 2003, **125**, 14832-14836.
75. Z. Niu and Y. Li, *Chem. Mater.*, 2014, **26**, 72-83.
76. T. Moriai, T. Tsukamoto, M. Tanabe, T. Kambe and K. Yamamoto, *Angew. Chem. Int. Ed.*, 2020, **59**, 23051-23055.
77. T. Imaoka, H. Kitazawa, W.-J. Chun and K. Yamamoto, *Angew. Chem. Int. Ed.*, 2015, **54**, 9810-9815.

78. M. Nesselberger, M. Roefzaad, R. F. Hamou, P. U. Biedermann, F. F. Schweinberger, S. Kunz, K. Schloegl, G. K. H. Wiberg, S. Ashton, U. Heiz, K. J. J. Mayrhofer and M. Arenz, *Nat Mater.*, 2013, **12**, 919-924.
79. K. Yamamoto, T. Imaoka, W.-J. Chun, O. Enoki, H. Katoh, M. Takenaga and A. Sonoi, *Nat Chem.*, 2009, **1**, 397-402.
80. S. Vajda, M. J. Pellin, J. P. Greeley, C. L. Marshall, L. A. Curtiss, G. A. Ballentine, J. W. Elam, S. Catillon-Mucherie, P. C. Redfern, F. Mehmood and P. Zapol, *Nat Mater.*, 2009, **8**, 213-216.
81. M. Takahashi, H. Koizumi, W.-J. Chun, M. Kori, T. Imaoka and K. Yamamoto, *Sci Adv.*, 2017, **3**.
82. M. Huda, K. Minamisawa, T. Tsukamoto, M. Tanabe and K. Yamamoto, *Angew. Chem. Int. Ed.*, 2018, **58**, 1002-1006.
83. T. Imaoka, Y. Akanuma, N. Haruta, S. Tsuchiya, K. Ishihara, T. Okayasu, W.-J. Chun, M. Takahashi and K. Yamamoto, *Nature Communications*, 2017, **8**, 688.
84. J. Kiss, Á. Kukovecz and Z. Kónya, *Catalysis Letters*, 2019, **149**, 1441-1454.
85. A. Kuzume and K. Yamamoto, *Dalton Trans.*, 2020, **49**, 13512-13518.
86. M. Wakizaka, H. Muramatsu, T. Imaoka and K. Yamamoto, *Eur. J. Inorg. Chem.*, 2020, 1759-1762.
87. C. Copéret and J.-M. Basset, *Adv. Synth. Catal.*, 2007, **349**, 78-92.
88. *Japan Pat.*, 235250, 1997.
89. C. Copéret, M. Chabanas, R. P. Saint-Arroman and J.-M. Basset, *Angew. Chem. Int. Ed.*, 2003, **42**, 156-181.
90. C. Copéret, F. Allouche, K. W. Chang, M. Conley, M. F. Delley, A. Fedorov, I. Moroz, V. Mougel, M. Pucino, Keith Searles, K. Yamamoto and P. Zhizhko, *Angew. Chem. Int. Ed.*, 2017.
91. C. C. Liu and G. E. Maciel, *J. Am. Chem. Soc.*, 1996, **118**, 5103-5119.
92. D. G. H. Ballard, *J. Polym. Sci.*, 1975, **13**, 2191-2212.
93. W. Mowat, J. Smith and D. A. Whan, *J.C.S Chem. Comm.*, 1974, 34-35.
94. D. G. H. Ballard, *Adv. Catal.*, 1973, **23**, 263-325.
95. D. G. H. Ballard, E. Jones, R. J. Wyatt, R. T. Murray and P. A. Robinson, *Polymer*, 1974, **15**, 169-174.

96. N. Millot, S. Soignier, C. C. Santini, A. Baudouin and J.-M. Basset, *J. Am. Chem. Soc.*, 2006, **128**, 9361-9370.
97. L. Calucci, C. Forte, G. Pampaloni, C. Pinzino and F. Renili, *Inorg. Chim. Acta*, 2010, 33-40.
98. K. J. Cluff, Janet and Blumel, *Chem. Eur. J.*, 2016, **22**, 16561-16575.
99. F. J. Karol, G. L. Karapinka, C. Wu, A. W. Dow, R. N. Johnson and W. L. Carrick, *J. Polym. Sci.: Part A*, 1972, **10**, 2621-2637.
100. M. Lappert, A. Protchenko, P. Power and A. Seeber, *Metal Amide Chemistry*, John Wiley & Sons, Ltd, New York, 2008.
101. A. O. Bouh, G. L. Rice and S. L. Scott, *J. Am. Chem. Soc.*, 1999, **121**, 7201-7210.
102. M. E. Eter, B. Hamzaoui, E. Abou-Hamad, J. D. Pelletier and J.-M. Basset, *Chem. Commun.*, 2013, **49**, 4616-4618.
103. B. Hamzaoui, M. E. Eter, E. Abou-hamad, Y. Chen, J. D. A. Pelletier and J.-M. Basset, *Chem. - Eur. J.*, 2015, **21**, 4294-4299.
104. R. M. Gauvin, O. Coutelier, E. Berrier, A. Mortreux, L. Delevoye, J.-F. Paul, A.-S. Mamede and E. Payen, *Dalton Trans.*, 2007, 3127-3130.
105. T. Deschner, K. W. Tornroos and R. Anwander, *Inorg. Chem.*, 2011, **50**, 7217-7228.
106. Y. Liang, E. S. Erichsen and R. Anwander, *Dalton Trans.*, 2013, **42**, 6922-6935.
107. Y. Liang and R. Anwander, *Dalton Trans.*, 2013, **42**, 12521-12545.
108. B. Hu, N. M. Schweitzer, G. Zhang, S. J. Kraft, D. J. Childers, M. P. Lanci, J. T. Miller and A. S. Hock, *ACS Catal.*, 2015, **5**, 3494-3503.
109. H. S. Ahn, J. Yanoc and T. D. Tilley, *Energy Environ. Sci.*, 2013, **6**, 3080-3087.
110. D. Gajan, K. Guillois, P. Delicé`re, J.-M. Basset, J.-P. Candy, V. r. Caps, C. Cope´ret, A. Lesage and L. Emsley, *J. Am. Chem. Soc.*, 2009, **131**, 14667-14669.
111. M. J. Lamb, D. C. Apperley, M. J. Watson and P. W. Dyer, *Top. Catal.*, 2018, **61**, 213-224.
112. J. C. Park, J. I. Kwon, S. W. Kang, D. H. Chun, H.-T. Lee, H. Junga and J.-I. Yang, *RSC. adv.*, 2017, **7**, 8852-8857.
113. G. Khandelwal, K. Sharma and V. Kumar, *Micro and Nano Technologies*, 2019, 89-111.

114. F. Quignard, A. Choplin and R. Teissier, *J. Mol. Catal. A: Chem.*, 1997, **120**, L27-L31.
115. G. Saggio, A. de Mallmann, B. Maunders, M. Taoufik, J. Thivolle-Cazat and J.-M. Basset, *Organometallics*, 2002, **21**, 5167-5171.
116. M. Taoufik, A. de Mallmann, E. Prouzet, G. Saggio, J. Thivolle-Cazat and J.-M. Basset, *Organometallics*, 2001, **20**, 5518-5521.
117. F. Rataboul, A. Baudouin, C. Thieuleux, L. Veyre, C. Coperet, J. Thivolle-Cazat, J.-M. Basset, A. Lesage and L. Emsley, *J. Am. Chem. Soc.*, 2004, **126**, 12541-12550.
118. C. Larabi, N. Merle, S. b. Norsic, M. Taoufik, A. Baudouin, C. Lucas, J. Thivolle-Cazat, A. de Mallmann and J.-M. Basset, *Organometallics*, 2009, **28**, 5647-5655.
119. S. Soignier, M. Taoufik, E. Le Roux, G. Saggio, C. Dablemont, A. Baudouin, F. Lefebvre, A. de Mallmann, J. Thivolle-Cazat and J.-M. Basset, *Organometallics*, 2006, **25**, 1569-1577.
120. M. Delgado, C. C. Santini, F. O. Delbecq, A. Baudouin, A. De Mallmann, C. Prestipino, S. Norsic, P. Sautet and J.-M. Basset, *J. Phys. Chem. C*, 2011, **115**, 6757-6763.
121. M. D. Ward, T. V. Harris and J. Schwartz, *Chem. Commun.*, 1980, 357-359.
122. M. D. Ward and J. Schwartz, *J. Mol. Catal.*, 1981, **11**, 397-407.
123. M. D. Ward and J. Schwartz, *J. Am. Chem. Soc.*, 1981, **103**, 5253-5255.
124. H. C. Foley, S. J. DeCanio, K. D. Tau, K. J. Chao, J. H. Onuferko, C. Dybowski and B. C. Gates, *J. Am. Chem. Soc.*, 1983, **105**, 3074-3082.
125. P. Dufour, C. C. Santini, C. Houtman and J. M. Basset, *J. Mol. Catal.*, 1991, **66**, L23-L26.
126. P. Dufour, C. Houtman, C. C. Santini and J.-M. Basset, *J. Mol. Catal.*, 1992, **77**, 257-272.
127. S. L. Scott, P. Dufour, C. C. Santini and J.-M. Basset, *J. Chem. Soc., Chem. Commun.*, 1994, 2011-2012.
128. S. L. Scott, A. Mills, C. Chao, J.-M. Basset, N. Millot and C. C. Santini, *J. Mol. Catal. A: Chem.*, 2003, **204**, 457-463.
129. M. Rimoldi and A. Mezzetti, *Catal. Sci. Technol.*, 2014, **4**, 2724-2740.
130. F. Heroguel, D. Gebert, M. D. Detwiler, D. Y. Zemlyanov, D. Baudouin and C. Coperet, *J. Catal.*, 2014, **316**, 260-269.

131. D. A. Ruddy, J. Jarupatrakorn, R. M. Rioux, J. T. Miller, M. J. McMurdo, J. L. McBee, K. A. Tupper and T. D. Tilley, *Chem. Mater.*, 2008, **20**, 6517-6527.
132. Y. S. Choi, E. G. Moschetta, J. T. Miller, M. Fasulo, M. J. McMurdo, R. M. Rioux and T. D. Tilley, *ACS Catal.*, 2011, **1**, 1166-1177.
133. F. Héroguel, G. Siddiqi, M. D. Detwiler, D. Y. Zemlyanov, O. V. Safonova and C. Copéret, *J. Catal.*, 2015, **321**, 81-89.
134. P. Laurent, L. Veyre, C. Thieuleux, S. Donet and C. Coperet, *Dalton Trans.*, 2013, **42**, 238-248.
135. D. W. Sindorf and G. E. Maciel, *J. Phys. Chem.*, 1982, **86**, 5208-5219.
136. J. M. Thomas, R. Raja and D. W. Lewis, *Angew. Chem. Int. Ed.*, 2005, **44**, 6456-6482.
137. M. Widenmeyer, S. Grasser, K. Köhler and R. Anwender, *Microporous Mesoporous Mater.*, 2001, **44**, 327-336.
138. J. Jarupatrakorn and T. D. Tilley, *J. Am. Chem. Soc.*, 2002, **124**, 8380-8388.
139. P. Mania, R. Verel, F. Jenny, C. Hammond and I. Hermans, *Chem. - Eur. J.*, 2013, **19**, 9849-9858.
140. P. Mania, S. Conrad, R. Verel, C. Hammond and I. Hermans, *Dalton Trans.*, 2013, **42**, 12725-12732.
141. M. P. Conley, M. F. Delley, G. Siddiqi, G. Lapadula, S. Norsic, V. Monteil, O. V. Safonova and C. Coperet, *Angew. Chem. Int. Ed.*, 2014, **53**, 1872-1876.
142. M. F. Delley, F. Nunez-Zarur, M. P. Conley, A. Comas-Vives, G. Siddiqi, S. Norsic, V. Monteil, O. V. Safonova and C. Coperet, *Proc. Natl. Acad. Sci. U.S.A.*, 2014, **111**, 11624-11629.
143. Giuseppe Lapadula, A. Bourdolle, F. Allouche, M. P. Conley, I. d. Rosal, L. Maron, W. W. Lukens, Y. Guyot, C. Andraud, S. Brasselet, C. Coperet, O. Maury and R. A. Andersen, *Chem. Mater.*, 2014, **26**, 1062-1073.
144. G. Evans and C. Smith, *Comprehensive Renewable Energy*, 2012, **5**, 155-204.
145. C. Smith, A. K. Hill and L. Torrente-Murciano, *Energy Environ. Sci.*, 2020, **13**, 331-344.
146. H. Alawisi, H. D. Arman and Z. J. Tonzetich, *Organometallics*, 2021, **40**, 1062-1070.
147. R. Ghosh, N. C. Jana, S. Panda and B. Bagh, *ACS Sustainable Chem. Eng.*, 2021, **9**, 4903-4914.
148. S. Yuan, G. Gao, L. Wang, C. Liu, L. Wan, H. Huang, H. Geng and M. Chang, *Nat Commun.*, 2020, **11**, 621.

149. C. S. G. Seo and R. H. Morris, *Organometallics*, 2019, **38**, 47-65.
150. D. M. Sedgwick and G. B. Hammond, *J. Flu. Chem.*, 2018, **207**, 45-58.
151. M. Niaounakis, in *Management of Marine Plastic Debris: Prevention, Recycling, and Waste Management*, 2017, pp. 215-315.
152. R. Hoffmann, *American Scientist*, 1998, **86**, 326-329.
153. C. Vogt, M. Monai, G. J. Kramer and B. M. Weckhuysen, *Nat. Catal.*, 2019, **2**, 188-197.
154. S. Hübner, J. G. d. Vries and V. Farina, *Adv. Synth. Catal.*, 2016, **358**, 3-25.
155. V. R. Choudhary and M. G. Sane, *Indian J. Chem. Technol.*, 1998, **5**, 199-208.
156. M. Zahid, J. Li, A. Ismail, F. Zaera and Y. Zhu, *Catal. Sci. Technol.*, 2021, **11**, 2433-2445.
157. S. A. Korili and G. P. Sakellaropoulos, *Studies in Surface Science and Catalysis*, 1993, **75**, 2725-2728.
158. L. J. Durndell, K. Wilson and A. F. Lee, *RSC Adv.*, 2015, **5**, 80022-80026.
159. J. Vakros, *Catalysts*, 2021, **11**, 1-4.
160. F. Chen, B. Sahoo, C. Kreyenschulte, H. Lund, M. Zeng, L. He, K. Junge and M. Beller, *Chem. Sci.*, 2017, **8**, 6239-6246.
161. J. Hervochon, V. Dorcet, K. Junge, M. Beller and C. Fischmeister, *Catal. Sci. Technol.*, 2020, **10**, 4820-4826.
162. Y. Cao, K. Liu, C. Wu, H. Zhang and Q. Zhang, *Appl. Catal. A, General*, 2020, **592**, 1-9.
163. F. Michalek, A. Lagunas, C. Jimenoa and M. A. Pericas, *J. Mater. Chem.*, 2008, **18**, 4692-4697.
164. Q. Zhang, J. Bu, J. Wang, C. Sun, D. Zhao, G. Sheng, X. Xie, M. Sun and L. Yu, *ACS Catal.*, 2020, **10**, 10350-10363.
165. E. A. Gelder, S. D. Jackson and C. M. Lok, *Chem. Commun.*, 2005, 522-524.
166. P. Zhou, Z. Zhang, L. Jiang, C. Yu, K. Lv, J. Sun and S. Wang, *Appl. Catal. B, Environmental*, 2017, **210**, 522-532.
167. Z. S. Nanadegani, F. Nemati, A. Elhampour and Y. Rangraz, *J. Solid State Chem.*, 2020, **292**, 1-10.

168. Y. Bonita, V. Jain, F. Geng, T. P.O'Connell, N. X. Ramos, N. Rai and J. C. Hicks, *Appl. Catal. B, Enviromental*, 2020, **277**, 1-11.
169. B. Dragoi, A. Ungureanu, C. Ciotonea, A. Chirieac, S. Petit, S. Royer and E. Dumitriu, *Microporous Mesoporous Mater.*, 2016, **224**, 176-189.
170. H. X. Li, X. F. Chen, M. H. Wang and Y. P. Xu, *Appl. Catal. A: General*, 2002, **225**, 117.
171. P. Gallezot and D. Richard, *Catal. Rev. Sci. Eng.*, 1998, **40**, 81-126.
172. Y. Yang, D. Rao, Y. Chen, S. Dong, B. Wang, X. Zhang and M. Wei, *ACS Catal.*, 2018, **8**, 11749-11760.
173. Z. Wu, J. Zhao, M. Zhang, W. Li and K. Tao, *Catal. Commun.*, 2010, **11**, 973-976.
174. X. Wang, X. Liang, P. Geng and Q. Li, *ACS Catal.*, 2020, **10**, 2395-2412.

Chapter 2: Silica-based Catalyst Supports

2.0 Introduction to Silica-based Catalyst Supports

2.0.1 Silica as a Catalyst Support for the Synthesis of Nanoparticles

The use of silica as an oxide support is a key element of this project and, as such, the characterisation and quantification of its reactive surface groups is an important topic. The nature of the surface of the silica supports can be considered as the foundation on which the rest of the project depends because of so-called support effects.¹⁻³ In particular for this project, the silica's surface sites will control the binding of the cobalt-containing nanoparticle precursor, the density of the metal loading, and potentially how well the nanoparticle precursor can be reduced, as well as how residual reactive surface groups may affect future catalysis. Indeed, here the oxide (silica) support is intrinsically necessary in order to immobilize the formed metal nanoparticle species, through a reduction in their mobility (*i.e.* helping to prevent sintering) and also offering chemical stabilization, which means that together these oxide supports can be considered as solid capping agents, contrasting with the various molecular capping agents commonly used in the preparation of nanoparticles (see section 1.0.3). As discussed in Section 1.0.4.1, the surface of silica comprises predominantly silanol groups and/or siloxane bridges,⁴ the ratio of which can be easily and uniformly controlled by simple procedures such as calcination⁵ or silylation.⁶ Generally in SOMC, a ML_mX_n species reacts with a silanol, resulting in a loss of ligand X (as X-H) *via* protonation, so control of the surface silanol density is needed to control the binding of the metal to the silica surface.⁷ This chapter explores the use of thermal methods to control the silanol density on a silica surface, as well as methods for the characterisation and quantification of the silanols on the support. The silica supports discussed in this chapter are Aeroperl 300/30, SBA-15, and KIT-6, whose properties will be briefly summarised below.

2.0.1.1 Properties of Aeroperl® 300/30 Silica

Aeroperl® 300/30 is a commercially available fumed silica produced by Evonik Industries. It has a specially formed micro-granular (20-60 μm) hydrophilic structure; it was designed to act as a carrier and filler. In particular, Aeroperl® 300/30 was selected due to its high surface area (270-330 $\text{m}^2 \text{g}^{-1}$), large pore volume (1.5 – 1.9 $\text{cm}^3 \text{g}^{-1}$), and high chemical purity. Furthermore, it was selected as an oxide catalyst support for this project following previous successful use in the lab/group.

2.0.1.2 Properties of SBA-15 Silica

SBA-15 is an example of a mesoporous silica with a uniform 2-D structure comprising elongated hexagonal pores as shown in Figure 2.1.⁸ It is often considered to be a particularly mechanically stable silica, due to the sturdy hexagonal framework.⁸ SBA-15 silica also has a high surface area (500-900 $\text{m}^2 \text{g}^{-1}$) with a pore volume usually in the range of 0.4-1.0 $\text{cm}^3 \text{g}^{-1}$,⁹ which together facilitate access to a high degree of active surface sites to be available for reaction. SBA-15 was selected as a

potential oxide support for this project due to its uniform, robust structure, high surface area, and simple synthesis that can be varied to adjust the mesostructure and pore size.

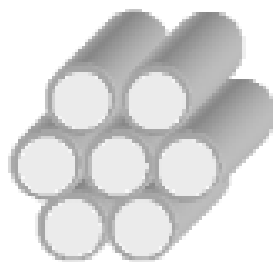


Figure 2.1. Representation of the structure of SBA-15¹⁰

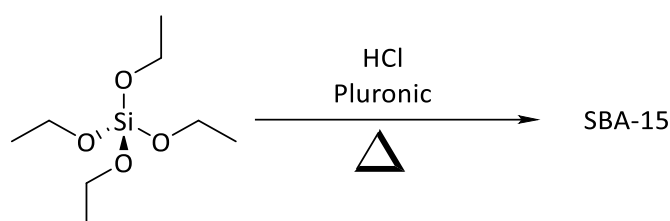
SBA-15 is a commonly used support in catalysis as the long channels through which reagents can flow down can be loaded with a catalyst or nanoparticles. However, one common problem encountered with SBA-15 relates to its 2-D structure - the thin channels have the potential to become blocked or obstructed during a catalytic reaction, preventing substrates from passing through to the catalyst and therefore hindering or stopping the reaction. In a similar manner, a combination of capillary forces and diffusion effects can limit the ease and uniformity of metal distribution within the pores typically prepared by aqueous impregnation methods (in contrast to a fumed silica, for example). Additionally, SBA-15 can only be used as a catalyst support in reactions where no solid can form, since the presence of solids can lead to blocking of the pores.

2.0.1.2.1 Synthesis of SBA-15

Typically SBA-15 has a narrow range of pore diameter sizes, which can be tuned easily during synthesis, usually between 5-15 nm, though pore diameter can be increased by incorporation of a swelling agent during its preparation.⁹ This control of microporosity can be achieved by changing the ratio of silica source and templating agent (typically a triblock polymer comprising ethylene {EO} and propylene {PO} oxides),^{11, 12} as well as altering reaction and aging temperatures, and the reaction solvent used, with co-solvents and swelling agents being used to vary the morphology.¹³ The ratio of the ethylene (EO) and propylene (PO) oxide units in the triblock copolymer (EO:PO:EO) can allow good control over the geometric arrangement of the resulting silica due to the initial formation of cylindrical and spherical micelles in water, formed with a hydrophobic PO core and a hydrophilic EO corona. A lower EO:PO ratio results in an *p6mm* hexagonal morphology (the hexagonal morphology needed for SBA-15), while a higher ratio results in a cubic morphology.⁹

The SBA-15 used in this project was synthesised using a triblock copolymer (Pluronic-123; {EO}₂₀{PO}₇₀{EO}₂₀) as an organic template under acidic conditions (pH <1), with TEOS (tetraethyl orthosilicate) as the source of silica (Scheme 2.1). The reaction temperature for the synthesis was kept between 35-40 °C, which favours formation of highly ordered mesostructures.¹³ No co-solvents or

swelling agents were used in this project. The necessary aging process for the generation of SBA-15's pore structure was done in an oven at 100 °C over a 24 h period under a static atmosphere. The organic patterning template was subsequently removed by washing with EtOH and water, followed by calcination in static air at 550 °C in a muffle furnace for 6 h to give SBA-15 as a fine white powder.¹⁴ Using TEOS, the silica source in this synthesis, typically produces a "rope-like" mesoporous silica.⁹ The silica precipitates from the reaction mixture at pH <1 due to the formation of silicate ions that then self-assemble into silica. The synthesis of SBA-15 was confirmed by PXRD, which showed characteristic 100, 110 and 200 reflections at 0.8, 1.4 and 1.8 ° that correspond to the known hexagonal pattern.¹⁵



Scheme 2.1. Synthesis of SBA-15

To limit the effects of variation in the SBA-15's morphology and pore-size on this project, and therefore limit any changes in the support effects that may affect precursor loading, reduction, or catalysis when comparing the produced nanoparticles, the reaction conditions and synthesis were kept the same throughout the entire project. This resulted in a consistent SBA-15 source material, which was checked by PXRD following each synthesis.

2.0.1.3 Properties of KIT-6

KIT-6 is another mesoporous silica used in this project, which has a 3-D intersecting cylindrical pore structure system. In contrast to SBA-15, KIT-6 comprises a highly inter-connected cubic 3-D porous network, based on two continuous interpenetrating channels as shown in Figure 2.2. The advantage of this pore structure in terms of the use of KIT-6 in catalytic applications is that if one channel becomes blocked, the reactants still have other ways to access the inner pores and therefore interact with any reactive sites.

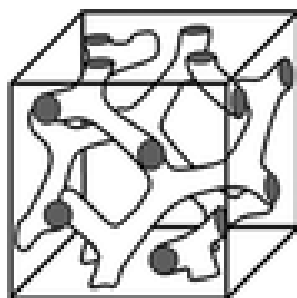
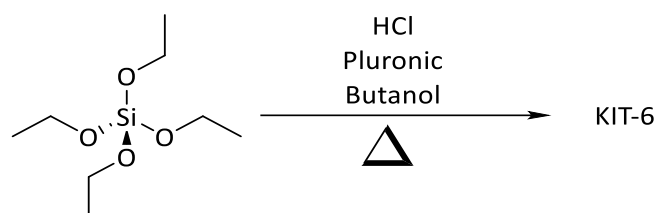


Figure 2.2. Representation of the structure of KIT-6 ¹⁶

2.0.1.3.1 Synthesis of KIT-6

KIT-6 shares a similar synthesis to that of SBA-15, using acidic conditions, Pluronic-123 as templating agent, and TEOS as the silica source, Scheme 2.2. However, for the synthesis of KIT-6, butanol is added as a co-surfactant prior to TEOS addition. The resulting mesopore diameter size of KIT-6 synthesised with these reagents/conditions is typically 7-9 nm, although this is something that can be controlled by varying synthetic conditions, with pores up to 12 nm in diameter being accessible by increasing the reaction temperature.¹⁷



Scheme 2.2. Synthesis of KIT-6

Compared to SBA-15, the synthetic methodology used for the synthesis of KIT-6 provides less scope for the tuning of the silica's structure during its preparation. KIT-6 has a *1a3d* symmetry and the synthesis has to be controlled in order to create that symmetry in the mesostructure. However, *p6mm* symmetry (*i.e.* hexagonal as found for SBA-15) or a mix of *1a3d/p6mm* can be made if the ratio of butanol to TEOS is not carefully controlled, as larger amounts of butanol increases the extent of *p6mm* silica formation.¹⁷ The *1a3d* cubic phase is synthesised within a certain, narrow, range of butanol concentrations (2-5 %). Any alterations to the ratios of TEOS:Pluronic-123:butanol:HCl must be done carefully when tuning KIT-6's pore size, to ensure the resulting product has the correct crystalline phase.¹⁷ As for SBA-15, all samples of KIT-6 prepared during this project were synthesised using identical reaction conditions and for each batch, the structure was verified by PXRD.

2.1 Preparation of Silica for Tethering Organometallic Precursors by Controlling the Hydroxyl Density

The preparation of an oxide support will affect the way that organometallic precursors, such as those used in this project, namely $[\text{Co}(\text{N}(\text{TMS})_2)_2\text{THF}]$ and $\text{Co}(\text{dmp})_2$, will bind to the surface of silica. In particular, controlling the number of hydroxyl sites available to react with the cobalt-containing precursor will control the total metal loading (as well as the chemical composition of the immobilised pro-nanoparticle precursors). Thus, preparing the silica in a way that will increase or decrease the hydroxyl density on the surface will increase or decrease the metal loading, respectively.

It was proposed in this project that isolated organometallic complexes tethered on the surface of the oxide support are a potentially important route for subsequent synthesis of sub-nanosized metal

particles, *i.e.* a low metal density/low metal loading on the silica surface. A large density of metal-containing organometallic species (*i.e.* nanoparticle precursor material) on the surface would increase the amount of metal available and hence potentially allow for the formation of larger nanoparticles or bulk metal phases, as opposed to the small nanoparticles that are the target of this project. To create isolated reactive sites on the surface of silica (for the tethering of metal species), a pre-treatment is necessary to remove surface water and to alter the number of hydroxyl groups. While there are chemical methods for modifying the surface of silica to remove SiOH sites such as silylation,¹⁸ the simplest method to remove hydroxyl groups with the fewest, most readily controlled experimental parameters is calcination, which is the approach that has been used extensively throughout this PhD study.⁵

2.1.1 Calcination of Silica to Reduce the Surface Hydroxyl Density

The calcination and hence surface hydroxyl density alteration of the silicas used in this project was achieved by heating a sample of the support under a flow of dry inert gas or under vacuum. The concentration of hydroxyl groups remaining on the surface can be controlled by varying the temperature and duration of heating. In this project, solely temperature dependence has been studied, with the calcination time being fixed at 24 h for all samples. Since calcined silica has the potential to readily take up water and re-hydroxylate, the calcined samples were handled such that air and moisture were excluded at all times and stored/manipulated in a nitrogen-filled glovebox.

In order to probe the calcination temperature effects on hydroxyl density, Aeroperl 300/30 silica samples were calcined at 200, 400, 600, 700, and 800 °C, with the resulting materials being referred to as **A-SiO₂₋₂₀₀**, **A-SiO₂₋₄₀₀**, **A-SiO₂₋₆₀₀**, *etc.* Similarly, various calcined SBA-15 and KIT-6 materials were studied in a similar manner and will be referred to as **S-SiO_{2-x}** and **K-SiO_{2-x}**, respectively, where x is the calcination temperature. Each material has also been assigned a number to distinguish calcination attempts; for example, the Aeroperl 300/30 sample first calcined at 600 °C is referred to as **A-SiO₂₋₆₀₀ 1**, the second sample calcined as **A-SiO₂₋₆₀₀ 2**, and so on.

2.2 Analysis of Calcined Silica to Determine the Hydroxyl Density

Given the importance of the functional groups present at the surface of silicas (namely silanol moieties) for binding the target organometallic complexes to the surface, a reliable method for determining the nature and density of surface functional groups was needed. In particular, the density of these reactive functional groups is important since it will determine the density of the tethered organometallic, thus accurate quantification of the number of surface groups is especially important.

Two techniques were examined for identifying the nature of and quantifying the density of reactive surface groups on silica, solid state nuclear magnetic resonance (SS-NMR) spectroscopy and chemical

titration. In parallel, BET (Brunauer-Emmett-Teller) analysis was used to probe any thermally-induced changes surface area of the various silica supports.

2.2.1 Brunauer-Emmett-Teller (BET) Analysis of Prepared Oxide Supports

In addition to surface area and hydroxyl density, an important factor when considering the tethering of an organometallic to a silica surface, is the physical stability of the silica. When silica is calcined at high temperatures, there is a risk that the desirable porous structure of the support will collapse, decreasing the surface area and pore volume.¹⁹ High surface areas are normally preferable in catalysis, as it increases the number of surface sites for reaction. An accurate determination of the surface area of the supports is vital in calculating the silanol density of the supports. To ensure that calcination of the silica does not lead to pore collapse or significant changes in silica morphology, Brunauer-Emmett-Teller (BET) analysis of the calcined silica samples will probe whether the silica supports chosen are stable at a particular calcination (and reaction) temperature.

Silica samples were analysed by BET at Johnson Matthey and were undertaken using nitrogen gas as the adsorbate. Uncalcined samples were subject to a one-hour nitrogen purge at 140 °C before analysis.

2.2.1.1 BET Analysis of Aeroperl 300/30 Silica

The results from BET analysis of samples of Aeroperl 300/30* silica calcined between 200 and 700 °C are shown in Table 2.1. The BET analyses were not repeated, with results being those of a single determination.[†] The BET surface area ranged from 262 m² g⁻¹ to 283 m² g⁻¹ (±2 %) with no significant loss of surface area or change in pore volume observed for any of the samples of Aeroperl 300/30 calcined, consistent with the Aeroperl 300/30 silica structure being robust up to 700 °C. Aeroperl 300/30 has a range of average pore volumes of between 1.7 cm³ g⁻¹ and 1.9 cm³ g⁻¹ with an average of 1.8 cm³ g⁻¹, and a range of average pore diameters between 24.9-27.5 nm.²⁰

* Samples taken from the same batch of Aeroperl 300/30.

[†] NB. To ensure reproducibility, the BET instrument was calibrated at routine short intervals using commercial standards.

Table 2.1. BET analysis of Aeroperl 300/30 silica; data were measured by Johnson Matthey; measurement uncertainty on BET surface area is +/- 2%.

	Calcination temperature (°C)	BET surface area (m ² g ⁻¹)	Pore Volume [0.99ads] (cm ³ g ⁻¹)	Average Pore Diameter (Å)	C Value from BET
Aeroperl 300/30 SiO ₂₋₇₀₀	700	262	1.8	275	79
Aeroperl 300/30 SiO ₂₋₆₀₀	600	273	1.9	274	85
Aeroperl 300/30 SiO ₂₋₄₀₀	400	283	1.9	264	92
Aeroperl 300/30 SiO ₂₋₂₀₀	200	270	1.8	269	100
Aeroperl 300/30 SiO _{2-uncalcined}	n/a [‡]	265	1.7	249	103

An initially unforeseen, but interesting trend was also noticed in relationship to the *C value* resulting from the BET analysis as a function of calcination temperature. The *C value* (or sometimes called *C constant* or *BET constant*) is related to the heat of adsorption of nitrogen gas in the first adsorbed layer on the surface being measured, *i.e.* the affinity of the solid surface for the adsorbate, and consequently its value is an indication of the magnitude of the adsorbent/adsorbate interactions (Equation 2.1).²¹ The heat of adsorption on the surface can be affected by surface groups such as hydroxyl groups and adsorbed water molecules; the more hydroxyl groups present, the higher the heat of adsorption on the surface and therefore the higher the *C value*. For most oxides and silicates, *C* falls between 50 - 200.¹⁹

[‡] Sample was not calcined

$$C = \exp\left(\frac{K_1 - K_L}{RT}\right)$$

Equation 2.1. The C value, calculated from the gradient and intercept of the isotherm, and related to the heat of adsorption on the surface.²¹

K_1 = heat of adsorption for the first layer

K_L = heat of adsorption for second layer and higher (is equal to the heat of vaporisation)

R = gas constant

T = temperature

There is a clear trend in the values of C measured for the variously calcined samples of Aeroperl 300/30 silica. As the calcination temperature increases from uncalcined silica to 200 to 700 °C, so the C value decreases (Figure 2.3). This trend between calcination temperature and the C value is proposed to be due to the changing water content/hydroxyl density on the surfaces of the silica. The silicas calcined at lower temperatures have a higher number of surface hydroxyl groups present and therefore a higher heat of adsorption and higher C value.²² This is further evidence that higher calcination temperatures decrease the hydroxyl density on the surface of silica, and that this change can be indirectly probed through BET analysis.

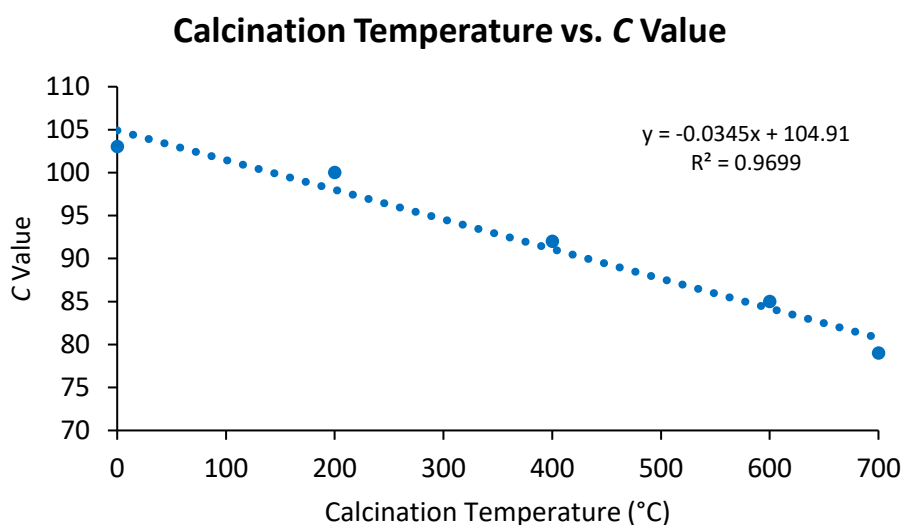


Figure 2.3. Calcination Temperature vs. C value

A linear relationship exists between the value of C (determined via BET) with the calcination temperature.

2.2.1.2 BET Analysis of SBA-15

Data for BET analysis of SBA-15 calcined at 600 and 700 °C are shown in Table 2.2. BET analysis was not performed on SBA-15 samples calcined below 550 °C. This is because the synthetic process for SBA-15 synthesis includes a calcination at 550 °C in air to remove the organic templating agent and

therefore the structure of SBA-15 is only generated at by thermolysis 550 °C and hence inherently retained at this temperature.

SBA-15 has a significantly higher surface area than that of Aeroperl 300/30 silica (see Section 2.0.1), 530 - 828 m² g⁻¹ for the former and a smaller pore volume (0.5 – 1.3 cm³ g⁻¹) and pore diameter (31 - 68 Å). According to the literature, the typical SBA-15 surface area spans 500 - 900 m² and 0.4 - 1.0 cm³ g⁻¹.⁹ The surface area decreases significantly from that of material calcined at 600 °C to that treated at 800 °C. This is consistent with the structure of SBA-15 silica not being stable at higher temperatures and undergoing collapse of the pore structure, decreasing the surface area.

Table 2.2. BET analysis on SBA-15 support; data was received from Johnson Matthey; measurement uncertainty on BET surface area is +/- 2%.[§]

	Calcination temperature (°C)	BET surface area (m ² g ⁻¹)	Pore Volume [0.99ads] (cm ³ g ⁻¹)	Average Pore Diameter (Å)
SBA-15 SiO ₂₋₇₀₀	700	530	0.5	31
SBA-15 SiO ₂₋₆₀₀	600	739	0.9	69
SBA-15 SiO _{2-uncalcined}	n/a**	828	1.3	68

2.2.1.3 BET Analysis of KIT-6

Similar BET analysis of various samples of KIT-6, which had previously been calcined at 600 and 700 °C, was undertaken and the data presented in Table 2.3. As the synthesis of KIT-6 and SBA-15 is very similar (see Section 6.0.3.1 and 6.0.3.2 for synthetic methods), the silicas were analysed at the same calcination temperatures.

Again, as anticipated, KIT-6 has a higher surface area (570 - 712 m² g⁻¹) than Aeroperl 300/30 silica, but a lower surface area than that determined for the SBA-15 prepared herein. Uncalcined KIT-6 also has a smaller pore volume and pore diameter than Aeroperl 300/30, but a larger pore volume and pore diameter than SBA-15, with a pore volume and pore diameter of 0.5 - 1.1 cm³ g⁻¹ and 36 - 53 Å, respectively. The surface area of KIT-6 decreases as the calcination temperature increases due to the pore structure collapsing.

[§] The C-values were not determined

** Sample was not calcined

Table 2.3. BET analysis on KIT-6 support; data was received from Johnson Matthey; measurement uncertainty on BET surface area is +/- 2%.^{††}

	Calcination temperature (°C)	BET surface area (m ² g ⁻¹)	Pore Volume [0.99ads] (cm ³ g ⁻¹)	Average Pore Diameter (Å)
KIT-6 SiO ₂₋₇₀₀	700	570	0.5	37
KIT-6 SiO ₂₋₆₀₀	600	666	0.6	36
KIT-6 SiO _{2-uncalcined}	n/a ^{††}	712	1.1	53

2.2.1.4 Summary of BET Analysis of Variously Calcined Silica Supports

Irrespective of calcination temperature, all of the silica samples analysed by BET gave data consistent with mesoporous materials, with pore diameters in the range of 2 - 50 nm.²³ Based on these BET analyses, Aeroperl 300/30 will allow larger organometallic species into its internal pore structure, due to having a significantly larger pore diameter than either SBA-15 or KIT-6. If an organometallic precursor of interest is too large to fit into SBA-15 and KIT-6's pore structure, these supports could become unsuitable supports for this project as the organometallic precursor will only be able to bind outside the pores on the external oxide surface. This would limit the use of the much larger surface area than both SBA-15 and KIT-6 offer.

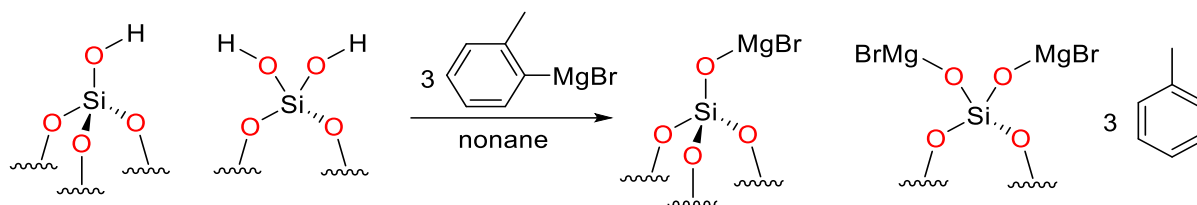
2.2.2 Determination of Hydroxyl Density by Titration with *o*-Tolyl Magnesium Bromide

As indicated earlier, surface hydroxyl density will be a crucial parameter in controlling metal loading and surface dispersion, consequently it is vital to have a reliable method in hand for its determination. Here, chemical titration was chosen as a simple, quantitative method of determining the hydroxyl density on the surface of the silica supports. The method used involved treating the silica of interest with a Grignard reagent, here *ortho*-tolylmagnesium bromide, which reacts with one hydroxyl group on the silica surface, releasing one toluene molecule as shown in Scheme 2.3.²⁴ The quantity of toluene released can then be determined by quantitative gas chromatography (GC) using nonane as an internal standard, therefore allowing the number of hydroxyl groups present to be calculated. To prevent extra toluene being produced from degradation of unreacted Grignard, any excess Grignard reagent was quenched with an aldehyde prior to GC quantification of liberated toluene. The aldehyde initially used as a quenching agent was propanal, producing 1,1-di-*o*-tolylpropan-1-ol as a product. However, propanal readily degrades on exposure to air (*via* oxidation) over a relatively short time span. Consequently, to ensure consistency, benzaldehyde was used as a more reliable (stable) quenching agent. The reaction of the aldehyde and Grignard reagent is shown in Scheme 2.4. No differences

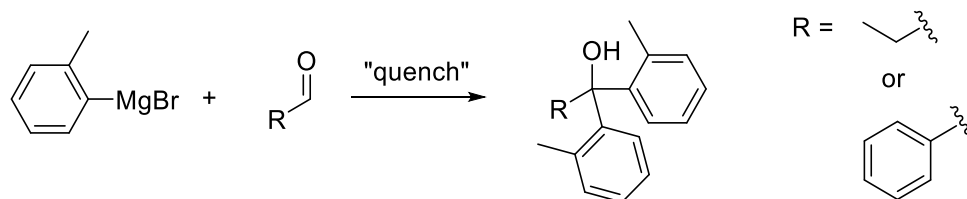
^{††} The C-values were not determined

^{††} Sample was not calcined

between fresh propanal and benzaldehyde as quenching agents were observed, with the OH densities calculated for the same silica sample being the identical regardless of quenching agent as anticipated.



Scheme 2.3. Representative reaction of tolylmagnesium bromide with the silica surface to produce toluene in a Grignard titration. Nonane is used as an internal GC standard.



Scheme 2.4. Reaction of excess tolylmagnesium bromide remaining after Grignard titration of OH groups on the silica being quenched by propan-1-al or benzaldehyde, to produce 1,1-di-o-tolylpropan-1-ol or 1,1-di-o-tolylbenzyl alcohol, respectively. The quenching of the excess Grignard by aldehyde prevents further production of unwanted toluene

The silica/Grignard titration was performed anaerobically under nitrogen in dry pentane, to avoid producing additional toluene as a result of Grignard hydrolysis. The area of the toluene and nonane GC signals were calculated from the GC chromatogram using appropriate calibration curves. From this and the known mass of silica used, the density of hydroxyl groups per gram of silica was calculated. The Grignard titration was repeated three times with every silica sample to produce results with quantified errors; results are given in Table 2.4, Table 2.5, and Table 2.6.

Prior to carrying out the analysis of the variously dehydroxylated silicas, a “blank” titration of the Grignard was performed to determine the amount of free toluene already present in the sample of Grignard used. The toluene present in the Grignard solution was taken into account when calculating the amount of toluene produced from each titration of support.^{§§}

From the data in Table 2.4, Table 2.5, and Table 2.6, as expected there is a clear correlation between the hydroxyl density of the surface and the support’s calcination temperature, something true for all three silica supports studied, namely Aeroperl 300/30, SBA-15, and KIT-6. This is demonstrated further

^{§§} An aliquot of the Grignard was reacted with the quenching agent (performed with both propanal and benzaldehyde) as a “blank” titration using the same reaction conditions as a titration with silica involved. In the blank titration, 0.19 mmol of toluene was detected when quenched by propanal and 0.13 mmol of toluene was detected when using benzaldehyde, compared to the 1.8 mmol of Grignard reagent added. This shows that the Grignard reagent had no significant decomposition/presence of toluene, and that the quenching agents were water-free and did not produce significant amounts of toluene during quenching.

in Figure 2.4, where calcination temperature is plotted against the OH density per nm², showing decreasing hydroxyl density as calcination temperature was increased. The trend lines indicate a non-linear relationship for each silica, showing how the rate of loss of hydroxyl groups from the surface decreases at higher and higher calcination temperatures.

Table 2.4. The surface hydroxyl density of Aeroperl 300/30 silica calcined at different temperatures, derived from titration with *o*-tolylmagnesium bromide. Standard errors in the hydroxyl concentration were obtained by the standard deviation divided by the square root of the number of samples. The density in OH nm⁻² was obtained by using the surface area calculated from the BET analysis

	Hydroxyl density (mmol g ⁻¹)	Standard Error (mmol g ⁻¹)	Hydroxyl density (OH nm ⁻²)	Standard Error (OH nm ⁻²)
Aeroperl 300/30 SiO₂₋₇₀₀ 1	0.6	0.2	1.4	0.4
Aeroperl 300/30 SiO₂₋₆₀₀ 1	0.8	0.1	1.8	0.2
Aeroperl 300/30 SiO₂₋₄₀₀ 1	1.4	0.1	3.1	0.1
Aeroperl 300/30 SiO₂₋₂₀₀ 1	2.2	0.2	4.8	0.4

Table 2.5. The surface hydroxyl density of SBA-15 silica calcined at different temperatures, derived from titration with *o*-tolylmagnesium bromide. Standard errors in the hydroxyl concentration were obtained by the standard deviation divided by the square root of the number of samples. The density in OH nm⁻² was obtained by using the surface area calculated from the BET analysis

	Hydroxyl density (mmol g ⁻¹)	Standard Error (mmol g ⁻¹)	Hydroxyl density (OH nm ⁻²)	Standard Error (OH nm ⁻²)
SBA-15 SiO₂₋₇₀₀ 1	1.8	0.2	1.3	0.2
SBA-15 SiO₂₋₆₀₀ 1	2.5	0.1	1.8	0.1
SBA-15 SiO₂₋₄₀₀ 1	3.4	0.3	2.5	0.2
SBA-15 SiO₂₋₂₀₀ 1	5.6	0.3	4.1	0.2

Table 2.6. The surface hydroxyl density of KIT-6 silica calcined at different temperatures, derived from titration with *o*-tolylmagnesium bromide. Standard errors in the hydroxyl concentration were obtained by the standard deviation divided by the square root of the number of samples. The density in OH nm⁻² was obtained by using the surface area calculated from the BET analysis

	Hydroxyl density (mmol g ⁻¹)	Standard Error (mmol g ⁻¹)	Hydroxyl density (OH nm ⁻²)	Standard Error (OH nm ⁻²)
KIT-6 SiO₂₋₇₀₀ 1	1.8	0.1	1.6	0.1
KIT-6 SiO₂₋₆₀₀ 1	2.2	0.1	2.0	0.1
KIT-6 SiO₂₋₄₀₀ 1	2.9	0.2	2.6	0.2
KIT-6 SiO₂₋₂₀₀ 1	5.8	0.3	5.3	0.2

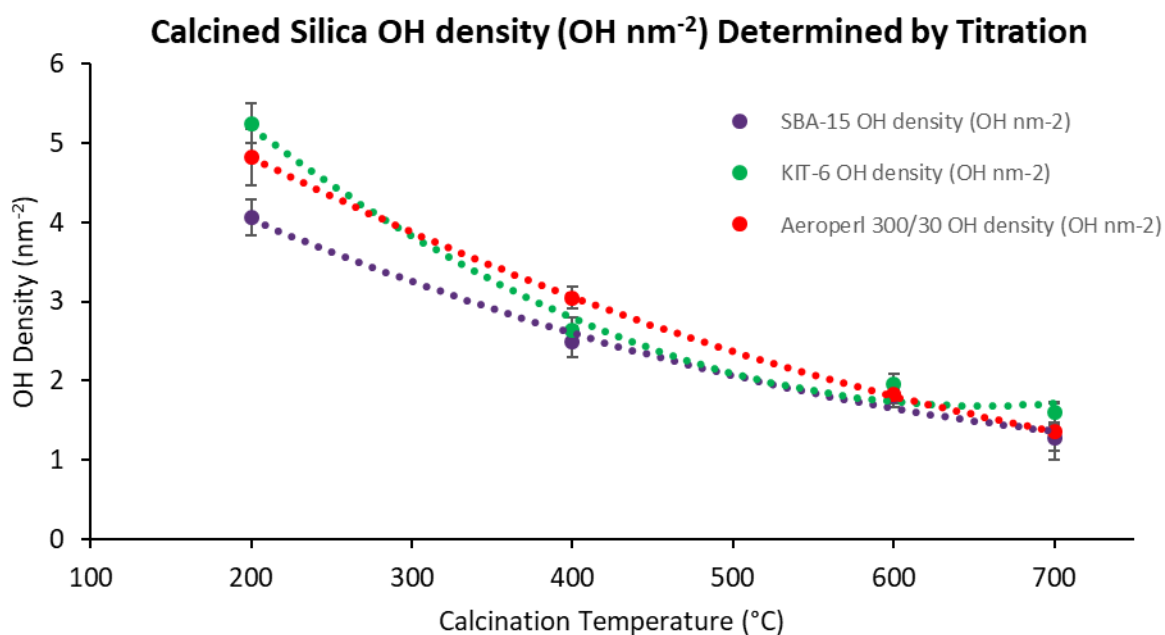


Figure 2.4. Calcination Temperature vs. OH Density (OH nm⁻²) for Aeroperl 300/30, SBA-15, and KIT-6. Three trend lines correlate the calcination temperature with the hydroxyl density calculated on the surface for each type of silica, showing how increasing calcination temperature decreases the hydroxyl density in the samples

For all three silicas, the material subject to the lowest calcination temperature, namely **SiO₂₋₂₀₀**, has the highest hydroxyl density by weight as expected, with KIT-6 and SBA-15 having the highest hydroxyl density by weight at 5.81 and 5.59 mmol g⁻¹, respectively, compared to Aeroperl 300/30 at 2.16 mmol g⁻¹. When corrected for the surface area as determined by BET, all three **SiO₂₋₂₀₀** silicas fall into a similar range of hydroxyl densities, 4.06 - 5.25 OH nm⁻². This is true for all calcination temperatures, with KIT-6 and SBA-15 having significantly higher hydroxyl density by weight than Aeroperl 300/30, but when corrected by surface area, they all show a similar range at every temperature. The silicas calcined at 200 °C have the largest hydroxyl density (OH nm⁻²) differences between the three silicas, and the smallest hydroxyl density differences at 600 °C. The lowest hydroxyl density in all three silica is **SiO₂₋₇₀₀** within the range 1.28 – 1.60 OH nm⁻². KIT-6 silica generally has the highest hydroxyl density, with the exception of material calcined at 400 °C where Aeroperl 300/30 has the highest hydroxyl density. SBA-15 silica has the lowest hydroxyl density across all temperatures. This difference between the hydroxyl densities of KIT-6 and SBA-14 after calcination is proposed to be due to the ease with which water can escape the pore structure. Water release from SBA-15 is limited by its 2D mesostructured nature, while KIT-6 has a highly interconnected 3D structure that has more pathways through which water can escape more easily.

The hydroxyl density ranges reported in Table 2.4, Table 2.5, and Table 2.6 lie between 1.28 - 5.25 OH nm⁻² at calcination temperatures across the window 200 and 700 °C. This falls roughly in the range expected for hydroxyl density of calcined silica according to previous literature studies.¹⁹ The silanol

density can be considered as a physicochemical constant, independent of the silica type, and as stated previously the density of fully hydroxylated silica is 4.9 OH nm^{-2} . It has been recorded that this value will typically quickly fall to approximately 2.3 OH nm^{-2} upon calcination up to $400 \text{ }^\circ\text{C}$, though the rate of dehydroxylation slows down considerably at temperatures higher than $400 \text{ }^\circ\text{C}$ as condensation becomes more difficult.¹⁹ This latter observation is consistent with the study presented herein.

To determine the reproducibility of the extent of dehydroxylation achieved through calcination in this project, several different batches of Aeroperl 300/30 silica calcined at $600 \text{ }^\circ\text{C}$ were analysed by Grignard titration. The silica samples were **A-SiO₂₋₆₀₀ 1-5**, and their hydroxyl densities are given in Table 2.7.

Table 2.7. The surface hydroxyl density of different batches of Aeroperl 300/30 silica calcined at the same temperature, derived from titration with o-tolylmagnesium bromide. Standard errors in the hydroxyl concentration were obtained by the standard deviation divided by the square root of the number of samples. The density in OH nm^{-2} was obtained by using the surface area calculated from the BET analysis

	Hydroxyl density (mmol g^{-1})	Standard Error (mmol g^{-1})	Hydroxyl density (OH nm^{-2})	Standard Error (OH nm^{-2})
Aeroperl 300/30 SiO₂₋₆₀₀ 1	0.8	0.1	1.8	0.2
Aeroperl 300/30 SiO₂₋₆₀₀ 2	0.8	0.1	1.9	0.3
Aeroperl 300/30 SiO₂₋₆₀₀ 3	0.9	0.1	1.9	0.2
Aeroperl 300/30 SiO₂₋₆₀₀ 4	0.9	0.1	1.9	0.3
Aeroperl 300/30 SiO₂₋₆₀₀ 5	0.9	0.1	2.0	0.2

The average hydroxyl density of Aeroperl SiO₂₋₆₀₀ is 1.9 OH nm^{-2} . The values determined for each batch of **A-SiO₂₋₆₀₀** fall within error, suggesting that both the thermal calcination performed in this project and the analysis methodology give a reliable, reproducible silanol density on a silica surface. Consequently, as the project evolved, Grignard titration of each batch of silica was not undertaken routinely.

2.2.3 Solid State Nuclear Magnetic Resonance (SS-NMR) Spectroscopic Studies of Prepared Oxide Supports

An important factor in binding the target cobalt nanoparticle precursors {[Co(N(TMS)₂)₂THF] and Co(dmp)₂} to the surface of the silica is the role played by the oxide surface's reactive functional groups (*i.e.* silanols on the silica surface). Consequently, to better understand the surface prior to metal functionalisation, solid state NMR (SS-NMR) spectroscopy was used to quantify the different types of silanol species present on the oxide surface and to explore how the silanol density varies as a function of calcination temperature.

The use of ²⁹Si SS-NMR spectroscopy for the differentiation of the types of OH-groups on the surface of silica, and the ratio between them, is well-established.²⁵⁻²⁷ Similarly, the use of ¹H SS-NMR

spectroscopy has also been well-documented in the literature for the determination of surface species on silica, having been employed to detect the presence of both silanols and tethered species.

2.2.3.1 ²⁹Si CP MAS NMR (Cross Polarisation-Magic Angle Spinning-Nuclear Magnetic Resonance) Spectroscopy For Surface Specific Characterisation of Silanols

²⁹Si CP MAS NMR spectroscopy has been demonstrated to be a surface-specific technique for characterising types of silicon on the silica surface.²⁸ Magic angle spinning (MAS) is a common technique employed in solid state NMR spectroscopy, used to improve/narrow broad spectral resonances.²⁹ Interactions dependent on $(3\cos^2\theta-1)$ in NMR spectroscopy (anisotropic, isotropic and orientation) cause line broadening in the spectrum. By spinning the sample at a “magic” angle of 54.74 °, the anisotropic interactions are averaged to zero, as they are orientation-dependent, while the isotropic interactions remain. If the sample is spinning fast enough, the orientations of all crystallites are averaged, reducing signal broadening. Cross polarisation (CP) is a process that excites abundant ¹H nuclei, the energy is then transferred to a second “rare spin” in this case silicon-29, with a pulse to create a stronger signal than direct excitation (DE). The CP method ignores ²⁹Si nuclei that are not near any protons; since nearly all protons are on the silica surface, this can be classified as a surface-specific identification technique. It is able to discriminate between geminal silanols (~90 ppm), vicinal silanols (~100 ppm) and siloxane bridges (~110 ppm) on the surface of silica.³⁰

2.2.3.2 ²⁹Si SS-NMR Analysis of Silica Supports

Initial studies by a former PhD student (M. J. Lamb) in the Dyer group have shown use of ²⁹Si SS-NMR to be a potentially promising approach to differentiate geminal silanols, isolated silanols and siloxane bridges (seen in Figure 2.5), which produce Q₂, Q₃ and Q₄ peaks, respectively, in ²⁹Si SS-NMR spectra.²⁴ One of the current project’s aims was to quantify the changes that occur during dehydroxylation and how the temperature of calcination treatments can alter the silanol density, as well as to assess the reproducibility of the results that can be obtained. The quantification of the hydroxyl density of the calcined silica is an important step for reliably synthesising reproducible sub-nanosized particles, as the OH density determines the metal loading on the support. As a starting point for investigating this NMR spectroscopic analysis approach, both cross polarisation (CP) and direction excitation (DE) ²⁹Si SS-NMR experiments were performed on Aeroperl 300/30 silica. The samples initially analysed by SS-NMR were **A-SiO₂₋₂₀₀ 1**, **A-SiO₂₋₄₀₀ 1**, **A-SiO₂₋₆₀₀ 1**.

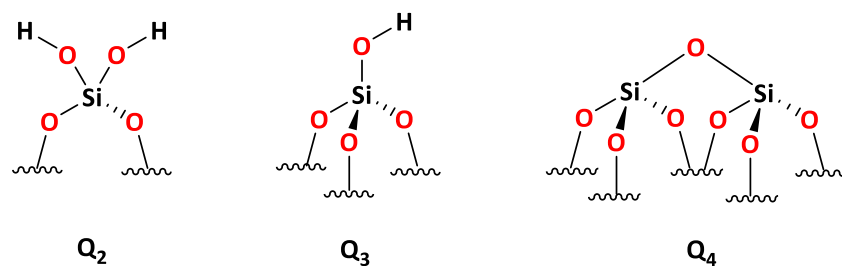


Figure 2.5. The structure of the species found on the surface of silica and their corresponding peak name, Q_x , which denotes adjacent oxygen connectivity

Figure 2.6 shows a comparison of the DE and CP SS-NMR spectra obtained for **A-SiO₂₋₆₀₀ 1**. These spectra are representative of the typical CP and DE spectra that were obtained for all blank silica samples in this project. Figure 2.7 and Figure 2.8 show the DE and CP spectra of **A-SiO₂₋₆₀₀ 1**, respectively, identifying the Q_2 , Q_3 , and Q_4 peaks in each spectrum, and correlating these with their corresponding surface structure(s). The Q_2 resonances appear at a ^{29}Si SS-NMR chemical shift of *ca* -90 ppm, with the resonances corresponding to Q_3 at *ca* -100 and Q_4 at *ca* -110 ppm. In the DE spectrum, only the Q_3 and Q_4 resonances can be observed, with the Q_4 signal dominating the spectrum. The Q_2 , Q_3 and Q_4 resonances can be clearly seen in the CP experiment, with the Q_3 signal dominating the spectrum here.

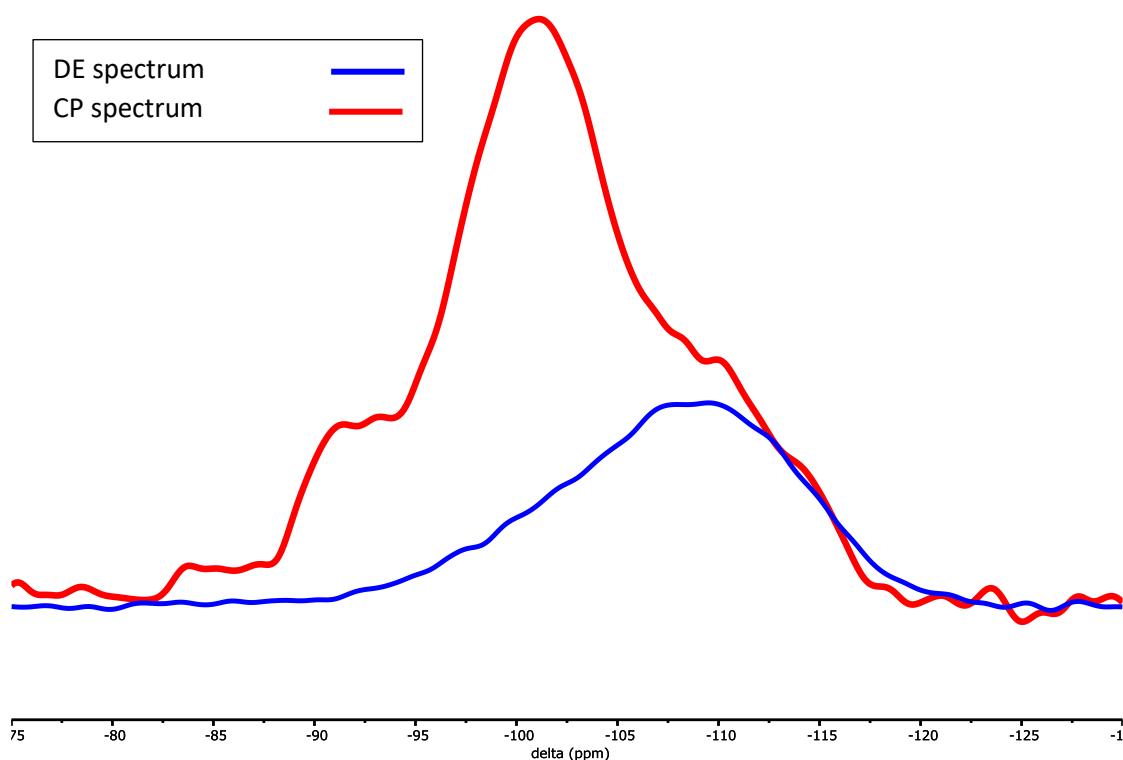


Figure 2.6. Comparison of the ^{29}Si CP (red) and DE (blue) spectra of **A-SiO₂₋₆₀₀ 1**. Acquisition frequency 79.437 MHz, spin-rate 6 kHz.

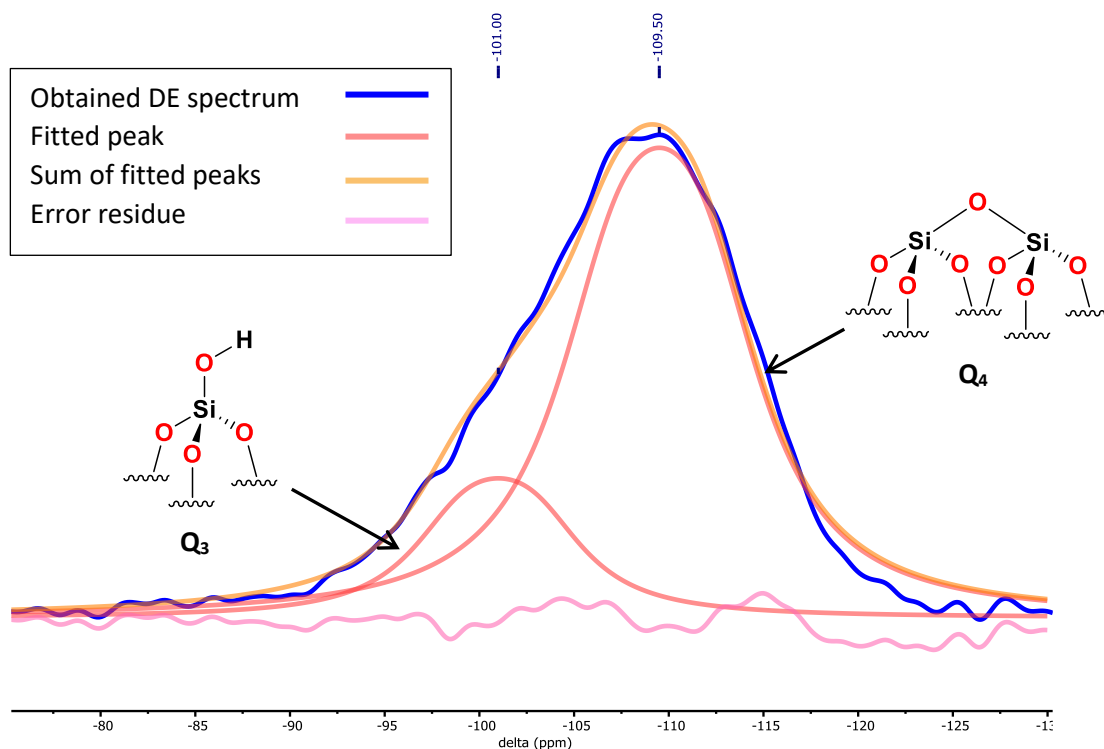


Figure 2.7. An example of the Q_3 and Q_4 resonances in a typical ^{29}Si SS-NMR DE spectrum (A-SiO_{2-600} **1**), and the structure of the corresponding surface species. Acquisition frequency 79.437 MHz, spin-rate 6 kHz.

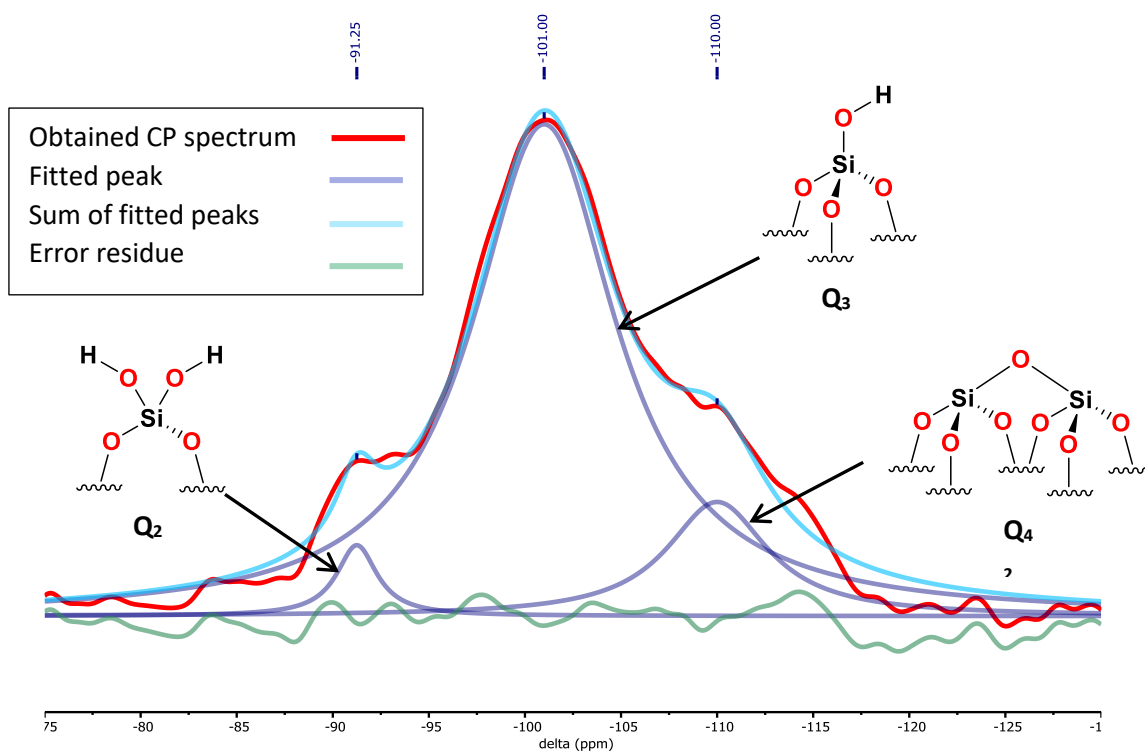


Figure 2.8. An example of the Q_2 , Q_3 , and Q_4 resonances in a typical ^{29}Si SS-NMR CP spectrum (A-SiO_{2-600} **1**), and the structure of the corresponding surface species. Acquisition frequency 79.437 MHz, Spin-rate 6 kHz.

Analysis of samples of each of **A-SiO₂₋₂₀₀ 1**, **A-SiO₂₋₄₀₀ 1**, **A-SiO₂₋₆₀₀ 1**, reveal the Q₂, Q₃ and Q₄ resonances in every CP spectrum, while only Q₃ and Q₄ resonances are easily identifiable in the DE spectra. In the DE spectra (Figure 2.7), compared to the CP spectra (Figure 2.8), it is difficult to identify the presence of the Q₂ signal. Since quantifying the ratio of Q₂:Q₃:Q₄ is important for the later tethering of organometallic precursors *via* these silanol functionalities, the DE spectra are consequently not suitable for this task as the Q₂ peak is impossible to fully resolve. Since the silanol density (Q₂ + Q₃) at the oxide surface is what will control the binding of the nanoparticle precursors, so CP SS-NMR spectroscopy is the technique of choice for the identification of these groups. However, the disadvantage of using CP experiments is that the resulting spectra are not typically quantitative. This disadvantage can be mitigated by the combined use of other characterisation techniques used in this project, such as chemical titration, which was discussed earlier in the chapter (Section 2.2.2).

CP SS-NMR experiments are preferable over the corresponding DE SS-NMR experiments for determining the ratio of the Q₂:Q₃:Q₄ species from the spectra of **A-SiO₂₋₆₀₀ 1**. Therefore, the CP spectra of **A-SiO₂₋₂₀₀ 1** and **A-SiO₂₋₄₀₀ 1** were obtained as well. A comparison of the spectra of (**A-SiO₂₋₂₀₀ 1**, **A-SiO₂₋₄₀₀ 1**, **A-SiO₂₋₆₀₀ 1**) is given in Figure 2.9; the spectra are not off-set nor are their intensities altered in the figure.

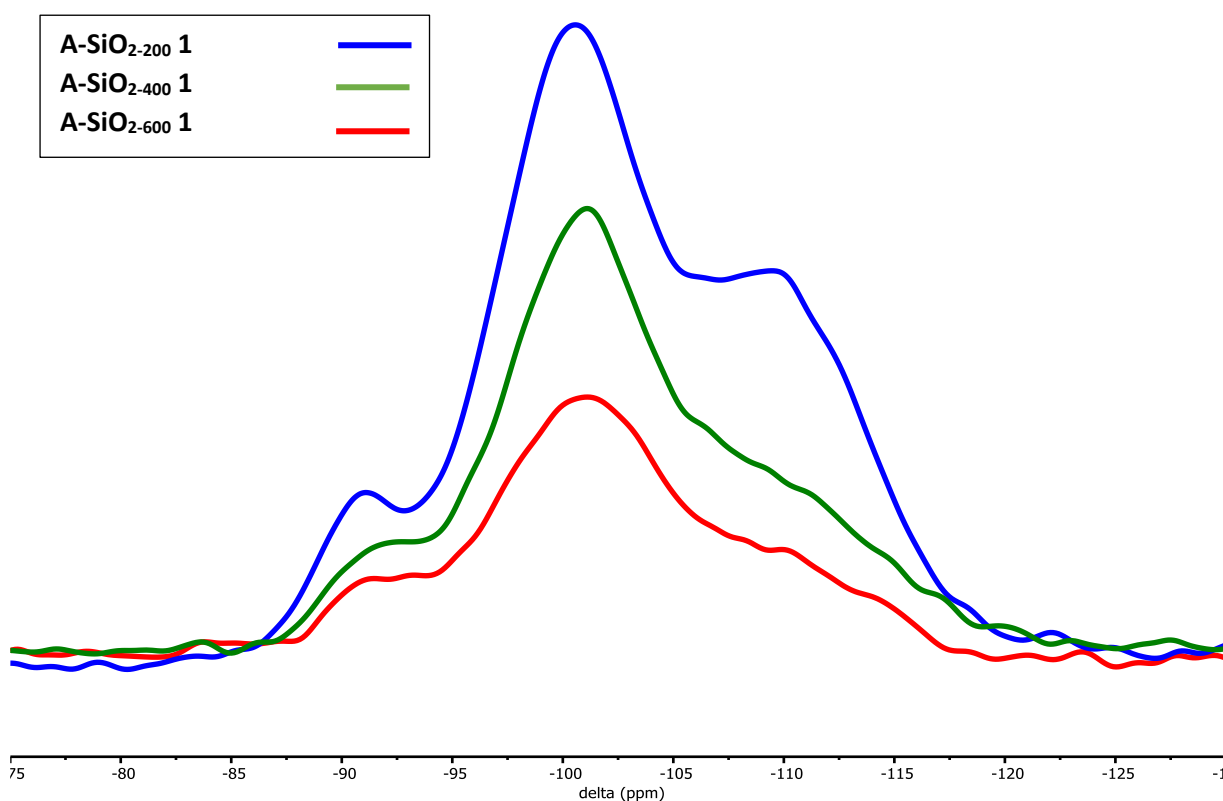


Figure 2.9. CP ²⁹Si SS-NMR spectra of **A-SiO₂₋₂₀₀ 1** (blue), **A-SiO₂₋₄₀₀ 1** (green), and **A-SiO₂₋₆₀₀ 1** (red) calcined samples, Acquisition frequency 79.437 MHz, spin-rate 6 kHz.

The first notable difference between the CP ^{29}Si SS-NMR spectra of the three silica samples calcined at various temperatures is the signal intensity; the signal intensity decreases as calcination temperature increases. This trend has been verified further by comparing the maximum intensity of the spectra (the Q_3 signal) with calcination temperature (Figure 2.10). The difference in peak intensity is a consequence of the use of CP NMR spectroscopic analysis methods. As discussed above, the CP NMR spectroscopic experiment excites ^1H nuclei, then uses a second RF pulse to transfer the energy to nearby silicon atoms. As the majority of hydrogen atoms in silica will be present in the surface hydroxyl groups, removing the hydroxyl groups lowers the amount of ^1H NMR signal that will be received. Samples that have been calcined at higher temperatures have a lower OH density and therefore will have a lower signal intensity. However, this CP NMR spectroscopic method cannot be used to easily quantify the hydroxyl density of the silica samples as CP NMR spectroscopy is usually not quantitative.³¹ Indeed, the intensity of a spectrum can vary significantly, even with spectra of the same silica, or spectra of the same sample analysed without repacking the rotor; these effects upon the resulting ^{29}Si CP NMR spectra are discussed later in the chapter (Section 2.2.3.2.2, Figure 2.13). Consequently, although CP NMR spectroscopic experiments are not quantitative as the transfer of energy from the hydrogen atom to the silicon atom is not 100% effective, these ^{29}Si CP NMR spectra do offer an indication that the hydroxyl density does decrease with increasing calcination temperature. To make comparisons between the three spectra easier, the intensities of the **A-SiO₂₋₄₀₀ 1** and **A-SiO₂₋₆₀₀ 1** spectra have been scaled to match the **A-SiO₂₋₂₀₀ 1** spectrum, using the Q_3 resonances, Figure 2.11.

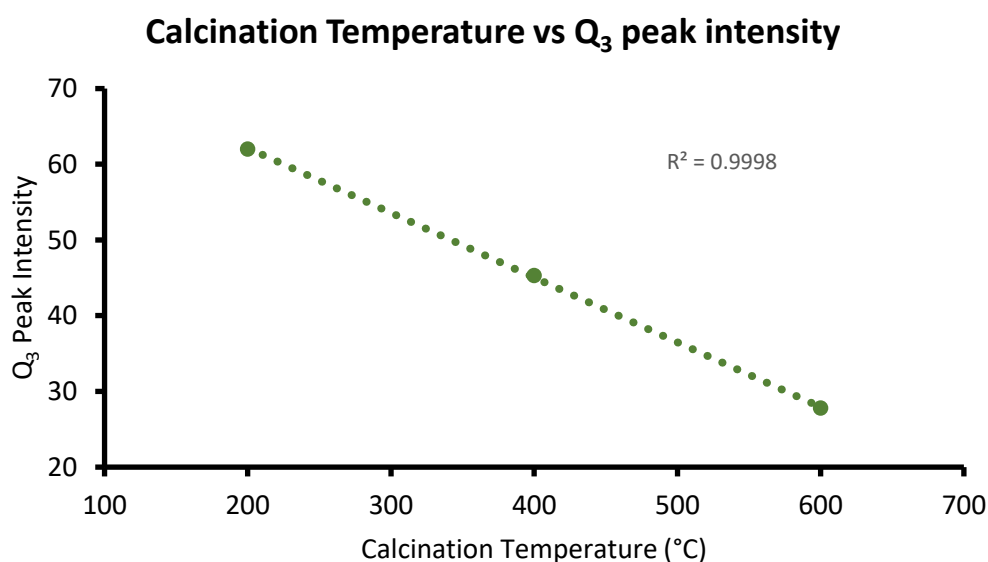


Figure 2.10. Calcination Temperature vs Q_3 resonance intensity from CP SS-NMR spectra of **A-SiO₂₋₂₀₀ 1**, **A-SiO₂₋₄₀₀ 1**, and **A-SiO₂₋₆₀₀ 1**.

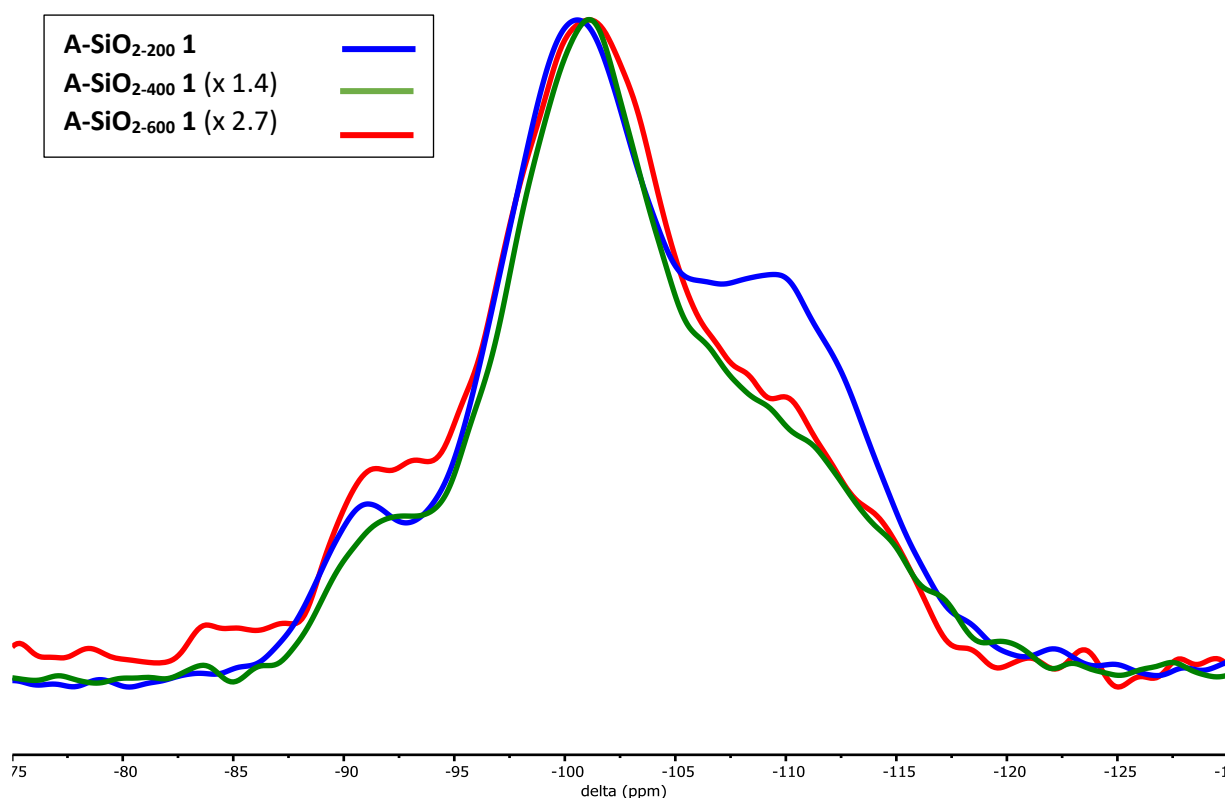


Figure 2.11. CP ^{29}Si SS-NMR spectra of **A-SiO₂₋₂₀₀ 1**, **A-SiO₂₋₄₀₀ 1**, and **A-SiO₂₋₆₀₀ 1** calcined samples. Acquisition frequency 79.437 MHz, spin-rate 6 kHz. The **A-SiO₂₋₄₀₀ 1** spectrum has been scaled by 1.4 and the **A-SiO₂₋₆₀₀ 1** by 2.7 so the spectra are at similar relative intensity to facilitate easier comparison.

From the spectral data given in Figure 2.11, which compares the effect of different temperatures of calcination of Aeroperl 300/30 silica, *i.e.* at 600, 400, and 200 °C, adjusted to a comparable scale, it is clear that the spectra for the three samples (**A-SiO₂₋₂₀₀ 1**, **A-SiO₂₋₄₀₀ 1**, and **A-SiO₂₋₆₀₀ 1**) are very similar. This similarity between the spectra in Figure 2.11 can be attributed to the CP NMR experiment itself. The delay times of the CP NMR experiment cannot easily be optimised due to the silicon-29 nuclei in vicinal/isolated silanols, geminal silanols, and siloxane bridges having quite different relaxation times.³⁰ Indeed this type of effect has been reported previously when undertaking quantitative CP (QCP) SS-NMR of silicas, which relies on the reciprocity relation between CP and cross depolarisation (CDP) to enhance quantification.³²

2.2.3.2.1 Deconvolution of CP ^{29}Si SS-NMR Spectra of Calcined Silicas Using Manual Fitting in MestReNova

As the silica has been successfully calcined (as demonstrated by chemical titration, and further indicated by the relative intensities of the CP spectra), it is expected that at lower temperatures ($T < 400$ °C according to Zhuravlev³³) the Q₃ resonance intensity would initially sharply decrease. This decrease in intensity of the Q₃ resonance is expected due to the loss of vicinal silanols as calcination temperature increases, losing 50% of their density between 200 and 300 °C, and leaving no vicinal

silanols by 400 °C.³³ Consequently, the rate of decrease of the area of the Q₃ resonance would be expected to significantly slow at calcination temperatures of 400 °C and above, as the Q₃ peak will comprise only isolated silanols, which are much harder to remove from the silica surface *via* condensation.³³ The Q₂ resonance would be expected to show a consistent and noticeable decrease in the Q₂:Q₃:Q₄ ratio as calcination temperature increases (decreasing by two thirds from 200 to 600 °C), since geminal silanols are more readily removed than isolated silanols and may be completely removed at temperatures higher than 800 °C.³³ The Q₄ peak is also expected to increase in intensity as the calcination temperature is increased from 200 to 400 and then to 600 °C and more siloxane bridges form. However, the expected scale of change in the Q₂:Q₃:Q₄ ratio is unknown. Therefore, deconvolution of the Q₂, Q₃ and Q₄ components of the various spectra was investigated as a possible way to identify small changes in the ratio of these three silanol species.

To deconvolute the ²⁹Si CP SS-NMR spectra shown in Figure 2.11, the spectroscopic data were analysed in MestReNova (version: 12.0.1-20560, released: 03/01/18), correcting the baseline and phasing as described in the experimental section (See Section 6.0.2.3), before peak fitting with a Gaussian fit and manually changing the peak width, height, position and area until a minimum residual error was reached. However, for each spectrum different fits appeared to be possible with similar residual errors, *i.e.* a global minima could not be found, possibly as a result of human error due to manually changing parameters. Table 2.8 below shows how the same spectra could show different results depending on which minimum in residual error was reached.

A key problem is that fits were attempted using three Gaussians to represent the Q₂, Q₃ and Q₄ signals, but the low intensity of the Q₂ resonance makes fitting this feature difficult. Furthermore, the choice of three Gaussians is relatively arbitrary (there may be legitimate reasons to use a different number of peaks or different line shapes), as has already been pointed out in the literature.³⁴ From the data given in Table 2.8 it can be seen that there is up to 10% of the total silicon content being assigned differently between the two different deconvolution attempts. These differing results lead to the conclusion that there were too many parameters for this method of deconvolution to be accurate, reliable, or repeatable for small differences to be observed.

Table 2.8. Two different attempts at deconvolution of one CP ²⁹Si SS-NMR spectrum using MestReNova

Silica Sample	Deconvolution attempt 1				Deconvolution attempt 2				Difference		
	Q ₂ % area	Q ₃ % area	Q ₄ % area	Residual Error	Q ₂ % area	Q ₃ % area	Q ₄ % area	Residual Error	Q ₂ % area	Q ₃ % area	Q ₄ % area
A-SiO ₂ -600 1	2.1	18.5	79.3	2.1	2.5	18.4	79.1	2.5	0.4	0.1	0.2
A-SiO ₂ -400 1	3.1	45.6	51.3	3.2	3.2	35.5	61.3	3.3	0.1	10.1	10.0
A-SiO ₂ -200 1	2.8	14.5	82.7	0.8	0.6	24.3	75.1	0.6	2.2	9.8	7.6

2.2.3.2.2 Analysing the Reproducibility of the Acquisition of the ^{29}Si SS-NMR Spectra of Calcined Silica

Given the uncertainty that results from the deconvolution procedure as described above, it was decided that it was important to investigate the reliability and reproducibility of the spectral acquisition process itself. This is necessary to establish whether the difficulty of seeing small changes in the peak fits is important or within the statistical noise that results from the experiment's reproducibility. Thus, to investigate the experimental reproducibility, in addition to the analysis of the individual silica samples **A-SiO₂₋₂₀₀ 1**, **A-SiO₂₋₄₀₀ 1**, **A-SiO₂₋₆₀₀ 1**, further analyses were run for a batch of SiO₂₋₆₀₀ (**A-SiO₂₋₆₀₀ 1'** and **A-SiO₂₋₆₀₀ 1''**) by repeating the NMR spectroscopic analysis of the same material emptied and then repacked into the same rotor. This was done to determine whether the calcined silica was consistent through the batch and whether the packing of the rotor was reliable each time. The results of these reproducibility tests are given in Figure 2.12.

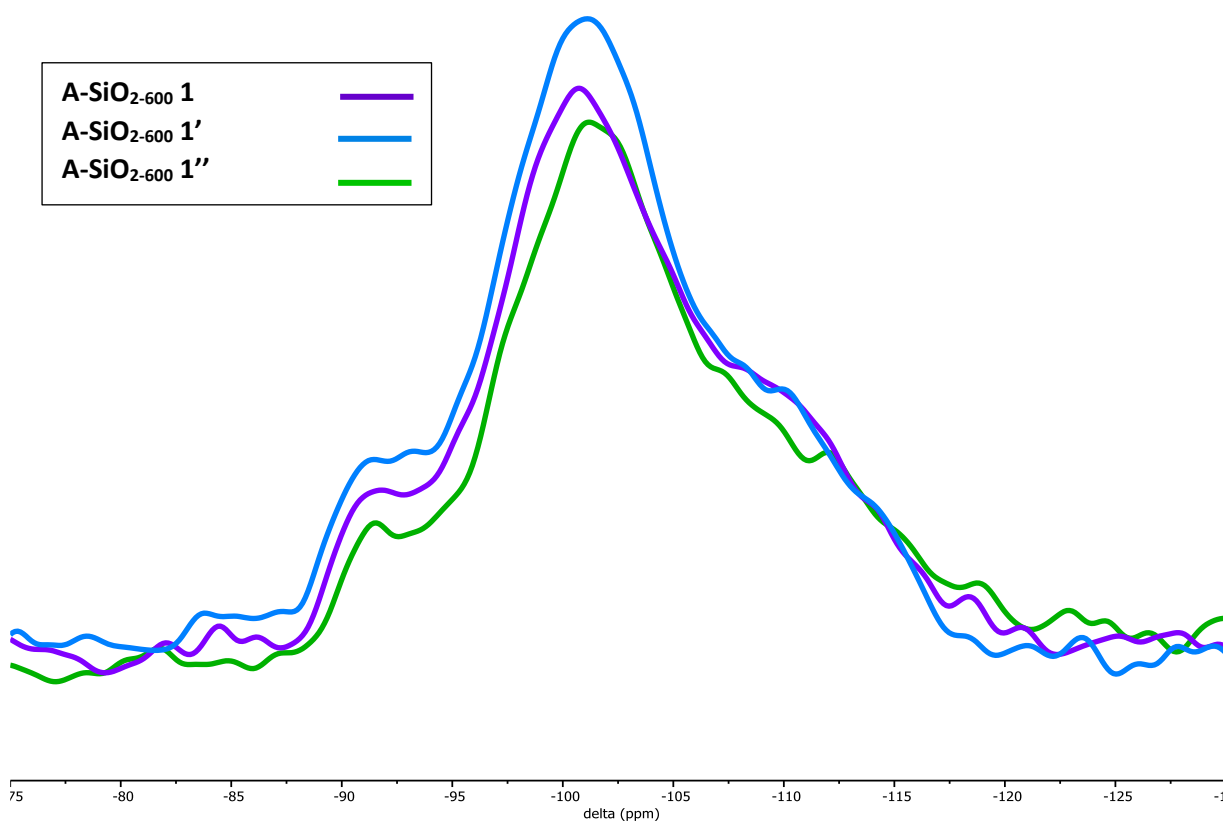


Figure 2.12. The CP ^{29}Si SS-NMR spectra of **A-SiO₂₋₆₀₀ 1** ran three times with the rotor repacked between each run. Acquisition frequency 79.437 MHz, spin-rate 6 kHz.

Despite being the same silica sample that was carefully repacked into the same rotor, there are appreciable differences between the spectra resulting from each run as shown in Figure 2.12. The exact reasons why the CP ^{29}Si SS-NMR spectra are different are currently unknown. However, it is suspected to be due to the silica packing slightly differently within the NMR rotor. A similar lack of

reproducibility is observed in the DE data obtained from one sample that is packed, emptied, and then repacked into a rotor.

To confirm whether the cause of the spectral changes between the three spectra (Figure 2.12) are due to the packing of the silica in the rotor, the first sample (**A-SiO₂₋₆₀₀ 1**) was run consecutively two more times, without repacking the rotor. These spectra will be referred to as **A-SiO₂₋₆₀₀ 1a** and **A-SiO₂₋₆₀₀ 1b**. This experiment was undertaken to test whether SS-NMR spectroscopy could return consistent spectra for an unchanged sample. The resulting spectra (**A-SiO₂₋₆₀₀ 1**, **A-SiO₂₋₆₀₀ 1a**, and **A-SiO₂₋₆₀₀ 1b**) are shown in Figure 2.13; the spectra are not off-set nor are their intensities altered in the figure.

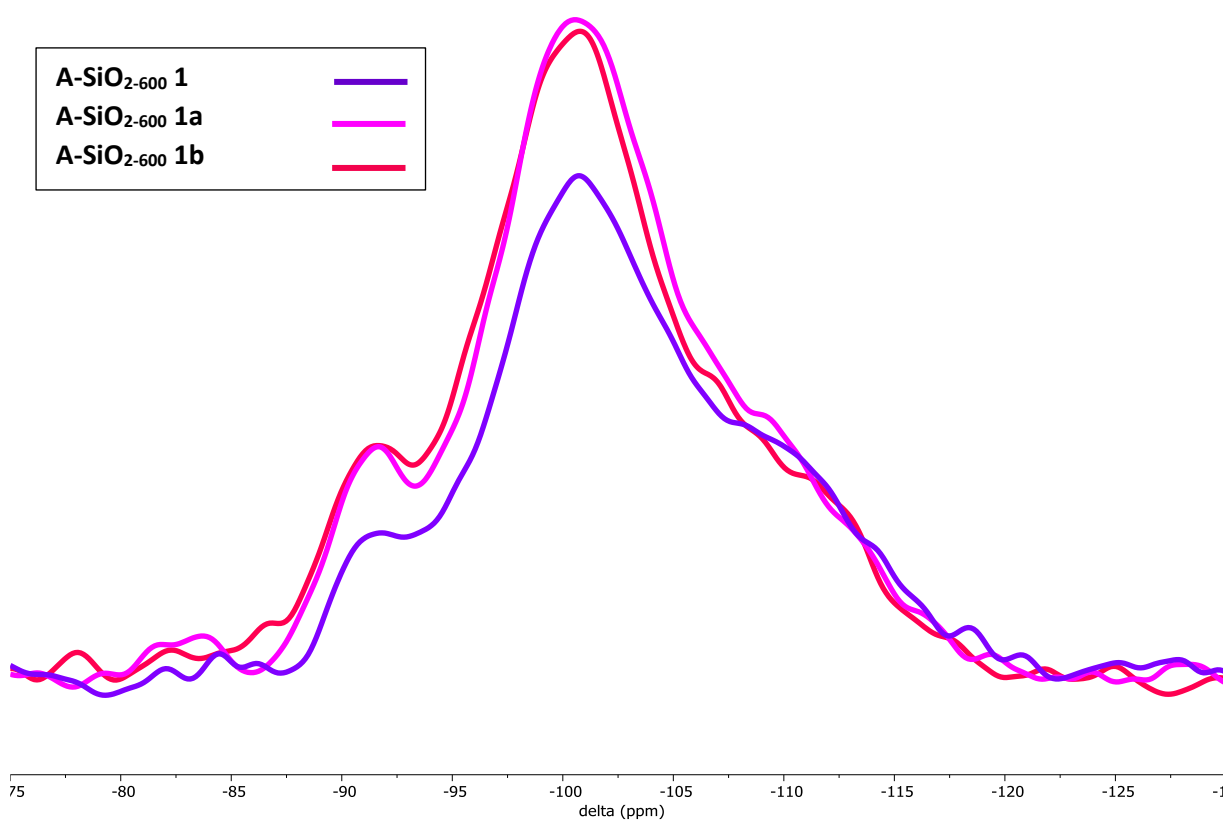


Figure 2.13. CP ²⁹Si SS-NMR spectra of **A-SiO₂₋₆₀₀ 1** acquired three times without repacking the rotor between each run. Frequency 79.437 MHz, Spin-rate 6 kHz.

Noticeably, the **A-SiO₂₋₆₀₀ 1** spectrum has a lower intensity than that of **A-SiO₂₋₆₀₀ 1a** and **A-SiO₂₋₆₀₀ 1b** spectra (Figure 2.13), adjusted in Figure 2.14 for easier comparison of peak shape. This change in signal intensity between the first run and the two next runs is thought to be due to the shifting of the silica within the rotor during the first experiment, despite the rotor being packed as tightly and as fully as possible when charging. As the rotor spins (6 kHz), the silica physically moves inside the rotor due to centrifugal forces. In the next two runs, it is assumed that the silica does not move any further, so the spectral intensity does not alter again. This change in intensity also shows how using the intensity of ²⁹Si CP SS-NMR spectra to quantify the hydroxyl group density is not a viable (or at least neither easy

nor quickly reproducible) approach, though it still gives a rough indication of changes in silanol density between silica samples calcined at different temperatures.

The three spectra shown in Figure 2.14 (**A-SiO₂₋₆₀₀ 1**, **A-SiO₂₋₆₀₀ 1a**, and **A-SiO₂₋₆₀₀ 1b**) are very similar to each other, in comparison to the three spectra in Figure 2.11 (comparing different temperatures) or the three spectra in Figure 2.12 (comparing the repacking of **A-SiO₂₋₆₀₀ 1**), which show differences between each spectra. This suggests that SS-NMR spectroscopy can return essentially consistent results on the same sample, and that the observed differences are due to the variation of sample packing within the rotor.

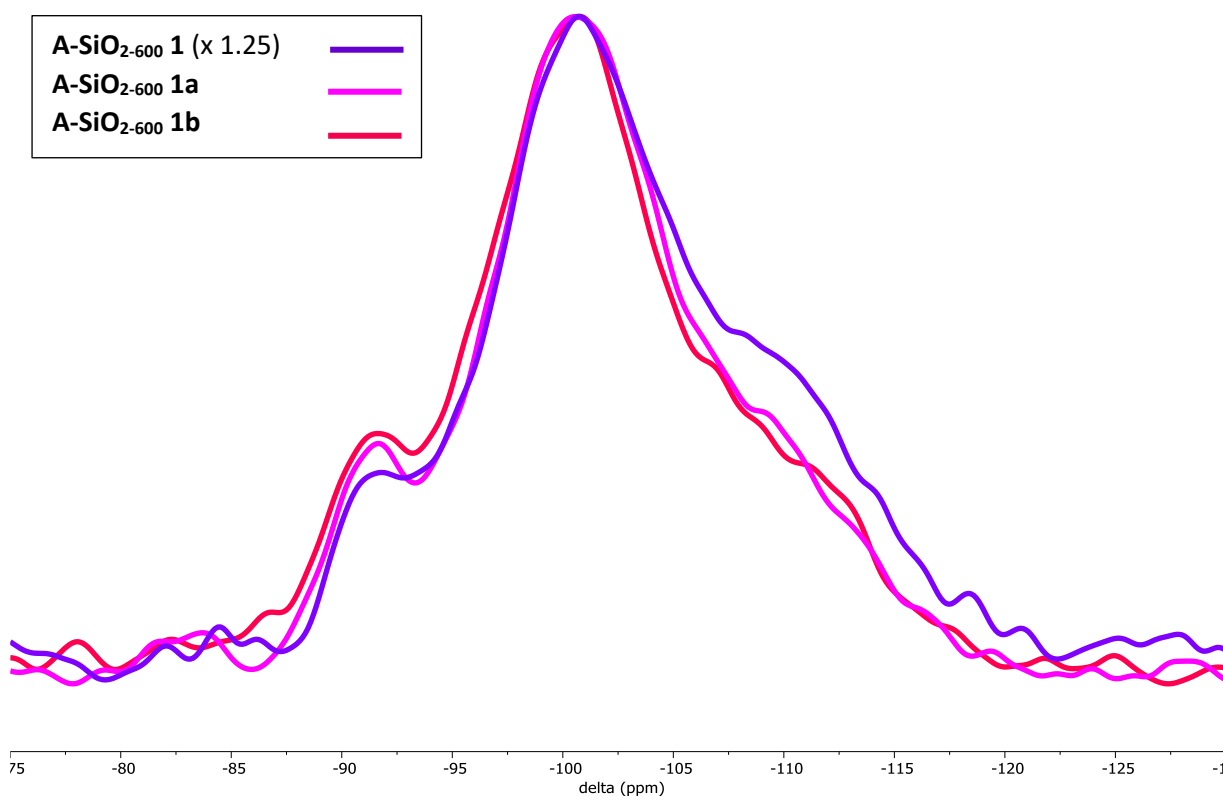


Figure 2.14. CP ²⁹Si SS-NMR of **A-SiO₂₋₆₀₀ 1**, run three times with the rotor repacked between each run. Acquisition frequency 79.437 MHz, spin-rate 6 kHz. The spectrum of **A-SiO₂₋₆₀₀ 1** has been scaled by 1.25 so the spectra are at similar relative intensity for easier comparison.

The experiment of running a sample three times without repacking the rotor between each run was also done for SiO₂₋₂₀₀, re-acquiring **A-SiO₂₋₂₀₀ 1** to obtain spectra for **A-SiO₂₋₂₀₀ 1a** and **A-SiO₂₋₂₀₀ 1b**. Figure 2.15 shows the CP NMR spectra for **A-SiO₂₋₂₀₀ 1**, **A-SiO₂₋₂₀₀ 1a**, and **A-SiO₂₋₂₀₀ 1b**, and Figure 2.16 shows the adjusted spectra of Figure 2.15 for easier comparison of the peak shapes. As found for the spectroscopic analysis of **A-SiO₂₋₆₀₀ 1**, the spectrum from the first run has a lower intensity than that of the spectra from the second and third runs. This further supports the notion that the increase of

intensity between the first run and the second/third run is a physical effect caused by the spin of the rotor moving the silica into a different position. The change of intensity is likely a feature inherent to SS-NMR spectroscopy (*i.e.* the rotor spinning) rather than a chance chemical change (such as adventitious rehydroxylation).

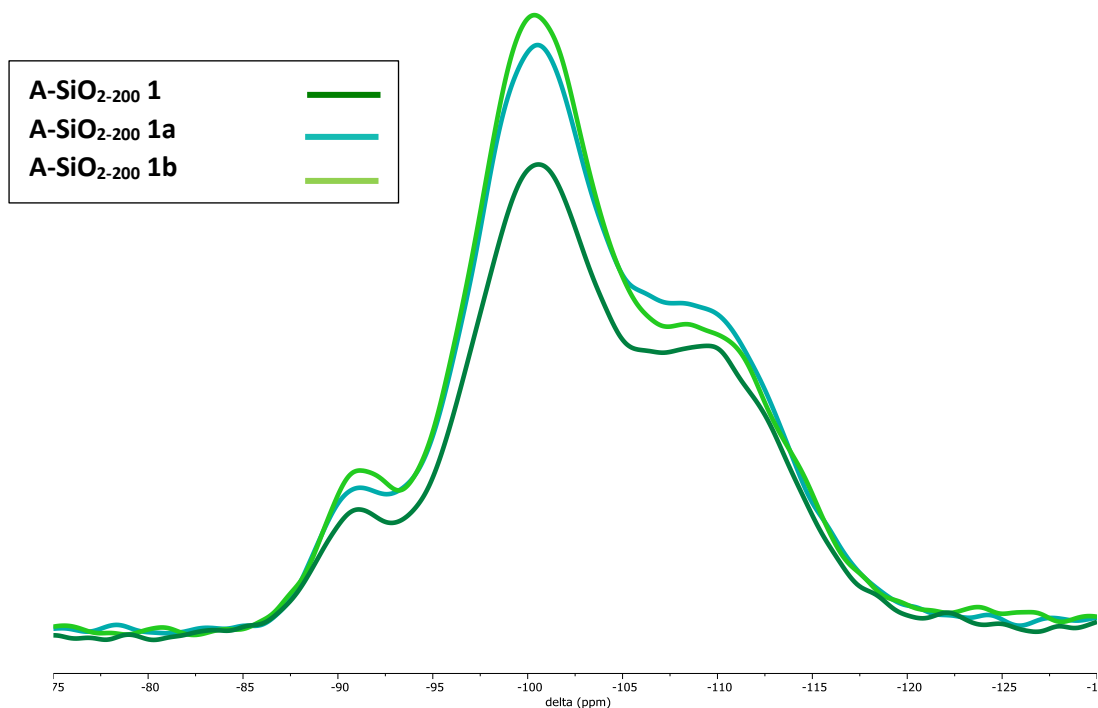


Figure 2.15. CP ^{29}Si SS-NMR spectra of **A-SiO₂₋₂₀₀ 1** same sample run three times without repacking the rotor between each run. Acquisition frequency 79.437 MHz, spin-rate 6 kHz.

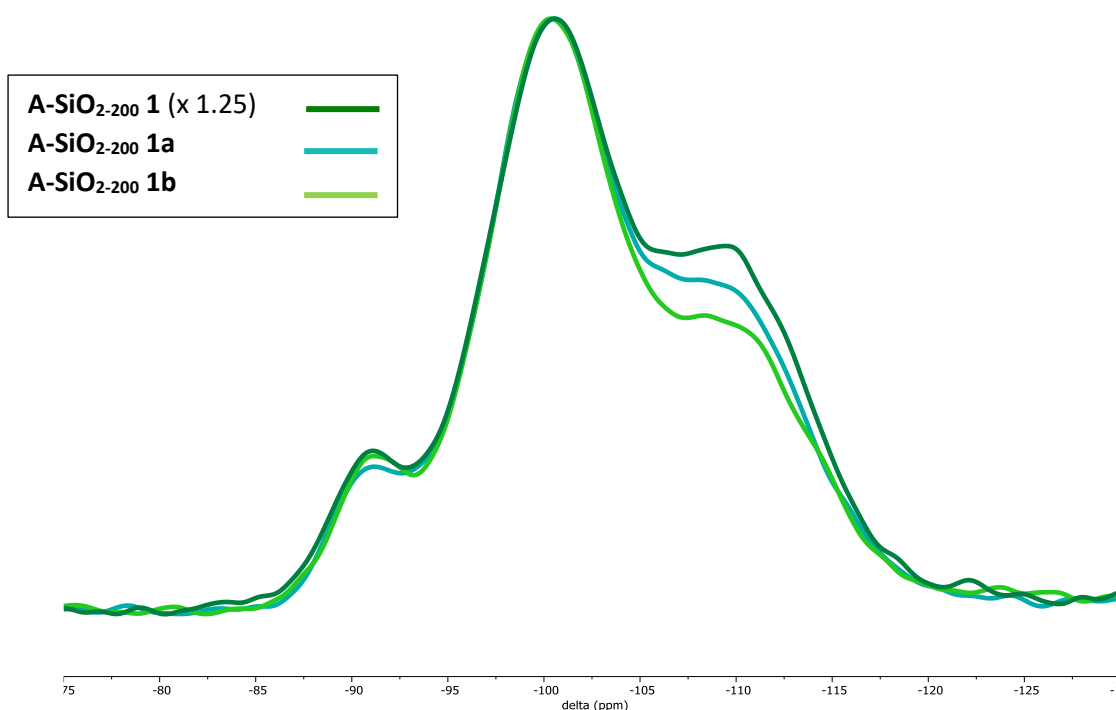


Figure 2.16. CP ^{29}Si SS-NMR spectra of **A-SiO₂₋₂₀₀ 1** acquired three times with the rotor repacked between each run. Acquisition frequency 79.437 MHz, spin-rate 6 kHz. The **A-SiO₂₋₂₀₀ 1** spectrum has been scaled by 1.25 so the spectra are at similar relative intensity for easier comparison.

2.2.3.2.3 Deconvolution of ^{29}Si SS-NMR Spectra of Calcined Silicas Using Automatic Fitting in MestReNova

Given the difficulty encountered in initial attempts to conduct NMR spectral deconvolution using the MestReNova software, as described in Section 2.2.3.2.1, which led to unreliable or irreproducible results for deconvolution of the same spectrum, an attempt was made to remove the element of human error. MestReNova's fitting algorithm was employed to find the optimal peak fit, instead of manually applying changes to the width and height of the peaks. The peak positions were locked (with a small degree of freedom of ± 2 ppm) at -91.25 (Q_2), -101 (Q_3) and -110 (Q_4) ppm, and the inbuilt automatic fitting routine used to deconvolute the spectra from the samples described in Section 2.2.3.2 (Figure 2.9, Figure 2.12, Figure 2.13, and Figure 2.15).

Table 2.9 shows the results from deconvolutions of both the CP and DE spectra of **A-SiO₂₋₂₀₀ 1**, **A-SiO₂₋₄₀₀ 1**, and **A-SiO₂₋₆₀₀ 1** and any subsequent reruns done on those samples using MestReNova's automatic fitting. While overall this approach led to a lower residual error and increased confidence in the reliability of the results, different error minima could still be reached in different attempts. The CP experiment has more potential for discriminating the different silanol species present compared to the DE experiment, as MestReNova's fitting algorithm was unsuitable at picking the Q_2 out of the tail of the Q_4 peak in the DE spectra.

Table 2.9. Deconvolution of CP and DE ²⁹Si SS-NMR spectra for variously calcined samples of Aeroperl 300/30 silica using MestReNova, using MestReNova's automatic fitting feature (version: x64 24/01/18)

Silica Sample	CP				DE			
	Q ₂ % area	Q ₃ % area	Q ₄ % area	Residual Error	Q ₂ % area	Q ₃ % area	Q ₄ % area	Residual Error
A-SiO ₂₋₆₀₀ 1	2.1	77.7	20.2	0.6	15.0	85.0	0.2	
A-SiO ₂₋₆₀₀ 1a	3.4	82.1	14.5	0.9	23.3	76.7	0.1	
A-SiO ₂₋₆₀₀ 1b	4.8	84.3	10.9	0.6	18.5	81.5	0.3	
A-SiO ₂₋₆₀₀ 1'	1.0	66.9	32.1	0.7	19.9	80.1	0.1	
A-SiO ₂₋₆₀₀ 1''	3.4	83.2	13.5	0.9	14.5	85.5	0.2	
A-SiO ₂₋₄₀₀ 1	1.9	73.4	24.7	1.2	10.9	89.1	0.2	
A-SiO ₂₋₂₀₀ 1	1.3	67.1	31.6	6.8	20.3	79.7	0.3	
A-SiO ₂₋₂₀₀ 1a	1.1	69.7	29.2	8.1	17.2	82.8	0.2	
A-SiO ₂₋₂₀₀ 1b	1.6	71.7	26.7	7.8	11.1	88.9	0.3	

2.2.3.2.4 Deconvolution of ²⁹Si SS-NMR Spectra of Calcined Silicas Using Origin

To confirm whether different minima of the area of the Q peaks could be reached with a different fitting algorithm, Origin software (OriginLab Corporation; version: 01/06/2018) was employed to repeat the deconvolutions attempted using MestReNova (Table 2.10). Like the method used for spectral fitting done using MestReNova, the chemical shifts of the resonances were locked (with a small degree of freedom of ± 2 ppm) at -91.25 (Q₂), -101 (Q₃) and -110 (Q₄) ppm, and Origin's fitting algorithm used to find the optimal fit with as little human input/manual changes as possible in order to limit human error. Unlike the results obtained using MestReNova, the minima found were more consistent, and the fitting achieved using the Origin software overall had a lower degree of error than that achieved using MestReNova, particularly for deconvolution of spectra of silica calcined at 200 °C, which had a large residual error in the MestReNova fittings.

Table 2.10. Deconvolution of CP and DE spectra using Origin (version: 01/06/2018)

Silica Sample	CP						DE					
	Q ₂ % area	Area Error	Q ₃ % area	Area Error	Q ₄ % area	Area Error	Q ₂ % area	Area Error	Q ₃ % area	Area Error	Q ₄ % area	Area Error
A-SiO₂₋₆₀₀ 1	9.1	0.2	53.2	1.0	37.8	1.0	0.6	0.1	11.0	0.4	88.4	0.4
A-SiO₂₋₆₀₀ 1a	11.7	0.2	56.8	0.2	31.5	0.2	1.2	0.1	13.8	0.8	85.0	0.8
A-SiO₂₋₆₀₀ 1b	14.3	0.3	47.7	1.3	38.0	1.3	2.7	0.1	20.2	1.3	77.1	1.3
A-SiO₂₋₆₀₀ 1'	11.6	0.3	61.5	0.9	26.9	0.7	0.6	0.1	33.0	0.3	66.5	0.2
A-SiO₂₋₆₀₀ 1''	13.4	0.4	49.4	2.2	37.3	2.1	3.2	0.2	18.6	0.5	78.2	0.4
A-SiO₂₋₄₀₀ 1	12.7	0.2	45.7	0.8	41.7	0.7	3.0	0.1	16.1	0.7	80.9	0.7
A-SiO₂₋₂₀₀ 1	11.3	0.1	52.3	0.3	36.4	0.2	3.4	0.2	16.5	0.6	80.2	0.5
A-SiO₂₋₂₀₀ 1a	9.9	0.1	51.2	0.2	38.9	0.2	1.6	0.1	34.8	0.3	65.2	0.3
A-SiO₂₋₂₀₀ 1b	11.2	0.1	55.5	0.3	33.2	0.2	6.3	0.6	13.4	0.7	80.3	0.4

2.2.3.2.5 Comparison of Deconvolution Fittings Derived by Automatic Fitting MestReNova and by Origin

As the total silanol count on the silica surface is already known thanks to chemical titration (discussed in Section 2.2.2), the density of geminal and vicinal/isolated silanols can be derived from the ratio of the Q₂:Q₃ resonances obtained from the spectral deconvolutions of the CP spectra made using MestReNova and Origin software (Table 2.9 and Table 2.10, respectively). For example, the known hydroxyl density of **A-SiO₂₋₄₀₀ 1** is 1.4 mmol g⁻¹ determined by chemical titration (Table 2.4). According to the spectral deconvolution made using Origin (Table 2.10), the Q₂:Q₃ ratio is calculated to be 22:78. When that ratio is applied to 1.4 mmol g⁻¹, the density of the Q₂ and Q₃ silanols is 0.3 mmol g⁻¹ and 1.1 mmol g⁻¹, respectively. The ratio of the Q₂:Q₃ peaks is expected to change relative to calcination temperature, depending on the rate of loss of the different silanol species. The data showing the ratio of the geminal OH density (Q₂ OH density) and the vicinal/isolated OH density (Q₃ OH density) derived from using both MestReNova and Origin software is given below in Table 2.11. The densities of different silanol species on Aeroperl 300/30 silica calcinated at different temperatures, reported in Table 2.11, are given below in Figure 2.17 (derived using MestReNova software) and Figure 2.18 (derived using Origin software).

Table 2.11. Quantity of different OH species (geminal silanols vs isolated/vicinal silanols) for variously-calcined samples of Aeroperl-300/30 silica as determined by combining deconvolution data with chemical titration data. Comparison of data obtained from CP ^{29}Si SS-NMR spectral deconvolutions done using both MestReNova and Origin software.

Silica Sample	Chemical Titration	MestReNova		Origin		Difference between MestReNova and Origin (mmol g^{-1})
	Total OH density (mmol g^{-1})	Geminal OH density (mmol g^{-1})	Q ₃ OH density (mmol g^{-1})	Geminal OH density (mmol g^{-1})	Q ₃ OH density (mmol g^{-1})	
A-SiO ₂₋₆₀₀ 1	0.8	0.02	0.78	0.1	0.7	0.1
A-SiO ₂₋₆₀₀ 1a	0.8	0.03	0.77	0.1	0.7	0.1
A-SiO ₂₋₆₀₀ 1b	0.8	0.04	0.76	0.2	0.6	0.2
A-SiO ₂₋₆₀₀ 1'	0.8	0.01	0.79	0.1	0.7	0.1
A-SiO ₂₋₆₀₀ 1''	0.8	0.03	0.77	0.2	0.7	0.1
A-SiO ₂₋₄₀₀ 1	1.4	0.04	1.36	0.3	1.1	0.3
A-SiO ₂₋₂₀₀ 1	2.2	0.04	2.16	0.4	1.8	0.3
A-SiO ₂₋₂₀₀ 1a	2.2	0.03	2.17	0.4	1.8	0.3
A-SiO ₂₋₂₀₀ 1b	2.2	0.05	2.15	0.4	1.8	0.3

Density of Different Silanols vs Calcination Temperature
(Derived from MestReNova)

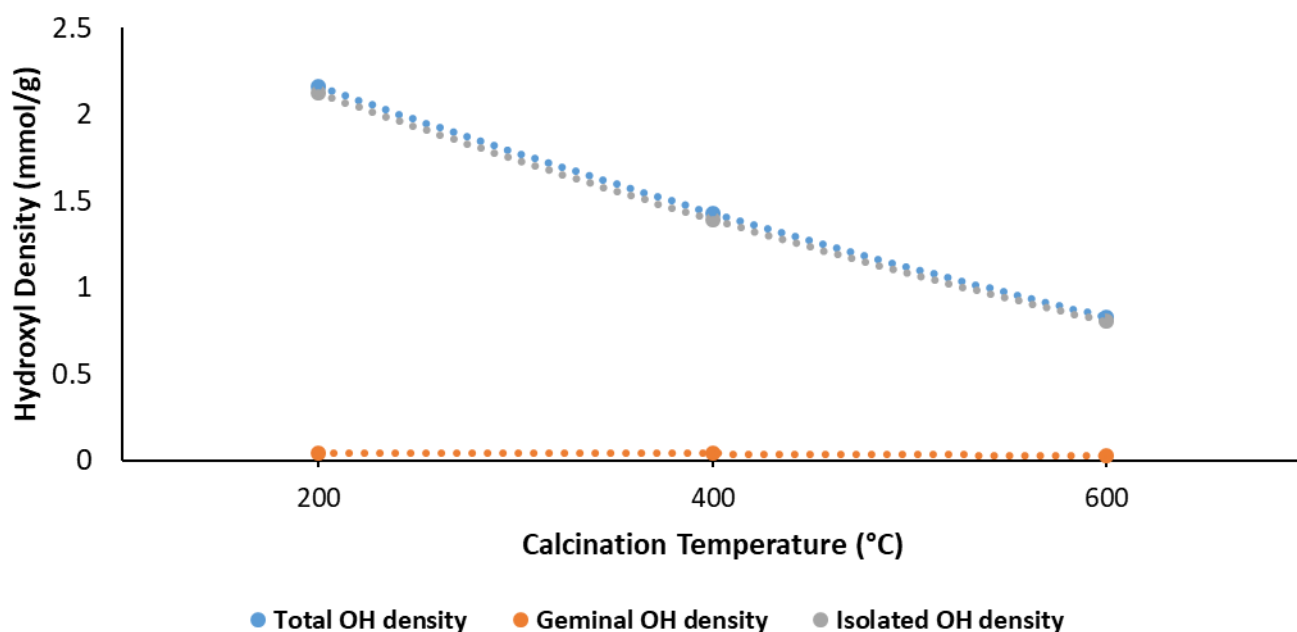


Figure 2.17. Density of different OH species (geminal and isolated/vicinal silanols) vs calcination temperatures. OH density calculated by combining the deconvolution data of CP ^{29}Si SS-NMR spectra using the MestReNova software package (Table 2.11) and chemical titration (Table 2.4).

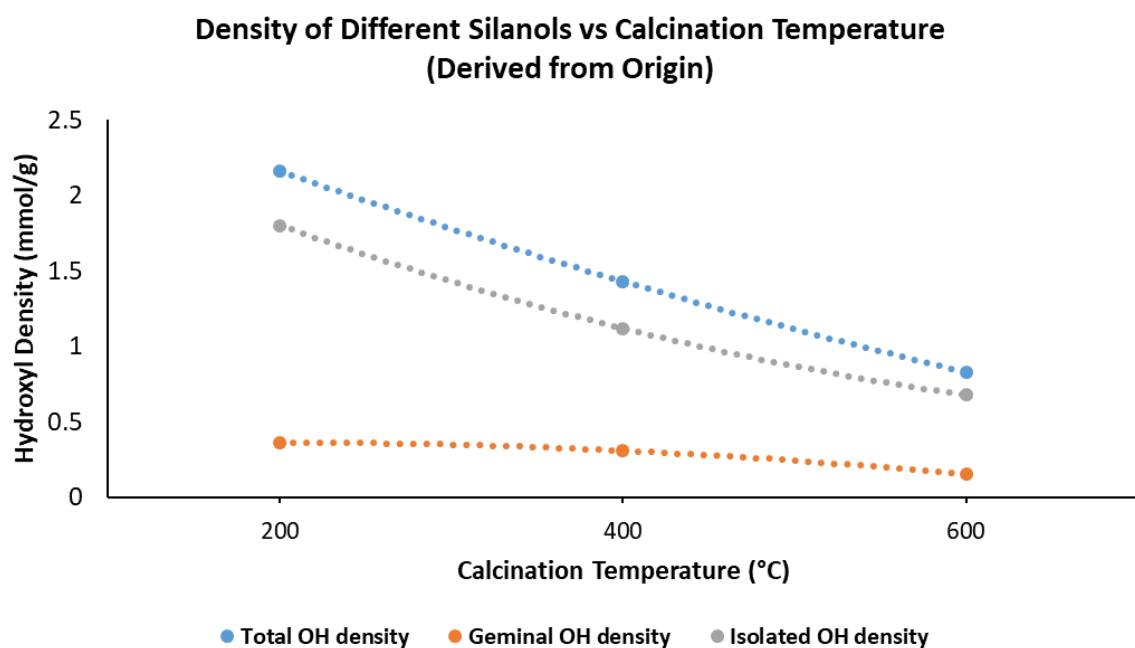


Figure 2.18. Density of different OH surface species (geminal and isolated/vicinal silanols) vs calcination temperatures. OH density calculated by combining the deconvolution data of CP ^{29}Si SS-NMR spectra using the Origin software package (Table 2.11) and chemical titration (Table 2.4).

Spectral deconvolution using the MestReNova software gives rise to a much lower geminal density than the density obtained when deconvolution is undertaken using the Origin software package (Table 2.11). According to Zhuravlev, the expected geminal density for silicas calcined between 200 and 600 °C is 0.1 – 0.3 mmol g⁻¹.³³ Deconvolution *via* MestReNova gives a geminal density of 0.01 – 0.05 mmol g⁻¹, which is much lower than suggested in the literature. There is also no trend in the data from the MestReNova predictions that correlate the geminal silanol density with calcination temperature. In contrast, deconvolution of the ^{29}Si SS-NMR spectra using the Origin software package (seen in Table 2.11) gives a geminal density of 0.1 – 0.4 mmol g⁻¹, which correlates well with the generalised values reported previously by Zhuravlev.³³

As the deconvolution data from MestReNova in Table 2.11 show no trend, higher error, and do not agree with the general data described in the literature, the data derived by spectral fitting using Origin software (in Table 2.11) was subsequently used for the quantification of the number and density of each different silanol groups on the surface of the various silica supports employed throughout this thesis study. Overall, the density of isolated and geminal silanols on the surface of Aeroperl 300/30 decreases at roughly the same rate as the calcination temperature increases. The density of the geminal silanols falls to 42% of their original concentration, while the density of isolated + vicinal silanols together falls to 38% of their concentration. Following calcination at 600 °C (24 h), there remains a mix of isolated/vicinal (Q₃) and geminal (Q₂) silanols on the surface of Aeroperl 300/30.

2.2.3.3 ^1H SS-NMR Spectroscopic Analysis of Silica Supports

Another way to determine the density of silanol groups on the surface of the silicas is through use of ^1H SS-NMR spectroscopy. ^1H SS-NMR spectroscopy will not differentiate the silanol types on the surface, but by using a standard for quantification purposes, it is possible to use ^1H SS-NMR spectroscopy to directly derive the OH-density through NMR spectral measurements. This offers a non-destructive alternative to chemical titration.

Use of a standard is an important part of determining the hydroxyl density through ^1H SS-NMR spectroscopic experiments, hence it must be chosen carefully. It was decided that an external standard would be preferable to an internal standard in this project, as the calcined silica samples are treated as being air-sensitive, so handling is more complicated due to requiring the use of a glove box. Weighing an exact weight of both the calcined silica sample and standard to the precision needed, and then mixing the calcined silica sample and standard in a homogeneous fashion would be difficult in a glove box. There is also the risk of an internal standard reacting with the silica's surface silanol groups when mixed. Since there is such a low concentration of protons in the silica samples, an external standard must also have a very low number of protons to be comparable. Consequently, taking these considerations together, potassium phosphate dihydrate was chosen as an external standard. The integral scale for the potassium phosphate was set to 100, and the spectra of the calcined silica were obtained on the same scale. The number of hydrogens per integral was calculated from the potassium phosphate dihydrate spectrum, shown in Figure 2.19 below. The ^1H SS-NMR spectra of **A-SiO₂₋₂₀₀ 1**, **A-SiO₂₋₄₀₀ 1**, **A-SiO₂₋₆₀₀ 1**, and **A-SiO₂₋₇₀₀ 1** obtained are shown in Figure 2.20.

Potassium phosphate dihydrate:

Molar mass = 248.31 g/mol

Standard weight = 9.2 mg

Number of hydrogen atoms in formula = 4

Integration = 100

$$H \text{ in standard (g)} = \frac{(\text{number of hydrogen atoms} \times \text{mass of hydrogen})}{\text{molar mass of potassium phosphate dihydrate}} \times \frac{\text{standard weight}}{1000}$$

$$H \text{ in standard (g)} = \frac{(4 \times 1.01 \text{ g/mol})}{248.31 \text{ g/mol}} \times \frac{9.2 \text{ mg}}{1000}$$

$$H \text{ in standard (g)} = 1.50 \times 10^{-4} \text{ g}$$

$$H \text{ (g) per integration} = \frac{\text{Hydrogen in standard (g)}}{\text{Integration}}$$

$$H \text{ (g) per integration} = 1.50 \times 10^{-6}$$

Figure 2.19. Calculating the hydrogen (g per integration) from the external standard – potassium phosphate dihydrate

H (g) per integration is the weight of hydrogen represented by the integration in the NMR spectrum

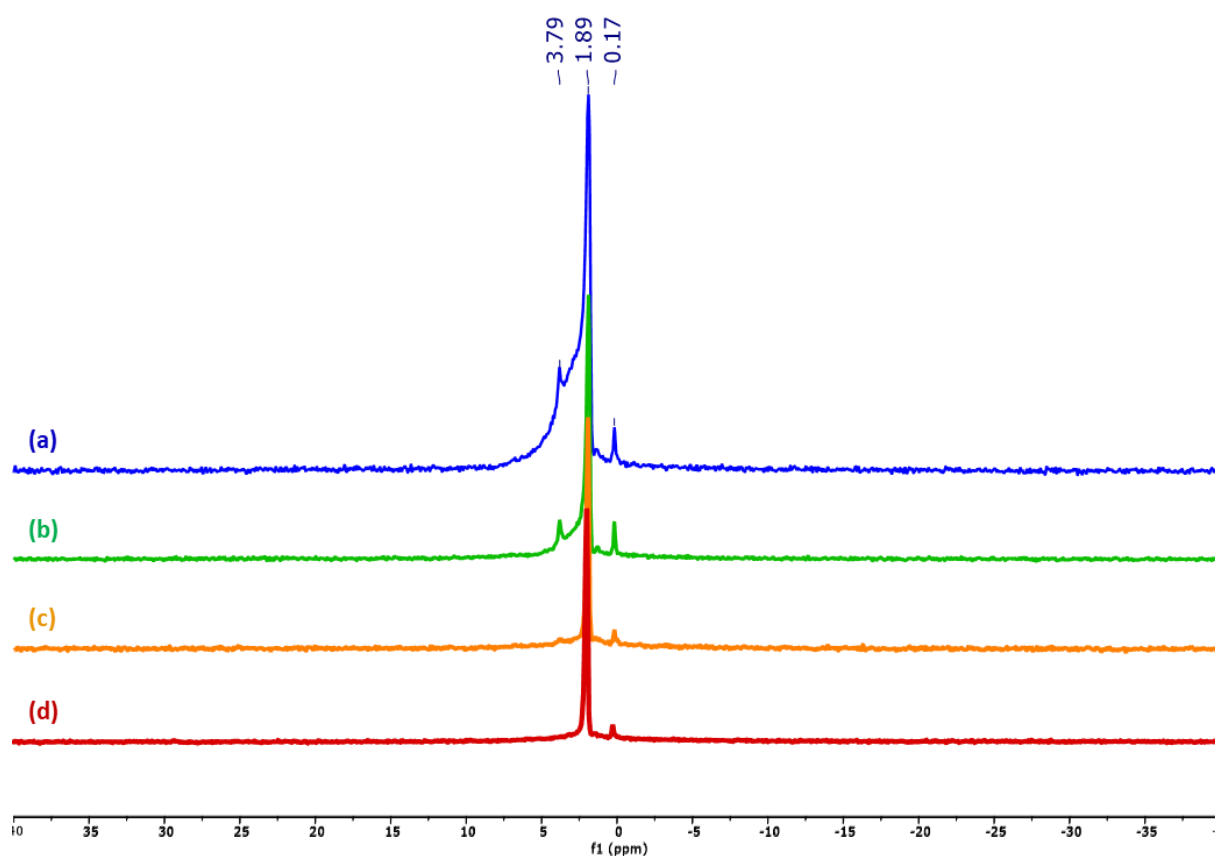


Figure 2.20. ^1H SS-NMR spectra of calcined Aeroperl 300/30 silica, acquisition frequency 400.17 MHz, spin-rate 40 kHz

(a) 200 °C (b) 400 °C (c) 600 °C (d) 700 °C

In each of the ^1H SS-NMR spectra shown in Figure 2.20, there is a distinct major resonance at a chemical shift of 1.89 ppm that dominates the spectrum, which has been assigned to the silanol hydroxyl resonance. There are two smaller resonances in each of the spectra: the signal at 0.17 ppm is assigned to residual silicon grease, arising from contamination of the sample during the calcination process and subsequent manipulation using a Schlenk line/glovebox; the origins of the second resonance at 3.79 ppm are unknown, but it has tentatively been attributed to an impurity.

As the calcination temperature rises, the intensity of the resonances at 0.17 and 3.79 ppm decrease, with the higher frequency 3.79 ppm resonance not being visible in the spectrum of silica calcined at 700 °C (**A-SiO₂₋₇₀₀ 1**). It is thought that calcination under a nitrogen flow removes these impurities. The intensity of the main resonance at 1.89 ppm decreases with calcination temperature, correlating and consistent with the removal of surface hydroxyl groups. The integration of the resonance at 1.89 ppm was used in conjunction with the number calculated using the method described in Figure 2.19, 1.50×10^{-6} H (g) per integration, to calculate the OH-density of the silica surface. An example of this calculation is given below in Figure 2.21, which shows how the silanol density of **A-SiO₂₋₂₀₀ 1** was calculated. The OH density calculated by ^1H SS-NMR for **A-SiO₂₋₂₀₀ 1**, **A-SiO₂₋₄₀₀ 1**, **A-SiO₂₋₆₀₀ 1**, and **A-SiO₂₋₇₀₀ 1** is shown below in Table 2.12.

A – SiO₂₋₂₀₀ 1:

Sample weight = 3.8 mg

Integration = 5.98

$$H \text{ in } \mathbf{A - SiO_{2-200} 1} (g) = \frac{\text{Integration}}{H (g) \text{ per integration}}$$

$$H \text{ in } \mathbf{A - SiO_{2-200} 1} (g) = \frac{5.98}{1.50 \times 10^{-6}}$$

$$H \text{ in } \mathbf{A - SiO_{2-200} 1} (g) = 8.95 \times 10^{-6} g$$

$$H (g) \text{ per gram of } \mathbf{A - SiO_{2-200} 1} = \frac{H \text{ in } \mathbf{A - SiO_{2-200} 1} (g)}{\text{Sample weight} / 1000}$$

$$H (g) \text{ per gram of } \mathbf{A - SiO_{2-200} 1} = \frac{8.95 \times 10^{-6} g}{3.8 \text{ mg} / 1000}$$

$$H (g) \text{ per gram of } \mathbf{A - SiO_{2-200} 1} = 2.36 \times 10^{-3}$$

$$OH \text{ mmol per gram of } \mathbf{A - SiO_{2-200} 1} = \frac{H (g) \text{ per gram of } \mathbf{A - SiO_{2-200} 1}}{\text{mass of hydrogen}} \times 1000$$

$$OH \text{ mmol per gram of } \mathbf{A - SiO_{2-200} 1} = \frac{2.36 \times 10^{-3}}{1.01 \text{ g/mol}} \times 1000$$

$$OH \text{ mmol per gram of } \mathbf{A - SiO_{2-200} 1} = 2.33 \text{ (OH mmol per gram)}$$

Figure 2.21. Calculation of the hydroxyl density of **A-SiO₂₋₂₀₀ 1**, using the hydrogen (g per integration) as calculated using the method described in Figure 2.19. The hydroxyl density for the other silica samples was calculated with the same method.

Table 2.12. The surface hydroxyl density of Aeroperl 300/30 silica calcined at different temperatures, derived from ¹H SS-NMR. The density in nm² was obtained by using the surface area calculated from the BET analysis

	Hydroxyl density (mmol g ⁻¹)	Hydroxyl density (nm ⁻²)
Aeroperl 300/30 SiO₂₋₇₀₀ 1	0.3	0.6
Aeroperl 300/30 SiO₂₋₆₀₀ 1	0.6	1.2
Aeroperl 300/30 SiO₂₋₄₀₀ 1	1.5	3.2
Aeroperl 300/30 SiO₂₋₂₀₀ 1	2.3	5.2

The hydroxyl density, as derived by ¹H SS-NMR spectral analysis, is found to decrease as calcination temperature increases, similar to the trend in hydroxyl density determined from chemical titration, as expected. A comparison of the hydroxyl density derived by chemical titration and that determined by ¹H SS-NMR spectroscopic analysis is shown in Figure 2.22.

OH-density Derived by Titration vs ^1H SS-NMR

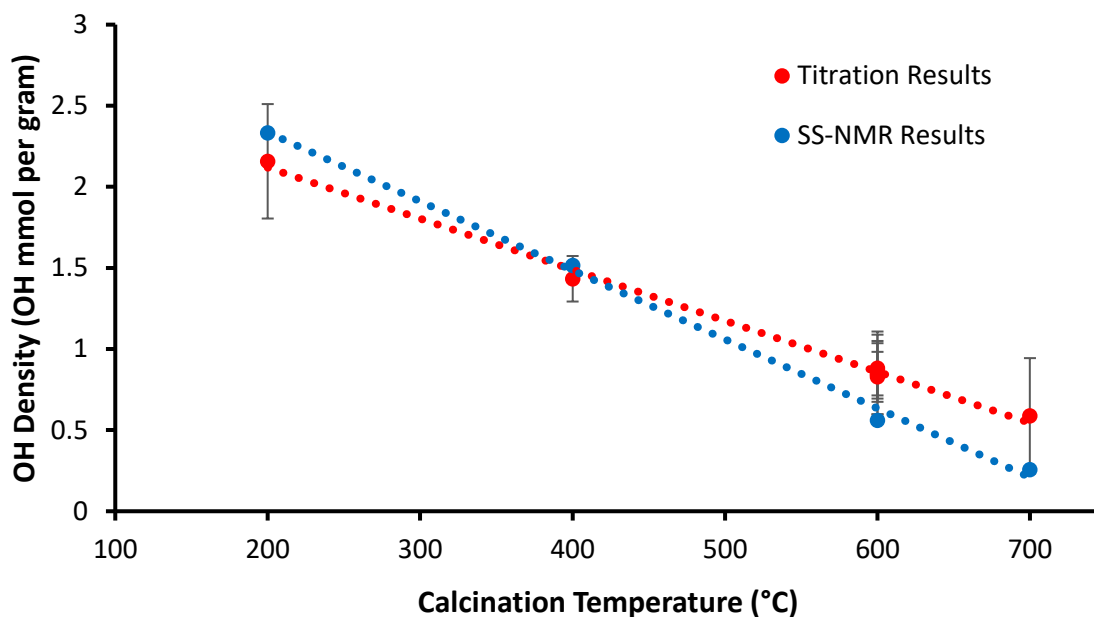


Figure 2.22. Comparison of the hydroxyl density of Aeroperl 300/30 silica as determined by chemical titration and ^1H SS-NMR spectroscopy

Both the titration and SS-NMR spectroscopy results are in good agreement with one another. The ^1H SS-NMR spectroscopic data give a slightly a higher (~ 0.2 mmol per gram) hydroxyl density than that determined by chemical titration at the lower calcination temperatures (200 and 400 °C), and the reverse at higher calcination temperatures (600 and 700 °C). Thus, taken together, these results indicate that use of ^1H SS-NMR spectroscopy is a promising method for the determination of the hydroxyl density of silicas.

2.3 Conclusions

While the nature and characteristics of various types of silica are well described in the literature,^{4, 19, 35, 36} this project has undertaken an in-depth study of the quantification of the OH density of various silicas calcined at different temperatures. It has been shown successfully that ^{29}Si SS-NMR spectroscopy, ^1H SS-NMR spectroscopy, and chemical titration methods can be used and give results for silanol density that are in good agreement with one another.

This project has shown that chemical titration using *o*-tolylmagnesium chloride is a highly reliable method for determining hydroxyl density, with a low error and a high reproducibility. This titration methodology has been shown to be highly versatile as it is able to reliably determine hydroxyl density on different silicas with different internal structure and surface areas. The data obtained from such chemical titrations be combined with BET-determined surface area to give hydroxyl density per unit area, a parameter that is essential for evaluating the ensuing density of metal-containing sites having

modified the silicas' silanol groups by reaction with metal-containing derivatives. As anticipated, our chemical titration data confirm that silicas' silanol density decreases with an increase in calcination temperature.

In a parallel study, it has been shown that ^1H SS-NMR spectroscopy can also be used to quantify the OH surface density of silicas. Unlike chemical titration, this methodology can provide a quick determination of the silanol density without destroying the sample.

Similarly, the use of ^{29}Si SS-NMR spectroscopy for the analysis of variously calcined silicas has been explored. While more complicated than ^1H SS-NMR spectroscopy due to the need for deconvolution of the ^{29}Si SS-NMR spectra, acquisition and analysis of the ^{29}Si SS-NMR spectra of silicas is useful since it provides a method for quantification and identification of the different types of silanol groups present. With these techniques, the oxide supports that are used in this project have been characterised to a suitable level for tethering cobalt precursors.

2.4 References

1. F. Rascón, R. Wischert and C. Copéret, *Chem. Sci.*, 2011, **2**, 1449-1456.
2. P. Denton, A. Giroir-Fendler, H. Praliaud and M. Primet, *J. Catal.*, 2000, **189**, 410-420.
3. J. Handzlik, J. Ogonowski, J. Stoch, M. Mikołajczyk and P. Michorczyk, *Appl. Catal., A: General*, 2006, **312**, 213-219.
4. A. P. Legrand, *The Surface Properties of Silicas*, John Wiley, Chichester, 1998.
5. C. Copéret, *Pure Appl. Chem.*, 2009, **81**, 585-596.
6. E. F. V. P. Van Der Voort, *J. Liq. Chromatogr. Relat.*, 1996, **19**, 2723-2752.
7. C. Copéret, M. Chabanas, R. P. Saint-Arroman and J.-M. Basset, *Angew. Chem. Int. Ed.*, 2003, **42**, 156-181.
8. R. M. Guillet-Nicolas, R. Ahmad, K. A. Cychosz, F. Kleitz and M. Thommes, *New J. Chem*, 2016, **40**, 4351-4360.
9. Y. K. Priyanka Verma, Kohsuke Mori, Robert Raja, Hiromi Yamashita, *Nanoscale*, 2020, **12**, 11333-11363.
10. E. C. d. Oliveira, C. T. G. V. M. T. Pires and H. O. Pastore, *J. Braz. Chem. Soc.*, 2006, **17**, 16-29.
11. P. Y. D. Zhao, B. F. Chmelka, G. D. Stucky, *Chem. Mater.*, 1999, **11**, 1174-1178.

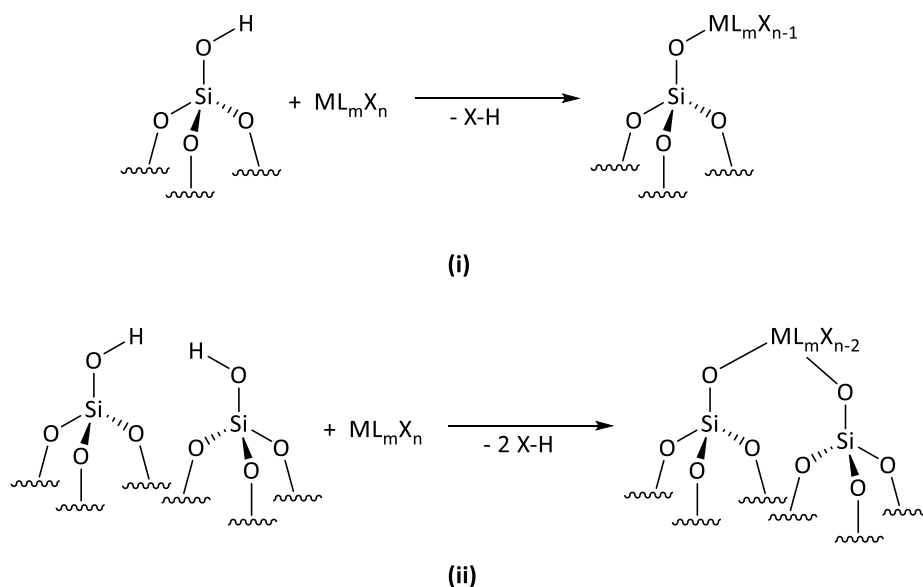
12. T. D. P. Yang, D. Zhao, P. Feng, D. Pine, B. F. Chmelka, G. M. Whitesides, G. D. Stucky, *Science*, 1998, **282**, 2244-2246.
13. B. T. Chengzhong Yu, Jie Fan, Galen D. Stucky, Dongyuan Zhao, *Chem. Commun.*, 2001, 2726-2727.
14. V. V. Pushkarev, K. An, S. Alayoglu, S. K. Beaumont and G. A. Somorjai, *J. Catal.*, 2012, **292**, 64-72.
15. R. R. Chang Hyun Ko, *Chem. Mater.*, 2000, **12**, 1961-1968.
16. Y. Ye, C. Jo, I. Jeong and J. Lee, *Nanoscale*, 2013, **5**, 4584-4605.
17. R. Q. Wei Wang, Weijun Shan, Xiaoyang Wang, Quanli Jia, Jing Zhao, Cuiping Zhang, Hongqiang Ru, *Microporous Mesoporous Mater.*, 2014, **194**, 167-173.
18. E. Oakton, G. Vilé, D. S. Levine, E. Zocher, D. Baudouin, J. Pérez-Ramírez and C. Copéret, *Dalton Trans.*, 2014, **43**, 15138-15142.
19. E. F. Vansant, P. V. D. Voort and K. C. Vrancken, *Characterisation and Chemical Modification of the Silica Surface*, Elsevier, Wilrijk, Belgium, 1995.
20. Z. Wang, B.-N. Ye, Y.-T. Zhang, J.-X. Xie, W.-S. Li, H.-T. Zhang, Y. Liu and N.-P. Feng, *AAPS PharmSciTech*, 2019, **20**, 289.
21. P. J. Pomonis, D. E. Petrakis, A. K. Ladavos, K. M. Kolonia, G. S. Armatas, S. D. Sklari, P. C. Dragani, A. Zarlaha, V. N. Stathopoulos and A. T. Sdoukos, *Microporous Mesoporous Mater.*, 2004, **69**, 97-107.
22. C. Copéret, A. Comas-Vives, M. P. Conley, D. P. Estes, A. Fedorov, V. Mougel, H. Nagaie, F. Núñez-Zarur and P. A. Zhizhko, *Chem. Rev.*, 2016, **116**, 324-421.
23. S. MacQuarrie and A. J. Carrier, *Micro and Nano Technologies*, 2019, 129-152.
24. M. J. Lamb, D. C. Apperley, M. J. Watson and P. W. Dyer, *Top. Catal.*, 2018, **61**, 213-224.
25. J. V. O. Glesby and J. F. Stebbins, *American Mineralogist*, 2000, **85**, 722-731.
26. J. Casanovas, F. Illas and G. Pacchioni, *Chem. Phys. Lett.*, 2000, **326**, 523-529.
27. D. K. Murray, *J. Colloid Interface Sci.*, 2010, **352**, 163-170.
28. D. Gajan, D. Levine, E. Zocher, C. Copéret, A. Lesageb and L. Emsley, *Chem. Sci.*, 2011, **2**, 928-931.

29. F. Blanc, J.-M. Basset, C. Copéret, A. Sinha, Z. J. Tonzetich, R. R. Schrock, X. Solans-Monfort, E. Clot, O. Eisenstein, A. Lesage and L. Emsley, *J. Am. Chem. Soc.*, 2008, **130**, 5886-5900.
30. D. K. Murray, *J. Colloid Interface Sci.*, 2010, **352**, 163-170.
31. G. Metz, M. Ziliox and S. O. Smith, *Solid State Nucl Magn Reson.*, 1996, **7**, 155-160.
32. H. Zhao, Q. Chen and S. Zhang, *Microporous Mesoporous Mat.*, 2012, **155**, 240-244.
33. L. T. Zhuravlev, *Colloids and Surfaces A: Physicochem. Eng. Aspects*, 2000, **173**, 1-38.
34. J. Mahler and A. Sebald, *Solid State Nuc. Magn. Reson.*, 1995, **5**, 63-78.
35. L. T. Zhuravlev, *Langmuir*, 1987, **3**, 316-318.
36. J. T. Marta Szekeres, Imre Dékány, *Langmuir*, 2002, **18**, 2678-2685.

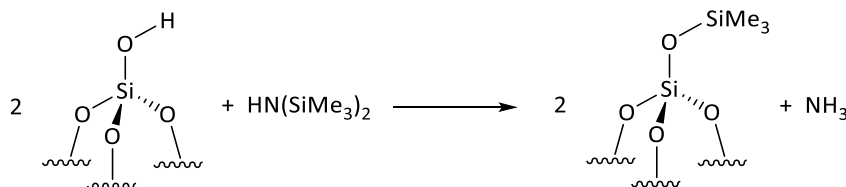
Chapter 3: Tethering of Co-Precursors to Pre-treated Silica Supports

3.0 Introduction to Cobalt Organometallic Compounds Tethered To Silica

A key factor in controlling the covalent tethering of organometallic species to the surface of an oxide support is the density of the reactive surface groups (*e.g.* silanols, SiOH, in the case of silica) present at the surface. Thus, the theoretical maximum number of metal-containing species that can be directly tethered to the surface equates to the number of silanol groups, assuming one hydroxyl group reacts with one metal centre. Clearly, however, this is a simplistic model as not all hydroxyl groups may react with a metal complex or, indeed, multiple hydroxyl groups may react with a single metal species. Additionally, if the silanols are not spatially isolated, due to limited hydroxylation, bis-grafted surface species may form alongside mono-grafted species, and the ratio will move from 1:1 OH:metal towards 2:1 OH:metal (Scheme 3.1). Furthermore, reaction between a surface SiOH group and a metal-containing complex may be prevented by pore size constraints and diffusivity effects, or if there is a competing reaction with the SiOH groups (*e.g.* silylation, as seen in Scheme 3.2).¹



Scheme 3.1. (i) The formation of a mono-grafted metal species M with a 1:1 OH:M reaction
(ii) The formation of a bis-grafted M species with a 2:1 OH:M reaction



Scheme 3.2. The silylation of the silica surface by the reaction of SiOH and $\text{HN(SiMe}_3)_2$

In this project, the aim is to deposit cobalt-containing species on the surface of silica and to control the cobalt loading on silica through variation of the hydroxyl density on the silica surface. The hydroxyl density of various silicas calcined at different temperatures has already been determined as described

in Section 2.2.2. The value of the theoretical maximum cobalt loading for each silica assumes that all hydroxyl groups will react with a metal centre in a 1:1 ratio and form only mono-grafted surface metal-species. The maximum possible loading of cobalt on variously-calcined silicas is given in Table 3.1.

Table 3.1. Maximum cobalt w.t. % loading on calcined silicas according to their hydroxyl densities, assuming a 1:1 OH:Co reaction, forming mono-grafted surface species

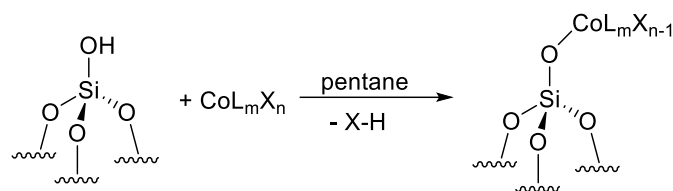
Silica	OH density (mmol g ⁻¹)	Theoretical maximum Co w.t. % loading
A-SiO ₂₋₇₀₀	0.59	3.5
A-SiO ₂₋₆₀₀	0.83	4.9
A-SiO ₂₋₄₀₀	1.43	8.4
A-SiO ₂₋₂₀₀	2.16	12.7
K-SiO ₂₋₇₀₀	1.77	10.4
K-SiO ₂₋₆₀₀	2.16	12.7
K-SiO ₂₋₄₀₀	2.92	17.2
K-SiO ₂₋₂₀₀	5.81	34.2
S-SiO ₂₋₇₀₀	1.76	10.4
S-SiO ₂₋₆₀₀	2.49	14.7
S-SiO ₂₋₄₀₀	3.43	20.2
S-SiO ₂₋₂₀₀	5.59	32.9

During the project work described in this thesis, the focus has been on tethering cobalt precursors to silicas calcined at 600 °C (SiO₂₋₆₀₀), as the surface of SiO₂₋₆₀₀ contains primarily isolated silanols (Section 2.2.3.2.5).² For note, it has been confirmed that all of the silicas described and used in this project (Aeroperl 300/30, KIT-6, and SBA-15) maintain their surface area at a calcination temperature of 600 °C. At calcination temperatures higher than 600 °C, the pore structures of KIT-6 and SBA-15 begin to collapse, which results in a decreased surface area. Generally, high surface area is preferred in catalysis applications, so KIT-6 and SBA-15 silica calcined above 600 °C were deemed unsuitable for this project.

As stated in Section 1.1.1.2, a range of cobalt species (summarised Figure 1.17) have been selected for their potential to react with the silica surface (*via* its silanols) to afford Si–O–CoL_x species, which will subsequently in later steps be converted into surface-bound Co⁰ species. It is hoped that each of the cobalt complexes chosen (Section 1.1.1.2), with the exception of complex **6**, will react with the surface OH groups, binding to the silica *via* protonation and ligand displacement. Complex **6** does not contain any ligands available for protonation and cannot react with the silanol groups through the same mechanism. However, work by Gürtler suggests that Co₂(CO)₈ can bind to hydroxyl sites on the surface of silica gel, tethering to up to a third of available hydroxyl groups.³ Indeed, Co₂(CO)₈ is often used to form nanoparticles on surfaces, as it decomposes into Co⁰ very easily through either thermo- or photo-

mediated decomposition pathways,⁴ so it has been included in this project as a potential precursor to sub-nanosized particles.

Scheme 3.3 describes the general reaction between the chosen cobalt precursors **1-5,7,8** (Figure 1.7, p43) and the silica support. In all cases, pentane was used as a solvent for these reactions since it is volatile, thus easy to remove, and does not contain any halogen atoms (*e.g.* as in DCM) or coordinating groups, (*e.g.* THF), which may interfere with the tethering process, later nanoparticle formation, or catalytic performance. The reaction between the cobalt species and the surface silanols occurs at room temperature by stirring the silica in a solution of the metal precursor, as is typical of SOMC-like reactions found in literature,⁵ to product a product with the nomenclature “**(complex number)/silica**”.*



Scheme 3.3. General schematic methodology for tethering cobalt organometallic complexes to the surface of silica

3.1 [Co(N(TMS)₂)₂(THF)] (**2**) + Silica Support

Complex **2**, [Co(NTMS₂)₂(THF)], is a highly reactive cobalt silylamide species; there are previous examples in the literature that describe the use of metal silylamide complexes as successful precursors for the formation of very small nanoparticles on the surface of silica, such as [Ag(N(TMS)₂)₂]₄ by Oakton *et al.*⁶ Moreover, there is also literature precedent for tethering complex **2** to the surface of silica, as reported by Liang *et al.*, who tethered complex **2** to calcined SBA-15 and KIT-6 silica by stirring the support and complex together in hexane.⁷ According to Liang *et al.*, complex **2** can form the mono- and bis-grafted surface species. The coordinated THF of **2** stays bound to the cobalt centre during the tethering process, preferentially losing the amide ligands, as summarised in Figure 3.1.⁷

* For example, complex **4** tethered to the surface of KIT-6 silica calcined at 400 °C is called **(4)/K-SiO₂₋₄₀₀**, and complex **7** tethered to the surface of Aeroperl 300/30 silica calcined at 700 °C is called **(7)/A-SiO₂₋₇₀₀**, *etc.*

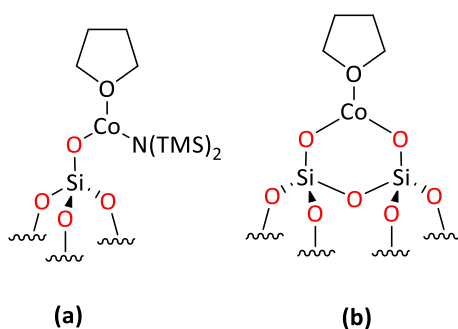
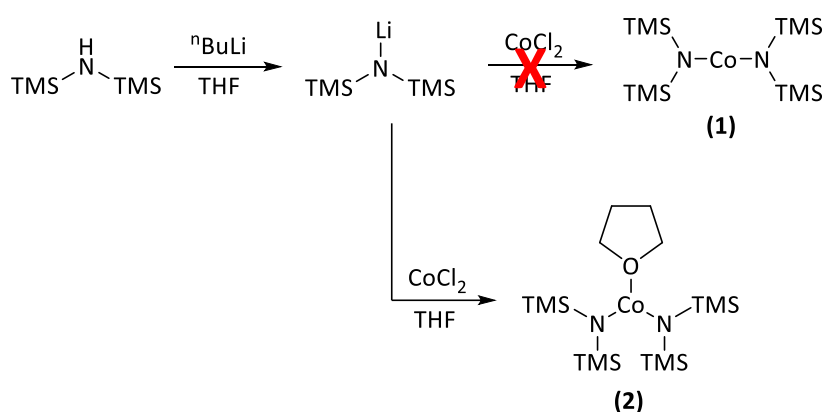


Figure 3.1. Possible surface structures of **(2)**/ SiO_2 , proposed by Liang *et al.*⁷

3.1.1 Synthesis of $[\text{Co}(\text{N}(\text{TMS})_2)_2(\text{THF})]$ (**2**) + Silica Support

3.1.1.1 Synthesis of Complex **2** for Impregnation onto Silica Support

The synthesis of complex **1** was attempted following a method analogous to that previously reported by Bradley *et al.* for the synthesis of $[\text{Cr}(\text{N}(\text{TMS})_2)_3]$,⁸ namely through reaction of the appropriate chloride (here CoCl_2) and lithium amide (Scheme 3.4). It was reported in the literature that the Co-analogue is more unstable than the Cr-analogue, something verified in this project, which made finding a synthetic procedure that produced the complex with high purity and a large scale (> 1 g) difficult. Other literature methods for producing complex **1** were often unreliable and gave poor yields or impure products. By modifying Bradley *et al.*'s chromium silyl-amide synthesis and shortening the reaction time from 18 h to 3 h, a paramagnetic cobalt silyl amide complex was successfully isolated in good yield. However, CHN analyses of the isolated material revealed that the product was the THF adduct **2**, an already known compound in literature, not the target base free complex **1** (Scheme 3.4).

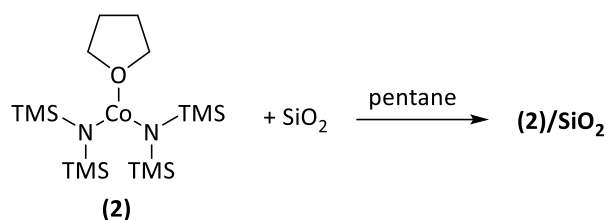


Scheme 3.4. Attempted synthesis of complex **1** and subsequent synthesis of complex **2**

3.1.1.2 Impregnation of $[\text{Co}(\text{N}(\text{TMS})_2)_2(\text{THF})]$ (**2**) onto Silica Supports

Solutions of the complex $[\text{Co}(\text{N}(\text{TMS})_2)_2(\text{THF})]$ (**2**) react readily with the variously-calcined silica supports at room temperature as evidenced by the dark green coloured solution of complex **2** decolourising as the reaction proceeds, which is accompanied by the silica changing colour from white to a light green (Scheme 3.5). The reaction is very fast (*i.e.* the time taken for complete decolourisation

of the starting solution of **2**), occurring within 30 minutes, forming **(2)/SiO₂**. It is noteworthy that **(2)/SiO₂** must be isolated quickly as complex **2** is unstable in solution and begins to decompose after 1 h, despite use of rigorously dried solvents and anaerobic/anhydrous conditions.



Scheme 3.5. Addition of complex 2 to silica

These silica-immobilised cobalt systems such as **(2)/SiO₂** are very reactive, changing colour from light green to light blue when placed under vacuum, left in a dry pentane solution for longer than 2 hours, stored in a sealed vial in a nitrogen-filled glovebox for longer than 24-48 h, or exposed to atmosphere or moisture. A representative example of this colour change is shown in Figure 3.2. The reactive nature of **(2)/SiO₂**, which while promising for the synthesis of sub-nanosized particles as it seems to readily decompose, makes synthesis, handling, and characterisation difficult.

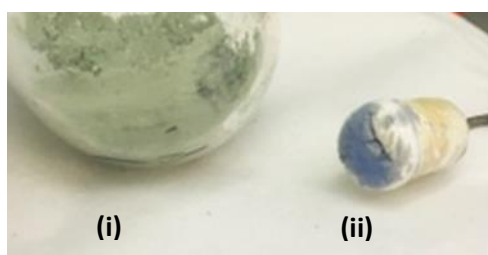


*Figure 3.2. (i) Freshly prepared **(2)/SiO₂** – green in colour; (ii) blue colouration observed after exposure of **(2)/SiO₂** to air*

3.1.2 Analysis of the Cobalt Surface Structure of [Co(N(TMS)₂)₂(THF)] Tethered onto the Surface of Aeroperl 300/30 Silica ((2)/A-SiO_{2-x})

3.1.2.1 Cobalt-loading on Aeroperl 300/30 Silica Determined by ICP-OES

The cobalt loading of the material resulting from reaction of complex **2** with Aeroperl 300/30 silica was determined by ICP-OES (see Section 6.0.2.4 for method). The ratio of complex **2**:A-SiO₂ in the reaction was the same across all calcined silicas (2.2 mmol Co per gram of silica). The different cobalt loadings from reactions of complex **2** with variously calcined silicas are summarised in Table 3.3. There is a clear trend between the calcination temperature and the w.t. % loading of cobalt on the silica; for silicas calcined at higher temperatures, the subsequent metal loading is lower. This decrease in metal uptake is attributed to the lower surface hydroxyl density of silicas calcined at higher temperatures. Less metal is tethered to the silica as there are less available OH surface sites for reaction with the cobalt complex as anticipated. The percentage of –Si-OH groups that react with a cobalt metal centre also increases as calcination temperature is increased.

The metal loadings determined by ICP-OES are lower than the theoretical maximum calculated in Section 3.0 (Table 3.2), with Co loadings of 28 - 52 % of the total theoretical maximum being achieved, assuming that one cobalt centre reacts with one silanol (Table 3.3). This lower than anticipated cobalt loading has been attributed to a competitive silylation reaction occurring, something that was also proposed by Liang *et al.*, namely that free $\text{HN}(\text{TMS})_2$ reacts with surface OH groups to form SiMe_3 surface sites and NH_3 (Scheme 3.2).⁷

Table 3.3. Co metal loading of complex **2** on Aeroperl 300/30 silica calcined at different temperatures, as determined by ICP-OES

Material	OH density (mmol g ⁻¹)	Cobalt (mmol g ⁻¹)	Cobalt w.t. % loading	% of OH groups that reacted with a Co
(2)/A-SiO₂₋₂₀₀	2.16	0.61	3.6	28
(2)/A-SiO₂₋₄₀₀	1.43	0.49	2.9	34
(2)/A-SiO₂₋₆₀₀	0.83	0.39	2.2	47
(2)/A-SiO₂₋₇₀₀	0.59	0.31	1.8	52

3.1.2.2 ²⁹Si SS-NMR Spectroscopic Analysis of **(2)/A-SiO₂₋₆₀₀**

The SS-NMR spectroscopic studies described in Section 2.2.3 have already shown that ²⁹Si SS-NMR can be used to differentiate geminal silanols, isolated silanols, and siloxane bridges in the prepared silica supports. As CP ²⁹Si SS-NMR spectroscopy can differentiate the densities of the different silanol species present, it was hoped that SS-NMR spectroscopy could also monitor the changes in the silanol density as the silanols react with a metal complex.

To this end, ²⁹Si SS-NMR CP and DE NMR spectra were obtained of **(2)/A-SiO₂₋₆₀₀** (Figure 3.3), and compared to the spectra obtained for blank silica (**A-SiO₂₋₆₀₀**, see Section 2.2.3). The most notable difference between the blank silica spectra and **(2)/A-SiO₂₋₆₀₀** is that there is no observable peak in the CP spectrum of the latter. This could be due to the loss of surface hydroxyl groups as all silanols react with either complex **(2)** or free $\text{HN}(\text{TMS})_2$. However, a total loss of all silanol species is unlikely, as a cobalt analysis by ICP-OES results suggest that only 47% of OH species reacted with a Co metal centre (Table 3.3). There may also be silanol sites within the Aeroperl 300/30 silica structure that are inaccessible by complex **(2)** and $\text{HN}(\text{TMS})_2$ due to silica pore size constraints, and therefore have not reacted. However, it is more likely that the presence of the cobalt species, likely still paramagnetic Co^{II}, is interfering with the cross-polarisation NMR process.⁹ This interference in the NMR process may be seen by the lack of any observable peak in the CP spectrum, as it would be expected that the Si atoms in the HMDS ligand that are bound to the cobalt centre would still be observable in the CP spectrum, as well as an indication of surface SiMe_3 groups (from the reaction of $-\text{SiOH}$ with liberated $\text{HN}(\text{TMS})_2$) that are reported to form on the silica surface in previous literature studies.^{10, 11}

In contrast to the results of the CP NMR experiment described above, the ^{29}Si SS-NMR DE spectroscopic analysis of **(2)/A-SiO₂₋₆₀₀** (Figure 3.3) features a single, noisy, broad resonance at 107 ppm ($\nu_{1/2} \sim 2385$ Hz), which is at a similar chemical shift to the signal obtained in the DE spectrum of blank **A-SiO₂₋₆₀₀**, which has been attributed to the Q₄ species. The poor resolution and intensity of the DE NMR spectrum is thought to be caused by the presence of a paramagnetic cobalt centre. The peak in the DE spectrum in Figure 3.3 is too featureless to deconvolute.

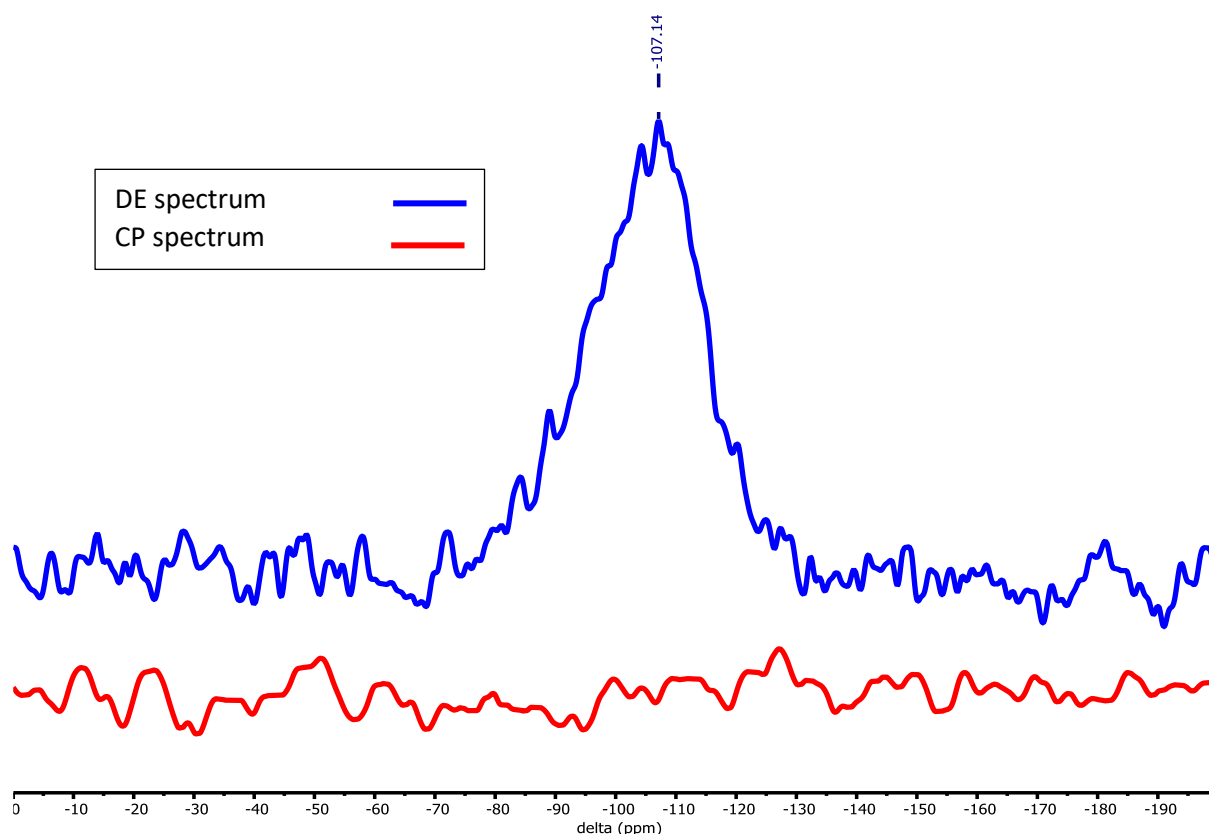


Figure 3.3. DE and CP ^{29}Si spectra of **(2)/A-SiO₂₋₆₀₀**, Frequency 79.437 MHz, Spin-rate 6 kHz

3.1.2.3 ^1H SS-NMR Spectroscopy of **(2)/A-SiO₂₋₆₀₀**

In Section 2.2.3.3, ^1H SS-NMR spectroscopy was used to identify the -OH species in the calcined silicas, and will be therefore used to identify any remaining unreacted -OH groups. ^1H SS-NMR spectroscopy can also be used to identify the presence other surface species, such as surface -SiMe₃ and the HMDS ligand on -Co(NSiMe₃)_x. The ^1H SS-NMR spectrum of **(2)/A-SiO₂₋₆₀₀** is shown in Figure 3.4. This comprises two resolved and relatively sharp signals at -3.2 and 0.1 ppm, and another smaller signal at 8.6 ppm. Additionally, between 30 and -45 ppm, there is a “bump” visible in the baseline. The silanol OH signal at 1.8 ppm (identified in Section 2.2.3.3) is not seen in the ^1H SS-NMR spectrum of **(2)/A-SiO₂₋₆₀₀** (Figure 3.4), though it could be hidden by the resonance at 0.1 ppm (silicone grease). The signal at -3.2 ppm has been attributed to an -NSiMe₃ ligand on the cobalt metal centre. This signal has been assigned by comparison of the shift of similar discrete molecules, such as Me₂N-SiMe₃ (-6 ppm).¹² The resonance at 8.6 ppm is assigned to surface -OSiMe₃, formed from silylation of the silica

surface by free $\text{HN}(\text{TMS})_2$. A surface $-\text{OSiMe}_3$ species is likely to have a comparable chemical shift to those of the discrete molecular species $\text{Me}_3\text{Si-O-SiMe}_3$ (6 ppm)¹² and $(\text{Me}_3\text{Si-O})_4\text{Si}$ (8 ppm).¹² In this project, two surface species, $-\text{Co}(\text{NSiMe}_3)_x$ and $-\text{OSiMe}_3$, present in **(2)/A-SiO₂₋₆₀₀** have been identified in the ¹H SS-NMR analysis of **(2)/A-SiO₂₋₆₀₀**.

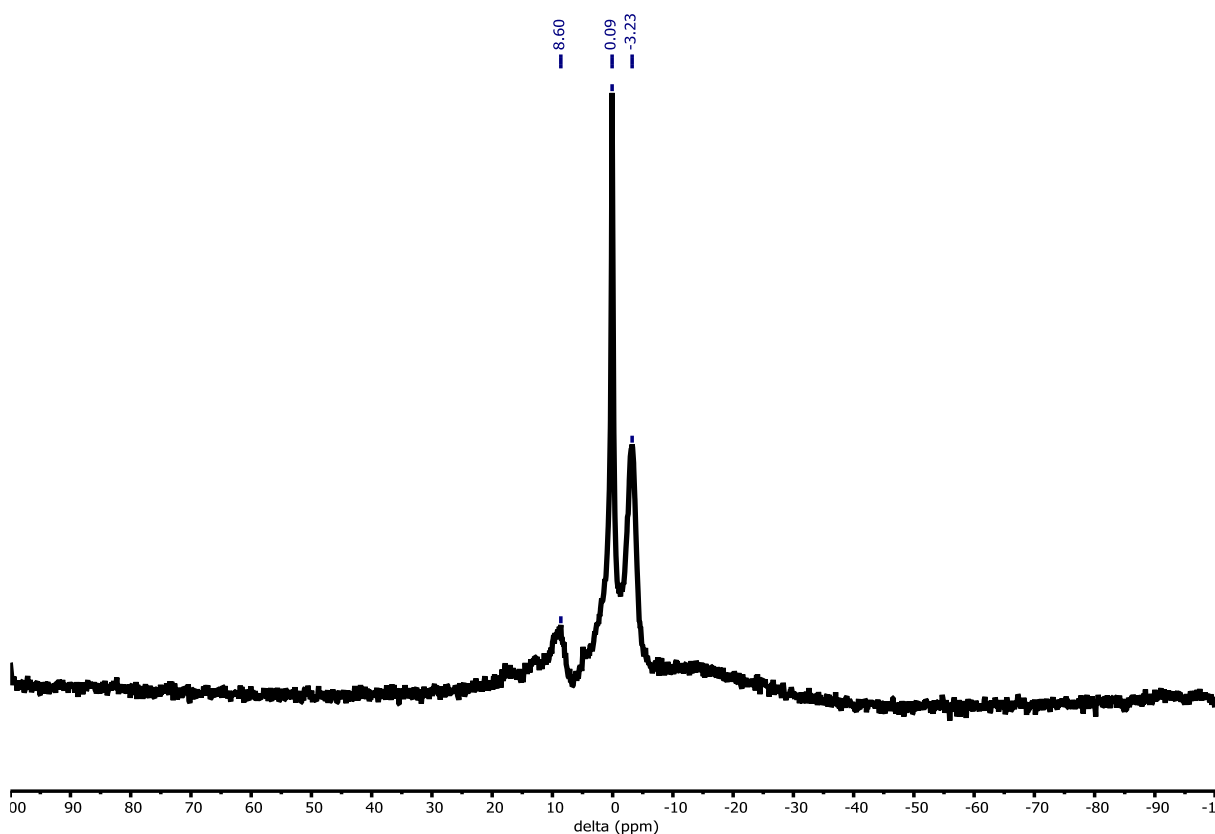


Figure 3.4. ¹H spectra of **(2)/A-SiO₂₋₆₀₀**, Frequency 400.17 MHz, Spin-rate 40 kHz

An ¹H SS-NMR spectrum of a sample of pure complex **2** was obtained (Figure 3.5), in order to compare it to **(2)/A-SiO₂₋₆₀₀** and identify any changes that the complex undergoes when tethered to the silica. Complex **2** is expected to exhibit 3 peaks in its ¹H NMR spectrum, two resonances representing the coordinated THF moiety and one resonance correlated to the HMDS ligands. As complex **2** is Co^{II} , and therefore d^7 and paramagnetic, and likely to have a spin of $S=3/2$ if trigonal planar, the NMR spectrum is likely to give an up-field shift for both the TMS and THF protons due to the presence of the paramagnetic material.¹³ Indeed, the experimentally-determined ¹H NMR spectrum of **2** shows narrow lines, and peaks at an unusually high chemical shift. It also exhibits a strong NOE (Nuclear Overhauser Effect) enhancement, as shown by significantly more signal with a short (1 s) recycle delay than that observed with a longer recycle delay (10 s). The peaks observed in the ¹H spectrum (between -22 – 11 ppm) of complex **2** were not identified.

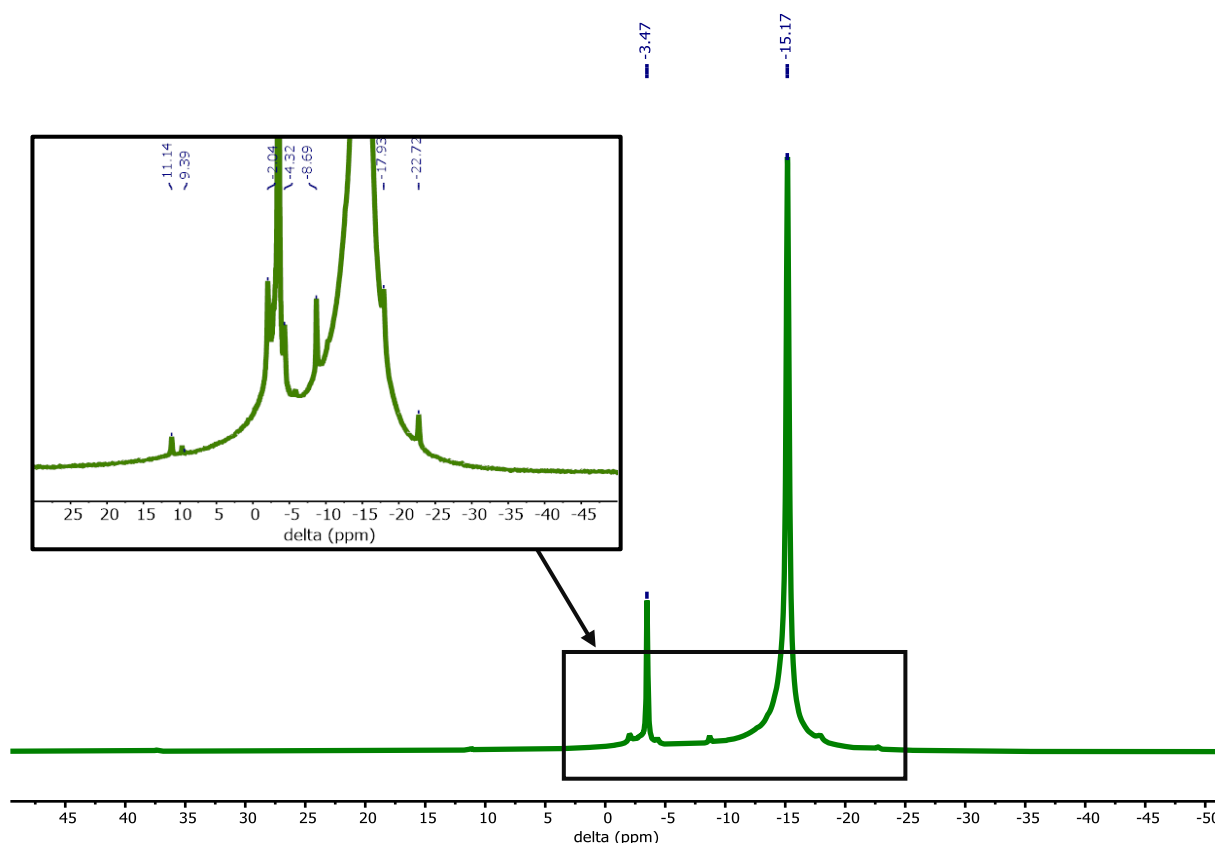
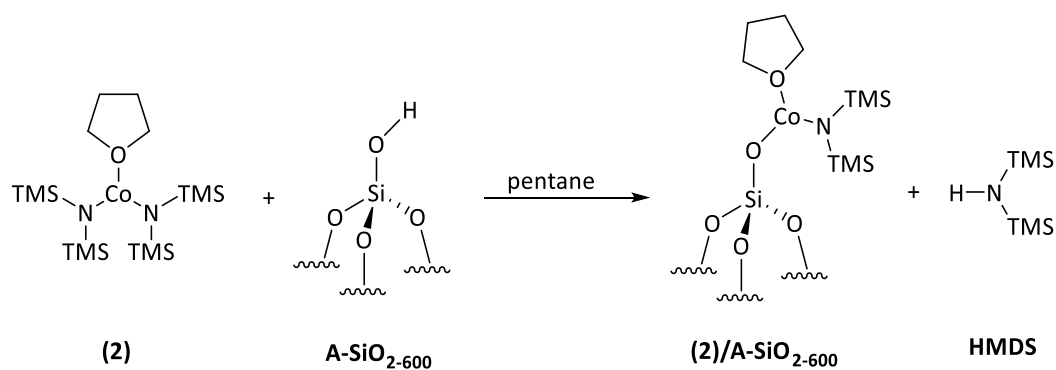


Figure 3.5. ^1H SS-NMR spectrum of complex **2**, frequency 400.17 MHz, Spin-rate 40 kHz

3.1.2.4 Determining the Degree of Surface Silylation through Analysis of the amount of $\text{HN}(\text{TMS})_2$ Ligand Present after the Synthesis of **(2)/A-SiO₂₋₆₀₀**

When complex **2** is tethered to the surface, free HMDS is lost from the cobalt centre (Scheme 3.6). The liberated HMDS can then react with the surface silanol species on the silica surface, in a competitive silylation reaction. One method that can be used to determine how many reactive $-\text{SiOH}$ groups remain on the surface, and the degree of surface silylation, is to analyse the amount of free HMDS present at the end of the reaction in conjunction with how much cobalt is on the surface. To this end, the solution following reaction of complex **2** with **A-SiO₂₋₆₀₀** in pentane was captured through vacuum transfer of all the volatile components into a clean ampule after the reaction was completed. An internal standard (nonane) was added, and GC analysis was used to determine the amount of $\text{HN}(\text{TMS})_2$ present (see Section 6.0.2.5).



Scheme 3.6. Reaction of complex **2** and **A-SiO₂₋₆₀₀** to form **(2)/A-SiO₂₋₆₀₀** and release of a free HMDS molecule

It is expected that for every one molecule of complex **2** that reacts with a surface -OH species, one molecule of HMDS will be released from the cobalt metal centre. If there was no silylation of the silica surface by HN(TMS)₂, a 1:1 ratio of Co:liberated HN(TMS)₂ would be expected, as no HN(TMS)₂ would be lost through reaction with silanols. This expected ratio assumes that the cobalt bound to silica is a mono-grafted species and has lost only one HMDS ligand during impregnation, which is a reasonable assumption given the low silanol density determined experimentally for **A-SiO₂₋₆₀₀** (see Section 2.2.2).

The results of the GC analysis of the volatile products isolated following reaction of complex **2** reacting with **A-SiO₂₋₆₀₀** in pentane show that for every one equivalent of cobalt tethered to **A-SiO₂₋₆₀₀**, 0.86 equivalents of liberated HN(TMS)₂ are detected. The less than 1:1 quantity of HN(TMS)₂ detected post reaction of **2** with **A-SiO₂₋₆₀₀** is suggestive of some of the HN(TMS)₂ released during the impregnation of complex **2** having reacted with the silica surface (Scheme 3.2). This is supported by ¹H SS-NMR analysis of **(2)/A-SiO₂₋₆₀₀**, which shows a signal at 8.6 ppm that can be assigned to surface -OSiMe₃ formed by silylation of the surface by HMDS (assigned in Section 3.1.2.3).

These GC data obtained are consistent with 47% of the **A-SiO₂₋₆₀₀** silanols having reacted with complex **2** (ICP-OES data, Section 3.1.2.1), and a further 13% of silica OH sites having reacted with HMDS to form surface -SiMe₃ sites, *i.e.*, 0.14 equivalents of HN(TMS)₂ reacted with silanols, forming 0.28 equivalents of surface -OSiMe₃ species. This leaves 40% of the OH sites in calcined **A-SiO₂₋₆₀₀** unreacted with either complex **2** or with free HMDS.

3.1.2.5 Surface Area Analysis of **(2)/A-SiO₂₋₆₀₀** to Determine Degree of Surface Functionalisation

It is known from the literature that the silica surface undergoes functionalisation, both metalation and silylation, when a metal silylamide reacts with silica. Previously, the surface area of the silica support has been used by Ahn *et al.*¹⁰ and Deschner *et al.*, as discussed in Section 1.0.6.2.1.,¹⁴ to probe the functionalisation of the silica surface when a metal silyl amide is tethered to silica. BET analysis of the support before and after the complex has been tethered can give some insight into the impregnation of complex **2** onto **A-SiO₂₋₆₀₀**. Here, a loss of surface area and decrease in pore size after the complex

has been tethered to the support is indicative of a combination of metal impregnation and surface silylation of the silica occurring. A small change in the surface area/pore size indicates a small amount of metalation/silylation, while a large change in the surface area/pore indicates a large amount of metalation/silylation.

Building on the work of Ahn *et al.*¹⁰ and Deschner *et al.*,¹⁴ the BET analysis of blank **A-SiO₂₋₆₀₀** and **(2)/A-SiO₂₋₆₀₀** were undertaken; results are shown in Table 3.4. These analyses show there is a decrease in both the surface area and pore volume for the cobalt-modified material, **(2)/A-SiO₂₋₆₀₀**, compared with those of the blank silica, indicating that metalation/silylation of the silica support has occurred. The BET-derived C value decreases from 85 to 30, as the heat of adsorption has decreased with the addition of complex **2** to the surface. From molecular modelling (see Section 6.0.2.11), the diameter of complex **2** is estimated to be ~12 Å,[†] while the median pore diameter of **A-SiO₂₋₆₀₀** is 349 Å, so molecules of **2** are small enough to easily diffuse through the pore structure. The average pore diameter increases after complex **2** has been attached to **A-SiO₂₋₆₀₀** to 444 Å (**(2)/A-SiO₂₋₆₀₀**). The increase in pore diameter has been attributed to a closing of smaller pores due to complex **2** blocking the pores, which as a result increases the average pore diameter overall.¹⁵

Mercury porosimetry of blank **A-SiO₂₋₆₀₀** and **(2)/A-SiO₂₋₆₀₀** was also performed (Table 3.5). These porosimetry analyses were also employed in this project as the BET measurements of **A-SiO₂₋₆₀₀** and **(2)/A-SiO₂₋₆₀₀** showed a Type II isotherm, indicating that larger pores were not being detected by N₂ physisorption. The porosimetry results reflect the same trends obtained from BET analysis, namely that pore volume decreases while median pore diameter increases when complex **2** is tethered to **A-SiO₂₋₆₀₀**.

Surface area analysis of **(2)/A-SiO₂₋₆₀₀** has been used to determine the degree of surface functionalisation. Both BET and mercury porosimetry analyses indicate that the metalation/silylation of the silica surface has occurred following a reaction of complex **2** and **A-SiO₂₋₆₀₀**, with a decrease in surface area and pore volume and an increase in the average pore diameter.

Table 3.4. BET analysis comparing **A-SiO₂₋₆₀₀** and **(2)/A-SiO₂₋₆₀₀**; data were measured by Johnson Matthey; measurement uncertainty on BET surface area is +/- 2%.

	BET surface area (m ² g ⁻¹)	Pore Volume [0.99ads] (cm ³ g ⁻¹)	Average Pore Diameter (Å)	C Value from BET
A-SiO₂₋₆₀₀	273	1.9	274	85
(2)/A-SiO₂₋₆₀₀	213	1.7	310	30

[†] Diameter of molecule was approximated according to the method described in Section 6.0.2.11

Table 3.5. Mercury porosimetry analysis comparing **A-SiO₂₋₆₀₀** and **(2)/A-SiO₂₋₆₀₀**; data were measured by Johnson Matthey; measurement uncertainty on intrusion volume is +/- 1%, measurement uncertainty on intrusion median pore diameter is +/- 0.2%

	Corrected Intrusion Volume (cm ³ g ⁻¹)	Median Pore Diameter (Å)
A-SiO₂₋₆₀₀	2.0	349
(2)/A-SiO₂₋₆₀₀	1.5	444

3.1.2.6 CHN Elemental Analysis of **(2)/A-SiO₂₋₆₀₀**

Elemental analysis was used to determine the number of -N(TMS)₂ ligands remaining bound to the cobalt metal centre after complex **2** was tethered to the silica surface. Following comparison of the CHN analysis data of blank **A-SiO₂₋₆₀₀** and **(2)/A-SiO₂₋₆₀₀**, it was determined that the cobalt species on the surface of **A-SiO₂₋₆₀₀** was a mono-grafted species, with one -N(TMS)₂ ligand still bound and a THF group coordinated to the cobalt (Figure 3.6).

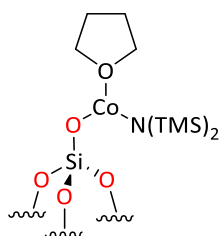


Figure 3.6. The surface cobalt species of **(2)/A-SiO₂**

For comparison, it was desirable to undertake a CHN analysis of blank **A-SiO₂₋₆₀₀** silica. However, this was problematic, as anticipated, due to difficulties arising from the lack of combustion of the silica; nevertheless, an analysis was undertaken to provide a baseline for comparison (Table 3.6). A trace amount of carbon was detected, which has been attributed to the presence of a low level of contaminant.

The values of the “expected” and “found” CHN analyses of **(2)/A-SiO₂₋₆₀₀** (2.2% w.t. Co) matched, confirming that the complex **2** is mono-grafted retaining one silyl amide ligand and one THF bound to the cobalt (Figure 3.6). The percentage of SiMe₃ surface species calculated in Section 3.1.2.4 is also confirmed.

Table 3.6. Expected and found CHN analyses of **A-SiO₂₋₆₀₀** and **(2)/SiO₂₋₆₀₀** (2.2% w.t. Co)

Material	Expected CHN	Found CHN
A-SiO₂₋₆₀₀ *	C 0.00; H 0.08; N 0.00	C 0.09; H 0.01; N 0.00
(2)/A-SiO₂₋₆₀₀	C 5.10; H 1.10; N 0.50	C 5.12; H 1.16; N 0.60

* note these values are likely an estimation due to limited combustion

3.1.3 Analysis of product from reaction of [Co(N(TMS)₂)₂(THF)] with KIT-6 ((2)/K-SiO_{2-x})

Following the successful immobilisation of complex **2** on Aeroperl 300/30 silica, in order to probe the effects of the pore structure, particularly pore diameter, upon immobilisation, reaction of **2** with KIT-6 was also explored. KIT-6 silica (K-SiO₂) has interconnecting inner pores and an average pore diameter (37 – 53 Å), which is smaller than the average pore diameter of Aeroperl 300/30 (249 – 275 Å). Complex **2** is a comparatively bulky molecule (diameter ~12 Å) due to the TMS groups and will have more difficulty diffusing through KIT-6's smaller pore diameter compared to Aeroperl 300/30's pores. To explore how a smaller pore diameter affects the loading of complex **2** onto silica, it is important to study how complex **2** is tethered onto KIT-6.

3.1.3.1 Cobalt loading of on KIT-6 Silica Determined by ICP-OES

The cobalt metal loading following immobilisation of [Co(N(TMS)₂)₂(THF)] (**2**) on KIT-6 previously calcined at different temperatures was determined by ICP-OES (Table 3.7). Like the results obtained following immobilisation of complex **2** on Aeroperl 300/30, there is a correlation between the OH density and the cobalt w.t. % loading; as the OH density decreases, the resulting cobalt loading also decreases. However, in contrast to the data obtained for Aeroperl 300/30, the metal loading was affected by which batch of calcined KIT-6 that was employed for grafting, something especially marked for samples of KIT-6 calcined at higher temperatures. For example, different batches of KIT-6 calcined at 600 °C gave different cobalt loadings (between 1.9 – 3.3 % w.t. Co), and various different batches of KIT-6 calcined at 700 °C gave cobalt loadings between 0.7 – 3.0 % w.t. Co. As stated in Section 2.1, it has been proposed that isolated silanols, and therefore isolated tethered organometallic complexes, are desirable for sub-nanosized cobalt particles; calcination of the silica at >600 °C is important to achieve isolated silanol species. Small experimental variations in the calcination process are thought here to affect the nature of the final KIT-6 materials obtained, which have slight differences in pore size due to how the pore structure collapsed at T = >600 °C (Section 2.2.1.3). The pore collapse of KIT-6 affects the access of complex **2** to the surface and hence the loading. Thus, inconsistency in cobalt loading in KIT-6 calcined at the same temperature is proposed to be due to slight variations in the pore structure collapse. Together, it was concluded that this makes KIT-6 an unsuitable support for this project.

Table 3.7. The average Co metal loading of complex **2** on KIT-6 silica calcined at different temperatures, as determined by ICP-OES

Material	OH density (mmol g ⁻¹)	Cobalt (mmol g ⁻¹)	Cobalt w.t. % loading	% of OH groups that reacted with a Co
(2)/K-SiO ₂₋₂₀₀	5.81	0.76	4.5	13
(2)/K-SiO ₂₋₄₀₀	2.92	0.64	3.8	22
(2)/K-SiO ₂₋₆₀₀	2.16	0.49	2.9	23
(2)/K-SiO ₂₋₇₀₀	1.77	0.46	2.7	26

3.1.4 Analysis of material from reaction of [Co(N(TMS)₂)₂(THF)] with SBA-15 ((2)/S-SiO_{2-x})

SBA-15 silica (**S-SiO₂**) is similar to KIT-6, with a comparatively smaller pore diameter (31 – 69 Å) compared with that of Aeroperl 300/30. In contrast, however, SBA-15 silica also has a 2D structure with less interconnecting pores than KIT-6 and Aeroperl 300/30 (249 – 275 Å). Consequently, as with KIT-6, it was of interest to probe how the relatively bulky complex **2** (diameter ~12 Å) penetrates within the channel network of SBA-15. Importantly, SBA-15 is more thermally stable than KIT-6 and does not show any decrease in surface area until >700 °C (Section 2.2.1.2).

3.1.4.1 Cobalt loading on SBA-15 Silica Determined by ICP-OES

The cobalt loading following immobilisation of complex **2** on SBA-15 calcined at different temperatures was determined by ICP-OES (Table 3.8). Like Aeroperl 300/30 and KIT-6, there is a correlation between calcination temperature and cobalt loading, with the silicas calcined at higher temperatures resulting in a lower cobalt loading. However, unlike with KIT-6, there were no problems with the cobalt loading due to the pore structure collapsing at calcination temperatures >600 °C. as would be expected for the more thermally robust SBA-15. Thus, SBA-15 is considered a more promising support than KIT-6 (Section 2.2.1.2).

Table 3.8. The average Co metal loading following immobilisation of complex **2** on SBA-15 silica calcined at different temperatures, as determined by ICP-OES

Material	OH density (mmol g ⁻¹)	Cobalt (mmol g ⁻¹)	Cobalt w.t. % loading	% of OH groups that reacted with a Co
(2)/S-SiO ₂₋₂₀₀	5.59	0.90	5.3	16
(2)/S-SiO ₂₋₄₀₀	3.43	0.75	4.4	22
(2)/S-SiO ₂₋₆₀₀	2.49	0.70	4.1	28
(2)/S-SiO ₂₋₇₀₀	1.76	0.58	3.4	33

3.1.5 Conclusions for Reactions of [Co(N(TMS)₂)₂(THF)] with Silica Supports

Of the oxide supports discussed, immobilisation of complex **2** on Aeroperl 300/30 and SBA-15, (**2**)/A-SiO₂ and (**2**)/S-SiO₂, have shown the most promise. Compared to KIT-6, Aeroperl 300/30 and SBA-15 silica have the most consistent cobalt loading across all calcination temperatures (1.8 – 3.6 w.t. %). This is likely due to the larger pore size of Aeroperl 300/30 (*cf.* diameter of **2** of ~12 Å). Additionally, both Aeroperl 300/30 and SBA-15 show no collapse in pore structure or decrease in pore size at temperatures chosen for calcination. Due to the air sensitivity of (**2**)/SiO_{2-x}, characterising the material proved challenging. A paramagnetic cobalt is also present, so probing the surface structure through SS-NMR spectroscopy (directly or indirectly) is challenging. The surface structure of (**2**)/A-SiO₂₋₆₀₀ was determined to possess the mono-grafted, mono-amide species described in Figure 3.6. ICP-OES analysis confirmed the degree of loading of complex **2** to the silica surface, and CHN analysis was used

to determine the number of HMDS ligands still attached to the cobalt metal centre. BET analysis showed the change in pore size as functionalisation of the silica surface occurred during impregnation, which was determined to be a mix of metalation and silylation of the silica surface by released HMDS. GC analysis confirmed that 13% of the silanols reacted with HMDS to form surface $-\text{OSiMe}_3$ sites.

Compared to **(2)/A-SiO₂** and **(2)/S-SiO₂**, immobilisation of complex **2** on KIT-6 was less promising, with pore collapse in the support leading to issues of consistency in metal loading. This is suspected to be due to the differences in surface area from the uneven pore collapse of KIT-6, leading some batches of calcined KIT-6 to have a lower available surface area for reaction. Complex **2** is very bulky, so a small decrease in pore size will have a significant effect on cobalt loading.

3.2 Reactions of Cobalt Precursors Complexes 3 - 8 with Calcined Silica Support

The remainder of this chapter will discuss the deposition of other cobalt-containing complexes **3 – 8** on the surface of variously calcined silica. This section will mostly discuss using Aeroperl 300/30 as a support, particularly **A-SiO₂₋₆₀₀**, as it was shown to be the most promising support due to consistent and controlled cobalt loading of complex **2** (in Section 3.1).

3.2.1 CoCp₂ + Aeroperl 300/30 Silica ((3)/A-SiO_{2-x})

CoCp₂ (**3**) was selected as a potential cobalt-containing precursor in this study since it was previously reported by Lindblad and Rebenstorf that **3** can react with surface silanol groups *via* protonation and loss of the Cp ligand.¹⁶ The simplicity of the structure of CoCp₂ is important since there is only one available reaction pathway with surface SiOH groups (*i.e.* loss of a Cp moiety *via* protonation), simplifying chemistry that may occur at the surface. Additionally, if the surface reactivity can be controlled appropriately, then initial protonation of just one Cp ligand may be achieved, leaving a surface-bound CpCo fragment (Figure 3.7). Furthermore, the presence of the remaining η^5 -bound cyclopentadienyl motif by provide some steric protection of the surface-bound cobalt species, potentially limiting aggregation, prior to reduction. Additionally, the resulting CpH generated will be unreactive towards surface silanol groups in contrast to $\text{HN}(\text{SiMe}_3)_2$ generated from reaction of $\text{Co}(\text{N}(\text{SiMe}_3)_2)_2$ with silica. Hence, the resulting released CpH can easily be removed *in vacuo* or by washing with solvent. Furthermore, complex **3** has no heteroatom-containing substituents, which is beneficial in preventing potential poisoning of the surface of the silica or any newly formed sub-nanosized particles, as reactive heteroatom-containing substituents may react with the surface leaving heteroatoms bound to the material to act as poisons during catalysis.



Figure 3.8. (i) Purple **(3)**/SiO₂ prior to exposure to atmosphere (ii) Green **(3)**/SiO₂ after exposure to air

3.2 1.1 Analysis of **(3)**/A-SiO_{2-x}

3.2.1.1.1 Cobalt-loading of **(3)**/A-SiO₂ Determined by ICP-OES

The cobalt loading resulting from reaction of complex **3** with a number of different Aeroperl 300/30 silicas previously calcined at different temperatures was determined by ICP-OES (Table 3.9). Unlike the reaction of complex **2** with Aeroperl 300/30, consistent cobalt loadings could not be achieved on reacting complex **3** with the samples of the same calcined Aeroperl material. For example, the cobalt loading of complex **3** on SiO₂₋₇₀₀ ranged between 1.4 to 1.9 (\pm 0.4) Co w.t.% with each attempt at tethering the complex to portions of the same batch of the support. The inconsistent loading of cobalt on the silica was not related to the collapse of the pore structure, as was the case for complex **2** on KIT-6, as Aeroperl 300/30 is stable at all of the calcination temperatures used in this project. Moreover, the inconsistency in the loading with **3** was seen at all temperatures of calcination of the parent silica.

There is no pattern or correlation between the calcination temperature of the silica and the ensuing cobalt loading of complex **3** on the support. This suggests that complex **3** might not be reacting (*via* protonation) with the surface silanol groups, and therefore the cobalt loading is not controlled, with the reaction leading to simple deposition of physisorbed **3** on the silica. If complex **3** was reacting with the hydroxyl groups in an acid-base fashion, a correlation between cobalt loading and hydroxyl density would be expected. This is contrary to what was reported by Lindblad *et al.*,[‡] who stated that cobaltocene does react with surface -OH groups *via* protonation of a Co-Cp motif, and its loading onto silica-gel is controlled by the density of silanols.¹⁷

[‡] Lindblad *et al.* tethered CoCp₂ to the surface of silica gel by dissolving CoCp₂ in toluene and “splashing” the solution onto a pressed disc of the silica support in an argon atmosphere at room temperature. Excess toluene was then removed *in vacuo*.

Table 3.9. The Co metal loading of complex **3** on Aeroperl 300/30 silica calcined at different temperatures, as determined by ICP-OES

Material	OH density (mmol g ⁻¹)	Cobalt (mmol g ⁻¹)	Cobalt w.t. % loading	% of OH groups that reacted with a Co
(3)/A-SiO₂₋₂₀₀	2.16	0.42	2.5	20
(3)/A-SiO₂₋₄₀₀	1.43	0.31	1.8	22
(3)/A-SiO₂₋₆₀₀	0.83	0.22	1.3	27
(3)/A-SiO₂₋₇₀₀	0.59	0.29	1.7	49

3.2.1.1.2 Analysis of CpH formation during the synthesis of **(3)/A-SiO₂₋₆₀₀**

As a result of the discrepancies/lack of reproducibility in cobalt loading achieved on reacting variously-calcined samples of Aeroperl 300/30 silica with Cp₂Co, further investigation of the immobilisation process was undertaken. If complex **3** was indeed reacting with the surface hydroxyl groups *via* protonation, it is expected that a protonated cyclopentadiene (CpH) would be lost during the reaction. Thus, confirming the presence of liberated CpH in the reaction mixture would corroborate whether complex **3** was reacting with the silanols or not. To determine how many Cp rings were lost during the reaction described in Scheme 3.7, a GC chromatographic analysis of the recovered liquid phase material (a mixture of unreacted Cp₂Co, CpH, and pentane) was run against an internal standard of nonane (using the method described in Section 6.0.2.5). It was found that 0.089 mmol g⁻¹ of CpH was released during the synthesis of **(3)/A-SiO₂₋₆₀₀**.

The metal loading on the silica (0.83 mmol g⁻¹ of CoCp on the surface) as determined by ICP OES was compared to the amount of CpH released (0.089 mmol g⁻¹ of CpH) in the reaction. This gave the molar ratio of 1:9.3 CpH:Co/SiO₂₋₆₀₀. This calculated ratio differs significantly from the expected 1:1 ratio if complex **3** was reacting with the silanol species and releasing CpH. Consequently, it is inferred that both Cp rings must remain on cobalt during the attempted immobilisation on the silica surface. Therefore, it is unlikely complex **3** is reacting in an acid-base fashion with the silica surface, with cobaltocene instead being simply physisorbed to the oxide surface. It is proposed that the small amount of CpH detected is likely to be the result of a small amount of complex **3** decomposing during the reaction.

3.2.1.1.3 ²⁹Si SS-NMR Spectroscopic Analysis of **(3)/A-SiO₂**

In order to identify the surface structure of product resulting from the attempted immobilisation of complex **3** with **A-SiO₂**, and to explore whether it is similar to the structure reported by Lindblad and Rebenstorf who only used IR spectroscopy to confirm the presence of a CoCp species,¹⁶ ²⁹Si SS-NMR spectroscopy was performed. The DE spectra of **(3)/A-SiO₂₋₆₀₀** is shown in Figure 3.9. Spectra of **(3)/A-SiO₂₋₆₀₀** were obtained with a 300 s recycle delay (fully relaxed) as well as a 10 s delay. The relaxation times of the NMR spectral acquisition were altered in order to test if the cobalt surface species had a

significant impact on the relaxation time of the silicon, as the suspected Co surface species would be paramagnetic due to its 2+ oxidation state (d^7 configuration) and affect the relaxation of the silicon. Results from our NMR spectroscopic investigation shows that the relaxation of the silicon is slow, indicating that the silicon is not attached to a paramagnetic cobalt centre.

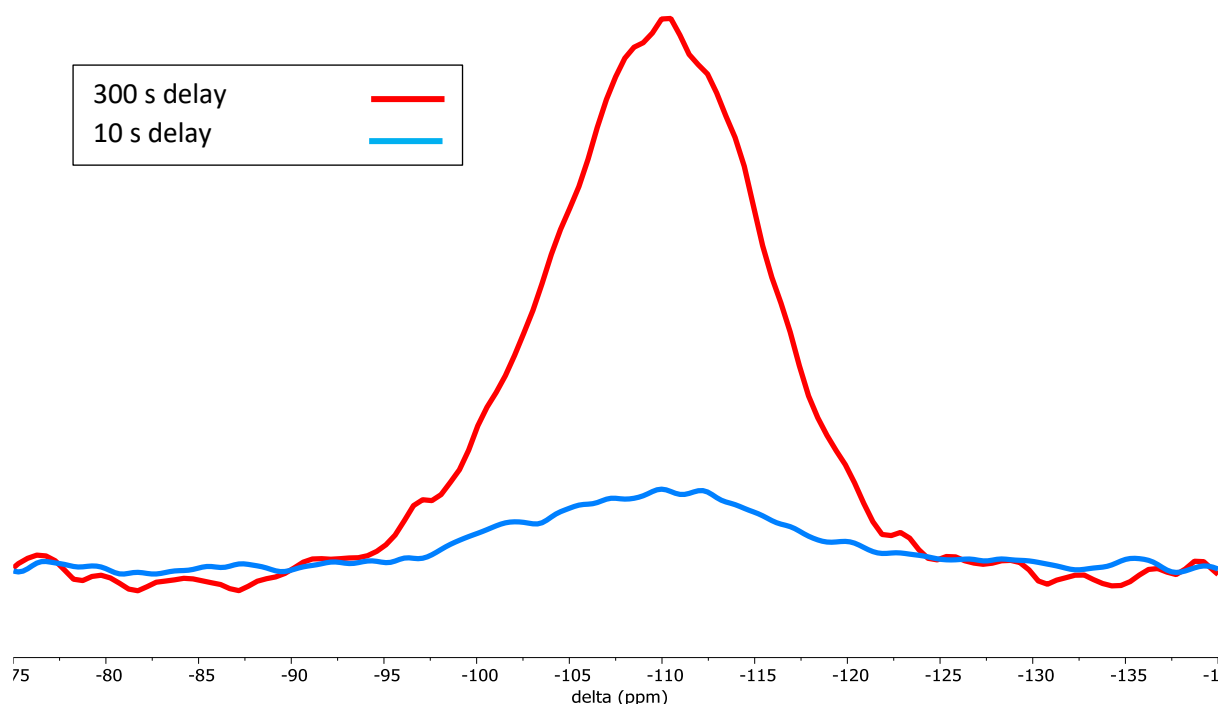


Figure 3.9. DE ^{29}Si SS-NMR spectra of $(\mathbf{3})/\text{A-SiO}_{2-600}$, comparing delay relaxation times to determine whether the presence of the cobalt affects the relaxation time of silicon, Frequency 79.437 MHz, Spin-rate 6 kHz

The CP ^{29}Si SS-NMR spectra of $(\mathbf{3})/\text{A-SiO}_{2-600}$ and blank A-SiO_{2-600} are shown in Figure 3.10. It was hoped that the presence of a paramagnetic Co^{II} surface species bound to the silica surface would lead to a decrease in the Q_2 and Q_3 peak intensity or that a change in chemical shift would be observed compared to that of the blank silica, with such effects having been observed previously in the SS-NMR spectral study of Lamb's paramagnetic Cr-amide surface species on silica.¹⁸ However, for the $\text{Cp}_2\text{Co}/\text{silica}$ reactions attempted here, no differences in the ^{29}Si chemical shifts between A-SiO_{2-600} and $(\mathbf{3})/\text{A-SiO}_{2-600}$ were observed, consistent with the paramagnetic cobalt not being directly attached to the silica surface (Figure 3.10). This supports the suggestion that complex $\mathbf{3}$ has not reacted in an acid-base fashion with the surface silanols – see Section 3.2.1.1.2 (above).

From the CP ^{29}Si SS-NMR spectra of $(\mathbf{3})/\text{A-SiO}_{2-600}$ and blank A-SiO_{2-600} recorded (Figure 3.10), it's clear there is a large change in signal intensity between that observed for $(\mathbf{3})/\text{A-SiO}_{2-600}$ and that for blank A-SiO_{2-600} silica. As mentioned in Section 2.2.3, changes in intensity in the CP spectrum, while not

quantitative, can give an indication of whether the Si-OH density is increasing or decreasing following reaction. Although this large decrease in signal intensity on moving from blank silica to **(3)/A-SiO₂₋₆₀₀** might initially suggest that most of the surface OH groups have reacted with complex **3**, it is more likely to be due to paramagnetic cobalt being present somewhere in the material, even if it is not directly attached to the silica surface (here physisorbed material is most likely). An example of paramagnetic cobalt affecting the acquisition of the CP spectrum is seen with **(2)/A-SiO₂₋₆₀₀** described in Section 3.1.2.2., where no ²⁹Si signal is observed due to the presence of paramagnetic cobalt bound to the silica. The observation of a ²⁹Si signal in the spectrum of **(3)/A-SiO₂₋₆₀₀** could indicate that the paramagnetic cobalt is not tethered to the silica surface, even if it is present in the material. Expansion of the CP spectra of **(3)/A-SiO₂₋₆₀₀**, Figure 3.11, shows that the resonance observed is similar to that seen in a typical CP ²⁹Si spectrum of silica (Section 2.2.3.1), but the signal is very noisy. The origin of the noise has been attributed to the effects of the presence of a paramagnetic cobalt.

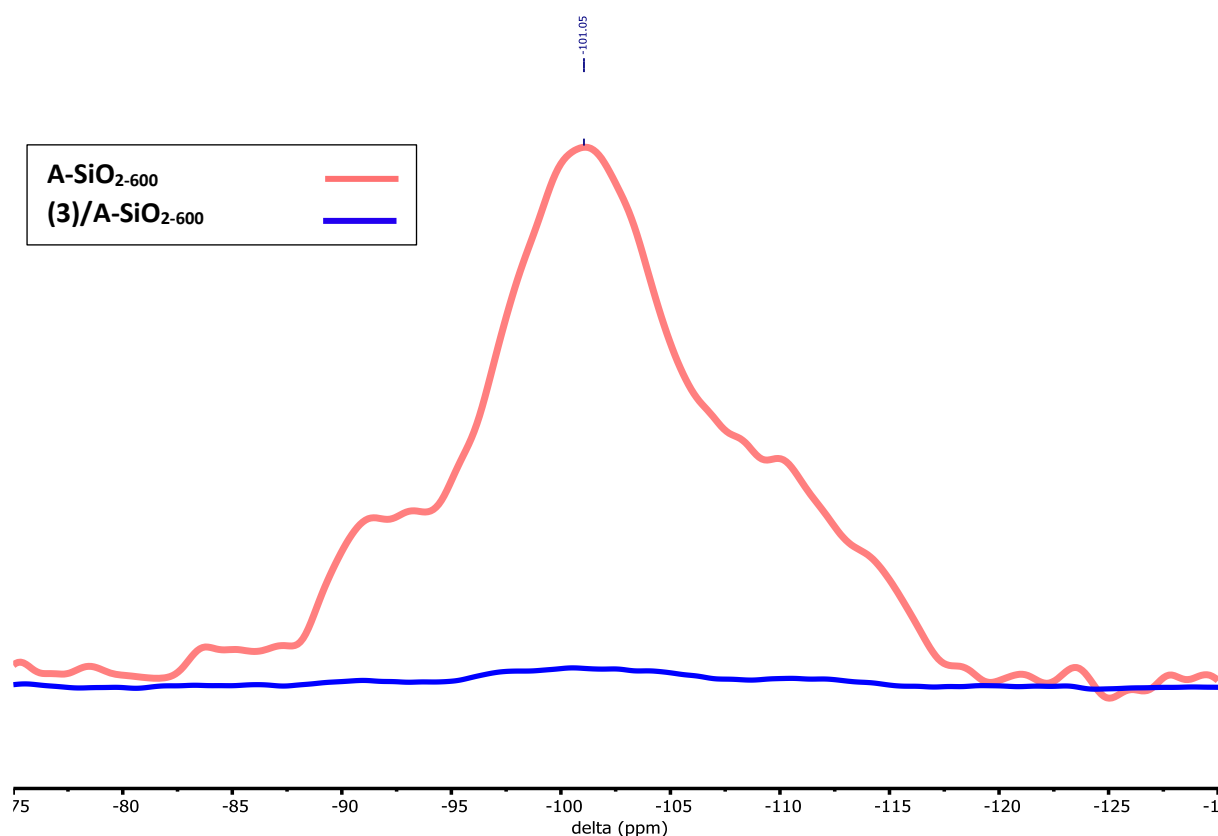


Figure 3.10. Comparison of the CP ²⁹Si SS-NMR spectra of **A-SiO₂₋₆₀₀** and **(3)/A-SiO₂₋₆₀₀**, using the same vertical scale, Frequency 79.437 MHz, spin-rate 6 kHz

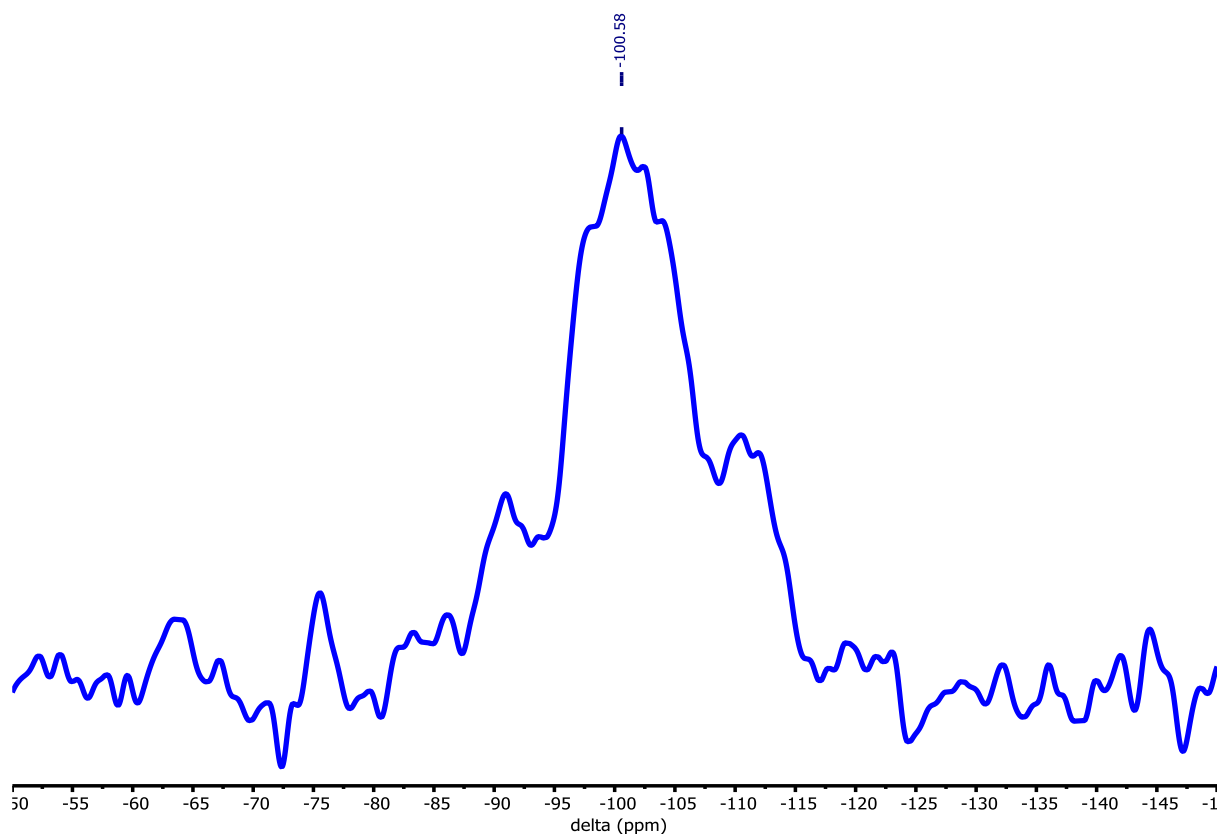


Figure 3.11. CP ^{29}Si SS-NMR spectrum of **(3)/A-SiO₂₋₆₀₀**; frequency 79.437 MHz, spin-rate 6 kHz

The ^1H SS-NMR spectra of **(3)/A-SiO₂₋₆₀₀** and complex **3** are given in Figure 3.12 and Figure 3.13, respectively, and the ^{13}C SS-NMR spectrum of **(3)/A-SiO₂₋₆₀₀** is given in Figure 3.14. There are two signals at 0.1 and 5.9 ppm in the ^1H SS-NMR spectrum of **(3)/A-SiO₂₋₆₀₀** (Figure 3.12). The resonance at 0.1 ppm has been attributed to adventitious grease. The resonance at 5.9 ppm is consistent with that expected from a cyclopentadienyl motif. It has been significantly shifted from the ^1H SS-NMR signal found for untethered complex **3**, which occurs at -44.8 ppm (Figure 3.13). There are also two peaks in the ^{13}C SS-NMR spectrum (Figure 3.14) at 0 ppm (silicone grease) and 85.2 ppm (an aromatic Cp ring). This latter ^{13}C SS-NMR chemical shift is entirely consistent with that reported previously for complex **3**, namely +84.5 ppm,¹⁹ which together supports the notion of the presence of physisorbed **3** on the silica surface.

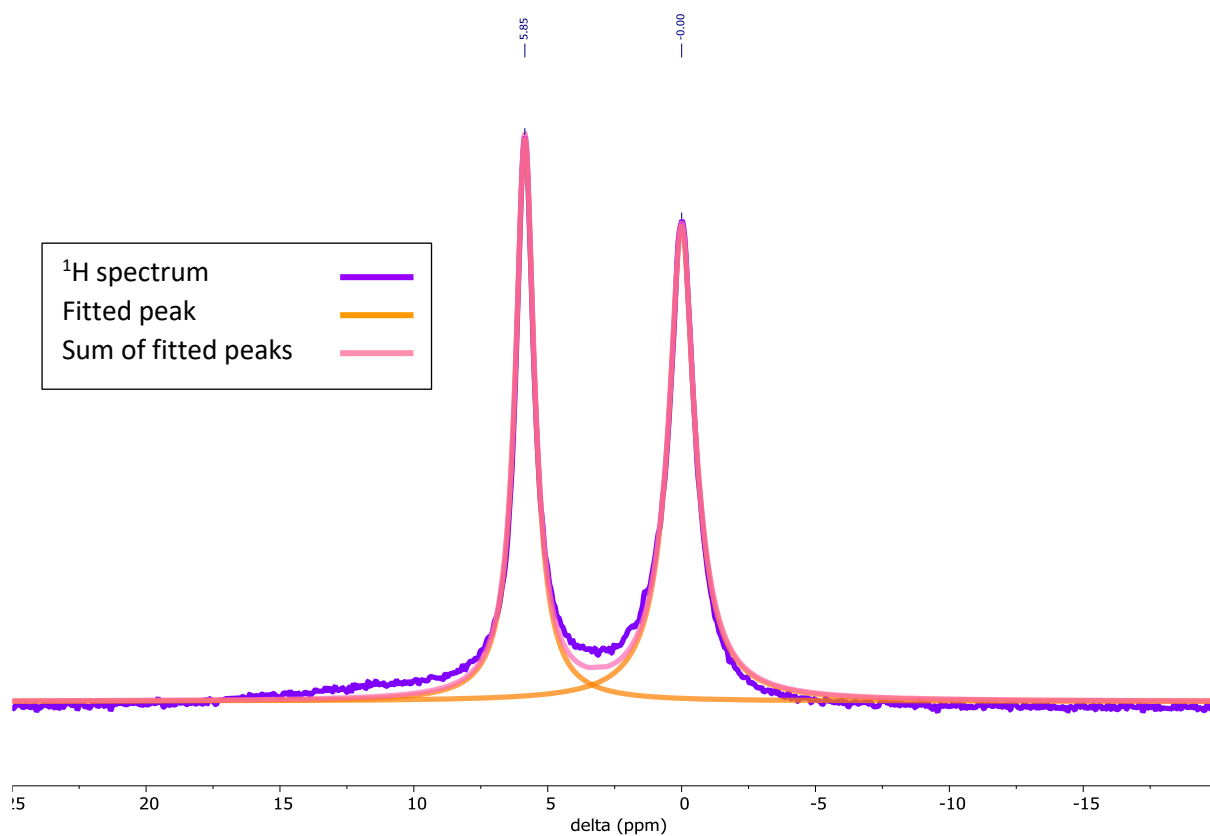


Figure 3.12. ^1H SS-NMR spectrum of **(3)**/*A-SiO*₂₋₆₀₀; frequency 400.17 MHz, spin-rate 40 kHz

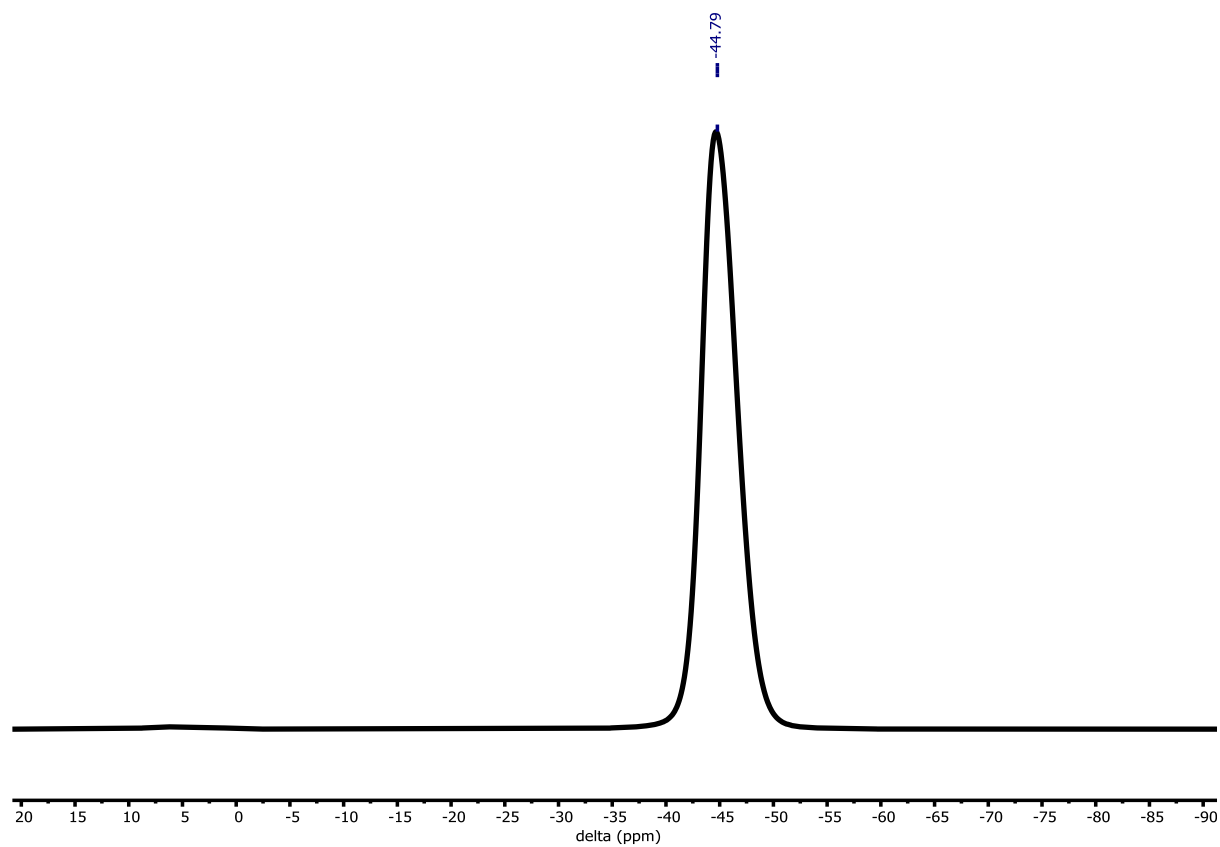


Figure 3.13. ^1H SS-NMR spectrum of complex **3**; frequency 400.17 MHz, spin-rate 40 kHz

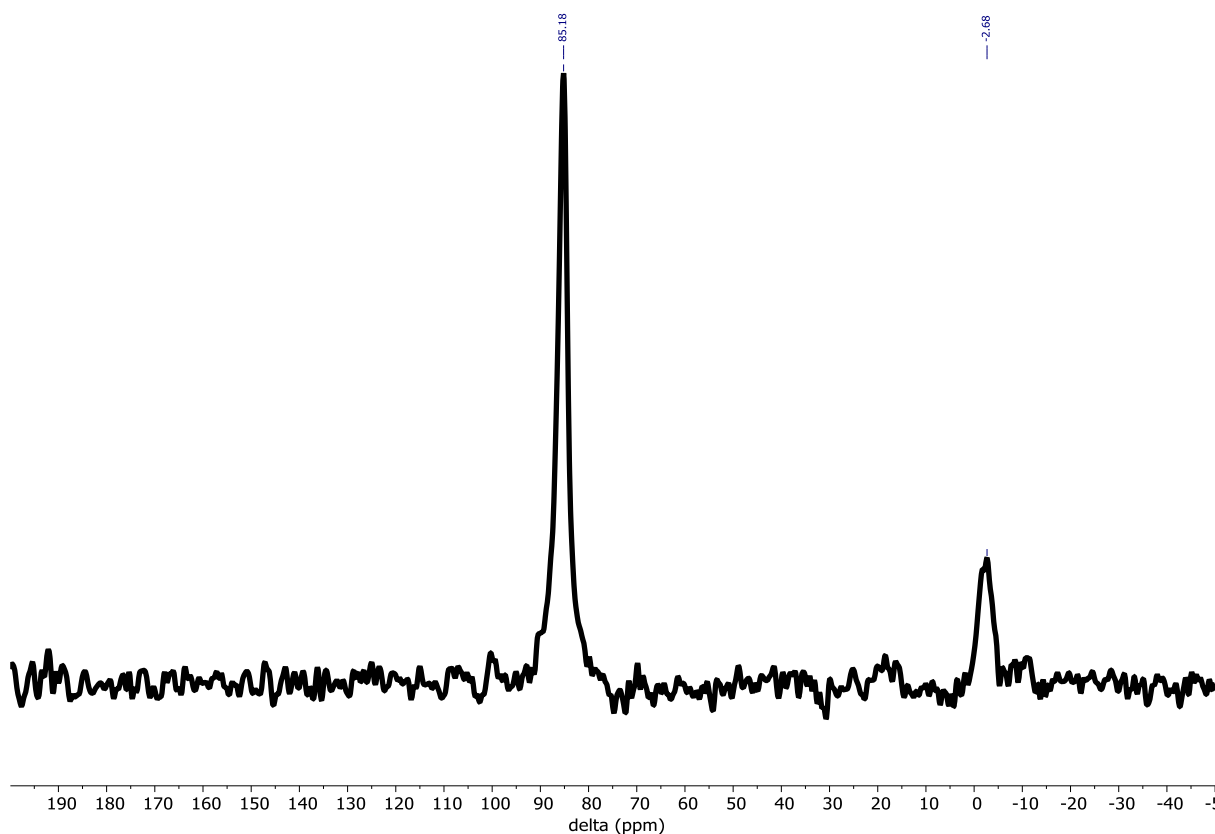


Figure 3.14. ^{13}C SS-NMR spectrum of **(3)/A-SiO₂₋₆₀₀**; frequency 100.6 MHz, spin-rate 10 kHz

3.2.1.1.4 CHN Elemental Analysis of **(3)/A-SiO₂₋₆₀₀**

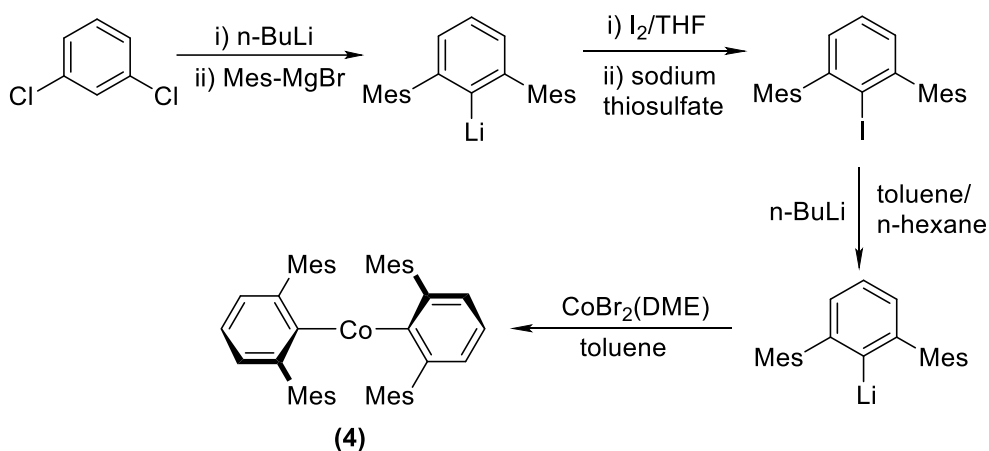
It was hoped that elemental analysis could be used to determine the number of Cp ligands present in **(3)/A-SiO₂₋₆₀₀**. The expected CHN for **(3)/A-SiO₂₋₆₀₀** is C 2.6; H 0.4; N 0, assuming that both Cp ligands are attached to the cobalt centre, and using the cobalt density derived from ICP-OES (0.22 mmol g^{-1}). The CHN analysis obtained experimentally of **(3)/A-SiO₂₋₆₀₀** is C 3.7 ; H 0.6 ; N 0. While the percentage hydrogen found matches the expected hydrogen (within the 0.5 % error normally accepted for combustible solids), the found carbon was 1.1 % higher than expected. This is likely due to trace amounts of grease present in **(3)/A-SiO₂₋₆₀₀**, as observed in the SS-NMR analyses. Thus, CHN elemental analysis of **(3)/A-SiO₂₋₆₀₀** does not give any conclusive evidence to the number of Cp-ligands still attached to the cobalt centre.

3.2.2 Co(dmp)₂ + Aeroperl 300/30 Silica (**(4)/A-SiO_{2-x}**)

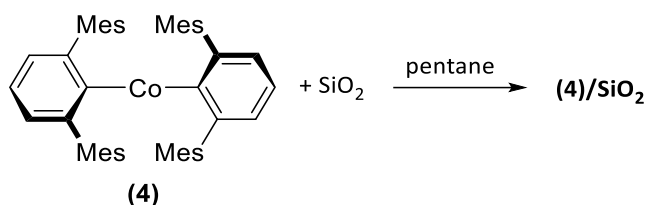
A study of the impregnation of Co(dmp)₂ (**4**) on SiO₂ was chosen since the steric bulk of the ligands of complex **4** will limit metal loading, which may control the size of any resulting nanoparticles further, giving even smaller nanoparticles. The bulkiness of the ligands on complex **4** may also aid in stabilisation of an electron deficient metal species on the surface of silica prior to reduction to the target cobalt nanoparticles. However, it should be noted that use of this complex may cause problems as a result of its bulk (16 \AA diameter), which is likely to hinder its travel through some of the smaller pores of the oxide support and hence could result in a lower cobalt coverage than some of the smaller

cobalt complexes and be more concentrated at the opening at the pores rather throughout the whole structure.

Complex **4** shows potential as an interesting study into the effects of bulky ligands when tethering to an oxide support. The synthesis of complex **4** was undertaken according to the reported literature method, with **4** subsequently being isolated as a material highly sensitive to both air and moisture (Scheme 3.8); successful formation of complex **4** was confirmed by CHN.²⁰ With complex **4** in hand, attempts were made to impregnate this material onto Aeroperl 300/30 silica according to Scheme 3.9. The possible surface structures of **(4)/A-SiO₂₋₆₀₀** are shown in Figure 3.15.



Scheme 3.8. Synthesis of complex **4**



Scheme 3.9. Synthesis of **(4)/SiO₂**

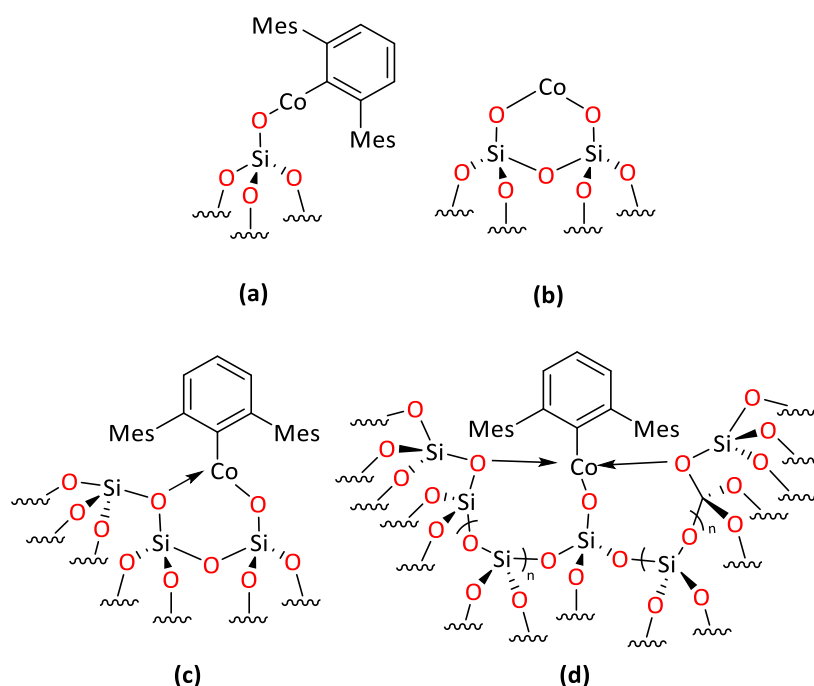


Figure 3.15. Possible surface cobalt species of **(4)**/ SiO_2

3.2.2.1 Analysis of **(4)**/ A-SiO_{2-x}

3.2.2.1.1 Cobalt-loading of **(4)**/ A-SiO_2 Determined by ICP-OES

The cobalt loading of complex **4** on Aeroperl 300/30 was derived using ICP-OES (Table 3.10). These analyses showed the same trends as those determined for complex **2** on Aeroperl 300/30, with a correlation between increasing calcination and decreasing cobalt loading. Compared to the reaction of complex **2** Aeroperl 300/30, use of complex **4** leads to a much lower loading silica (2.3 – 3.6 Co w.t. % vs. 0.7 – 1.7 Co w.t. % for complex **2** and **4**, respectively). This is proposed to be due to complex **4** being more bulky than complex **2** (16 Å diameter[§] vs. 12 Å for **2**), and hence may not reach far into the deeper pore structure of Aeroperl 300/30.

Table 3.10. Co metal loading of complex **4** on Aeroperl 300/30 silica calcined at different temperatures, as determined by ICP-OES

Material	OH density (mmol g ⁻¹)	Cobalt (mmol g ⁻¹)	Cobalt w.t. % loading	% of OH groups that reacted with a Co
(4) / A-SiO_{2-200}	2.16	0.29	1.7	34.7
(4) / A-SiO_{2-400}	1.43	0.19	1.1	22.5
(4) / A-SiO_{2-600}	0.83	0.12	0.7	14.3

3.2.2.1.2 DE ²⁹Si SS-NMR Spectroscopy of **(4)**/ A-SiO_{2-600}

As with **(2)**/ A-SiO_{2-600} and **(3)**/ SiO_{2-600} , SS-NMR was considered a powerful tool for identifying the surface structure of **(4)**/ A-SiO_{2-600} . DE ²⁹Si SS-NMR spectra were obtained of **(4)**/ A-SiO_{2-600} (Figure 3.16) with 10 s and 30 s delay relaxation times, in a similar manner to the spectra acquired during the study

[§] Diameter of molecule was approximated according to Section 6.0.2.11

undertaken for **(3)**/**A-SiO₂₋₆₀₀** (section 3.2.1.1.3). As seen in Figure 3.16, the DE ²⁹Si SS-NMR spectra of **(4)**/**A-SiO₂₋₆₀₀** are very similar to those determined for **(3)**/**A-SiO₂₋₆₀₀** (Figure 3.9), indicating that the relaxation of **(4)**/**A-SiO₂₋₆₀₀** is slow, as was found for **(3)**/**A-SiO₂₋₆₀₀**. Together these data suggest that the silicon in **(4)**/**A-SiO₂₋₆₀₀** is not near a paramagnetic cobalt, and that either the surface species of complex **4** are not paramagnetic or, more likely, that complex **4** is physisorbed instead of chemisorbed to the silica surface.

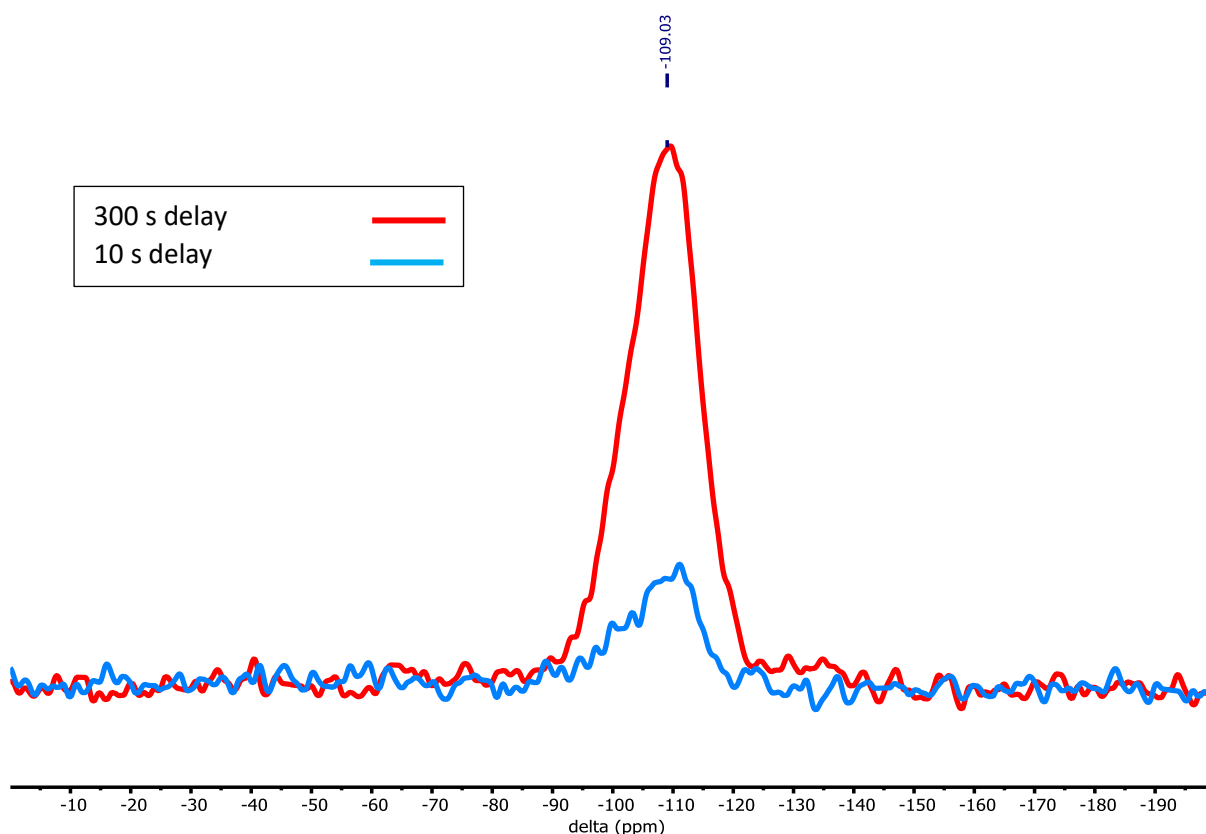


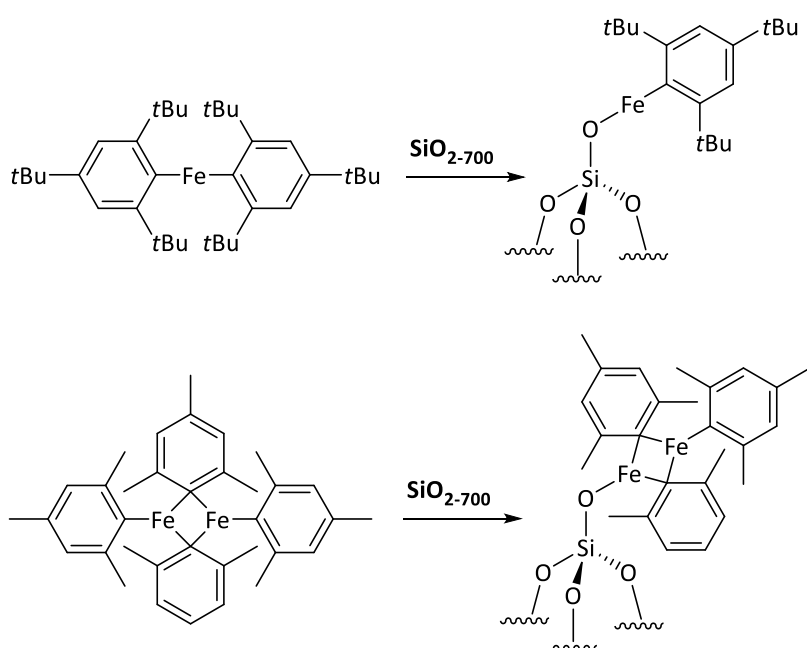
Figure 3.16. DE ²⁹Si SS-NMR spectra of **(4)**/**A-SiO₂₋₆₀₀**, comparing delay relaxation times to determine whether the presence of the cobalt affects the relaxation time of silicon; frequency 79.437 MHz, spin-rate 6 kHz

3.2.2.1.3 Elemental CHN Analysis of **(4)**/**A-SiO₂₋₆₀₀**

The theoretical elemental analyses for **(4)**/**A-SiO₂₋₆₀₀** were calculated using the same method as described in Section 6.0.2.7.1, assuming that complex **4** was bound to the silica surface as a mono-grafted species with cobalt retaining one dmp ligand, and using the cobalt density, 0.12 mmol g⁻¹ (derived from ICP-OES analysis, Section 3.2.2.1.1). The expected and found CHN percentages are C 2.6; H 0.4; N 0, and C 6.42 ; H 0.7; N 0, respectively. The experimentally-determined percentages of carbon and hydrogen found are much higher than the expected values; 2.4- and 1.75-times higher for carbon and hydrogen, respectively.

CHN analysis suggests that the cobalt surface species of **(4)**/**A-SiO₂₋₆₀₀** does not possess a mono-grafted organospecies (*i.e.* SiO-CoN(TMS)₂) as was found from the reaction of complex **2** with silica, but is more likely to comprise largely of complex **4** physisorbed to the silica. However, this is

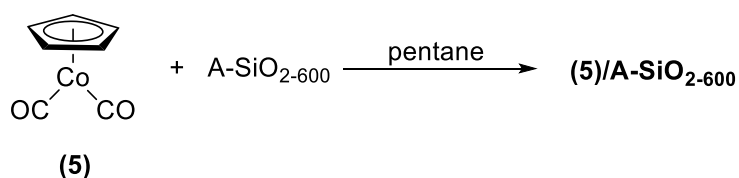
unlikely as similar iron complexes to complex **4**, with mesityl or substituted phenyl ligands, have formed mono-grafted species when grafted to a silica surface (calcined at 700 °C) as described previously in the literature by Roukoss *et al.* (Scheme 3.10),^{5, 21} who used comparable reaction conditions.** The CHN analysis values obtained may be due the potential presence of adventitious grease, and CHN analysis does not provide any information regarding binding in this example, therefore it is better to rely on Co ICP-OES analysis.



Scheme 3.10. Iron-phenyl/mesityl complexes, similar to complex **4**, forming mono-grafted surface species on the surface of silica calcined at 700 °C⁵

3.2.3 CoCp(CO)₂ + Aeroperl 300/30 Silica ((5)/A-SiO₂₋₆₀₀)

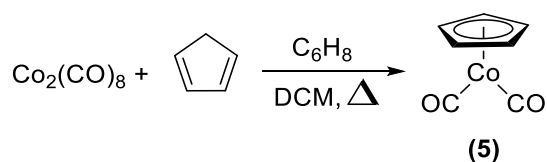
The complex CoCp(CO)₂ (**5**) was selected for immobilisation on silica as previous work by Gürtler has studied its binding to silica gel and alumina.³ Gürtler demonstrated that complex **5** can be reacted directly with the hydroxyl groups on the surface of oxides, reporting that a third of hydroxyl groups will bind to the cobalt metal centre. Consequently, the synthesis of (**5**)/A-SiO₂₋₆₀₀ was attempted as described in Scheme 3.11.



Scheme 3.11. Synthesis of (**5**)/A-SiO₂₋₆₀₀

** Roukoss *et al.* tethered the iron complexes in Scheme 3.10 to silica by immersing the silica in a pentane solution of the respective iron complex at 25 °C. The resulting material was isolated by filtration and any unreacted complex was washed away with excess pentane. The solid was then dried under vacuum.²⁰

The synthesis of complex **5** was performed according to a standard literature method *via* reaction of commercially available cobalt carbonyl $\text{Co}_2(\text{CO})_8$ with freshly “cracked” CpH (Scheme 3.12).²¹ The reaction was undertaken using anhydrous conditions in dry pentane under nitrogen and with the exclusion of light.^{††}



Scheme 3.12. Synthesis of complex 5

Complex **5** is a complex that has two different types of ligand that could be lost during the attempted tethering to a silica surface: the protonation of the Cp^- ring, or the displacement of two neutral carbonyl groups. Depending on the ligand lost, **(5)/A-SiO₂₋₆₀₀** could potentially have one of a number of different possible surface structures as shown in Figure 3.17. This makes complex **5** an interesting “bridge” between the reactions of the silica surface with CoCp_2 (complex **3**, Section 3.2.1) and $\text{Co}_2(\text{CO})_8$ (complex **6**, Section 3.2.4), which both contain only one type of ligand that could be lost. Which ligand is lost (CO ligands or Cp ring) should be able to be determined either directly by IR spectroscopy (by the presence of a strong CO stretching vibration) or indirectly by GC-MS (by the presence of CpH in the captured reaction solvent of complex **5** and silica).

^{††} This is due to the sensitive nature of both the starting materials and the resulting product, complex **5** readily decomposes at room temperature or in the presence of oxygen and light, which displaces the neutral CO ligands.

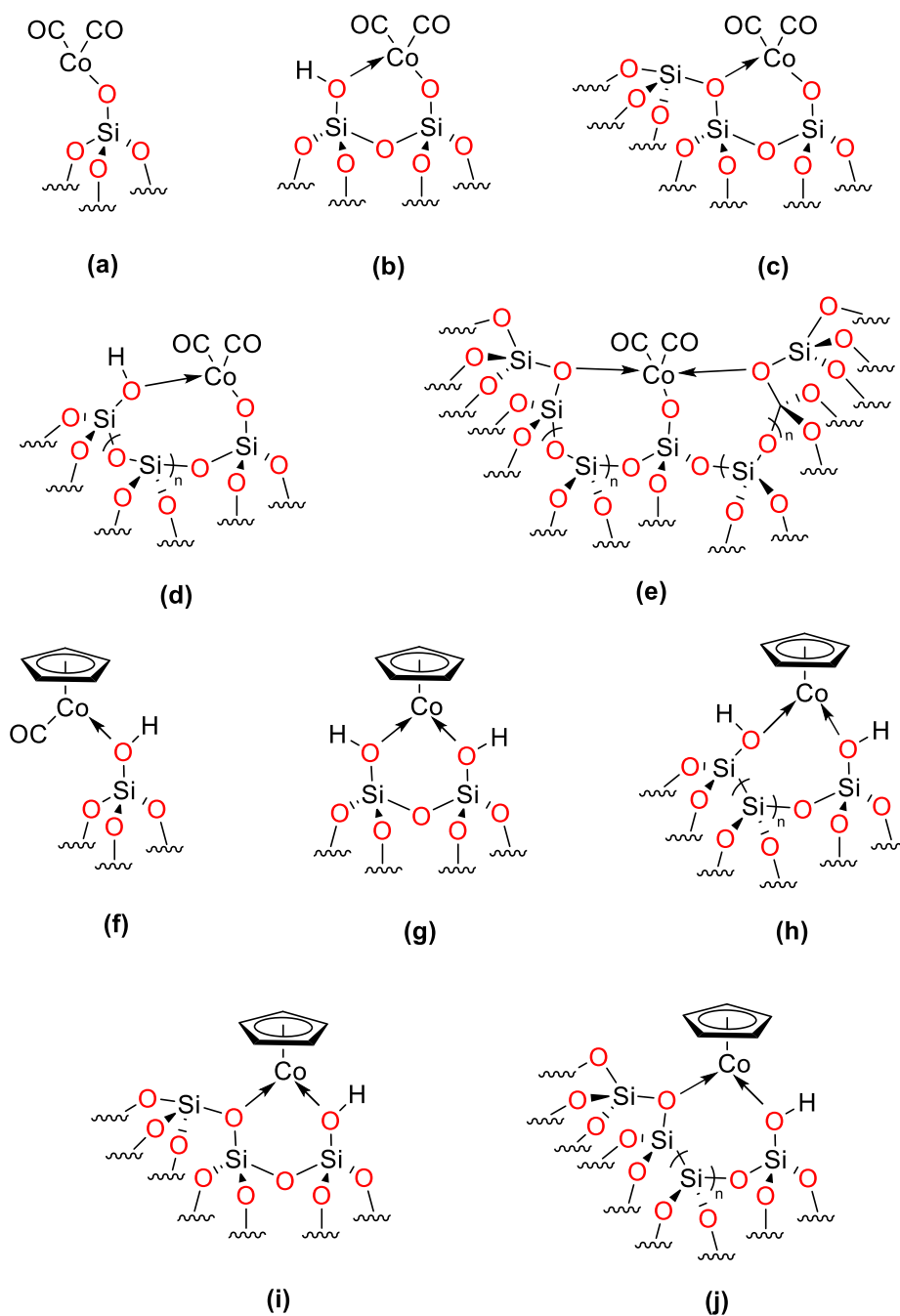


Figure 3.17. Potential surface structures of (5)/A-SiO₂₋₆₀₀, if tethering proceed via the loss of a ligand
 (a)-(e) Possible surface structures if Cp was tethered via the protonation of Cp ring, then subsequent loss
 (f)-(j) Possible surface structures if Co was tethered by displacement of neutral CO ligand(s) of CpH

3.2.3.1 Analysis of (5)/A-SiO₂₋₆₀₀

3.2.3.1.1 Cobalt-loading of (5)/A-SiO₂₋₆₀₀ Determined by ICP-OES

Following the synthesis of (5)/A-SiO₂₋₆₀₀, analysis of the resulting isolated materials was undertaken by ICP-OES (Table 3.11) to determine the cobalt loading on A-SiO₂₋₆₀₀. Due to project time constraints, the Co weight % loading could not be investigated for silicas calcined at different temperatures. The material resulting from reaction of complex 5 with silica shows a similar Co w.t. % loading (2 w.t. %) to that resulting from reaction of complex 2 with same silica under identical conditions (2.3 w.t. %).

Table 3.11. Co metal loading of complex **5** on Aeroperl 300/30 silica calcined at 600 °C, as determined by ICP-OES

Material	OH density (mmol g ⁻¹)	Cobalt (mmol g ⁻¹)	Cobalt w.t. % loading	% of OH groups that reacted with a Co
(5)/A-SiO ₂₋₆₀₀	0.83	0.34	2	40.9

3.2.3.1.2 DE ²⁹Si SS-NMR Spectroscopy of (**5**)/A-SiO₂₋₆₀₀

As with previous complexes (**2-4**) on the surface of silica, SS-NMR spectroscopy was employed in the hope of determining the surface structure of (**5**)/A-SiO₂₋₆₀₀. DE ²⁹Si SS-NMR spectra were taken of (**5**)/A-SiO₂₋₆₀₀, with a 10 s and 300 s delay relaxation times (Figure 3.18), using the same method as used for complexes **3** and **4**. The resulting spectra of (**5**)/A-SiO₂₋₆₀₀ are comparable to those observed for the other tethered cobalt complexes in this project, namely a noisy signal at -109 ppm with a slow relaxation time, indicating that a paramagnetic cobalt is not interacting with the silicon. However, unlike the materials resulting from use of the starting complexes **3** and **4** deposited on silica, the DE ²⁹Si SS-NMR spectrum of (**5**)/A-SiO₂₋₆₀₀ shows a second signal at -22 ppm in the spectrum with a 300 s delay relaxation. The origin of this resonance at -22 ppm is likely to be silicone grease.

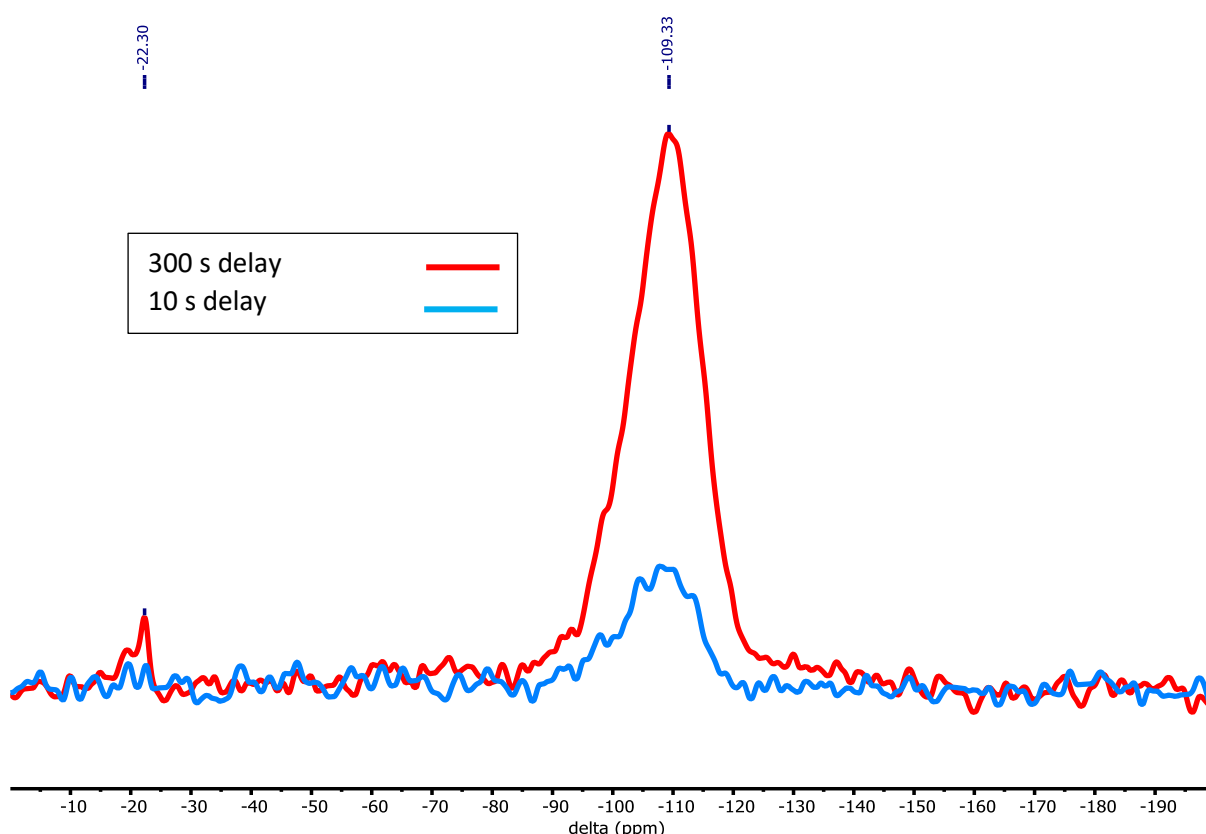


Figure 3.18. DE ²⁹Si SS-NMR spectra of (**5**)/A-SiO₂₋₆₀₀, comparing delay relaxation times to determine whether the present of the cobalt affects the relaxation time of silicon; frequency 79.437 MHz, spin-rate 6 kHz

3.2.3.1.3 Analysis of Loss of CpH ring during the synthesis of (**5**)/A-SiO₂₋₆₀₀

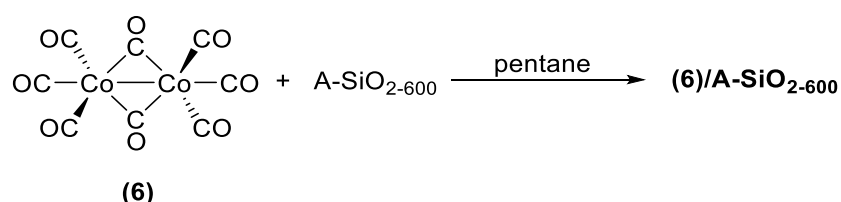
Another method for determining indirectly the surface structure of the product resulting from reaction of complex **5** with A-SiO₂₋₆₀₀ is to analyse the volatile components from the reaction in the

solvent recovered post impregnation by filtration, by GC-MS to identify the presence of released CpH, as described previously in Section 3.2.1.1.2. Following this approach, a mix of CpH and unreacted $\text{CoCp}(\text{CO})_2$ was identified by GC-MS, suggesting that the tethering proceeds *via* the loss of CpH. However, it should be kept in mind that complex **5** is unstable, unreacted $\text{CoCp}(\text{CO})_2$ left in the captured solvent may have degraded (despite significant care having been taken) and released CpH, skewing the results. To counter this potential problem and minimise the effects of unreacted $\text{CoCp}(\text{CO})_2$ decomposing in the captured solvent, the reaction of **5** + SiO_2 was carried out in the dark to avoid decomposition of complex **5** from UV, the reaction solution was isolated quickly after the reaction was finished, and GC analysis was carried out immediately after the reaction solution was isolated.

3.2.4 $\text{Co}_2(\text{CO})_8$ + Aeroperl 300/30 Silica ((**6**)/A-SiO₂₋₆₀₀)

The complex $\text{Co}_2(\text{CO})_8$ (**6**) is often used to form nanoparticles on oxide support surfaces as it decomposes readily into Co^0 through either thermo- or photo-mediated decomposition pathways.⁴ $\text{Co}_2(\text{CO})_8$ does not possess readily protonated or anionic ligands, which has led to the assumption made in this project that $\text{Co}_2(\text{CO})_8$ cannot be tethered to the surface *via* a covalent bond to a hydroxyl group. Since physisorption of $\text{Co}_2(\text{CO})_8$ was assumed, (**6**)/A-SiO₂₋₆₀₀ was not washed with solvent to avoid any loss/displacement of $\text{Co}_2(\text{CO})_8$ from the surface; instead the reaction solvent was cautiously removed under vacuum to leave $\text{Co}_2(\text{CO})_8$ deposited on the surface of silica. It was assumed that the cobalt loading was therefore not significantly controlled by the density of the hydroxyl groups on the surface, but simply by the amount of complex **6** added to the silica.

The material (**6**)/A-SiO₂₋₆₀₀ was subsequently isolated as a pale brown solid (Scheme 3.13). However, on exposure to light or warmth, (**6**)/A-SiO₂₋₆₀₀ darkened noticeably to dark brown over about 15 min. Consequently, (**6**)/A-SiO₂₋₆₀₀ was stored under nitrogen at -20 °C with the Schlenk wrapped in foil to avoid exposure to light.



Scheme 3.13. Synthesis of (**6**)/A-SiO₂₋₆₀₀

3.2.4.1 Analysis of (**6**)/A-SiO₂₋₆₀₀

Complex **6** is air-, temperature-, moisture-, and light-sensitive, and decomposes readily to metallic cobalt. The material resulting from treatment of silica with **6** is equally reactive. Therefore, complex **6**

has great potential for decomposing into nanoparticles. However, this decomposition has proven hard to control. Indeed, by simply allowing **(6)/A-SiO₂₋₆₀₀** to contact with air, the pale brown colour of **(6)/A-SiO₂₋₆₀₀** changes to pale green or pale purple, which has been confirmed to be a result of the formation of nanoparticles on the surface.

3.2.4.1.1 ²⁹Si SS-NMR spectroscopy of **(6)/A-SiO₂₋₆₀₀**

The DE and CP ²⁹Si SS-NMR spectra were obtained for **(6)/A-SiO₂₋₆₀₀** (Figure 3.19). The DE and CP ²⁹Si NMR spectra of **(6)/A-SiO₂₋₆₀₀** are similar to the typical DE and CP spectra of blank **A-SiO₂₋₆₀₀** silica (Section 2.2.3). There is no shift of the peak positions to indicate that the silica is affected by the presence of paramagnetic cobalt, nor a reduction in the intensity of the CP spectrum to indicate a decrease in the silanol density. The presence of paramagnetic cobalt for **(6)/A-SiO₂₋₆₀₀** is unlikely, as the presence of a paramagnetic cobalt is usually evident from the ²⁹Si CP SS-NMR spectra, as was the case for **(2)/A-SiO₂₋₆₀₀** and **(3)/A-SiO₂₋₆₀₀**. For example, **(2)/A-SiO₂₋₆₀₀** gives no signals in its ²⁹Si CP spectrum, while **(3)/A-SiO₂₋₆₀₀** gives a very poorly resolved/noisy ²⁹Si CP SS-NMR spectrum. In contrast, the ²⁹Si CP SS-NMR spectrum of **(6)/A-SiO₂₋₆₀₀** is well-resolved consistent with complex **6** not reacting with the silanols as previously stated by Gürtler *et al.*, but rather the reaction has deposited diamagnetic Co₂(CO)₈ or simply metallic cobalt on the surface.

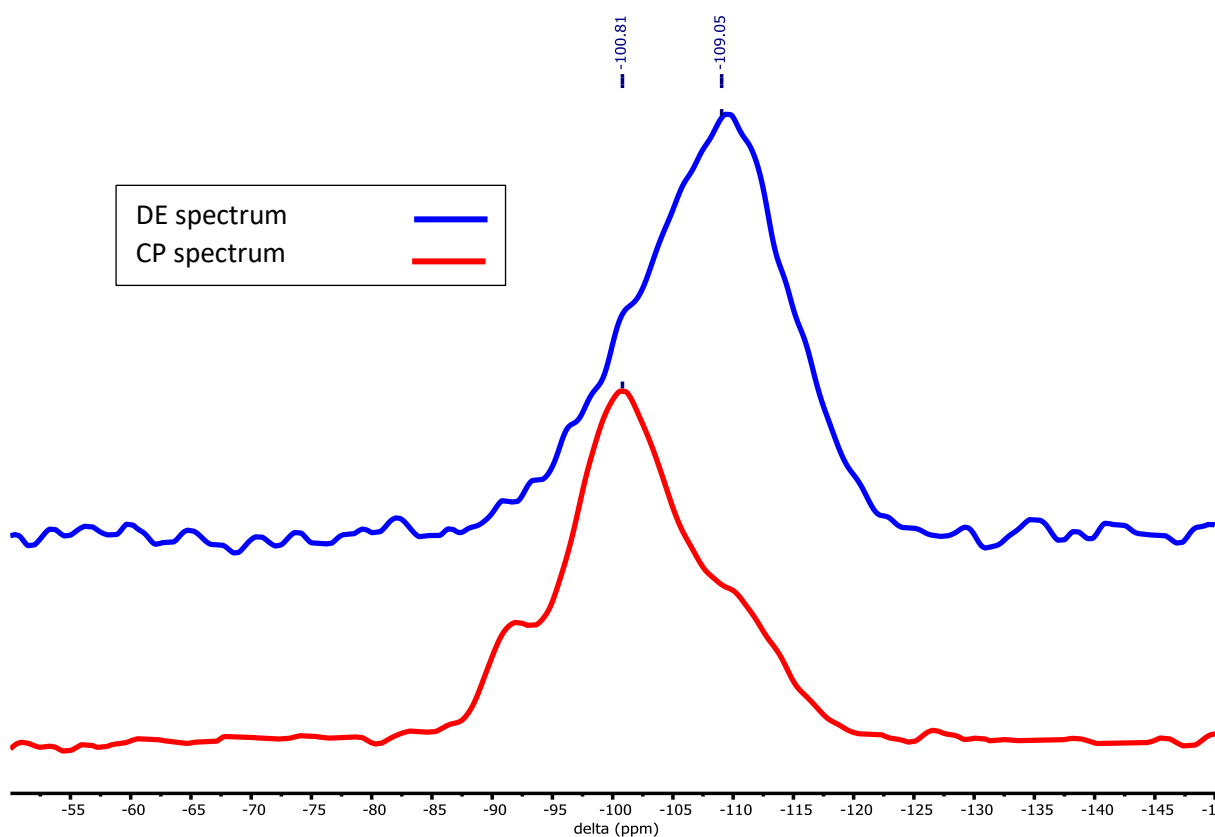


Figure 3.19. DE and CP ²⁹Si spectra of **(6)/A-SiO₂₋₆₀₀**; frequency 79.437 MHz, spin-rate 6 kHz

3.2.4.1.2 Transmission Electron Microscopy (TEM) of (6)/A-SiO₂₋₆₀₀ after exposure to laboratory atmosphere

As described in Section 3.2.4.1, after contact with air, the pale brown colour of (6)/A-SiO₂₋₆₀₀ changes to pale purple. This colour change of brown to purple is proposed to correspond to the formation of nanoparticles on the oxide surface. The presence of nanoparticles was indeed confirmed by Transmission Electron Microscopy (TEM), which showed the presence of nanoparticles with a size range of 3 - 7 nm, on the surface of silica (Figure 3.20), but with non-uniform spread across the silica surface. This non-uniform distribution is likely due to lack of control over the formation of the nanoparticles; the nanoparticles were formed spontaneously by exposure to normal laboratory atmosphere. As discussed in Section 1.1.1.4, it is the aim of this project to use a controlled reduction (e.g. – heating under hydrogen) of the nanoparticle precursor to product cobalt particles smaller than 1 nm. Therefore, such a lack of control over the formation of the nanoparticles is undesirable in this project.

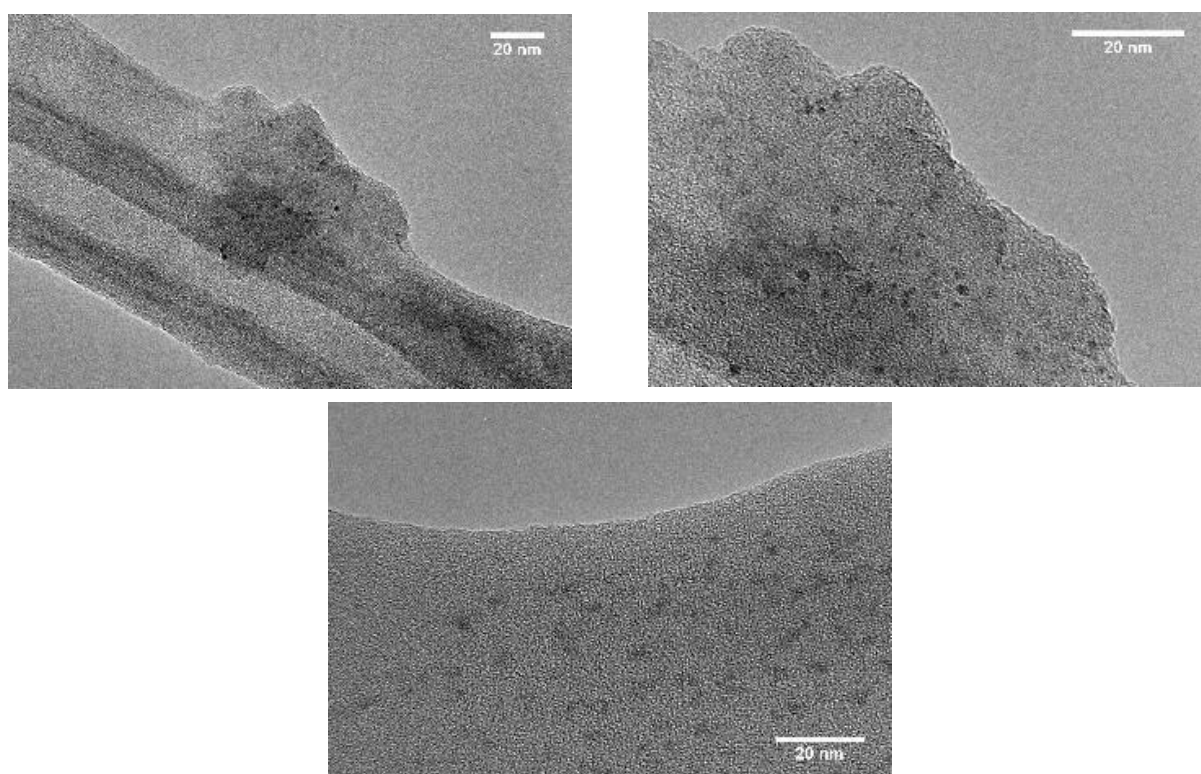


Figure 3.20. TEM images of nanoparticles formed on the surface of (6)/A-SiO₂₋₆₀₀
Average nanoparticle size = 4.4 nm

3.2.4.1.3 Powder X-Ray Diffraction (PXRD) of the nanoparticles on the surface of air-exposed (6)/A-SiO₂₋₆₀₀

Powder X-Ray Diffraction (PXRD) analysis (Mo source) was performed on the cobalt nanoparticles derived from (6)/A-SiO₂₋₆₀₀ through exposure to air; the resulting data is in Figure 3.21. This diffraction analysis was done with the view to demonstrating that PXRD can be used to identify the size of

nanoparticles produced. Here it is assumed that the Scherrer formula is always valid, and that the reflection width is inversely proportional to particle size, with larger clusters of cobalt giving sharper reflections as there is more material mediating diffraction.²³

Since the aim of the project is to prepare sub-nanosized particles, any sharp reflections in the PXRD analysis could possibly indicate the formation of undesirable larger cobalt particles. Notably, the PXRD analysis of the nanoparticles formed from exposing **(6)/A-SiO₂₋₆₀₀** to normal atmosphere showed one large very broad reflection at $2\theta = 11^\circ$, which is associated with the amorphous structure of Aeroperl 300/30 silica.^{24, 25} A smaller, sharper reflection is also seen at $2\theta = 18^\circ$, and another possible reflection at $2\theta = 21^\circ$, though this latter reflection at 21° is small enough that it could be regarded as part of the noise rather than a true reflection. While the reflections at 18° and 21° are at values of 2θ consistent with the presence of cobalt (*e.g.* as Co metal {f.c.c.²⁶ and hcp²⁷}, CoO^{28, 29} and Co₃O₄³⁰), they do not correspond well with any reflections reported in literature, including with any known cobalt carbonyl species such as Co₂(CO)₈³¹ or Co₄(CO)₁₂.³² The origin of these reflections is currently unknown, though the two reflections ($2\theta = 18^\circ$ and 21°) have the same spacing as f.c.c. cobalt metal (20° and 23°) suggesting a possible systematic shift of 2° . This shift may be due to the sample being badly positioned during the PXRD analysis, which is likely caused by issues with the sample holder.

With the data from PXRD showing the presence of metallic cobalt particles, and the analysis of the TEM images of **(6)/A-SiO₂₋₆₀₀** giving the sizes of the particles (3 – 7 nm), it was concluded that complex **6** would not be a suitable nanoparticle precursor for this project. While Co₂(CO)₈ did successfully form nanoparticles, there was no control over their formation or resulting size due to their spontaneous formation when **(6)/A-SiO₂₋₆₀₀** was exposed to air. The size of the resulting nanoparticles is also larger than the target particle size for this project, (<1 nm), which is undesirable for this project.

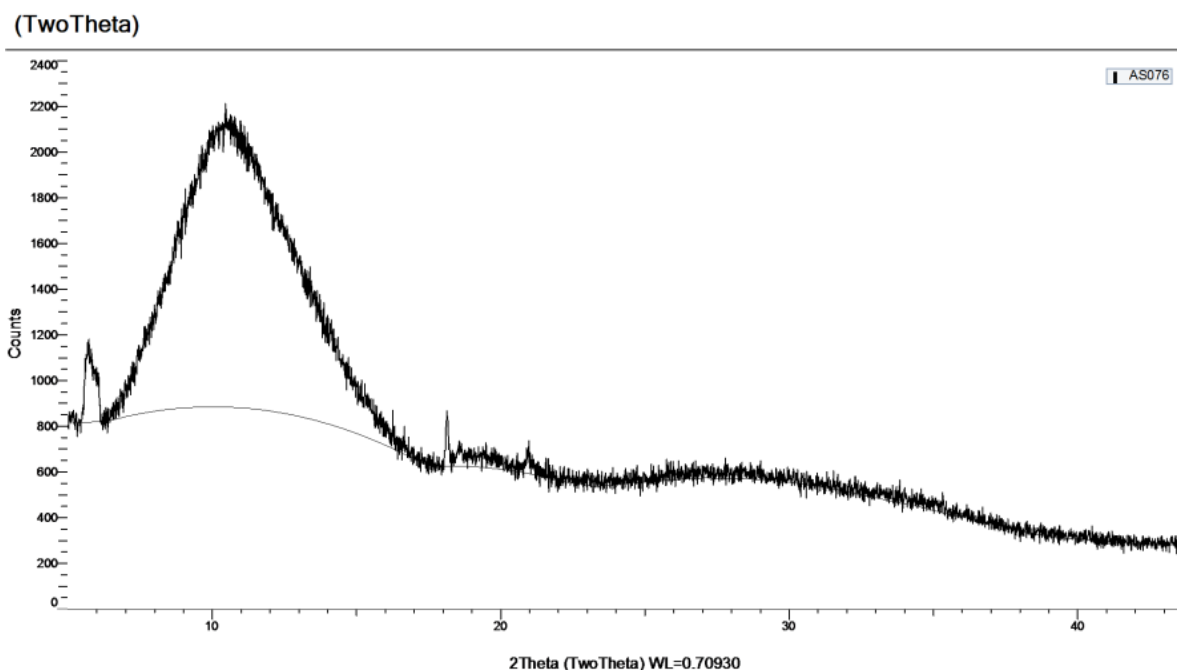
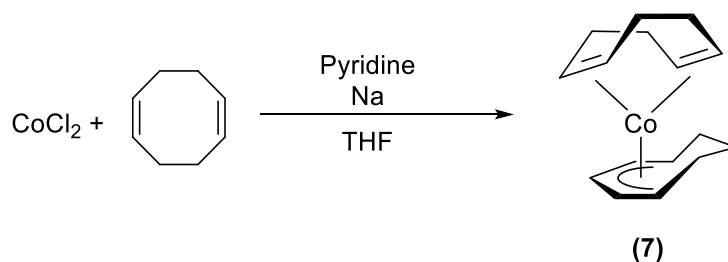


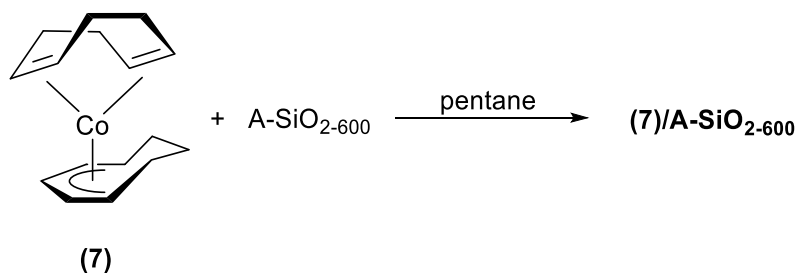
Figure 3.21. PXRD spectrum of **(6)**/**A-SiO₂₋₆₀₀** after nanoparticles had formed from exposure of the as-prepared sample to air

3.2.5 Co(C₈H₁₂)(C₈H₁₃) + Aeroperl 300/30 Silica (**(7)**/**A-SiO₂₋₆₀₀**)

The complex Co(C₈H₁₂)(C₈H₁₃) (**(7)**) was chosen as a possible organometallic precursor to silica-supported cobalt nanoparticles since it contains the 1,5-cyclooctadiene (COD) ligand and a partially hydrogenated COD motif, bound in an η^3 allyl-like fashion. COD is a highly labile ligand with no heteroatoms, which can be removed from the reaction mixture *in vacuo* or by washing with solvent and that cannot react with surface silanol groups. Additionally, complex **(7)** is a reasonably easy to access, but very reactive, starting material. Complex **(7)** was prepared as described in the literature (Scheme 3.14).^{33, 34} Subsequently, **A-SiO₂₋₆₀₀** silica was treated with this complex according to Scheme 3 with a view to synthesising **(7)**/**A-SiO₂₋₆₀₀** as illustrated in Scheme 3.15 through loss of either COD or the hydrogenated COD motif, affording a Co^{II} species, respectively, shown in Figure 3.22. The material resulting from this process, **(7)**/**A-SiO₂₋₆₀₀**, was initially isolated as a dark purple solid, but over time this changes colour to black, despite storage in a nitrogen-filled glovebox; this may suggest some instability of **(7)**/**A-SiO₂₋₆₀₀**.



Scheme 3.14. Synthesis of complex **(7)**



Scheme 3.15. Synthesis of (7)/A-SiO₂₋₆₀₀

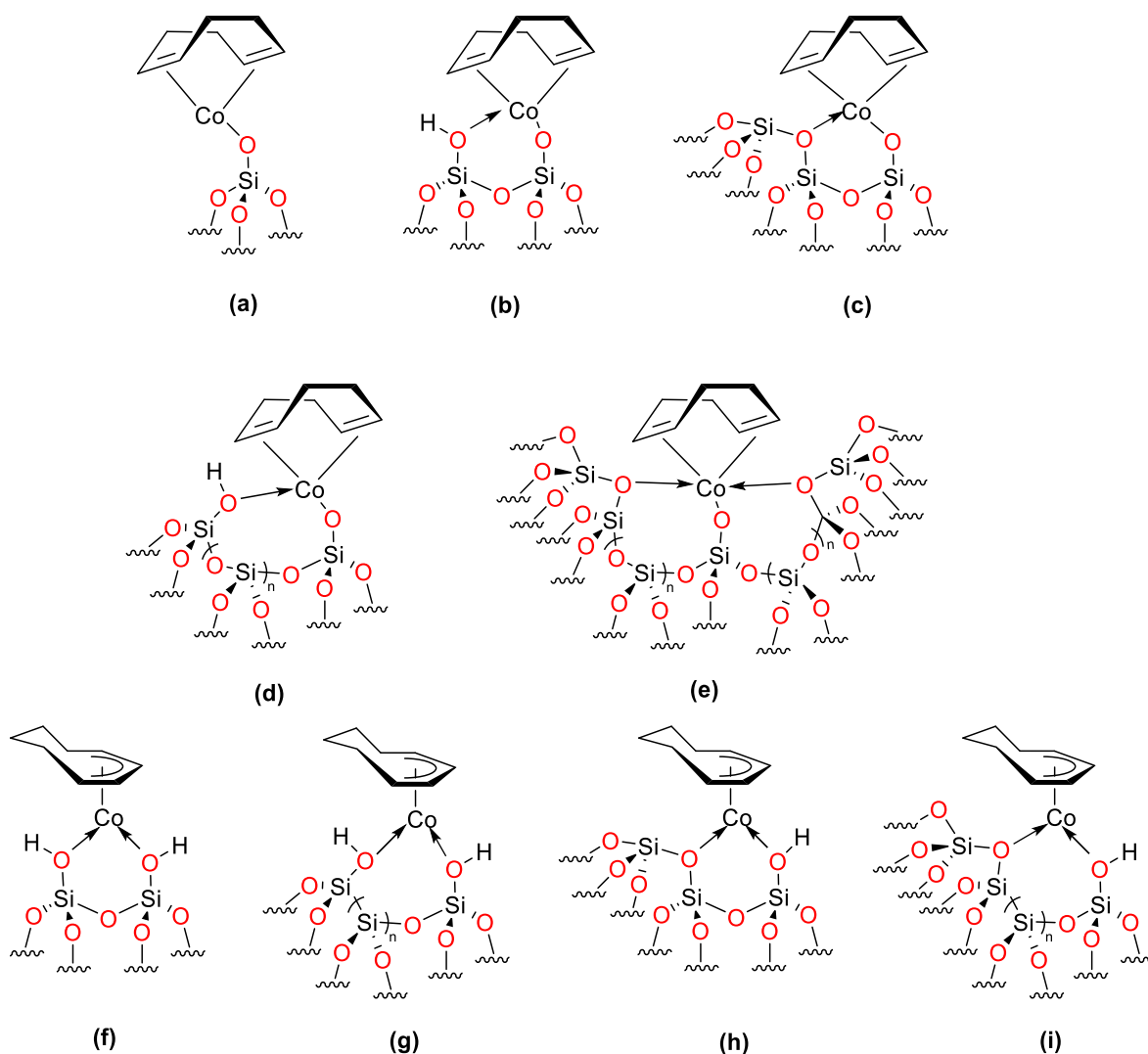


Figure 3.22. Possible surface structures of (7)/A-SiO₂₋₆₀₀, if tethering proceed via the loss of a ligand
 (a)-(e) Possible surface structures if Co was tethered by protonation of C₈H₁₃, then subsequent loss of C₈H₁₄
 (f)-(i) Possible surface structures if Co was tethered via displacement of labile COD ligand

3.2.5.1 Analysis of (7)/A-SiO₂₋₆₀₀

3.2.5.1.1 Cobalt-loading of (7)/A-SiO₂₋₆₀₀ Determined by ICP-OES

The cobalt loading of the material resulting from the treatment of A-SiO₂₋₆₀₀ with complex 7 (approximate diameter = 9 Å^{††}) was determined by ICP-OES (Table 3.12). The cobalt loading of this new material (7)/A-SiO₂₋₆₀₀ is lower than that determined for complex 2 and 5 on Aeroperl 300/30

^{††} Diameter of molecule was approximated according to Section 6.0.2.11

silica and higher than **(4)/A-SiO₂₋₆₀₀**. Complex **7** is less bulky than complex **4** (16 Å) and complex **2** (12 Å), and therefore it is expected that **(7)/A-SiO₂₋₆₀₀** would have a higher loading than both **(4)/A-SiO₂₋₆₀₀** and **(2)/A-SiO₂₋₆₀₀**, yet the loading of **(7)/A-SiO₂₋₆₀₀** is lower than **(2)/A-SiO₂₋₆₀₀** and higher than **(4)/A-SiO₂₋₆₀₀**. It was concluded that a factor other than ligand bulk was responsible for the relative cobalt loading of **(7)/A-SiO₂₋₆₀₀** compared to **(2)/A-SiO₂₋₆₀₀**.

Table 3.12. Co metal loading of complex **7** on Aeroperl 300/30 silica calcined at 600 °C, as determined by ICP-OES

Material	OH density (mmol g ⁻¹)	Cobalt (mmol g ⁻¹)	Cobalt w.t. % loading	% of OH groups that reacted with a Co
(7)/A-SiO₂₋₆₀₀	0.83	0.27	1.6	33

3.2.5.1.2 Analysis of Loss of the Ligand during the synthesis of **(7)/A-SiO₂₋₆₀₀**

As the tethering of complex **7** to the silica surface can proceed through either the loss of the C₈H₁₃ ligand or the COD ligand, to determine which ligand is displaced, analysis of the reaction solution (reaction of **7** with **A-SiO₂₋₆₀₀** in pentane) was undertaken. The reaction solution, obtained through the method described in Section 6.0.2.5, was analysed by GC-MS, which confirmed the presence of both COD and C₈H₁₄. Consequently, no conclusions can be drawn from this approach as to the mode of immobilisation of complex **7** following its reaction with **A-SiO₂₋₆₀₀**.

3.2.5.1.3 DE ²⁹Si SS-NMR Spectroscopy of **(7)/A-SiO₂₋₆₀₀**

Similar to previous complexes tethered onto silica that have been discussed in this chapter, DE ²⁹Si SS-NMR spectra were obtained of the **(7)/A-SiO₂₋₆₀₀** material, with both a 10 s and 300 s delay relaxation times (Figure 3.23). Each of these spectra of **(7)/A-SiO₂₋₆₀₀** shows a noisy resonance at -109 ppm and slow relaxation, which is a typical DE SS-NMR spectrum of the cobalt complexes tethered to silica in this project. Similar to the spectroscopic data obtained for previous materials, **(3)/A-SiO₂₋₆₀₀**, **(4)/A-SiO₂₋₆₀₀**, and **(5)/A-SiO₂₋₆₀₀**, there no change in the chemical shift of the signals in the spectrum was observed relative to the spectrum of **A-SiO₂₋₆₀₀** indicating the presence of a paramagnetic cobalt centre in **(7)/A-SiO₂₋₆₀₀**. Unfortunately, no further conclusions about the surface structure of **(7)/A-SiO₂₋₆₀₀** could be obtained through SS-NMR spectroscopy, and further study with more techniques into **(7)/A-SiO₂₋₆₀₀** would be needed.

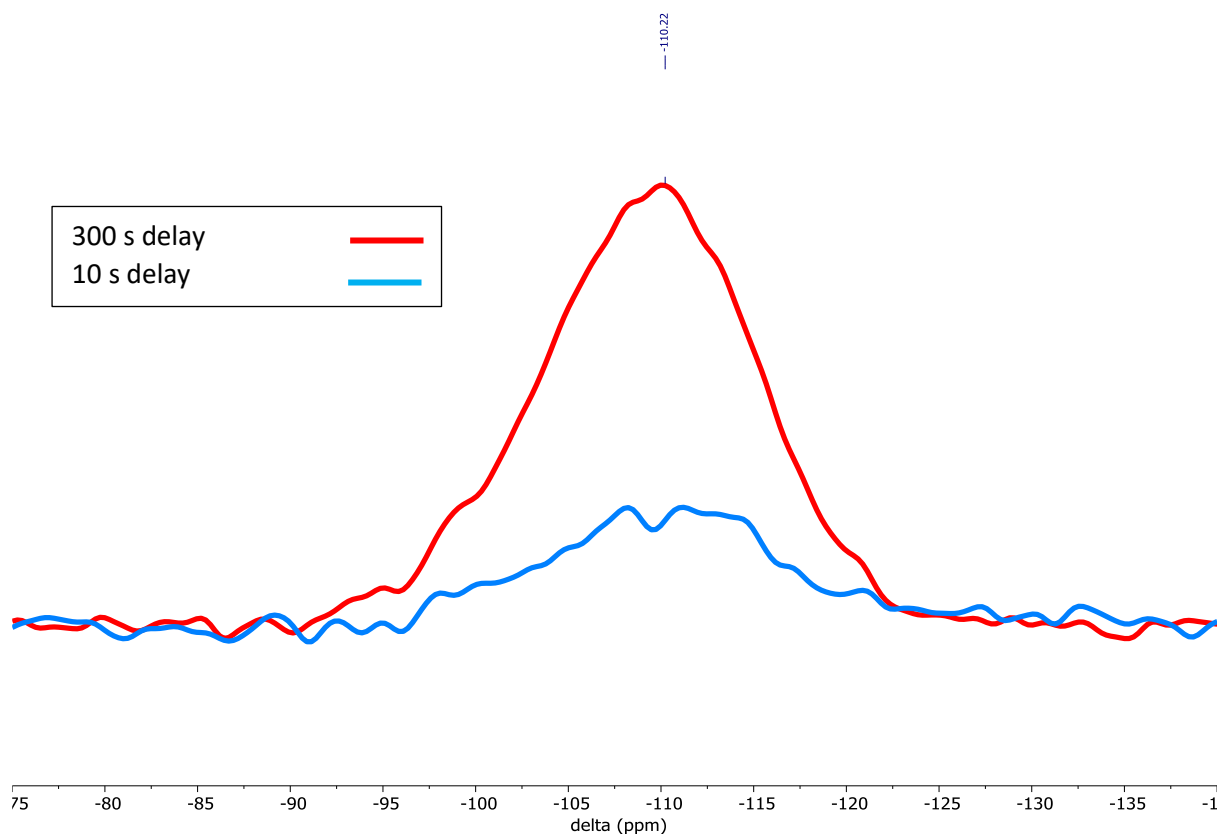
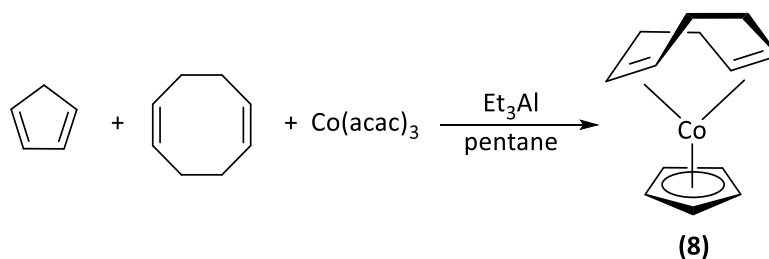


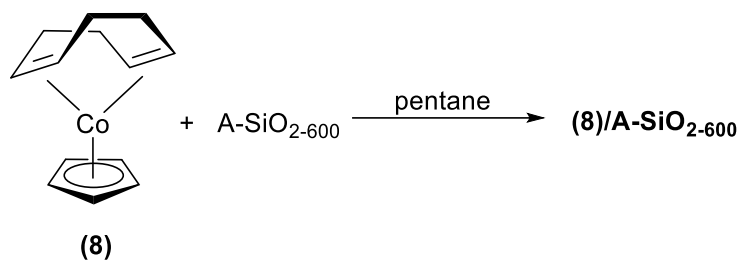
Figure 3.23. DE ^{29}Si SS-NMR spectra of **(7)**/ A-SiO_{2-600} , comparing delay relaxation times to determine whether the presence of the cobalt affects the relaxation time of silicon, Frequency 79.437 MHz, Spin-rate 6 kHz

3.2.6 CoCpCOD + Aeroperl 300/30 Silica (**(8)**/ A-SiO_{2-600})

The complex CoCpCOD (**8**) is another attractive cobalt-containing precursor, offering both a neutral and anionic ligand for reaction with partially dehydroxylated silica. Complex **8** provides an interesting comparison to complexes **3** and **7** since it could potentially be tethered to the surface through displacement of its neutral ligand or by protonation of the Cp ring and loss of CpH, as for complex **3**. Its synthesis is shown in Scheme 3.16.³⁵ **(8)**/ A-SiO_{2-600} was synthesised by the addition of complex **8** to SiO_{2-600} as a slurry in pentane to produce a pale brown solid after work-up (Scheme 3.17). Following its isolation through filtration, it is notable, that the resultant material **(8)**/ A-SiO_{2-600} does not change colour when exposed to normal laboratory atmosphere. Several possible structures on the surface of **(8)**/ A-SiO_{2-600} are shown in Figure 3.24.



Scheme 3.16. Synthesis of complex **8**



Scheme 3.17. Synthesis of (8)/A-SiO₂₋₆₀₀

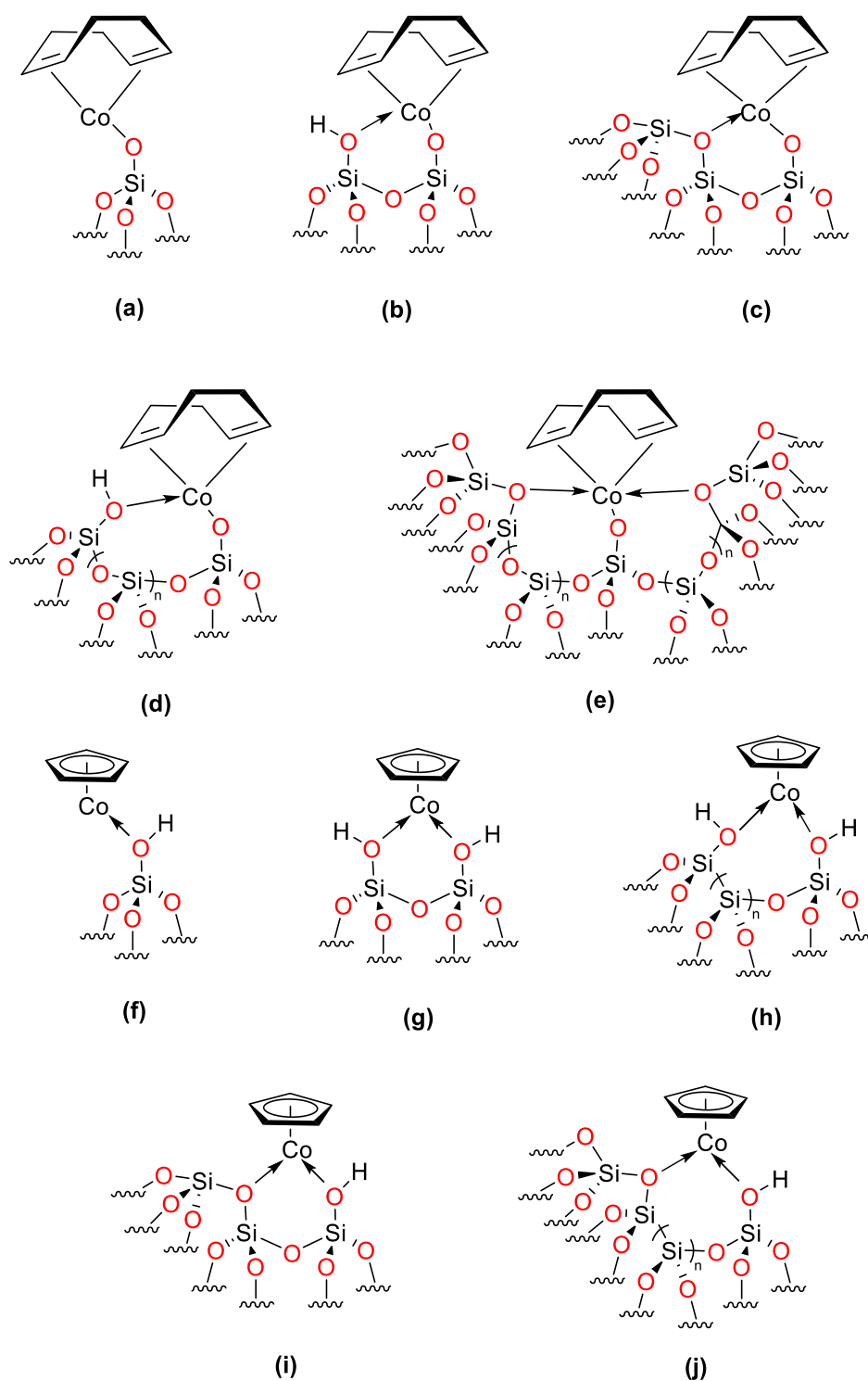


Figure 3.24. Possible surface structures of **(8)/A-SiO₂₋₆₀₀**, if tethering proceed via the loss of a ligand
 (a)-(e) Possible surface structure if Co was tethered via protonation of Cp ring, then subsequent loss of CpH
 (f)-(j) Possible surface structure if Co was tethered by displacement of labile COD ligand

3.2.6.1 Analysis of **(8)/A-SiO₂₋₆₀₀**

3.2.6.1.1 Cobalt-loading of **(8)/A-SiO₂₋₆₀₀** Determined by ICP-OES

The percentage weight loading of cobalt in the mater **(8)/A-SiO₂₋₆₀₀** was investigated by ICP-OES (Table 3.13). Despite targeting a cobalt loading of 2 w.t. %, the synthetic strategy employed for its preparation resulted in the formation of a material with a Co loading of only 0.2 w.t. % on Aeroperl

300/30 silica calcined at 600 °C, which is the lowest cobalt loading achieved using any of the complexes studied in this project. The low loading of cobalt on **(8)/A-SiO₂₋₆₀₀** suggests that complex **8** does not react easily with the surface silanol groups, as only 4.1% of all silanols of **A-SiO₂₋₆₀₀** reacted with complex **8** over a period of 3 hours at RT. It is possible that longer reaction times may increase this cobalt loading, however due to time constraints this experiment was not undertaken. Due to the very low cobalt loading achieved with complex **8**, no further analyses were undertaken.

Table 3.13. Co metal loading of complex **8** on Aeroperl 300/30 silica calcined at 600 °C, as determined by ICP-OES

Material	OH density (mmol g ⁻¹)	Cobalt (mmol g ⁻¹)	Cobalt w.t. % loading	% of OH groups that reacted with a Co
(8)/A-SiO₂₋₆₀₀	0.83	0.03	0.2	4.1

3.2.7 Conclusions for Cobalt Precursors for the Formation of Silica-immobilised Cobalt Nanoparticles

Of the cobalt complexes **3** – **8** investigated, complexes **3** and **4** both show promise as precursors for the controlled formation of nanoparticles immobilised on appropriately calcined silica. Both precursors can be impregnated onto the silica surface, and form highly unstable/reactive materials, **(3)/A-SiO₂** and **(4)/SiO₂**, that will be likely be easily reduced to nanoparticles.

The product resulting from treatment of silica with Cp₂Co (**3**) is difficult to characterise, and this project did not reach any conclusive answer to what the surface structure of **(3)/A-SiO₂₋₆₀₀** might be. Consequently, there remains questions as to the exact nature of the species present on the surface of silica following immobilisation, namely whether it is tethered to the surface as a CoCp–O–Si species, or physisorbed to the silica surface as CoCp₂. Furthermore, to date, the synthetic approach used gives little control over the metal loading of complex **3** on Aeroperl 300/30 silica, as the cobalt metal loading does not correlate with the silanol density of the prepared and calcined silicas. Work around the silica immobilisation of complex **4** shows an interesting start to a study into the effect of ligand bulk on the dispersion of cobalt on silica and how future nanoparticles may be affected. It was predicted that complex **4** would show a lower cobalt loading on silica due to being unable to access deeper into the narrower pores of the silica, which can be tentatively observed through ICP-OES when compared to complex **2** tethered to silica. It is thought that this lower cobalt loading may lead to smaller nanoparticles in the future.

The immobilisation of complexes **5**, **7**, and **8** require further study into their suitability as precursors to silica-immobilised cobalt nanoparticles. Complex **5** has two different types of ligand (a neutral L ligand [CO], and a X ligand [Cp]) that could be lost during the attempted tethering to a silica surface.

Complex **7** is of interest as it contains a COD ligand and a partially hydrogenated COD motif, which are both highly labile ligands that could facilitate tethering to the silica surface and the formation of nanoparticles. Complex **8** offers both a neutral and anionic ligand that could be lost during tethering to the silica surface. However, complexes **5**, **7**, and **8** have similar issues to complex **3**, as it is hard to determine how they are tethered to the silica surface. Future work into complexes **5**, **7**, and **8** would offer an interesting look into how the choice of precursor may affect tethering and nanoparticle formation

Work in this thesis has identified complex **6** as being an unsuitable cobalt-containing precursor for this project. While complex **6** can easily form nanoparticles on the surface of silica, there is no way to control the metal loading and dispersion of cobalt as complex **6** does not react with the silica silanols. **(6)/A-SiO₂** is also too reactive and spontaneously forms nanoparticles on its surface with no control over the resulting size of the nanoparticles.

The complex [Co(NTMS)₂](THF) shows the most promise in this project as a readily accessible and reproducible reagent for the preparation, but if given more time, there would be an interest in further studying some of these complexes as potential precursors. The next chapter will explore the reducibility of complexes **2** and **3**, and the formation of the corresponding cobalt-containing nanoparticles.

3.3 References

1. D. W. Sindorf and G. E. Maciel, *J. Phys. Chem.*, 1982, **86**, 5208-5219.
2. G. J. Young, *Colloid Sci.*, 1958, **13**, 67-85.
3. Gurtler, W. Miethe, H. Seidel and A. Saus, *J. prakt. Chem*, 1993, **355**, 47-54.
4. R. Tannenbaum, *Inorganica Chim. Acta*, 1994, **227**, 233-240.
5. C. Copéret, A. Comas-Vives, M. P. Conley, D. P. Estes, A. Fedorov, V. Mougel, H. Nagae, F. Núñez-Zarur and P. A. Zhizhko, *Chem. Rev.*, 2016, **116**, 324-421.
6. E. Oakton, G. Vilé, D. S. Levine, E. Zocher, D. Baudouin, J. Pérez-Ramírez and C. Copéret, *Dalton Trans.*, 2014, **43**, 15138-15142.
7. Y. Liang, E. S. Erichsen and R. Anwender, *Microporous Mesoporous Mater.*, 2014, **190**, 316-323.
8. D. C. Bradley, R. G. Copperthwaite, M. W. Extine, W. W. Reichert and M. H. Chisholm, in *Inorg. Synth.*, ed. B. E. Douglas, Hoboken, New Jersey, 2007, vol. Volume XVIII, pp. 112 - 119.

9. W. Kolodziejski and J. Klinowski, *Chem. Rev.*, 2002, **102**, 613 - 628.
10. H. S. Ahn, J. Yanoc and T. D. Tilley, *Energy Environ. Sci.*, 2013, **6**, 3080-3087.
11. Y. Liang, E. S. Erichsen and R. Anwender, *Dalton Trans.*, 2013, **42**, 6922-6935.
12. F. Uhlig and H. C. Marsmann, *29 Si NMR Some Practical Aspects*, Eigenverlag, Silicon Compounds: Silanes & Silicones edn., 2003.
13. B. B. Wayland and W. L. Rice, *Inorg. Chem.*, 1967, **6**, 2270-2273.
14. T. Deschner, K. W. Tornroos and R. Anwender, *Inorg. Chem.*, 2011, **50**, 7217-7228.
15. Q. Zheng, D. Wang, F. Yuan, Q. Han, Y. Dong and Y. Liu, *Catalysis Letters*, 2016, **146**, 1535 - 1543.
16. T. Lindblad and B. Rebenstorf, *J. Chem. Soc. Faraday Trans.*, 1991, **87**, 2473-2478.
17. A. M. Saib, D. J. Moodley, I. M. Ciobîc, M. M. Hauman, B. H. Sigwebel, C. J. Weststrate, J. W. Niemantsverdriet and J. v. d. Loosdrecht, *Catalysis Today*, 2010, **154**, 271-282.
18. M. J. Lamb, D. C. Apperley, M. J. Watson and P. W. Dyer, *Top. Catal.*, 2018, **61**, 213-224.
19. I. H. Kwak, H. G. Abbas, I. S. Kwon, Y. C. Park, J. Seo, M. K. Cho, J.-P. Ahn, H. W. Seo, J. Park and H. S. Kang, *J. Mater. Chem. A*, 2019, **7**, 8101-8106.
20. D. L. Kays and A. R. Cowley, *Chem. Commun.*, 2007, 1053-1055.
21. C. Roukoss, J.-M. Basset, C. Coperet, C. Lucas and E. Kuntz, *C. R. Chimie*, 2008, **11**, 620 - 627.
22. T. S. Piper, F. A. Coyron and G. Wilkinson, *J. Inorganic and Nuclear Chemistry*, 1955, **1**, 165-174.
23. P. Scardi, *Z. Kristallogr. Suppl.*, 2008, **27**, 101-111.
24. S. Musić, N. Filipović-Vinceković and L. Sekovanić, *Braz. J. Chem. Eng.*, 2011, **28**, 88-94.
25. J.-B. Park, C. Park, Z. Z. Piao, H. H. Amin, N. M. Meghani, P. H. L. Tran, T. T. D. Tran, J.-H. Cui, Q.-R. Cao, E. Oh and B.-J. Lee, *J. Drug Deliv. Sci. Technol.*, 2018, **46**, 365-377.
26. L. Romaka, V. V. Romaka, N. Melnychenko, Y. Stadnyk, L. Bohun and A. Horyn, *J. Alloys Compd.*, 2018, **739**, 771-779.
27. A. V. Morozkin, *Intermetallics*, 2012, **25**, 136-138.

28. J.-F. Liu, S. Yin, H.-P. Wu, Y. W. Zeng, X. R. Hu, Y. W. Wang, G. L. Lv and J.-Z. Jiang, *J. Phys. Chem. B*, 2006, **110**, 21588-21592.
29. H. N. Ok and J. G. Mullen, *Phys. Rev.*, 1968, **168**, 550-567.
30. W. L. Roth, *J. Phys. Chem. Solids*, 1964, **25**, 1-10.
31. G. G. Sumner and H. P. Klug, *Acta. Crys.*, 1964, **17**, 732-742.
32. C. H. Wei, *Inorg. Chem.*, 1969, **8**, 2384-2397.
33. D. Zitoun, C. Amiens and B. Chaudret, *J. Phys. Chem. B*, 2003, **107**, 6997-7005.
34. T. O. Ely, C. Pan, C. Amiens and B. Chaudret, *J. Phys. Chem. B*, 2000, **104**, 695-702.
35. H. Bönemann, W. Brijoux, R. Brinkmann, W. Meurers, R. Mynott, W. V. Philipsborn and T. Egolf, *J. Organomet. Chem.*, 1984, **272**, 231-249.

Chapter 4: Reduction of Silica-Grafted Organometallic Cobalt Species

4.0 Introduction to the Reduction of Cobalt Precursors on the Surface of (2)/A-SiO₂₋₆₀₀ and (3)/A-SiO₂₋₆₀₀

In Chapter 3, an exploration of the tethering of potential molecular cobalt nanoparticle precursors to the surface of calcined Aeroperl 300/30 silica was described. This current chapter will summarise attempts to reduce the silica-tethered precursors to nanoparticles *via* reduction under a flow of hydrogen. The overarching aim is to prepare small cobalt nanoparticles, hence the anticipated need for good site isolation of the molecular precursors on the silica surface since it is proposed in this project that, following reduction, the resulting cobalt atoms will be able to traverse the surface to agglomerate with other metal sites, forming very small nanoparticles as a result of the low surface density.

As indicated previously in Chapter 3, the **(2)/A-SiO₂₋₆₀₀** material showed the most promise for the potential production of the target small nanoparticles (Figure 4.1). Although the material **(2)/A-SiO₂₋₆₀₀** is highly reactive and air- and moisture-sensitive, which makes it hard to handle, it does suggest that it may be readily transformed into the target nanoparticles. Indeed, an analogous coinage metal silyl amide (*e.g.* [Ag(N(TMS)₂)₂]₄) has previously been reported in the literature to form small size-controlled nanoparticles on silica.¹ Importantly, this **(2)/A-SiO₂₋₆₀₀** material can be prepared with consistent/repeatable cobalt loading onto silica (2.3±0.1 w.t. % Co) and hence will be the main focus of this chapter.

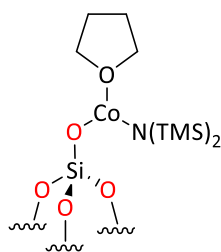


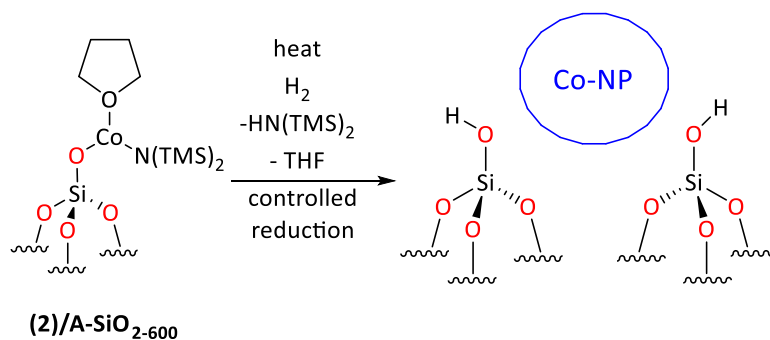
Figure 4.1. Proposed surface structure of **(2)/A-SiO₂₋₆₀₀**

In addition, the material formed from reaction of Cp₂Co (**3**) with Aeroperl 300/30, **(3)/A-SiO₂₋₆₀₀**, will also be discussed here. Although the **(3)/A-SiO₂₋₆₀₀** material is less well characterised than the **(2)/A-SiO₂₋₆₀₀** material, its high reactivity suggests again it as an amenable target for investigation for transformation to a supported nanoparticulate system.

From here-on, the following nomenclature will be used to describe the materials in this chapter: “(cobalt complex)/support (*treatment conditions*: temperature, gas)”. For example, **(2)/A-SiO₂₋₆₀₀** reduced at 200 °C under H₂ gas is described as **(2)/A-SiO₂₋₆₀₀ (200 °C, H₂)**. Some materials were exposed to air prior to the reduction treatment; this is indicated in information in the brackets before the treatment conditions, for example, **(2)/A-SiO₂₋₆₀₀ (air-exposed, 200 °C, H₂)**.

4.1 The Reduction of (2)/A-SiO₂₋₆₀₀

Building on prior literature reports,¹ it is anticipated that the reaction of (2)/A-SiO₂₋₆₀₀ with a reducing gas, e.g. H₂, will lead to the formation of small nanoparticles on the surface of silica (Scheme 4.1). By keeping the temperature of reduction low, sintering will be reduced, and the nanoparticles will remain small. The low loading and low surface density of the Co in (2)/A-SiO₂₋₆₀₀ and the low temperature of reduction will help control the size of the resulting nanoparticles, ideally keeping them small.



Scheme 4.1. The proposed decomposition of (2)/A-SiO₂₋₆₀₀ into cobalt nanoparticles

Before nanoparticle formation was attempted in this project, an assessment of the reduction temperature of (2)/A-SiO₂₋₆₀₀ was first undertaken. It is expected that to produce the smallest nanoparticles, the reduction of the immobilised complex must be carried out at the lowest possible temperature to minimise metal aggregation and the resulting formation of larger nanoparticles. Hence, here, Temperature Programmed Reduction (TPR) was used to determine the temperature of the onset of reduction of (2)/A-SiO₂₋₆₀₀.

4.1.1 Determining the Reduction Temperature of (2)/A-SiO₂₋₆₀₀ using Temperature Programmed Reduction

TPR allows determination of the temperature at which reduction occurs. By heating a sample of material for consideration under a constant flow of H₂/N₂ (here 10:40 ml min⁻¹) and raising the temperature at a steady rate, the temperature of reduction of the sample can be deduced from the mass of hydrogen consumed at a specific temperature. In the experiments undertaken herein, the H₂/N₂ flow was kept constant, regulated by a mass flow controller and the volume of hydrogen at the reactor outlet monitored by a Thermal Conductivity Detector (TCD). When reduction occurs, hydrogen is consumed and a decrease in the hydrogen concentration at the detector is recorded.

The TPR set-up used in this project is described in Figure 4.2, and the experimental method employed is described in detail in Section 6.0.2.8. The sample of interest is centred in the furnace between two quartz wool plugs, to ensure even heating across the entire sample. A CaCl₂ drying column is used to

catch any condensed water or ammonia that may be released from the silica surface at higher temperatures. HMDS and THF will also be released from the surface-bound complex **2** and will also be detected by the TCD. A portion of the released HMDS will go on to react with surface silanols, similar to the silylation of the silica, described in Section 3.1.2.5 (Scheme 4.2).

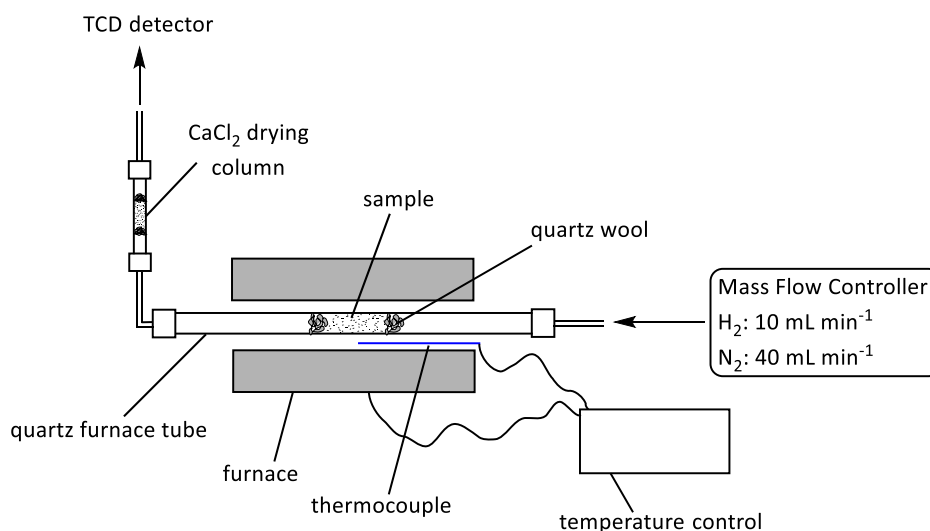
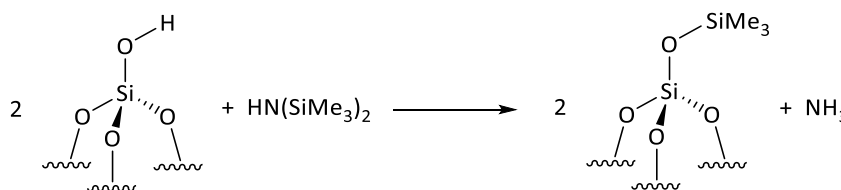


Figure 4.2. The general set up for TPR analysis



Scheme 4.2. The silylation of the silica surface by the reaction of SiOH and HN(SiMe₃)₂

For all manipulations of **(2)/A-SiO₂₋₆₀₀**, especially during the transfer of this material from the glovebox to the TPR set-up, significant care was taken as it is extremely air-sensitive. The material **(2)/A-SiO₂₋₆₀₀** rapidly changes colour from green to blue when exposed to air (Figure 4.3).

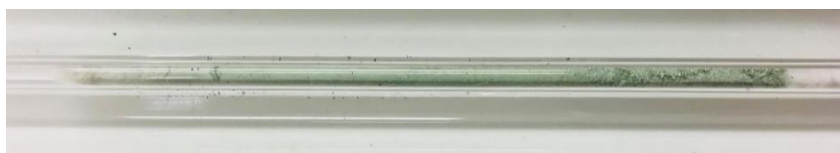


Figure 4.3. A quartz tube loaded with a sample of **(2)/A-SiO₂₋₆₀₀** (not exposed to air) before TPR analysis

4.1.1.1 TPR Analysis of **(2)/A-SiO₂₋₆₀₀**

In order to achieve a good resolution of the reduction features associated with **(2)/A-SiO₂₋₆₀₀** by TPR, a small quantity of material, and hence small solid bed of material, was used for the analysis (*i.e.* 50 mg of **(2)/A-SiO₂₋₆₀₀**) distributed over 3 cm in a 0.25 cm ID tube. Larger packed sample beds are likely to lead to poor gas flow and blockages that result in a non-uniform reaction and could potentially

impede loss of water and/or HMDS from the system. An example of a GC trace from analysis of the TPR exit gas stream of **(2)/A-SiO₂₋₆₀₀** is shown in Figure 4.4, and the same GC trace with a baseline adjustment and peak fitting is shown in Figure 4.5.

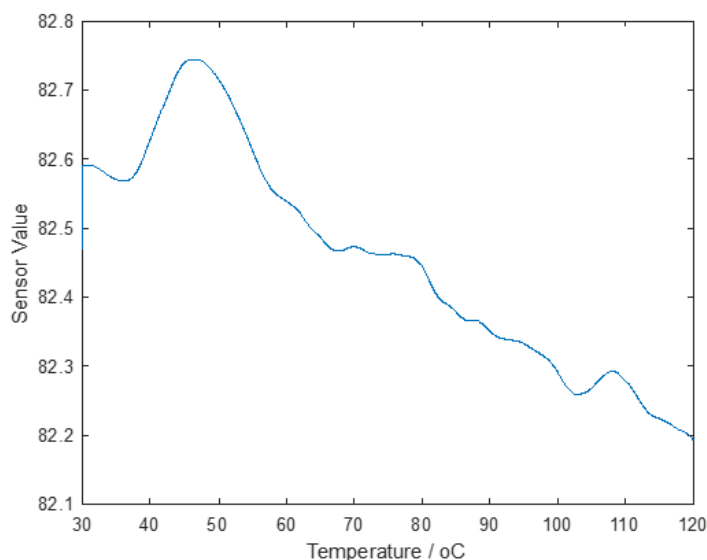


Figure 4.4. TPR Analysis of **(2)/A-SiO₂₋₆₀₀**, showing a temperature range of 30-120 °C; Conditions: temperature: 30 – 500 °C, ramp rate: 10 °C min⁻¹, gas: 10 ml/min H₂ + 40 mL/min N₂

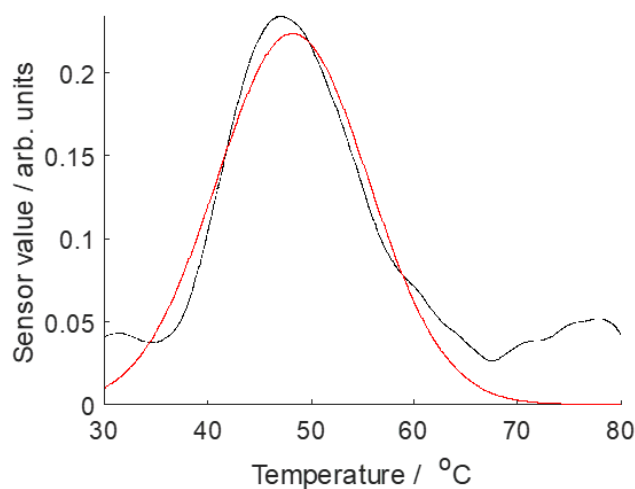


Figure 4.5. Peak fitting of TPR Analysis of **(2)/A-SiO₂₋₆₀₀**

From these TPR experiments it is seen that the onset of reduction of **(2)/A-SiO₂₋₆₀₀** occurs at ~35 °C, and is finished by ~70 °C. Oakton et al. reduced silver silyl amide on calcined silica, the silver analogue of **(2)/A-SiO₂₋₆₀₀**, with H₂ (0.5 bar) at 300 °C for 20 h to produce silver nanoparticles (2.1 nm).¹ However, Oakton did not perform TPR or determine the reduction temperature of the silver silyl amide, and it is unknown at what temperature silver silyl amide on calcined silica would form nanoparticles.

Using a Gaussian fit on the TPR of **(2)/A-SiO₂₋₆₀₀**, the H₂ consumption is calculated to be 0.07 ±0.01 mmol, since the Co content of **(2)/A-SiO₂₋₆₀₀** is 0.06 ±0.01 mmol, this indicates that reduction of **(2)/A-SiO₂₋₆₀₀** uses approximately 1 mmol of hydrogen per mmol of cobalt. This is consistent with **(2)/A-SiO₂₋₆₀₀** comprising a monografted cobalt amide species as described in Section 3.1.2, and hence elimination of one equivalent of HNTMS₂ and one equivalent of THF. However, this calculated H₂ consumption does not account for the impact of any HMDS and THF released that would also be detected by the TCD (0.06 ±0.01 mmol of each). This is further complicated by the possibility that an unknown amount of the released HMDS will react with the silica surface, similar to Section 3.1.2.5, and will not be detected by the TCD.

4.1.1.2 TPR Analysis of air-exposed **(2)/A-SiO₂₋₆₀₀**

TPR analysis of air-exposed **(2)/A-SiO₂₋₆₀₀** was carried out to give a GC trace of the analysis of the TPR exit gas stream (Figure 4.6). This trace was baseline-corrected to give Figure 4.7. Similar to the TPE analysis of **(2)/A-SiO₂₋₆₀₀**, air-exposed **(2)/A-SiO₂₋₆₀₀** was initially heated to 500 °C under a flow of H₂/N₂ (10:40 ml min⁻¹), but no signals appeared in the TPR-GC trace. Consequently, to verify that no reductions occur after 500 °C, another TPR analysis was attempted, this time where the sample was heated to 800 °C. A response was seen at 705 – 800 °C, and based on a prior report, the peak at 705 – 800 °C is attributed to a process whereby the formation of cobalt silicate occurs.² The sharper peaks between 75 – 95 minutes, denoted by an *, are due to a disruption in the hydrogen supply caused by operation of other equipment in the laboratory.

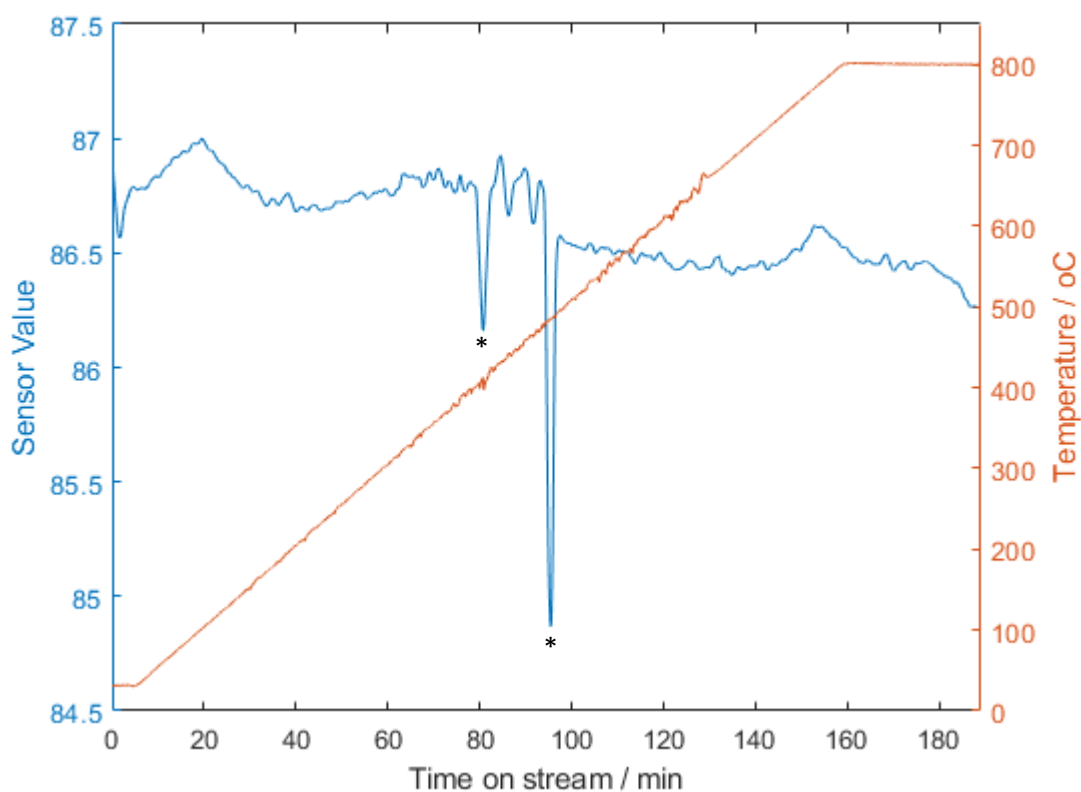


Figure 4.6. TPR Analysis of **(2)/A-SiO₂₋₆₀₀** up to 800 °C

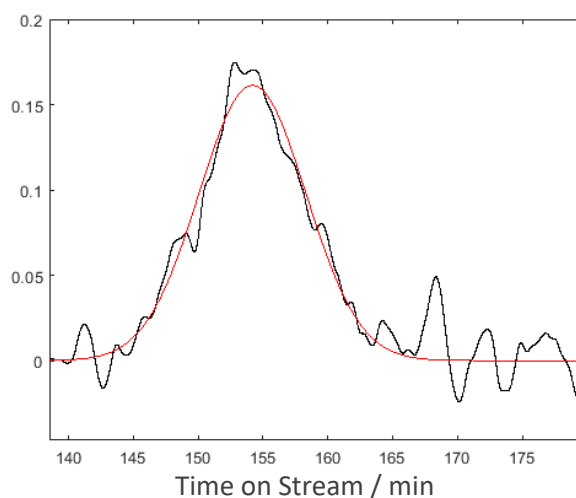


Figure 4.7. Peak fitting of TCD trace from TPR Analysis of **(2)/A-SiO₂₋₆₀₀** up to 800 °C

4.1.2 Methodology for Reducing **(2)/A-SiO₂₋₆₀₀** via Heating Under a Gas Flow

The set-up used to acquire TPR analysis is limited by the amount of material that can be charged into the quartz tube and allow unhindered, uniform gas flow (100 – 150 mg of material). Thus, a reliable method and a different set-up was developed to reduce at least 1 g of material.

The experimental set-up devised to achieve larger scale reduction of **(2)/A-SiO₂₋₆₀₀** is shown in Figure 4.8, and uses a silicone oil bath on a hotplate as heat source. By design, the arrangement mandates gas flows through the material from top to bottom. As indicated by TPR analysis, high reduction

temperatures are not needed as **(2)/A-SiO₂₋₆₀₀** is fully reduced at 150 °C, so a furnace is unnecessary. The design of this apparatus enables easy sample loading either using a Schlenk line or inside a glovebox.

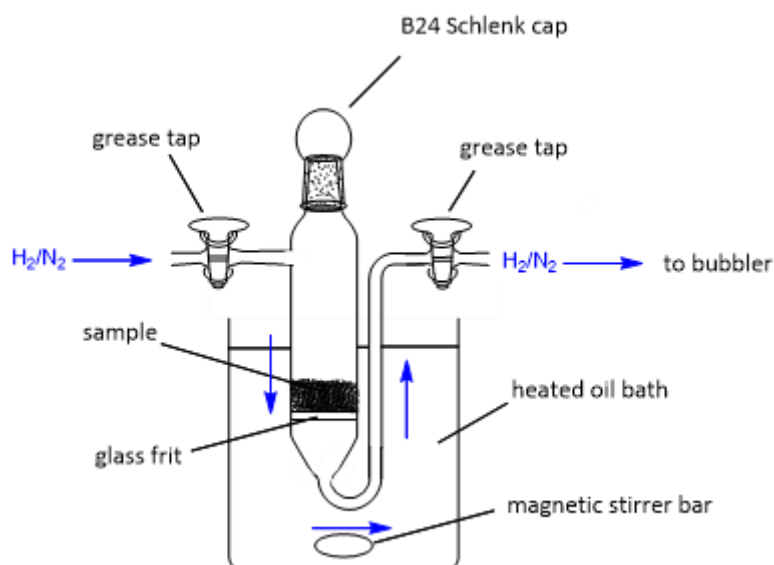


Figure 4.8. The general set-up for the reduction of **(2)/A-SiO₂₋₆₀₀**; blue arrows denote gas flow

4.1.2.1 Reduction of **(2)/A-SiO₂₋₆₀₀** under H₂/N₂ at 150 °C

As discussed in Section 4.1.1, the reduction of **(2)/A-SiO₂₋₆₀₀** is fully complete by 150 °C, so this temperature was chosen as the starting point for exploring the reduction of **(2)/SiO₂₋₆₀₀**. The reduction was achieved using a 5% hydrogen in nitrogen mix, mirroring the conditions used in the TPR analysis. Under a 5% H₂/N₂ gas flow at 150 °C, a colour change was observed during the reduction process, with **(2)/A-SiO₂₋₆₀₀** gradually changing from green to blue, something that is observed to occur over the reaction time and takes place in the same direction as the flow of gas (Figure 4.9). Despite the colour change clearly signifying that a reaction is occurring, the blue colour was unexpected as **(2)/A-SiO₂₋₆₀₀** turns black when reduced using the small scale TPR analysis experimental set-up (See Section 4.1.1).



Figure 4.9. The colour change from blue to green that **(2)/A-SiO₂₋₆₀₀** undergoes over time during reduction at 150 °C under H₂/N₂

Initially, there was a concern that the blue colour observed during the larger scale reduction experiments of **(2)/A-SiO₂₋₆₀₀**, (Figure 4.9) was due to air-exposure of the sample, since **(2)/A-SiO₂₋₆₀₀** turns pale blue when exposed to air. However, when the colour of an air-exposed sample of **(2)/A-SiO₂₋₆₀₀** is compared to that of a sample of **(2)/A-SiO₂₋₆₀₀** reduced at 150 °C under H₂/N₂ in the larger scale set-up, the colours are clearly different by eye (Figure 4.10): **(2)/A-SiO₂₋₆₀₀ (150 °C, H₂/N₂)** is a brighter blue colour than air-exposed **(2)/A-SiO₂₋₆₀₀**. Notably, when the blue reduced material **(2)/A-SiO₂₋₆₀₀ (150 °C, H₂/N₂)** is exposed to normal laboratory atmosphere, it undergoes a colour change, becoming paler, and becomes the same colour as air-exposed **(2)/A-SiO₂₋₆₀₀**.

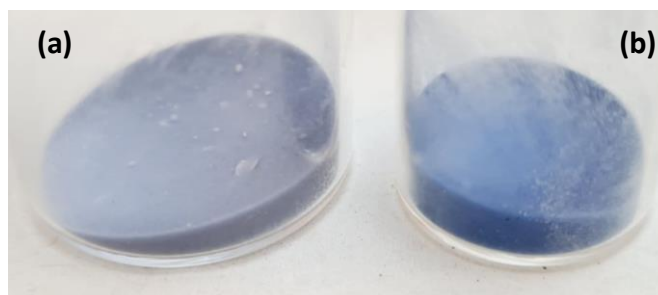


Figure 4.10. Comparison of the colour of air-exposed **(2)/A-SiO₂₋₆₀₀** and **(2)/A-SiO₂₋₆₀₀ (150 °C, H₂/N₂)**
(a) air-exposed **(2)/A-SiO₂₋₆₀₀**; (b) **(2)/A-SiO₂₋₆₀₀ (150 °C, H₂/N₂)**

4.1.2.2 Reduction of **(2)/A-SiO₂₋₆₀₀** at Different Temperatures

It was decided that a sample of **(2)/A-SiO₂₋₆₀₀** should be reduced at higher temperatures in order to determine the effects of higher temperatures on the reduction of **(2)/A-SiO₂₋₆₀₀**. A portion of **(2)/A-SiO₂₋₆₀₀** was reduced at 200 °C and 250 °C in the larger scale flow system (Figure 4.11) to form **(2)/A-SiO₂₋₆₀₀ (200 °C, H₂/N₂)** and **(2)/A-SiO₂₋₆₀₀ (250 °C, H₂/N₂)**.

The **(2)/A-SiO₂₋₆₀₀** material undergoes a colour change from green to black and blue when forming **(2)/A-SiO₂₋₆₀₀ (200 °C, H₂/N₂)** and **(2)/A-SiO₂₋₆₀₀ (250 °C, H₂/N₂)**; see Figure 4.11. The formation of the black material is a function of temperature; at higher temperatures, more of **(2)/A-SiO₂₋₆₀₀** turns black rather than blue. This can be seen as **(2)/A-SiO₂₋₆₀₀ (150 °C, H₂/N₂)** is entirely blue, while **(2)/A-SiO₂₋₆₀₀ (200 °C, H₂/N₂)** has a smaller layer of black material on the bottom and **(2)/A-SiO₂₋₆₀₀ (250 °C, H₂/N₂)** has a larger layer of black material. Even when the reductions of **(2)/A-SiO₂₋₆₀₀ (200 °C, H₂/N₂)** and **(2)/A-SiO₂₋₆₀₀ (250 °C, H₂/N₂)** are allowed to run for a longer period of time, the blue

material never turned black. The appearance of the blue colour occurs in the direction of the gas flow. Although the origins of these observed differences in colour as a function of distance from the H₂ inlet are unknown, the following are proposed:

1. There are two different reductions/reactions occurring;
2. The blue material is formed from reduction with hydrogen gas as it travels down the bed of the material;
3. The higher temperature causes a different reaction that results in a black material.

It is proposed that these three factors are likely happening simultaneously. It has also been observed that once the material has turned black due to heat, it does not react further with hydrogen to form the blue material between 250 – 700 °C. The reaction caused by heat was proposed to be the formation of isolated metal silicate sites on the surface of silica, something similar to the product of the thermolysis of lanthanide metal silylamide species, $[(\equiv\text{SiO})\text{M}(\text{N}(\text{SiMe}_3)_2)]$, reported previously.³

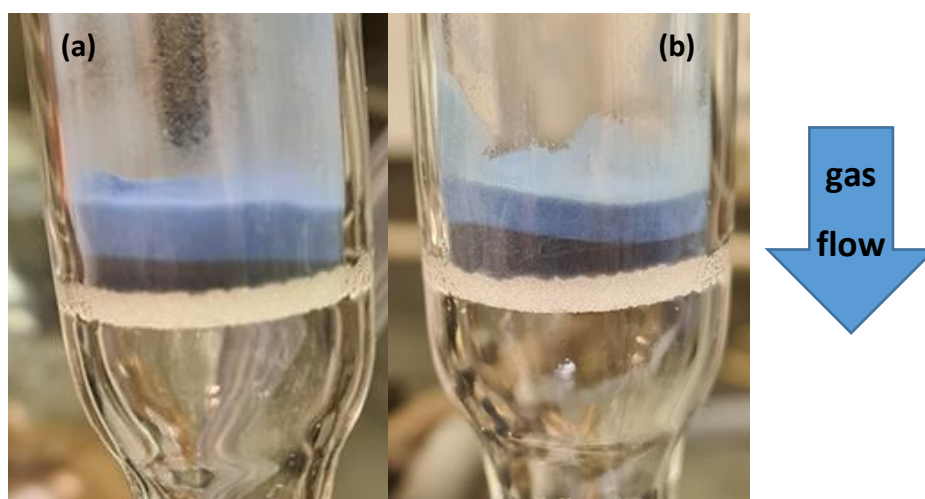


Figure 4.11. (a) **(2)/A-SiO₂₋₆₀₀ (200 °C, H₂/N₂)**; (b) **(2)/A-SiO₂₋₆₀₀ (250 °C, H₂/N₂)**

4.1.2.4 Thermal Treatment of **(2)/A-SiO₂₋₆₀₀** under N₂

To determine whether the blue and black layers in **(2)/A-SiO₂₋₆₀₀ (200 °C, H₂/N₂)** and **(2)/A-SiO₂₋₆₀₀ (250 °C, H₂/N₂)** (Figure 4.11) were due to a reaction of **(2)/A-SiO₂₋₆₀₀** with hydrogen or the effect of heat alone, **(2)/A-SiO₂₋₆₀₀** was heated to various different temperatures under a flow of nitrogen in the absence of hydrogen to form **(2)/A-SiO₂₋₆₀₀ (150 °C, N₂)**, **(2)/A-SiO₂₋₆₀₀ (200 °C, N₂)**, and **(2)/A-SiO₂₋₆₀₀ (250 °C, N₂)**. For each of these tests a colour change was observed during heating. The portion of **(2)/A-SiO₂₋₆₀₀** turned from green to completely black when heated without hydrogen, suggesting that the black material observed when reducing **(2)/A-SiO₂₋₆₀₀** at higher temperatures is likely due to thermolysis and not reduction by hydrogen gas. When this black material generated under a nitrogen atmosphere is subsequently heated under hydrogen at 250 °C, no further colour change occurs. When

(2)/A-SiO₂₋₆₀₀ (150 °C, N₂), (2)/A-SiO₂₋₆₀₀ (200 °C, N₂), and (2)/A-SiO₂₋₆₀₀ (250 °C, N₂) are exposed to air they turn pale blue.

4.1.2.5 Reduction of air-exposed (2)/A-SiO₂₋₆₀₀ under H₂/N₂ at 150 °C

Again, to probe the origins of the various observed colour changes associated with the thermolysis and/or reduction of (2)/A-SiO₂₋₆₀₀, an attempt was made to reduce a sample of air-exposed (2)/A SiO₂₋₆₀₀ under H₂/N₂ gas. This reduction attempt was performed to determine whether it was necessary or not to handle (2)/A-SiO₂₋₆₀₀ in the absence of air/moisture prior to its reduction. On treating the pale blue air-exposed (2)/A SiO₂₋₆₀₀ with 5% H₂/N₂ at 150 °C, no colour change was observed. This indicates that air-exposed (2)/A SiO₂₋₆₀₀ is not reduced at these relatively low temperatures (150 – 250 °C), which agrees with the TPR analysis that shows that air-exposed (2)/A-SiO₂₋₆₀₀ reacts at 705 – 800 °C (Section 4.1.1.2).

4.1.3 Analysis and Characterisation of (2)/A-SiO₂₋₆₀₀ after Reduction

Given the air- and moisture-sensitivity of the (2)/A-SiO₂₋₆₀₀ material after reaction with hydrogen, and its instability even when stored in a sealed vial in a nitrogen glovebox, the materials in question had to be freshly made before all analyses and catalysis test reactions. It was determined that the method of synthesis of batches of material were reproducible with identical ICP-EOS (Section 3.1.2.1), ²⁹Si SS-NMR (Section 4.1.3.2), and PXRD (Section 4.1.3.5) analyses being obtained for each batch of material.

4.1.3.1 Determining Cobalt Loading after Thermal Treatments of (2)/A-SiO₂₋₆₀₀ by ICP-EOS

Given that the cobalt loading of (2)/A-SiO₂₋₆₀₀ is known, 2.2 ±0.2 Co w.t. % (Section 3.1.2.1), it was of interest to explore if any cobalt was lost during the thermolysis/reduction process, if for example there was any volatile physisorbed cobalt-containing material present (*e.g.* unreacted cobalt amide complex), which may be lost through evaporation under the gas flow at elevated temperatures. Consequently, the variously treated (2)/A-SiO₂₋₆₀₀ samples were analysed by ICP-OES (Table 4.1). Across all of the materials obtained following application of the various reduction conditions, no loss of cobalt was found to have occurred upon thermolysis/reduction.

Table 4.1. Co metal loading of (2)/A-SiO₂₋₆₀₀ thermally treated under different conditions, as determined by ICP-OES

Material	Co w.t. % loading
(2)/A-SiO ₂₋₆₀₀	2.2 ±0.2
(2)/A-SiO ₂₋₆₀₀ (150 °C, N ₂ /H ₂)	2.4 ±0.2
(2)/A-SiO ₂₋₆₀₀ (200 °C, N ₂ /H ₂)	2.2 ±0.2
(2)/A-SiO ₂₋₆₀₀ (250 °C, N ₂ /H ₂)	2.3 ±0.2
(2)/A-SiO ₂₋₆₀₀ (150 °C, H ₂)	2.4 ±0.2
(2)/A-SiO ₂₋₆₀₀ (150 °C, N ₂)	2.2 ±0.2
(2)/A-SiO ₂₋₆₀₀ (air-exposed, 150 °C, N ₂ /H ₂)	2.1 ±0.2

4.1.3.2 SS-NMR Spectroscopic Analysis of (2)/A-SiO₂₋₆₀₀ after Thermal Treatments

In Section 3.1.2, an SS-NMR study (²⁹Si CP and DE; ¹H spectra) of (2)/A-SiO₂₋₆₀₀ is described. These spectroscopic investigations found that no signal could be observed in the ²⁹Si CP spectrum of (2)/A-SiO₂₋₆₀₀, while a single noisy signal was observed in its ²⁹Si DE spectrum, due to the presence of a paramagnetic Co^{II} species present in (2)/A-SiO₂₋₆₀₀. Additionally, two surface species, -Co(NSiMe₃)_x and -OSiMe₃ were identified in (2)/A-SiO₂₋₆₀₀ through its ¹H SS-NMR analysis. To compare the precursor material, (2)/A-SiO₂₋₆₀₀, with the materials obtained following reduction here, SS-NMR spectroscopic analysis was performed on (2)/A-SiO₂₋₆₀₀ (150 °C, H₂/N₂), (2)/A-SiO₂₋₆₀₀ (air-exposed, 150 °C, H₂/N₂), and (2)/A-SiO₂₋₆₀₀ (150 °C, N₂).

4.1.3.2.1 ²⁹Si SS-NMR Spectroscopic Analysis of (2)/A-SiO₂₋₆₀₀ (150 °C, H₂/N₂)

Acquisition of both ²⁹Si CP and DE NMR spectra was attempted with (2)/A-SiO₂₋₆₀₀ (150 °C, H₂/N₂). No signal could be detected in the cross-polarisation CP spectrum, while a noisy, broad signal was detected in the DE spectrum (Figure 4.12). Note, it was not possible to successfully deconvolute the resonance in the DE spectrum. These ²⁹Si CP and DE NMR spectroscopic results for (2)/A-SiO₂₋₆₀₀ (150 °C, H₂/N₂) are comparable to the results obtained by SS-NMR analysis of (2)/A-SiO₂₋₆₀₀ (Section 3.1.2.2).

The signal obtained in the DE spectrum of (2)/A-SiO₂₋₆₀₀ (150 °C, H₂/N₂) appears at 113 ppm, which is at a slightly different chemical shift to the signal obtained for (2)/A-SiO₂₋₆₀₀, which appears at 107 ppm. It was necessary to acquire the DE spectrum of (2)/A-SiO₂₋₆₀₀ (150 °C, H₂/N₂) with a 300 s delay as the absolute signal intensity was so low that optimising for the recycle delay was not easy. The longer delay (300 s) gives more signal than a shorter delay (10 s), indicating that the rate of relaxation of (2)/A-SiO₂₋₆₀₀ (150 °C, H₂/N₂) is low. The peak shift and low relaxation rate of the DE NMR spectrum may be potentially caused by the presence of paramagnetic cobalt.

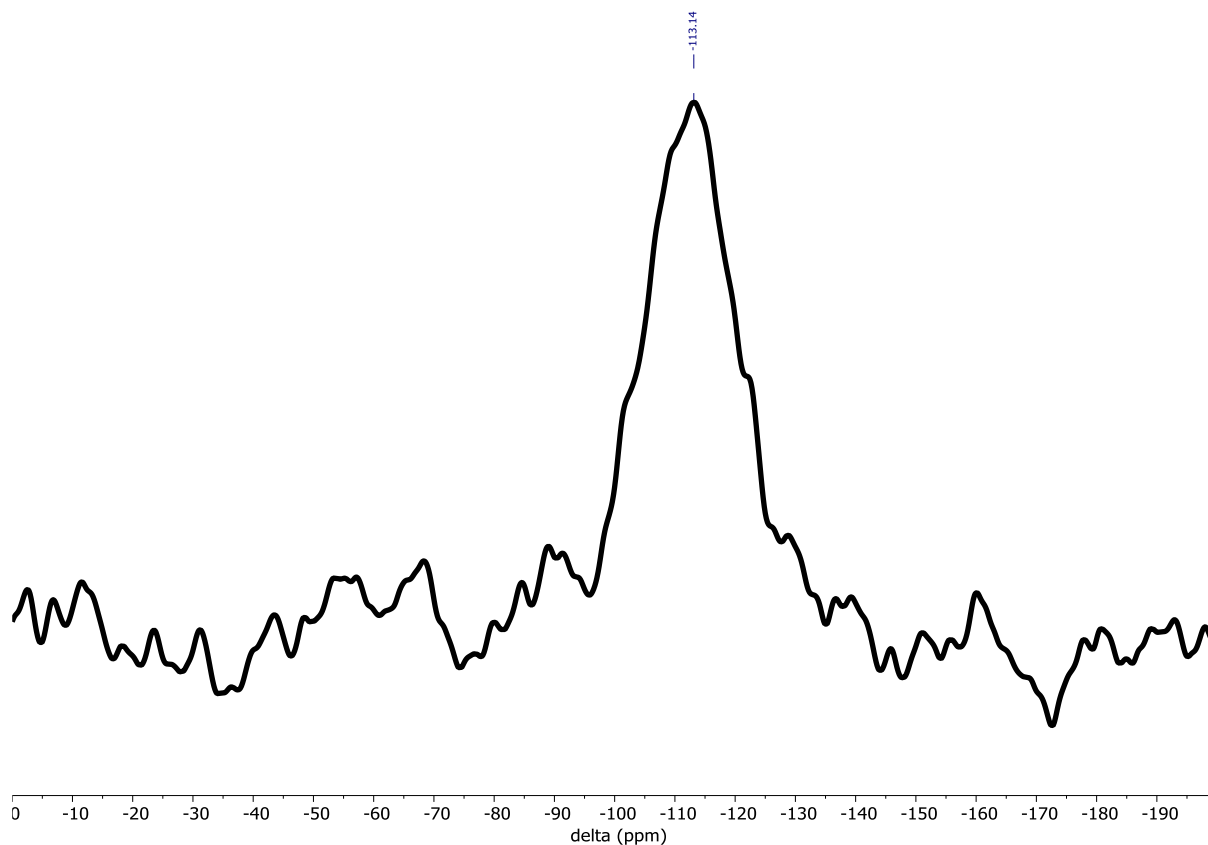
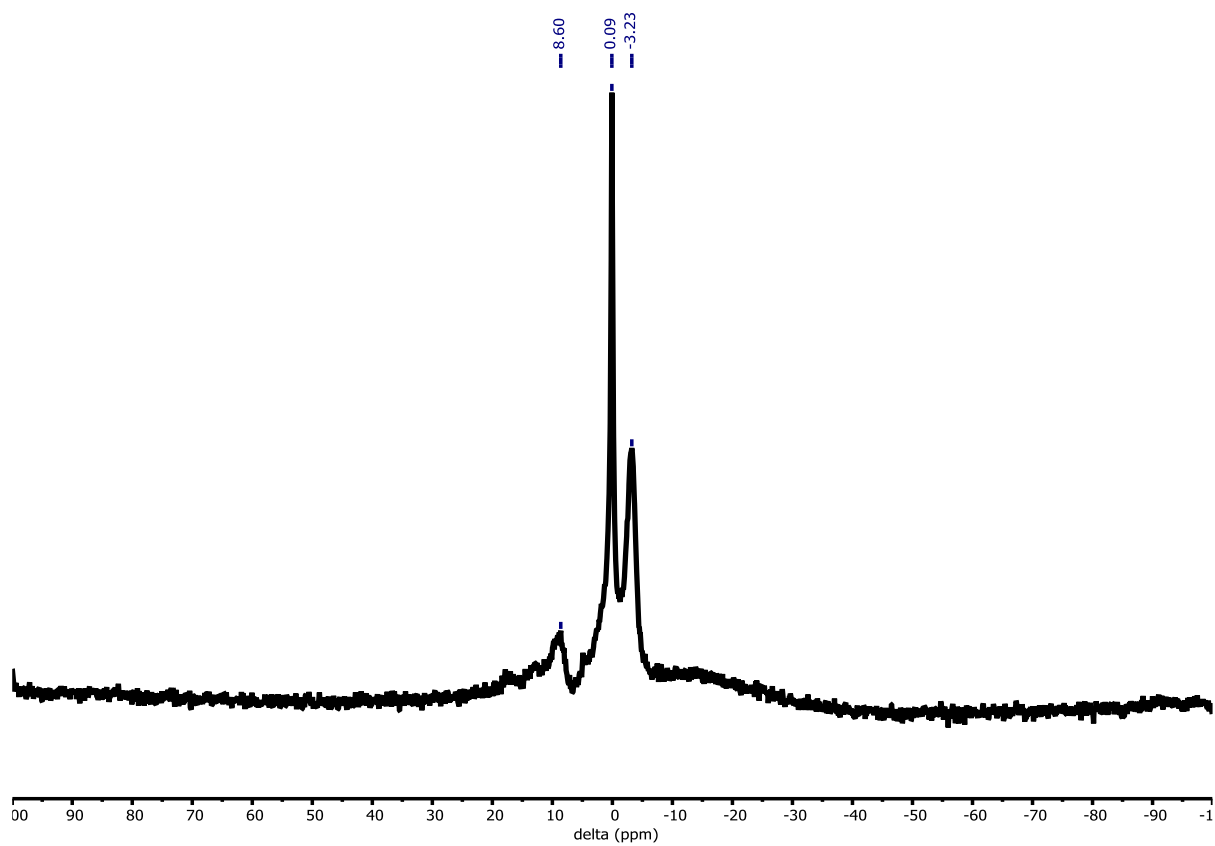
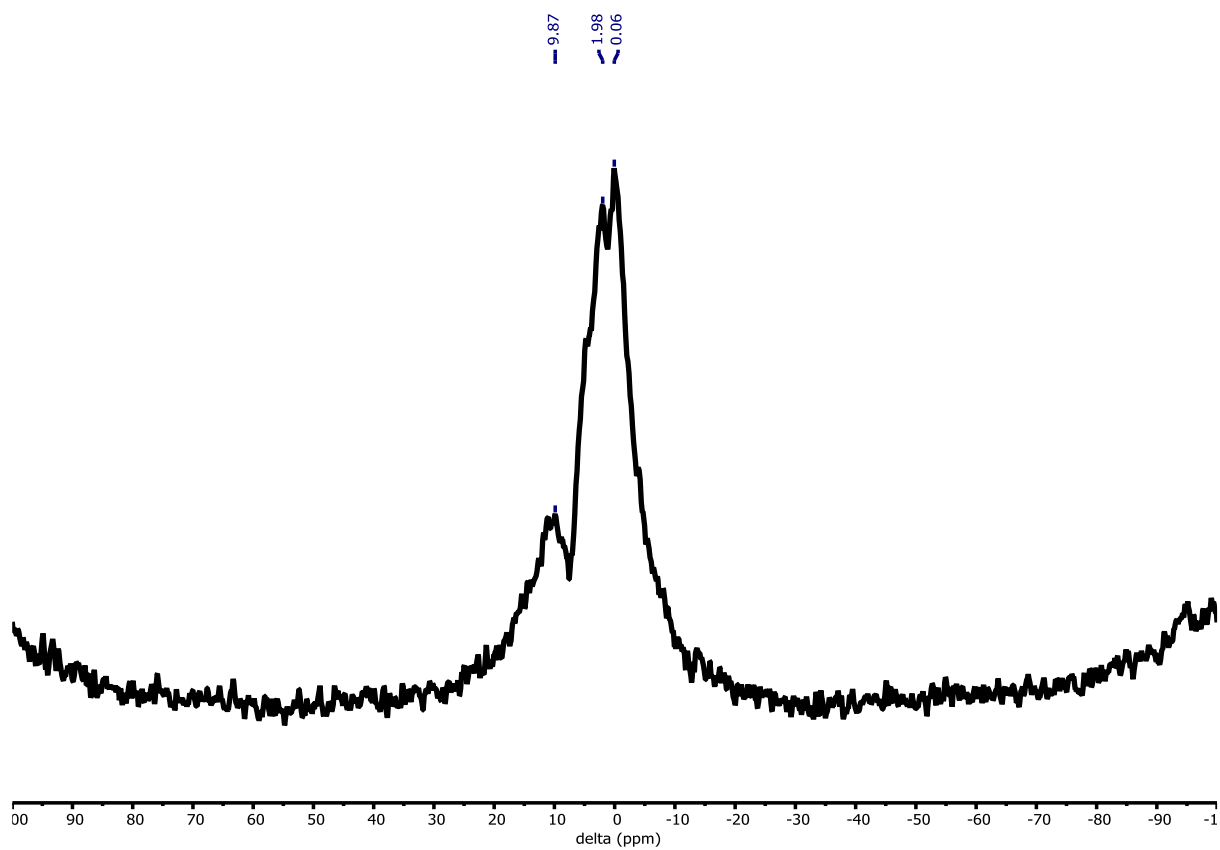


Figure 4.12. ^{29}Si SS-NMR DE spectrum of **(2)/A-SiO₂₋₆₀₀** (150 °C, H₂/N₂); frequency 79.495 MHz, spin-rate 6 kHz

4.1.3.2.2 ^1H SS-NMR Spectroscopic Analysis of **(2)/A-SiO₂₋₆₀₀** (150 °C, H₂/N₂)

The ^1H SS-NMR spectrum of **(2)/A-SiO₂₋₆₀₀** (150 °C, H₂/N₂) (Figure 4.13) was obtained and compared to that of **(2)/A-SiO₂₋₆₀₀** (Figure 4.14). Although there are two resonances in both spectra, these appear at different chemical shifts in the two samples.* Furthermore, it is proposed that both spectra are noisy due to the presence of a paramagnetic cobalt centre. The signals in the ^1H SS-NMR spectrum of **(2)/A-SiO₂₋₆₀₀** at 8.5 ppm and -3.2 ppm have been attributed to surface -OSiMe₃ and -NSiMe₃ species tethered to cobalt, respectively (Section 3.1.2.3). In the ^1H spectrum of **(2)/A-SiO₂₋₆₀₀** (150 °C, H₂/N₂), there are signals at 9.9 ppm and 2 ppm. The main signal, centred at 2.0 ppm, is broad and noisy and has not been unambiguously assigned, but based on its significant intensity, it is reasonable to suggest that this signal originates from surface Si-OH groups, which appear at 1.8 ppm in the ^1H SS-NMR spectrum of black **A-SiO₂₋₆₀₀** silica (Section 2.2.3.3). The signal at 9.9 ppm has been assigned to surface -OSiMe₃ species, and is shifted from 8.5 ppm in the unreduced sample. Together, this indicates that there is a loss of -NSiMe₃ tethered to the cobalt on **(2)/A-SiO₂₋₆₀₀** during reduction to **(2)/A-SiO₂₋₆₀₀** (150 °C, H₂/N₂), and that hydroxyl groups form on the silica surface, as proposed in Scheme 4.1.

* The resonance at 0.1 ppm in ^1H SS-NMR spectra of **(2)/A-SiO₂₋₆₀₀** and **(2)/A-SiO₂₋₆₀₀** (150 °C, H₂/N₂) is adventitious silicon grease.



4.1.3.2.3 ^{29}Si SS-NMR Spectroscopic Analysis of (2)/A-SiO₂₋₆₀₀ (air-exposed, 150 °C, H₂/N₂)

Both CP and DE ^{29}Si SS-NMR spectra were obtained for (2)/A-SiO₂₋₆₀₀ (air-exposed, 150 °C, H₂/N₂) (Figure 4.15). In the CP spectrum, the ^{29}Si signal has very low intensity and is nearly indistinguishable from the baseline, indicating that the material does not undergo cross-polarisation easily, possibly due to a lack of surface silanol species. The DE ^{29}Si SS-NMR spectrum of (2)/A-SiO₂₋₆₀₀ (air-exposed, 150 °C, H₂/N₂) presents a broad signal at -110 ppm, which has been assigned to be the Q₄ Si-OH motif (Section 2.2.3.2). The DE spectrum was also acquired with 10 s and 300 s delay relaxation times. With direct excitation and a short recycle delay (10 s), the resonance in the DE spectrum of (2)/A-SiO₂₋₆₀₀ (air-exposed, 150 °C, H₂/N₂) (Figure 4.16) is very weak, which is indicative of the influence of the cobalt not having a significant impact on the relaxation of the bulk of silicon in the sample (Section 4.1.3.2). Together, this indicates that the cobalt is no longer tethered to the silica surface through a silanol species and may be present as particles on the silica as proposed in Scheme 4.1.

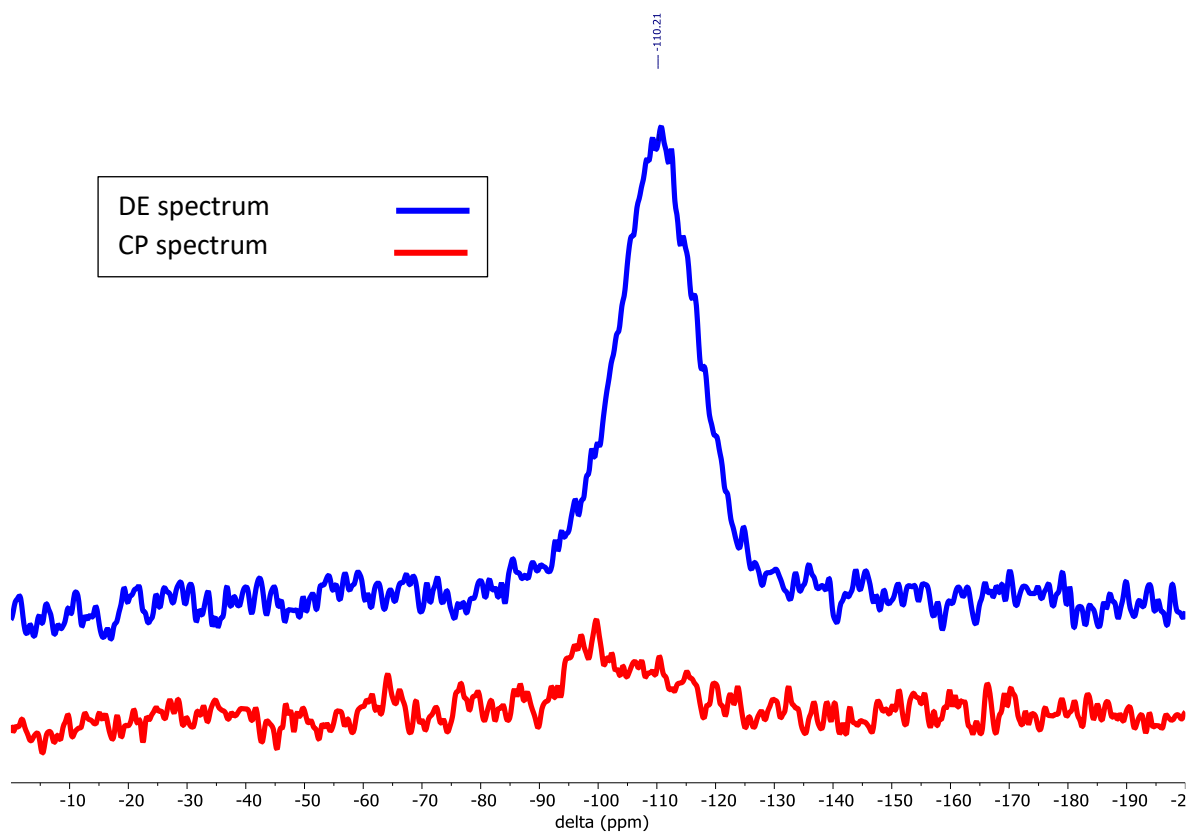


Figure 4.15. ^{29}Si SS-NMR DE and CP spectra of (2)/A-SiO₂₋₆₀₀ (air-exposed, 150 °C, H₂/N₂); frequency 79.495 MHz, spin-rate 6 kHz

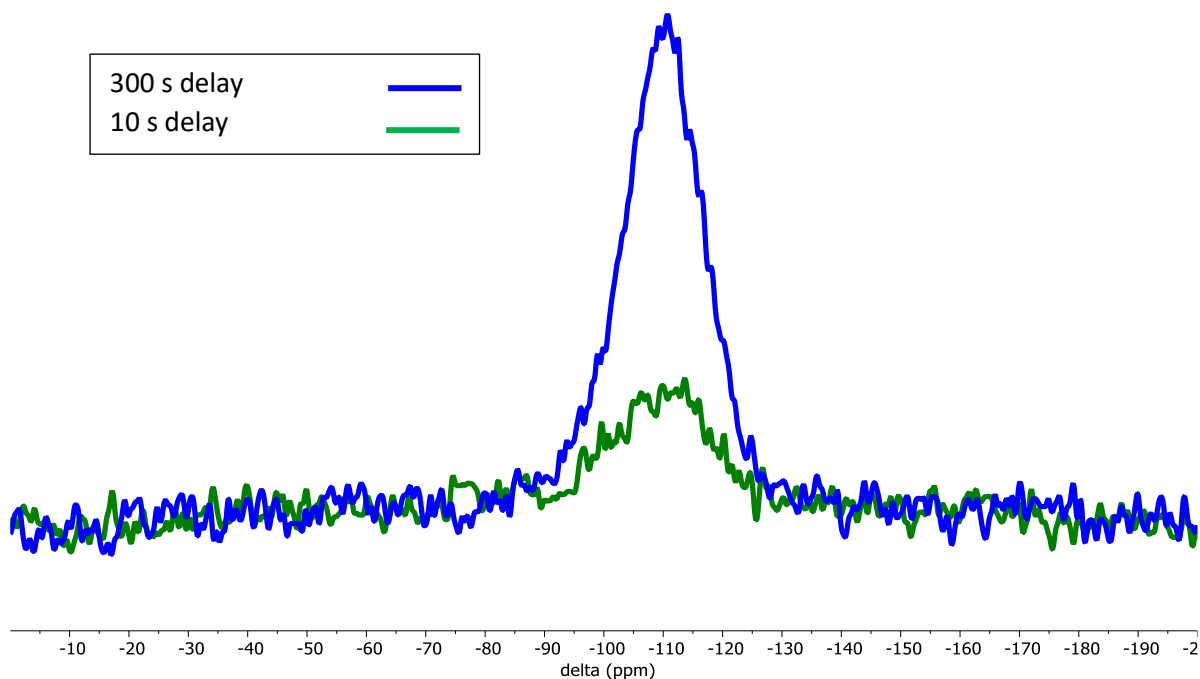


Figure 4.16. ^{29}Si SS-NMR spectra of **(2)/A-SiO₂₋₆₀₀** (air-exposed, 150 °C, H₂/N₂) comparing different relaxation times (10 vs. 300 s delay); frequency 79.495 MHz, spin-rate 6 kHz

4.1.3.2.4 ^1H SS-NMR Spectroscopic Analysis of **(2)/A-SiO₂₋₆₀₀** (air-exposed, 150 °C, H₂/N₂)

The results of air-exposure of **(2)/A-SiO₂₋₆₀₀** prior to reduction were probed by SS-NMR spectroscopy. A ^1H SS-NMR spectrum of **(2)/A-SiO₂₋₆₀₀** (air-exposed, 150 °C, H₂/N₂) was obtained (Figure 4.17). Analysis of the air-exposed materials reveals a broad peak at 1.3 ppm, which overlaps with the signal associated with surface -OSiMe₃ species (8.6 – 9.9 ppm)[†]. Comparing the ^1H SS-NMR spectrum of **(2)/A-SiO₂₋₆₀₀** (air-exposed, 150 °C, H₂/N₂) with the analogous ^1H SS-NMR spectrum of the material not exposed to air, **(2)/A-SiO₂₋₆₀₀** (150 °C, H₂/N₂) (Figure 4.13), it is clear that the surface of **(2)/A-SiO₂₋₆₀₀** (150 °C, H₂/N₂) undergoes a change (likely rehydroxylation) upon exposure to air. The peak at 1.3 ppm is attributed to surface -OH species (as previously assigned in Section 2.2.3.3) resulting from hydroxylation of siloxane bridges after air-exposure.⁴ Hence, it is clear that **(2)/A-SiO₂₋₆₀₀** (150 °C, H₂/N₂) should be treated as being air-sensitive and handled accordingly.

[†] Surface -OSiMe₃ species are observed in the analogous ^1H SS-NMR spectra of **(2)/A-SiO₂₋₆₀₀** (150 °C, H₂/N₂) (9.9 ppm, Figure 4.13) and **(2)/A-SiO₂₋₆₀₀** (8.6 ppm Figure 4.14).

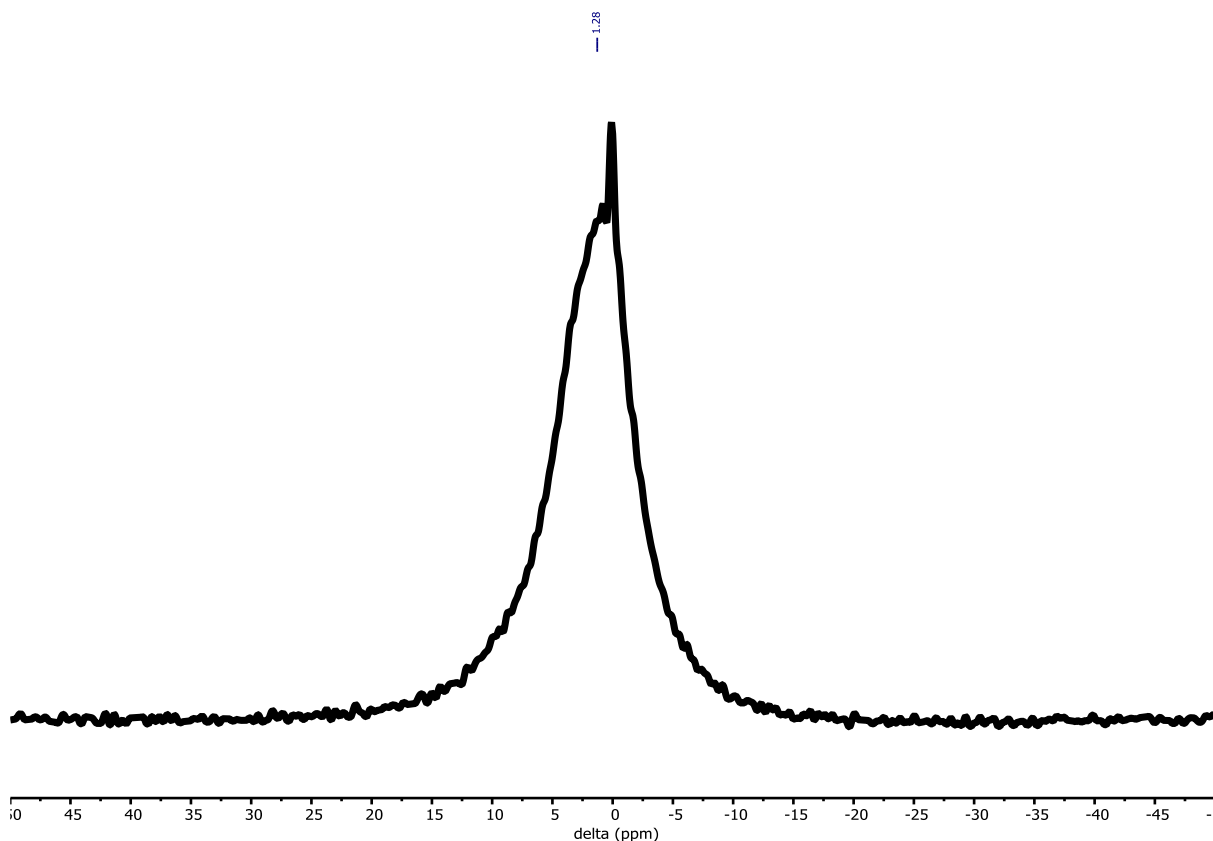


Figure 4.17. ^1H SS-NMR spectrum of **(2)/A-SiO₂₋₆₀₀** (air-exposed, 150 °C, H₂/N₂); frequency 400.17 MHz, spin-rate 40 kHz †

4.1.3.3 BET Analysis of **(2)/SiO₂₋₆₀₀** to Determine Further Silylation of the Surface After Reduction

It was described in Section 3.1.2.5 that the functionalisation of the silica surface during the tethering of complex **2** to **(2)/A-SiO₂₋₆₀₀** can be observed through the changes in the material's surface area: as functionalisation occurs (a combination of metallation/silylation), the surface area decreases.⁵ A component of the functionalisation of the silica surface described in 3.1.2.5 was caused by the silylation of the silica after release of free HMDS from the cobalt complex, which then reacts with the surface silanols. During the reduction of **(2)/A-SiO₂₋₆₀₀** under hydrogen gas, the second HMDS ligand on the cobalt centre is released (Scheme 4.1), which can be identified tentatively as described in Section 4.1.3.2.2. It has been reported previously in the literature that when late transition metal trimethylsilyl amide complexes are used to form nanoparticles on a silica surface, they will generate surface silanols and free HMDS (similar to the process proposed to occur during the reduction of **(2)/A-SiO₂₋₆₀₀** in Scheme 4.1).^{1, 6, 7} Thus, this second HMDS molecule has the potential to react further with the silanols on the silica surface, leading to additional silylation.^{1, 6, 7}

In order to probe if this secondary silylation reaction was indeed operative during the reduction of **(2)/A-SiO₂₋₆₀₀**, BET analysis was performed on a sample of **(2)/A-SiO₂₋₆₀₀** (150 °C, H₂/N₂) (Table 4.2). For **(2)/A-SiO₂₋₆₀₀** (150 °C, H₂/N₂), it was found that its surface area was lower than that of the starting

† The sharp resonance at 0.1 ppm is silicon grease.

material, indicating that some silylation has likely occurred after the second HMDS ligand was released from the cobalt centre. The decreased surface area of **(2)/A-SiO₂₋₆₀₀ (150 °C, H₂/N₂)** is not attributed to pore collapse from heating, as it has previously been shown that the pore structure collapse of **A-SiO₂** occurs at temperatures higher than 700 °C (Section 2.2.1.1). The decrease in surface area between the materials **(2)/A-SiO₂₋₆₀₀** and **(2)/A-SiO₂₋₆₀₀ (150 °C, H₂/N₂)** is not as large as the decrease seen between **A-SiO₂₋₆₀₀** and **(2)/A-SiO₂₋₆₀₀**: a difference of 24 m² g⁻¹ between **(2)/A-SiO₂₋₆₀₀** and **(2)/A-SiO₂₋₆₀₀ (150 °C, H₂/N₂)** vs 60 m² g⁻¹ between **A-SiO₂₋₆₀₀** and **(2)/A-SiO₂₋₆₀₀** (Section 3.1.2.5). This suggests that less silylation occurs during reduction of **(2)/A-SiO₂₋₆₀₀** than during the tethering of complex **2** to **(2)/A-SiO₂₋₆₀₀**. This is attributed to the constant gas flow through the sample of **(2)/A-SiO₂₋₆₀₀** during reduction, which removes the released HMDS from **(2)/A-SiO₂₋₆₀₀** as it is generated. BET analysis has confirmed that further silylation of the silica surface occurs during reduction, as the released HMDS reacts with the surface silanols and the surface area decreases from 213 m² g⁻¹ to 189 m² g⁻¹. This indicates that HMDS is lost from the cobalt centre during reduction of **(2)/A-SiO₂₋₆₀₀**.

Table 4.2. BET analysis of **(2)/A-SiO₂₋₆₀₀** and **(2)/A-SiO₂₋₆₀₀ (150 °C, H₂/N₂)**; data were measured by Johnson Matthey; measurement uncertainty on BET surface area is +/- 2%.

	BET surface area (m ² g ⁻¹)	Pore Volume [0.99ads] (cm ³ g ⁻¹)	Average Pore Diameter (Å)
(2)/A-SiO₂₋₆₀₀	213	1.7	310
(2)/A-SiO₂₋₆₀₀ (150 °C, H₂/N₂)	189	1.6	334

4.1.3.4 Analysing the Change of Magnetic Properties of Reduced **(2)/SiO₂₋₆₀₀** using a Gouy Balance

As the SS-NMR spectroscopic analysis of the reduced materials indicated that a paramagnetic cobalt was present (see Section 4.1.3.2), it was suggested that determination of the magnetic moment of the cobalt on the silica could be used as a quick/simple method to probe the amount of metallic cobalt formed at the surface during reduction. For simplicity and ease of access, a Gouy balance was used to measure the magnetic susceptibility of the various materials: **A-SiO₂₋₆₀₀**, complex **2**, **(2)/A-SiO₂₋₆₀₀**, and the reduced materials **(2)/A-SiO₂₋₆₀₀ (150 °C, H₂/N₂)**, **(2)/A-SiO₂₋₆₀₀ (air-exposed, 150 °C, H₂/N₂)**, and **(2)/A-SiO₂₋₆₀₀ (150 °C, N₂)**.

The magnetic measurements were recorded using the procedure described in Section 6.0.2.9. The Gouy tube was fitted with a Youngs tap and rigorously dried so that the samples could be charged into the tube in a nitrogen-filled glovebox without exposure to air. The necessary calibration constant for the Gouy balance was calculated using (NH₄)₂Fe(SO₄)₂·6H₂O (at T = 20 °C, C = 1.75 × 10⁻⁵). In order to provide a cobalt-containing reference material, **Co(NO₃)₂·6H₂O/A-SiO₂₋₆₀₀** (2.2% w.t. Co) was prepared by grinding Co(NO₃)₂·6H₂O and uncalcined silica until it was an homogeneous powder. The magnetic

susceptibility (χ_g) of the resulting material **Co(NO₃)₂·6H₂O/A-SiO₂₋₆₀₀** was calculated using Equation 4.1, while the molar magnetic susceptibility (χ_M) was calculated from Equation 4.2.

$$\chi_g = \frac{C \times l \times (R - R_0)}{m \times 10^7} \text{ (m}^3\text{kg}^{-1}\text{)}$$

Equation 4.1. Magnetic susceptibility formula

C = calibration constant

l = sample length (m)

m = sample mass (kg)

R = empty tube+ sample reading

R₀ = empty tube reading

$$\chi_M = M \cdot \chi_g \text{ (m}^3\text{mol}^{-1}\text{)}$$

Equation 4.2. Molar magnetic susceptibility formula

M = molar mass (kg/mol)

The effective magnetic moment (μ_{eff}) was calculated from the molar magnetic susceptibility (χ_M'), using Equation 4.3. χ_M' is obtained by adding diamagnetic corrections (Table 4.3) to χ_M . The magnetic moments calculated from the measurement obtained from the Gouy balance are in Table 4.4.

$$\mu_{\text{eff}} = 797.5 \times (\chi_M' \times T)^{0.5}$$

Equation 4.3. Effective magnetic moment formula

Table 4.3. Diamagnetic corrections relevant to this project⁸

Diamagnetic corrections (m³mol⁻¹)	
Co²⁺	1.51 × 10 ⁻¹⁰
Co³⁺	1.26 × 10 ⁻¹⁰

Table 4.4. Effective magnetic moments of (2)/A-SiO₂₋₆₀₀ and the materials obtained post-thermal treatment

Sample	Sample colour	χ_g (m ³ .kg ⁻¹)	χ_m (m ³ .mol ⁻¹)	μ_{eff} (μB)	μ_{eff} per Co (μB)
Complex 2 (neat)		3.1×10^{-8}	1.4×10^{-8}	1.62*	0.21
Co(NO ₃) ₂ .6H ₂ O/A-SiO ₂₋₆₀₀ [§]		3.1×10^{-9}	1.9×10^{-10}	0.25	0.0055
A-SiO ₂₋₆₀₀		0	0	0	n/a
(2)/A-SiO ₂₋₆₀₀	green	1.9×10^{-9}	1.1×10^{-10}	0.22	0.0049
Air-exposed (2)/A-SiO ₂₋₆₀₀	blue	2.5×10^{-9}	1.5×10^{-10}	0.24	0.0052
(2)/A-SiO ₂₋₆₀₀ (150 °C, H ₂ /N ₂)	blue	3.5×10^{-9}	2.1×10^{-10}	0.26	0.0057
(2)/A-SiO ₂₋₆₀₀ (air-exposed, 150 °C, H ₂ /N ₂)	blue	4.4×10^{-9}	2.7×10^{-10}	0.28	0.0062
(2)/A-SiO ₂₋₆₀₀ (150 °C, N ₂)	black	4.7×10^{-9}	2.8×10^{-10}	0.28	0.0063

* In reasonable agreement with the expected theoretical spin-only magnetic moment of 1.73 μB.

Blank A-SiO₂₋₆₀₀ silica is diamagnetic. Complex 2 is paramagnetic as a result of its Co²⁺, d⁷ metal centre, with an experimentally determined effective magnetic moment of 1.62 μB, which is in reasonable agreement with the expected theoretical spin-only magnetic moment of 1.73 μB.**

While metallic cobalt would be expected to be ferromagnetic, cobalt nanoparticles have been previously reported in the literature to have unusual magnetic properties.⁹ It has been reported that their shape and size both influence the magnetic properties of cobalt nanoparticles. For example, particle size can affect the magnetic moments of the particles, *i.e.* smaller Co-NPs (13 atoms) may have a larger average magnetic moment, and larger NPs (309 atoms) will have a smaller average magnetic moment.⁹ For metallic cobalt nanoparticles with a truncated octahedron shape (~ 2nm), the magnetic moments reported range from 1.57 (at the core of the nanoparticle) to 1.96 μB (at the vertex sites), with the bulk of the particles have a magnetic moment of 1.61 μB.¹⁰ This value is close to the expected theoretical spin-only magnetic moment of low-spin Co²⁺ (1.73 μB) and the experimentally determined effective magnetic moment of complex 2 (1.62 μB), and therefore it may not be possible to differentiate Co⁰ nanoparticles from Co²⁺. It would have been prudent to synthesise Co-NPs using a traditional method, to observe their magnetism on the Guoy balance as a comparison to the particles made in this project; however, due to laboratory time constraints, this was not undertaken.

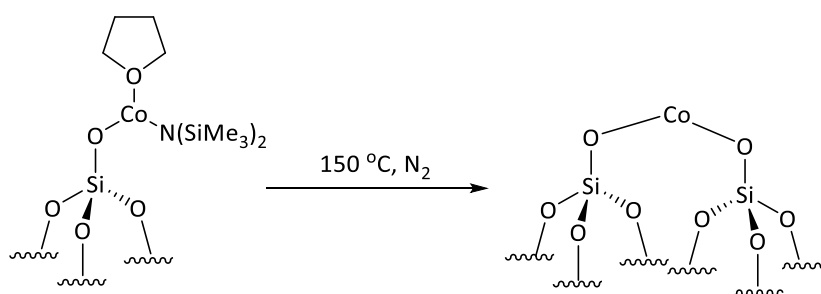
The value of μ_{eff} per cobalt for (2)/A-SiO₂₋₆₀₀ is 0.0049 μB, which is just 2.3% of the value of μ_{eff} per Co of complex 2 (0.21 μB), which is in reasonable agreement with the cobalt loading of (2)/A-SiO₂₋₆₀₀, 2.2 ±0.2 % (from ICP-EOS analysis), Table 4.4. The values of μ_{eff} of the reduced/thermally treated Co/silica materials, (2)/A-SiO₂₋₆₀₀ (150 °C, H₂/N₂), (2)/A-SiO₂₋₆₀₀ (air-exposed, 150 °C, H₂/N₂) and (2)/A-SiO₂₋₆₀₀ (150 °C, N₂), are similar, 0.0057 – 0.0063 μB μ_{eff} per cobalt, values that are 2.4 – 3% those of the value for complex 2; again these values are consistent with those expected for the presence of ~2 w.t.%

[§] Co loading: 2.3 w.t. % loading

** Theoretical spin-only magnetic moment calculated from the spin-only formula: $\sqrt{n(n+2)}$

cobalt. This indicates that reduction or heating under nitrogen does not significantly alter the magnetic susceptibility of the cobalt on the silica support. Since $\text{Co}(\text{NO}_3)_2 \cdot 6\text{H}_2\text{O}/\text{A-SiO}_{2-600}$ (Co^{2+} , 2.2% w.t. Co), used as a model for “ Co^{2+} on silica”, has a similar μ_{eff} of 0.25 μB to that of **(2)/A-SiO₂₋₆₀₀** and its derived materials (which lie in the range 0.22 – 0.28 μB), these data cannot be used to differentiate between Co^0 nanoparticles and supported Co^{2+} species as the expected magnetic moment for very small cobalt particles and Co^{2+} are similar (1.61 μB ¹⁰ and 1.73 μB ,^{††} respectively).

It is tentatively proposed that **(2)/A-SiO₂₋₆₀₀** may form a cobalt(II) silicate surface species when heated at 150 °C under nitrogen to form **(2)/A-SiO₂₋₆₀₀ (150 °C, N₂)**. This is supported by the literature, which states that metal silylamides can form isolated metal silicate sites on a silica surface under a thermal treatment at 500 °C.³ Consequently, it is proposed here that the surface structure of **(2)/A-SiO₂₋₆₀₀ (150 °C, H₂/N₂)** is as shown in Scheme 4.3.



Scheme 4.3. Cobalt silyl amide surface species forming a cobalt silicate surface species when heated under nitrogen

4.1.3.5 PXRD of **(2)/A-SiO₂₋₆₀₀ (150 °C, H₂/N₂)**, **(2)/A-SiO₂₋₆₀₀ (150 °C, N₂)**, and **(2)/A-SiO₂₋₆₀₀ (air-exposed, 150 °C, H₂/N₂)**

With a view to probing the nature of the cobalt-containing material present following thermolysis/reduction of **(2)/A-SiO₂₋₆₀₀**, PXRD analysis was performed on the materials **(2)/A-SiO₂₋₆₀₀ (150 °C, H₂/N₂)** (Figure 4.18), **(2)/A-SiO₂₋₆₀₀ (150 °C, N₂)** (Figure 4.19), and **(2)/A-SiO₂₋₆₀₀ (air-exposed, 150 °C, H₂/N₂)** (Figure 4.20). For none of these samples were any cobalt-containing nanoparticles observed (*i.e.* no reflections indicating Co metal {*fcc*¹¹ and *hcp*¹²}, CoO ^{13, 14}, or Co_3O_4 ¹⁵).^{††} Consequently, it was concluded that either the cobalt nanoparticles are too small to be detectable by PXRD (*i.e.* <3 nm based on previously-reported detection limits),¹⁶ or there are no nanoparticles present. The PXRD analysis of **(2)/A-SiO₂₋₆₀₀ (150 °C, H₂/N₂)**, **(2)/A-SiO₂₋₆₀₀ (150 °C, N₂)**, and **(2)/A-SiO₂₋₆₀₀ (air-exposed, 150 °C, H₂/N₂)** are similar (Figure 4.18 - Figure 4.20), with no significant differences between the samples being observed. The PXRD diffraction pattern obtained for the material **(2)/A-SiO₂₋₆₀₀ (150 °C, H₂/N₂)** (Figure 4.18) is the only material to show any assignable features; there is potentially a very

^{††} Theoretical spin-only magnetic moment calculated from the spin-only formula: $\sqrt{n(n+2)}$

^{‡‡} Quartz wool is detected in the PXRD pattern of **(2)/A-SiO₂₋₆₀₀ (150 °C, H₂/N₂)** and **(2)/A-SiO₂₋₆₀₀ (air-exposed, 150 °C, H₂/N₂)**. Quartz wool originated from the calcination of silica, where it is used as a plug to hold the sample in place during calcination.

board reflection at 41 – 58°, which is possible evidence of the presence of very small cobalt nanoparticles based of previous studies described in the literature.^{16, 17}

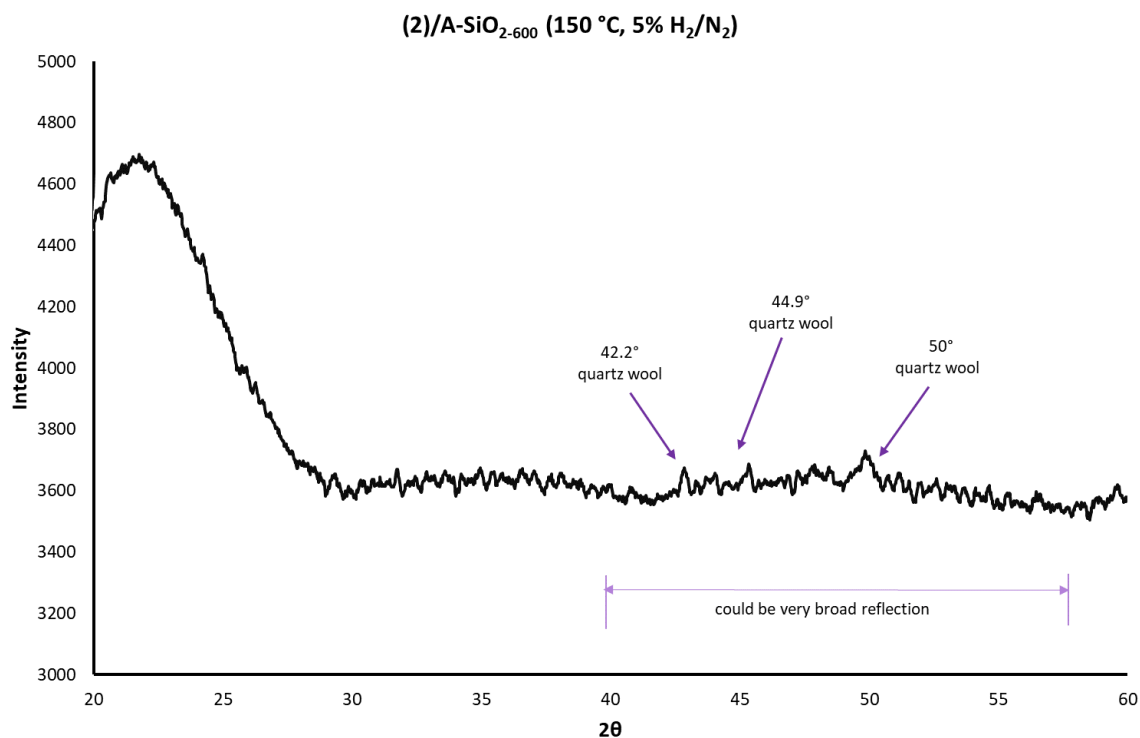


Figure 4.18. PXRD analysis of (2)/A-SiO₂₋₆₀₀ (150 °C, H₂/N₂)

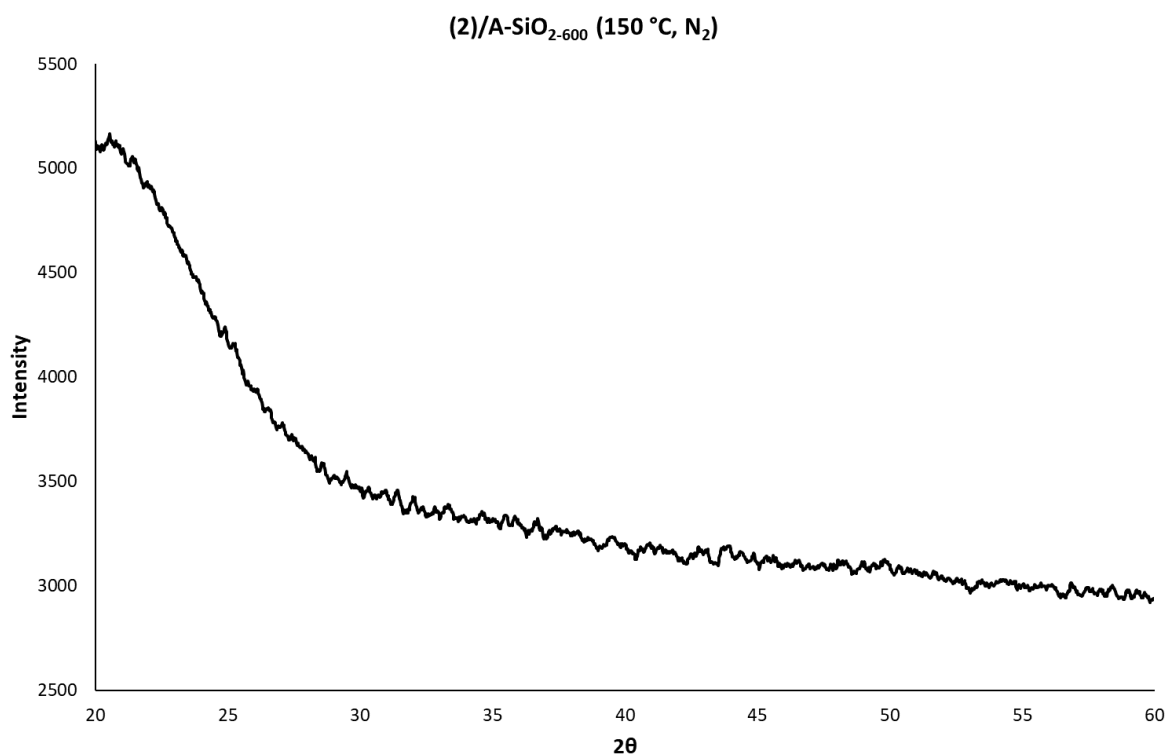


Figure 4.19. PXRD analysis of (2)/A-SiO₂₋₆₀₀ (150 °C, N₂)

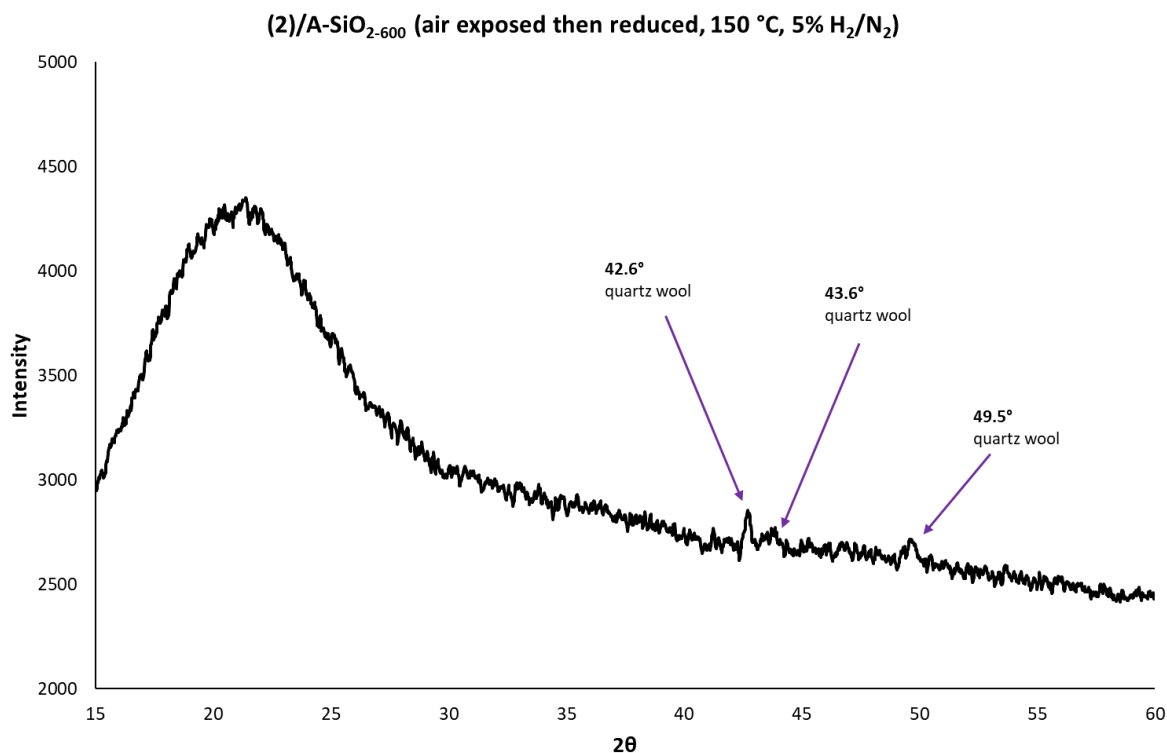


Figure 4.20. PXRD analysis of (2)/A-SiO₂₋₆₀₀ (air-exposed, 150 °C, H₂/N₂)

4.1.3.6 TEM Imaging of (2)/A-SiO₂₋₆₀₀ after Heating under Hydrogen

As none of the PXRD analyses described in Section 4.1.3.4 showed reflections that indicate the presence of cobalt nanoparticles (>3 nm), TEM imaging was also undertaken. However, for operational reasons it was initially not possible to admit the samples into the microscope without their exposure to atmosphere, so it is possible that any nanoparticles present may have become oxidised. This was rectified by later TEM imaging that was performed without exposure to air or moisture by Johnson Matthey. The results of both “non-air sensitive” and “air-sensitive” TEM imaging are discussed.

4.1.3.6.1 “Non-air” sensitive TEM Imaging of (2)/A-SiO₂₋₆₀₀ after Heating under Hydrogen

The resulting TEM images obtained from analysis of material introduced into the microscope without protection from air or moisture do not unambiguously confirm the presence of metallic cobalt particles. However, EDX analysis confirms that cobalt is present in all TEM images and is evenly dispersed across the silica surface.

The TEM images of the materials (2)/A-SiO₂₋₆₀₀ (150 °C, H₂) (Figure 4.21), air-exposed (2)/A-SiO₂₋₆₀₀ (Figure 22), and (2)/A-SiO₂₋₆₀₀ (150 °C, air-exposed, H₂) (Figure 4.23) show what look like potentially very small nanoparticles (0.5 - 3 nm). However, these particles do not appear to be metallic cobalt since it was found impossible to bring the images of these small particles into sharp focus against the silica oxide support background. Heavier metallic particles should sharpen into focus in TEM imaging as the oxide support in the image is put out of focus due to the difference in molecular weight; this

would allow the particles to be seen more easily against the support.^{18, 19} The particles in this project lose distinction like the silica support when the focus is lost, showing that they are therefore unlikely to be heavier metallic particles and may be a Co^{2+} species like cobalt(II) oxide or cobalt silicate. However, as the analysis of the magnetic moment could not confirm the oxidation state of the cobalt species (Co^0 vs. Co^{2+}), and the method of determining whether the cobalt Co^{2+} or metallic through defocusing is not conclusive (due to other possible reasons for the particles not being distinguished easily from the support, *e.g.* – the small size of the particles can make them hard to visualise),^{18, 19} the surface structure of the cobalt could not be definitively determined. While cobalt-containing particles are unquestionably present on the surface of the silica, it cannot be concluded as to whether they are metallic or not. It should also be kept in mind that the particles may have been oxidised to Co^{2+} due to exposure to air during the imaging process because of the exposure of the materials to air/moisture during introduction into the microscope.

The TEM image of the material **(2)/A-SiO₂₋₆₀₀ (150 °C, N₂)** (Figure 4.24) shows Co crystal lattice lines present on the silica (d-spacing = 0.25 nm). This lattice spacing matches the d-spacing of CoO (NaCl, Fm-3m) (d-spacing = 0.25 nm).²⁰ The TEM images of **(2)/A-SiO₂₋₆₀₀ (150 °C, N₂)** indicate that when heated without hydrogen present and after exposure to atmosphere, **(2)/A-SiO₂₋₆₀₀** possibly forms cobalt silicate sites on the surface of the silica instead of distinct nanoparticles, as seen in Scheme 4.3.

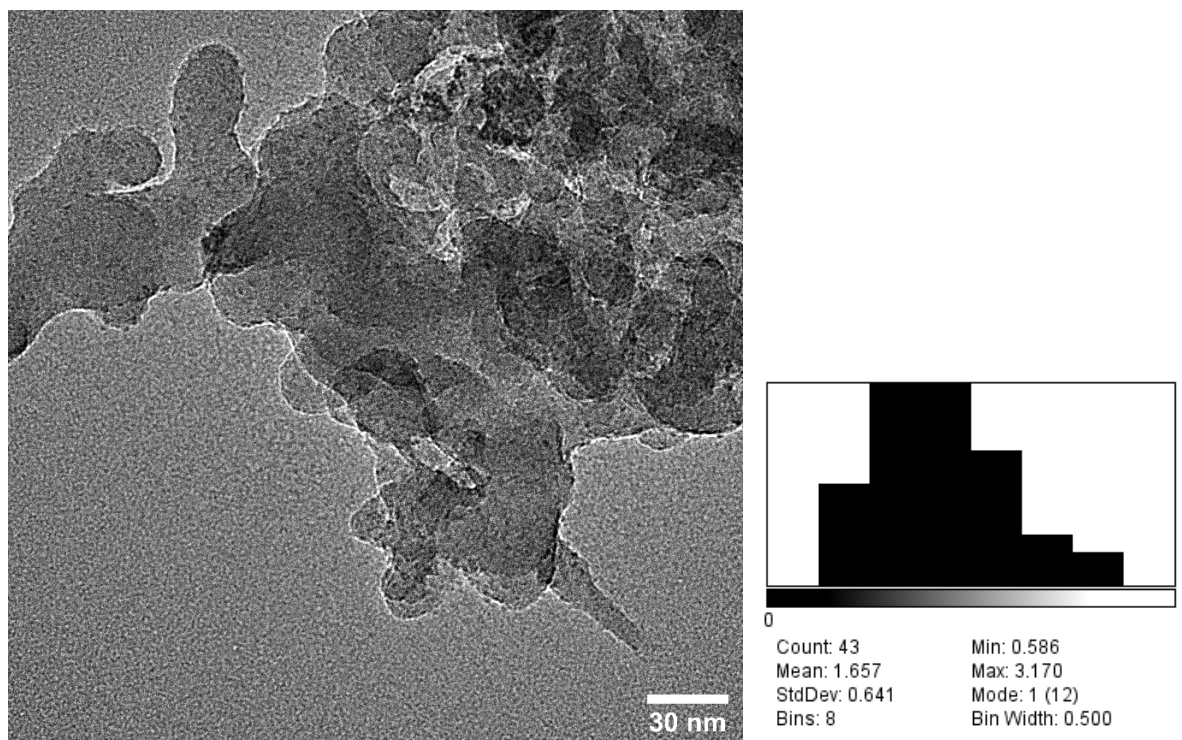


Figure 4.21. TEM image of **(2)/A-SiO₂₋₆₀₀ (150 °C, H₂)** and the distribution of potential cobalt oxide particle sizes

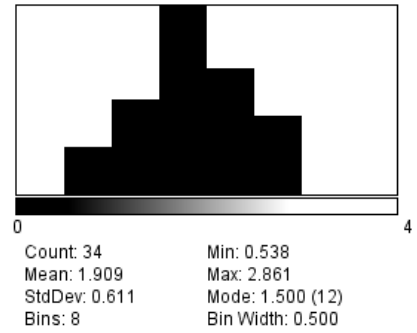
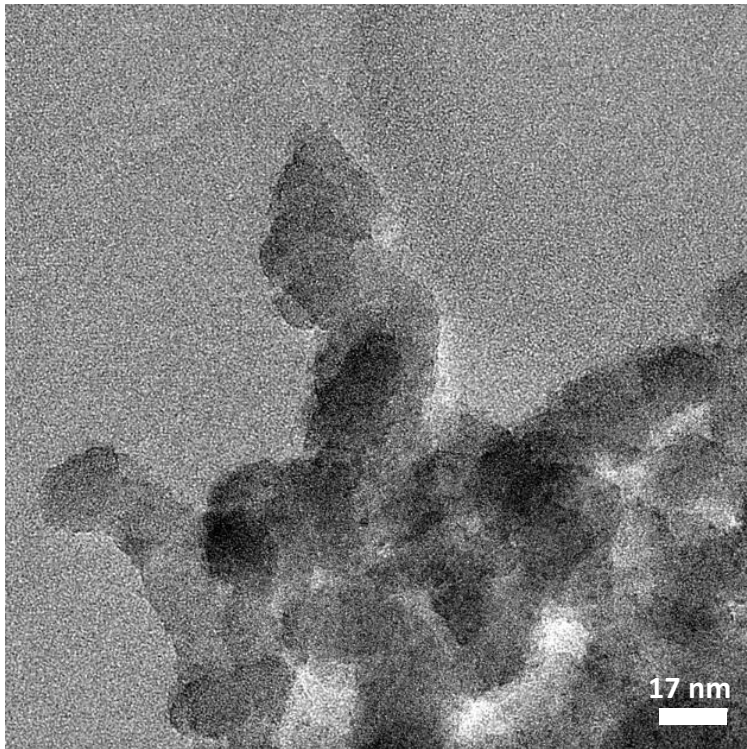


Figure 4.22. TEM image of air-exposed (2)/A-SiO₂₋₆₀₀ and the distribution of potential cobalt oxide particle sizes

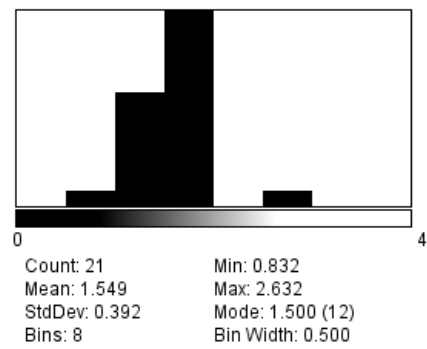
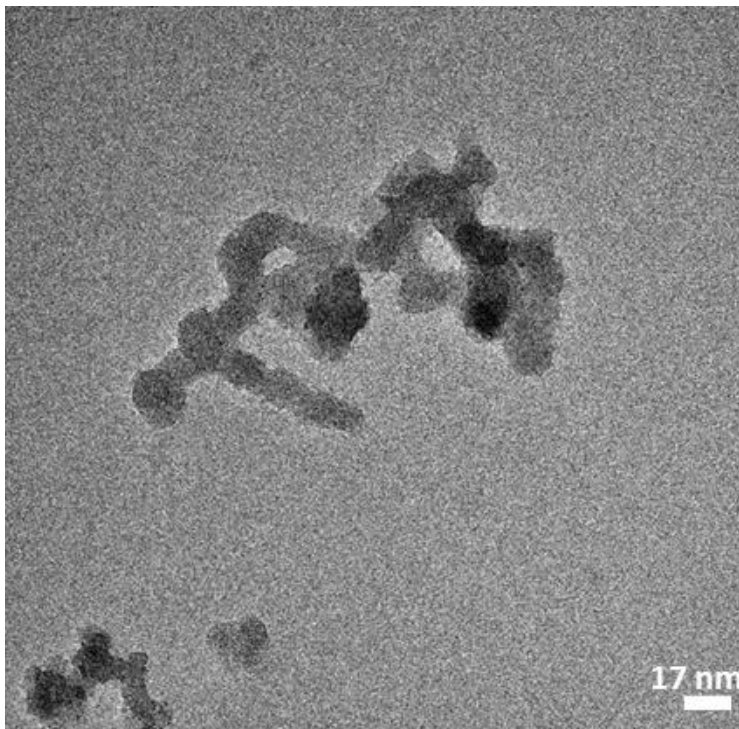


Figure 4.23. TEM image of (2)/A-SiO₂₋₆₀₀ (air-exposed, 150 °C, H₂) and the distribution of potential cobalt oxide particle sizes

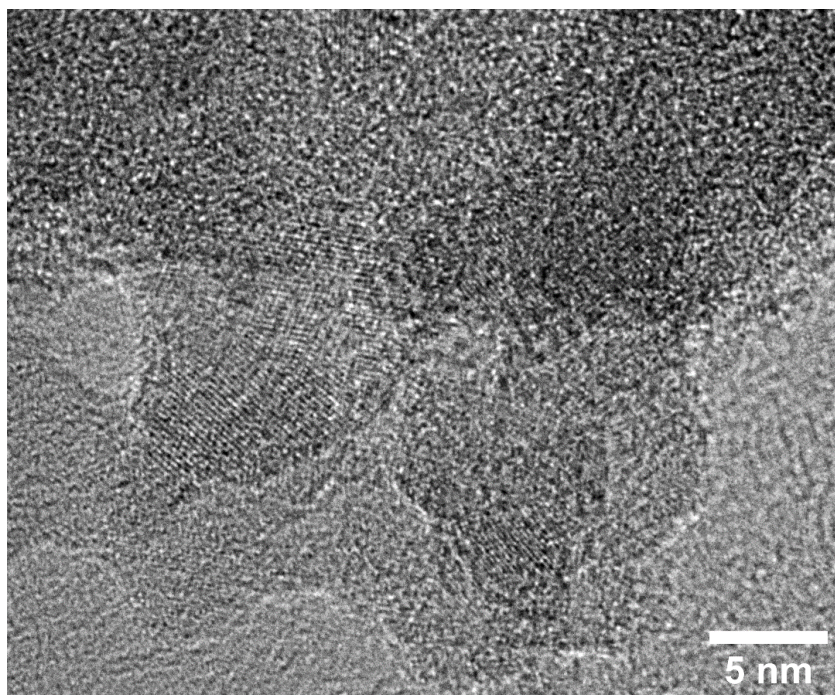


Figure 4.24. TEM image of **(2)/A-SiO₂₋₆₀₀ (150 °C, N₂)**

4.1.3.6.2 “Air-sensitive” TEM imaging of **(2)/A-SiO₂₋₆₀₀** after Heating under Hydrogen

While the TEM images reported in Section 4.1.3.6.1 show the presence of Co²⁺ particles on the surface of silica, this result is tentative at best, as part of the TEM imaging process exposed the material to atmosphere, potentially oxidising any metallic nanoparticles that were present. Consequently, TEM imaging of **(2)/A-SiO₂₋₆₀₀ (150 °C, H₂)** and **(2)/A-SiO₂₋₆₀₀ (150 °C, N₂)** without exposure to air (“air-sensitive TEM”) were undertaken to determine whether the particles were metallic cobalt or not.

The resulting TEM Images from “air-sensitive” TEM imaging of **(2)/A-SiO₂₋₆₀₀ (150 °C, H₂)** show small (approximately 1 nm), ill-defined features on the surface of the silica support (Figure 4.25). These features are possibly nanoparticles and were detected in areas where Co was also detected. The EELS Co maps indicated that the Co distribution was poorly defined. Like the images obtained for the “non-air sensitive TEM” (Figure 4.21), the nanoparticles here were also indistinct.

The TEM images of **(2)/A-SiO₂₋₆₀₀ (150 °C, N₂)** achieved without contact with air/moisture are shown in Figure 4.26. The images show relatively well-defined, bright features, typically 2-3 nm in diameter. These observed bright features may be cobalt particles since they generally correlate well with Co rich regions in the Co maps. This result contrasts with the TEM images obtained for materials exposed to air (Figure 4.24), which showed Co crystal lattice lines (d-spacing = 0.25 nm, CoO {NaCl, Fm-3m}). The lines seen in Figure 4.24 are thought to be due to the presence of cobalt silicate sites on the surface of the silica instead of distinct nanoparticles. However, the TEM images of **(2)/A-SiO₂₋₆₀₀ (150 °C, N₂)** achieved without exposure to air/moisture (Figure 4.26), suggest the possibility that heating

(2)/A-SiO₂₋₆₀₀ under nitrogen produces small cobalt particles, which then oxidise when they are exposed to the atmosphere to give CoO (NaCl, Fm-3m), as seen in the “non-air sensitive” TEM images (Figure 4.24).

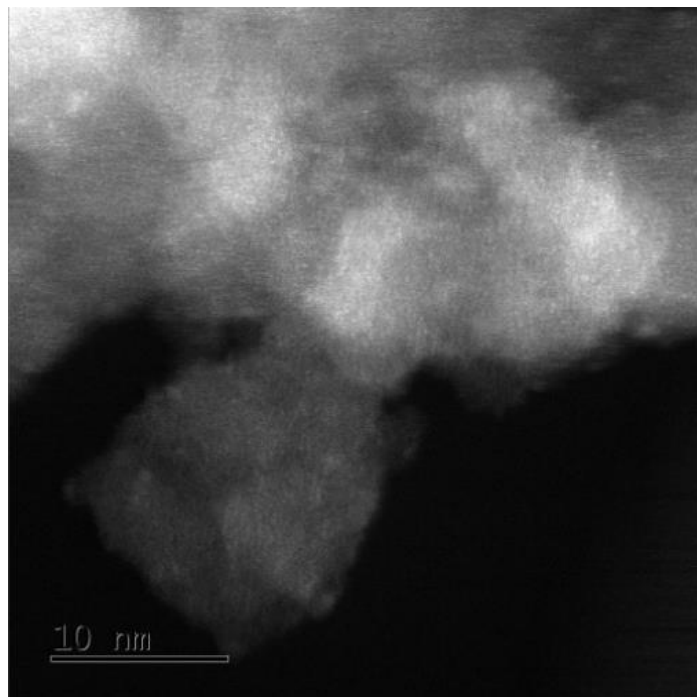


Figure 4.25. TEM image of (2)/A-SiO₂₋₆₀₀ (150 °C, H₂)

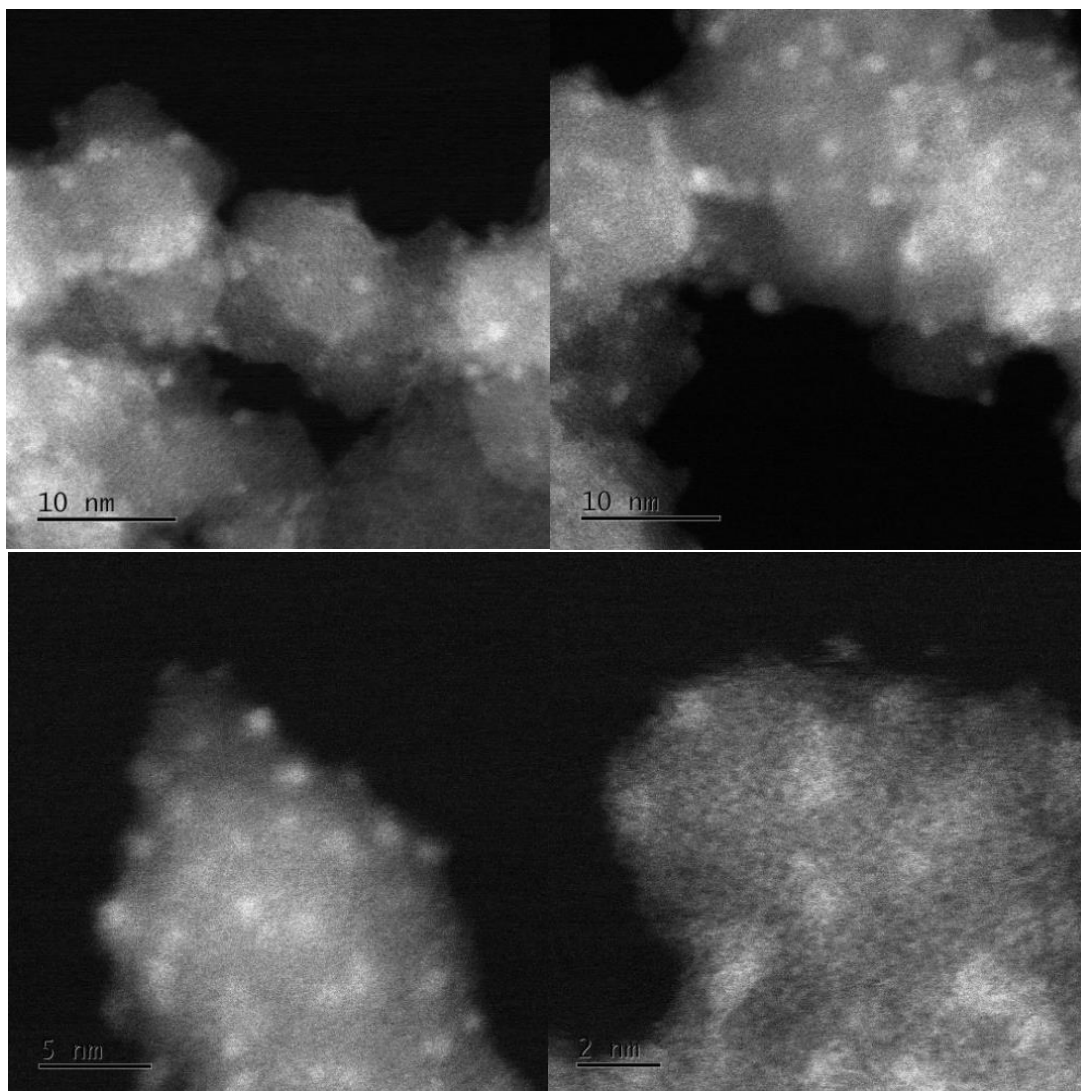
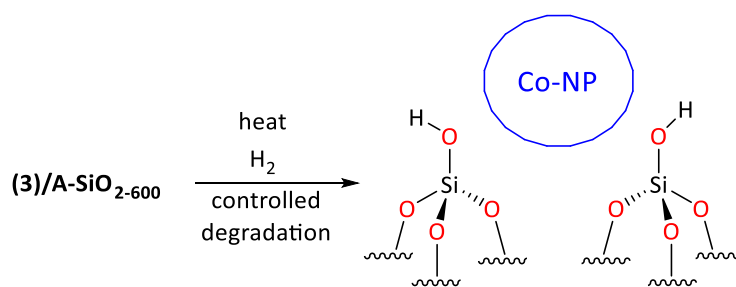


Figure 4.26. TEM images of **(2)/A-SiO₂₋₆₀₀** (150 °C, N₂)

4.2 The Reduction of **(3)/A-SiO₂₋₆₀₀**

Although the nature of the species present at the surface of **(3)/A-SiO₂₋₆₀₀**, where complex **3** is cobaltocene, was not clearly determined in this project, it was hoped that, as was the case for **(2)/A-SiO₂₋₆₀₀** (Section 4.1), the material would be amenable to reduction to nanoparticles (Scheme 4.4). Just as was done with **(2)/A-SiO₂₋₆₀₀**, an attempt to determine the reduction temperature of **(3)/A-SiO₂₋₆₀₀** was made through a TPR analysis.



Scheme 4.4. The proposed decomposition of $(3)/A-SiO_{2-600}$ into cobalt nanoparticles

4.2.1 Determining the Reduction Temperature of $(3)/A-SiO_{2-600}$ using Temperature Probe Reduction

TPR analysis was performed on a sample of $(3)/A-SiO_{2-600}$, using the same method used for the analysis of $(2)/A-SiO_{2-600}$ (Section 4.1.1). Disappointingly, the TPR analysis of the reduction of $(3)/A-SiO_{2-600}$ undertaken using this method did not show any hydrogen uptake (Figure 4.27), signifying no reduction occurred. However, during the TPR analysis, $(3)/A-SiO_{2-600}$ changes colour from purple to black. Additionally, purple crystals are seen to form throughout the TPR set-up (Figure 4.28). It was subsequently determined that these purple crystals are cobaltocene, which has sublimed from the surface of the silica. This result indicated that complex **3** is likely strongly physisorbed to the surface of silica, rather than reacting with the OH groups to form a -O-CoCp surface species as was reported previously by Lindblad *et al.*²¹

The colour change observed during TPR analysis of $(3)/A-SiO_{2-600}$ is likely to indicate that some of complex **3** present at the silica surface undergoes thermal degradation before sublimation from the surface occurs and/or that the thermal degradation products of cobaltocene were sequestered by the silica. Complex **3** is thermally stable up to 250 °C,²² but the TPR was heated $(3)/A-SiO_{2-600}$ up to 500 °C at a rate of 10 °C min⁻¹.

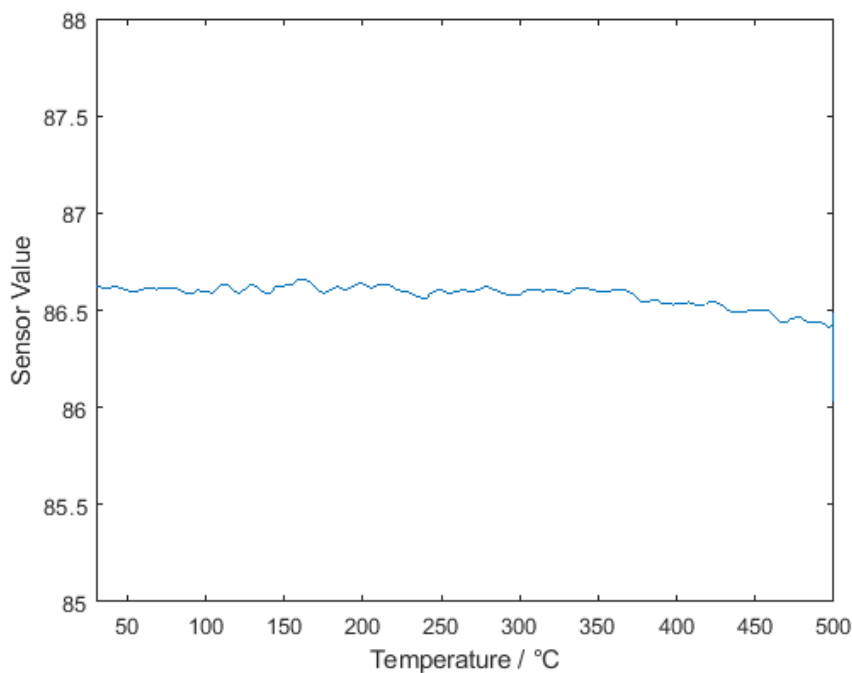


Figure 4.27. TPR Analysis of **(3)/A-SiO₂₋₆₀₀**

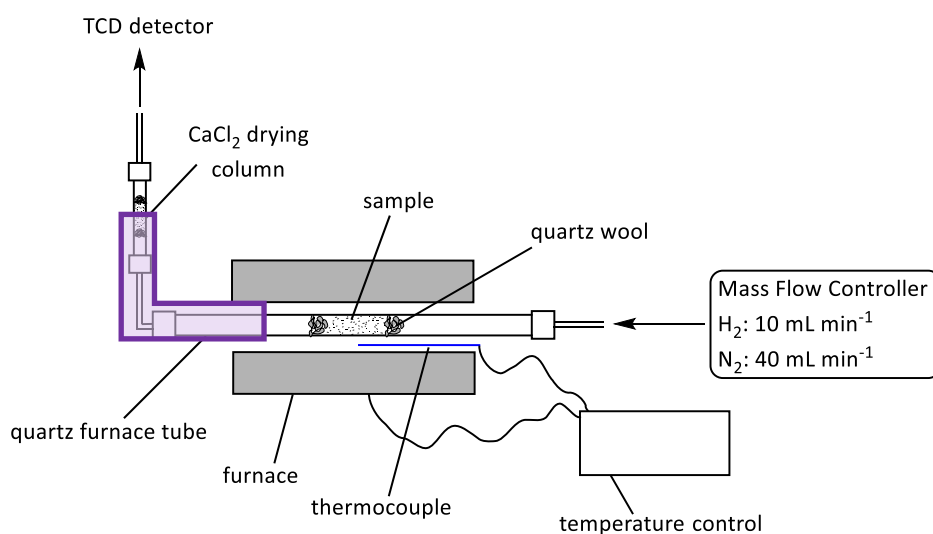


Figure 4.28. The general set up for TPR analysis with the area showing where the dark purple crystals of complex **3** were found after TPR analysis (highlighted by the purple box)

4.2.1.1 Investigating the Sublimation of Complex **3** from **(3)/A-SiO₂₋₆₀₀**

As TPR analysis has shown that some of complex **3** sublimates from the surface of **(3)/A-SiO₂₋₆₀₀** before decomposition, it was decided to investigate the sublimation of complex **3** from the silica surface. To this end, a portion of **(3)/A-SiO₂₋₆₀₀** was heated under vacuum to induce sublimation, within a vessel equipped with a cold finger present to collect any sublimed complex **3**. Although pure complex **3** sublimates at 40 °C under vacuum (0.1 mbar) when not on silica, heating a portion of the material **(3)/A-SiO₂₋₆₀₀** at 40 °C did not bring about any sublimation of complex **3**, consistent with moderately strong physisorption of complex **3** on the silica surface. Consequently, the temperature was slowly raised to

100 °C, with a ramp rate of 10 °C every 15 minutes, waiting for sublimation to occur. At ~90-100 °C, dark purple cobaltocene (**3**) condensed on the cold finger and the **(3)/A-SiO₂₋₆₀₀** material changed colour from purple to black. Confirmation of the dark purple crystals isolated on the cold finger as being Cp₂Co (**3**) was provided by CHN analysis. Together, these observations are consistent with the black material that results during TPR analysis of **(3)/A-SiO₂₋₆₀₀** being thermally decomposed complex **3** on silica (Section 4.2.1).

As it has been shown that complex **3** sublimates from the surface of **(3)/A-SiO₂₋₆₀₀** when heated, the loss of cobalt through sublimation was determined by ICP-OES (Table 4.5). The Aeroperl 300/30 silica does not turn white, so cobalt remains on the silica; complex **3** does not fully sublime from the surface and decomposes. From the data presented in Table 4.5 there is a clear loss of cobalt observed (0.5% w.t. Co) between **(3)/A-SiO₂₋₆₀₀** and **(3)/A-SiO₂₋₆₀₀** (post TPR). Approximately 38% of the cobalt present in **(3)/A-SiO₂₋₆₀₀** is lost due to sublimation of complex **3**, with the remaining 62% undergoing thermal decomposition and deposition on the surface of silica. Due to time constraints, this material could not be examined further. Despite the thermal degradation of the cobaltocene on the silica, since a significant quantity of cobalt is lost from the surface of **(3)/A-SiO₂₋₆₀₀** due to sublimation, this material is not deemed to be a suitable precursor for the preparation of silica-immobilised cobalt nanoparticles in a reproducible and well-defined manner.

Table 4.5. Co metal loading of **(3)/A-SiO₂₋₆₀₀** before and after TPR analysis/thermolysis, as determined by ICP-EOS

	(3)/A-SiO₂₋₆₀₀	(3)/A-SiO₂₋₆₀₀ (post TPR)
Cobalt w.t. % loading	1.3	0.8

4.3 Conclusions

Treatment of the material **(2)/A-SiO₂₋₆₀₀** under several different reactions conditions, across a range of temperatures (150, 200, 250 °C) and gas compositions (5% H₂/N₂, H₂, N₂) leads to the formation of Si-O-SiMe₃ surface species in each case as identified by SS-NMR spectroscopic analyses. This is in good agreement with surface area measurements of **(2)/A-SiO₂₋₆₀₀** (150 °C, H₂/N₂) that indicate further silylation of the silica surface occurs during the reaction of **(2)/A-SiO₂₋₆₀₀** with hydrogen as HMDS is generated, which in turn reacts with the silica. Magnetic studies on **(2)/A-SiO₂₋₆₀₀** and its derived materials to probe the cobalt loading and identity of the cobalt-containing species are inconclusive due to the similarity of the expected magnetic moment of Co²⁺ (1.73 μB) and cobalt nanoparticles (1.61 μB). When the μ_{eff} of **(2)/A-SiO₂₋₆₀₀** and its derived materials (spanning 0.22 – 0.28 μB) is compared to a “Co²⁺ on silica” standard (**Co(NO₃)₂·6H₂O/A-SiO₂₋₆₀₀**; Co²⁺, 2.2% w.t. Co), (0.25 μB), the values are similar. However, no conclusion about the oxidation state of the cobalt can be made without further study.

TEM images of **(2)/A-SiO₂₋₆₀₀ (150 °C, H₂)** (Figure 4.21), air-exposed **(2)/A-SiO₂₋₆₀₀** (Figure 4.22), and **(2)/A-SiO₂₋₆₀₀ (150 °C, air-exposed, H₂)** (Figure 4.23), where the sample has been exposed to the atmosphere, show what look like very small cobalt-containing particles (0.5 - 3 nm). In contrast, in the TEM image of **(2)/A-SiO₂₋₆₀₀ (150 °C, N₂)**, crystal lattice lines are observed with d-spacing that matches that of cubic CoO (NaCl, Fm-3m)¹⁸ on the surface of silica. While this was initially thought to indicate a layer of cobalt crystallites instead of nanoparticles, further study with “air-sensitive” TEM imaging showed that **(2)/A-SiO₂₋₆₀₀ (150 °C, N₂)** may have cobalt nanoparticles on the surface. So far, it has been tentatively concluded that heating **(2)/A-SiO₂₋₆₀₀** in the absence of hydrogen may produce small cobalt-containing nanoparticles (2-3 nm). The exact nature of these nanoparticles (metallic or oxide) has not been resolved.

The cobaltocene-derived material **(3)/A-SiO₂₋₆₀₀** was found to be an unsuitable precursor for silica-immobilised nanoparticle synthesis, as Cp₂Co (**3**) sublimed from the silica surface and no reduction occurred. Consequently, further investigation of this material was discontinued.

With materials with silica-immobilised cobalt-containing nanoparticles in hand, the derived materials of **(2)/A-SiO₂₋₆₀₀** and their use as hydrogenation catalysts will be explored.

4.4 References

1. E. Oakton, G. Vilé, D. S. Levine, E. Zocher, D. Baudouin, J. Pérez-Ramírez and C. Copéret, *Dalton Trans.*, 2014, **43**, 15138-15142.
2. J. M. Jabłoński, M. Wolczyk and L. Krajczyk, *J. Catal.*, 1998, **173**, 530 - 534.
3. G. Lapadula, A. Bourdolle, F. Allouche, M. P. Conley, I. d. Rosal, L. Maron, W. W. Lukens, Y. Guyot, C. Andraud, S. Brasselet, C. Coperet, O. Maury and R. A. Andersen, *Chem. Mater.*, 2014, **26**, 1062-1073.
4. L. T. Zhuravlev, *Colloids and Surfaces A: Physicochem. Eng. Aspects*, 2000, **173**, 1-38
5. Q. Zheng, D. Wang, F. Yuan, Q. Han, Y. Dong and Y. Liu, *Catalysis Letters*, 2016, **146**, 1535 - 1543.
6. D. Gajan, K. Guillois, P. Delicieux, J.-M. Basset, J.-P. Candy, V. r. Caps, C. Cope´ret, A. Lesage and L. Emsley, *J. Am. Chem. Soc.*, 2009, **131**, 14667-14669.
7. P. Laurent, L. Veyre, C. Thieuleux, S. Donet and C. Coperet, *Dalton Trans.*, 2013, **42**, 238-248.
8. G. A. Bain and J. F. Berry, *J. Chem. Educ.*, 2008, **85**, 532
9. X. M. Lin and C. M. Sorensen, *Langmuir*, 1998, **14**, 7140 - 7146.
10. J. R. Eone, O. M. Bengone and C. Goyhenex, *J. Phys. Chem. C*, 2019, **123**, 4531 - 4539.
11. L. Romaka, V. V. Romaka, N. Melnychenko, Y. Stadnyk, L. Bohun and A. Horyn, *J. Alloys Compd*, 2018, **739**, 771-779.
12. A. V. Morozkin, *Intermetallics*, 2012, **25**, 136-138.

13. J.-F. Liu, S. Yin, H.-P. Wu, Y. W. Zeng, X. R. Hu, Y. W. Wang, G. L. Lv and J.-Z. Jiang, *J. Phys. Chem. B*, 2006, **110**, 21588-21592.
14. H. N. Ok and J. G. Mullen, *Phys. Rev.*, 1968, **168**, 550-567.
15. W. L. Roth, *J. Phys. Chem. Solids*, 1964, **25**, 1-10.
16. S. Mourdikoudis, R. M. Pallares and N. T. K. Thanh, *Nanoscale*, 2018, **10**, 12871 - 12934.
17. W. Yan, V. Petkov, S. M. Mahurin, S. H. Overbury and S. Dai, *Catal. Commun.*, 2005, **6**, 404 - 408.
18. D. R. G. Mitchel, X. Wang and R. A. Caruso, *Micron*, 2008, **39**, 344 - 346
19. J. Liu, *Microsc. Microanal.*, 2004, **10**, 55 - 76
20. S. Sasaki, K. Fujino and Y. Takéuchi, *Proc. Japan Acad.*, 1979, **55**, 43 - 48.
21. T. Lindblad and B. Rebenstorf, *J. Chem. Soc. Faraday Trans.*, 1991, **87**, 2473-2478.
22. N.N. Greenwood, A. Earnshaw, *Chemistry of the Elements (Second Edition)*, Butterworth-Heinemann, Oxford, 1997, 1113-1143

Chapter 5: Catalytic Hydrogenation of Cinnamaldehyde with Supported Cobalt Catalysts

5.0 Introduction to Catalytic Hydrogenation Using Cobalt Nanoparticles

The work described so far in this thesis has been unable to definitively determine the surface structure of the products from heating of **(2)/A-SiO₂₋₆₀₀** {where **2** is [Co(N(TMS)₂)₂(THF)]} under hydrogen at relatively low temperatures <250 °C. However, there is some evidence that heating **(2)/A-SiO₂₋₆₀₀** under hydrogen at temperatures below 250 °C affords what are believed to be very small cobalt-containing particles (0.5 - 3 nm) on the silica surface. It has also been tentatively assumed that **(2)/A-SiO₂₋₆₀₀** may also afford cobalt-containing nanoparticles (2-3 nm) when heated in absence of hydrogen (<250 °C), (see Section 4.1.3). These cobalt-containing surface species have been difficult to characterise and analyse due to their air-sensitivity, leading to uncertainty about the exact surface structures present. Despite these uncertainties as to the exact nature of the cobalt species present on the silica surface following thermolysis of **(2)/A-SiO₂₋₆₀₀** under hydrogen, an exploration of the application of these supported cobalt-containing species in catalysis was carried out. With a view to gaining further insight into the nature of the supported cobalt materials prepared in this thesis by reduction of various supported cobalt complexes (see Chapter 4), a comparison of their catalytic hydrogenation activity and selectivity against that of previously reported cobalt systems was undertaken.

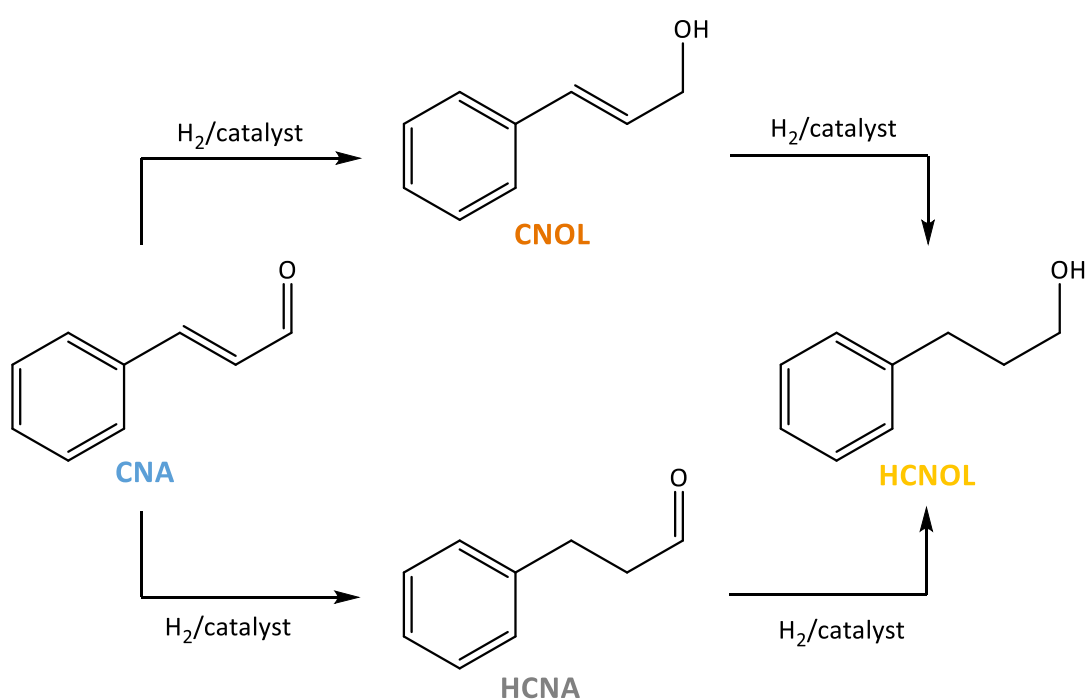
5.0.1 Catalytic Hydrogenation of Cinnamaldehyde (CNA)

As discussed in Section 1.1.3, an appropriate reaction of broad interest must be chosen to test and evaluate the catalytic performance of the various nanoparticle materials prepared herein. In this context, the catalytic hydrogenation of cinnamaldehyde (CNA) was chosen, as this reaction has two accessible and competing reaction pathways (Scheme 5.1) that could be used to explore, compare, and contrast catalytic selectivity, as well as substrate yield, as a function of nanoparticle composition and/or structure.

For α,β -unsaturated aldehydes, such as CNA, the hydrogenation of the C=C bond is favoured thermodynamically over the hydrogenation of the C=O bond.¹ The selective hydrogenation of the aldehyde over the alkene, to yield the non-thermodynamic hydrogenation product, is usually of greater interest.² Indeed, the selective reaction of CNA to the unsaturated CNOL is often used as a reaction to probe hydrogenation catalyst selectivity (Scheme 5.1).¹ It has been reported in the literature that cobalt-containing catalysts are particularly suitable for selective hydrogenation to the unsaturated alcohol, including intermetallic and bimetallic particles,^{3,4} cobalt oxide particles,⁵ metallic cobalt particles,^{6,7} and cobalt aluminate/silicate/titanate sites.⁸ However, the state of the cobalt can change the selectivity of the reaction with metallic cobalt having been found more selective towards CNOL⁵ and smaller particles (6 nm) being more selective towards CNOL than larger particles (30-40

nm).⁶ As cobalt nanoparticles are the catalysts studied in this project, it is hoped that the selectivity of the hydrogenation of CNA will reveal more about the catalysts in this project.⁹

The methodology used in this project for supported cobalt-containing nanoparticle-mediated CNA hydrogenation is based on that used by Dragoi *et al.*,⁹ which does not use either high reaction temperatures or high pressures of hydrogen. However, this method does require the reaction to be heated to 150 °C, which is coincidentally the temperature of reaction used for the preparation of the various potential catalysts as described in Chapter 4. This factor is important since further reaction of the catalytic materials could possibly occur during hydrogenation testing at this temperature, and hence the catalysts may change over the period of the reaction time.



Scheme 5.1. Possible routes for the hydrogenation of cinnamaldehyde (CNA) to cinnamyl alcohol (CNOL), hydrocinnamaldehyde (HCNA), and hydrocinnamyl alcohol (HCNOL)⁶

5.1 Results and Discussion

5.1.1 Catalyst Selection

It is important to establish how the various materials derived from **(2)/A-SiO₂₋₆₀₀** perform in CNA hydrogenation against a suitable reference catalyst. In this context, a suitable reference catalyst would be one that is already a well-established catalyst in the literature and one that can be prepared through a similar method to that used in this thesis, namely the reduction of a cobalt precursor on the surface of silica. Silica impregnated with Co(NO₃)₂·6H₂O (denoted here as **Co(NO₃)₂/SiO₂**) was chosen as a reference catalyst system, since it is a known cobalt catalyst for the hydrogenation of CNA, exhibiting selectivity towards CNOL as reported by Dragoi *et al.* (Scheme 5.1).⁹ Their catalyst was prepared by incipient wetness impregnation of SBA-15 silica with an aqueous or ethanolic solution of

Co(NO₃)₂·6H₂O to obtain a 5% Co wt. loading, followed by calcination in air at 500 °C, then reduction under hydrogen.⁹ Their sample prepared by aqueous impregnation was >60% selective to CNOL below 20% conversion of CNA. Consequently, to enable a comparison with the various Co/oxide support materials prepared during this thesis, Aeroperl 300/30 silica was impregnated with an aqueous solution of Co(NO₃)₂·6H₂O *via* incipient wetness to a 2.3% wt. Co loading, using a method similar to that of Dragoi *et al.*,¹⁰ and then calcined under air at 120 °C for 24 hours prior to reduction. In the study by Dragoi *et al.* and in this project, **Co(NO₃)₂/SiO₂** was reduced under hydrogen at 500 °C. The presence of nanoparticles in the resulting material (Co *fcc*,¹¹ size = 8 nm) was confirmed using PXRD analysis,^{*} with the cobalt loading (2.3% w.t. Co) being determined by ICP-OES methods. The cobalt particle size obtained here is comparable to that reported by Dragoi *et al.* (size = 9 nm).⁹

The hydrogenation of CNA was carried out using the **Co(NO₃)₂/SiO₂** (reference catalyst), employing the following reaction conditions: 9 h, 150 °C, 20 mL min⁻¹ H₂ bubbled into flask, stirring speed: 250 rpm; details of the experimental method used are given in Section 6.0.3.16. During the reaction, no colour change of the reaction solution occurred and no solid noticeably formed. Under these conditions, the reference catalyst **Co(NO₃)₂/SiO₂** showed 11 % yield of CNOL, as determined by GC-FID analysis of the reaction mixture post-work-up.[†] This CNA to CNOL yield is comparable to that reported by Dragoi *et al.*, ~20% conversion with a 65% selectivity towards CNOL.⁹ The yield of the products of the hydrogenation of CNA catalysed by the **Co(NO₃)₂/SiO₂** catalyst compared to Dragoi *et al.*'s catalysts is in very good agreement given different cobalt loading and support.

5.1.1.1 The Catalytic Performance for Hydrogenation of CNA Using (2)/A-SiO₂₋₆₀₀ Reduced at T = 150, 200, and 250 °C

The material **(2)/A-SiO₂₋₆₀₀** was reduced under 5% H₂/N₂ gas at different temperatures as described in Chapter 4, affording the various reduced systems denoted **(2)/A-SiO₂₋₆₀₀ (T °C, 5% H₂/N₂)** where T = 150, 200, and 250 °C, respectively. The material **(2)/A-SiO₂₋₆₀₀ (150 °C, 5% H₂/N₂)**, prepared as described in Section 4.1.2.1, a homogeneous blue colour, was used for catalysis without further elaboration. It was charged into the reaction vessel in a nitrogen-filled glovebox to avoid exposure to air. In contrast, as described in Section 4.1.2.2, when **(2)/A-SiO₂₋₆₀₀ (200 °C, 5% H₂/N₂)** and **(2)/A-SiO₂₋₆₀₀ (250 °C, 5% H₂/N₂)** are prepared using an identical methodology as for **(2)/A-SiO₂₋₆₀₀ (150 °C, 5% H₂/N₂)**, but with higher reduction temperatures, they are isolated as visibly inhomogeneous materials, comprising two different layers of coloured materials, blue and black, as

^{*} The mean crystallite size (8 nm) of Co in **Co(NO₃)₂/SiO₂** was calculated from the half-maximum breadth of the (111) peak of fcc Co metal determined by a Gaussian fit and the Scherrer equation: ($d_{hkl} = \lambda/\beta \cos\theta$), with a shape factor assumed to be 1.

[†] GC-FID is used to determine the number of moles of each expected reactant and product (CNA, CNOL, HCNA, and HCNOL) using an internal standard, as described in Section 6.0.3.16

shown in Figure 5.1. It proved impossible to eliminate this problem (see Chapter 4) and since the reduction set-up used did not allow for clean separation of the black and blue layers of **(2)/A-SiO₂₋₆₀₀ (200 °C, 5% H₂/N₂)** and **(2)/A-SiO₂₋₆₀₀ (250 °C, 5% H₂/N₂)**, so the two layers were thoroughly mixed prior to using for catalysis. This was thought to at least allow inclusion of material prepared at higher temperature in the study and would highlight whether dramatic differences were seen.

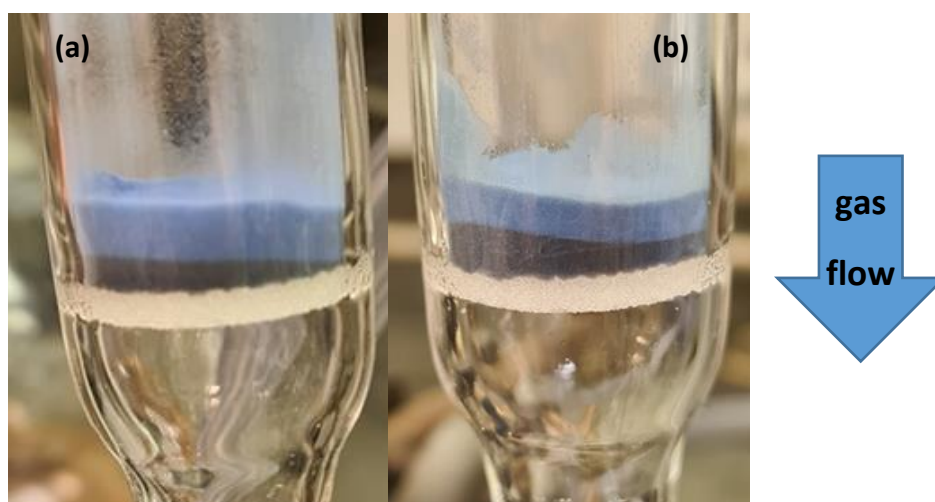


Figure 5.1. (a) **(2)/A-SiO₂₋₆₀₀ (200 °C, H₂/N₂)**; (b) **(2)/A-SiO₂₋₆₀₀ (250 °C, H₂/N₂)**

The catalytic hydrogenation of CNA using **(2)/A-SiO₂₋₆₀₀ (T °C, 5% H₂/N₂)**, where T = 150, 200, and 250 °C, was carried out using the same test conditions as employed with the reference catalyst **Co(NO₃)₂/SiO₂** (Section 5.1.1). During CNA hydrogenation, the reaction solution showed a visible colour change from colourless to bright yellow, with a yellow crystalline solid forming on the gas inlet frit (see Section 6.0.3.16 for reaction set-up). A colourless liquid also condensed on the sides of the flask. In contrast, no colour change, no formation of a yellow solid, and no condensation of liquid were observed when the reference catalyst **Co(NO₃)₂/SiO₂** was employed for the hydrogenation of CNA (under identical test conditions).

A preliminary catalysis/GC study was undertaken. The GC-FID derived % yields of each product and the amount (%) of CNA starting material remaining after the hydrogenation reaction using catalysts **(2)/A-SiO₂₋₆₀₀ (T °C, 5% H₂/N₂)**, where T = 150, 200, and 250 °C, are presented in Figure 5.2. All three catalysts (**(2)/A-SiO₂₋₆₀₀ (T °C, 5% H₂/N₂)**, where T = 150, 200, and 250 °C) give rise to low conversions of CNA to the various products (10 – 12% of CNA was converted), and no specific selectivity towards a particular product was observed.

The combined mass balance for CNA, CNOL, HCNA, and HCNOL is only 91-94%, indicating the formation of other side-products. The identity of the CNOL, HCNA, and HCNOL products was confirmed by GC-FID analysis of authentic samples. In contrast, under the same reaction conditions,

the reference catalyst $\text{Co}(\text{NO}_3)_2/\text{SiO}_2$ does not form any other products beyond CNOL, HCNA, and HCNOL upon hydrogenation of CNA, in agreement with the results reported for the related silica-supported catalyst described by Dragoi *et al.*, who used the same mild hydrogenation conditions as chosen for this project.⁹

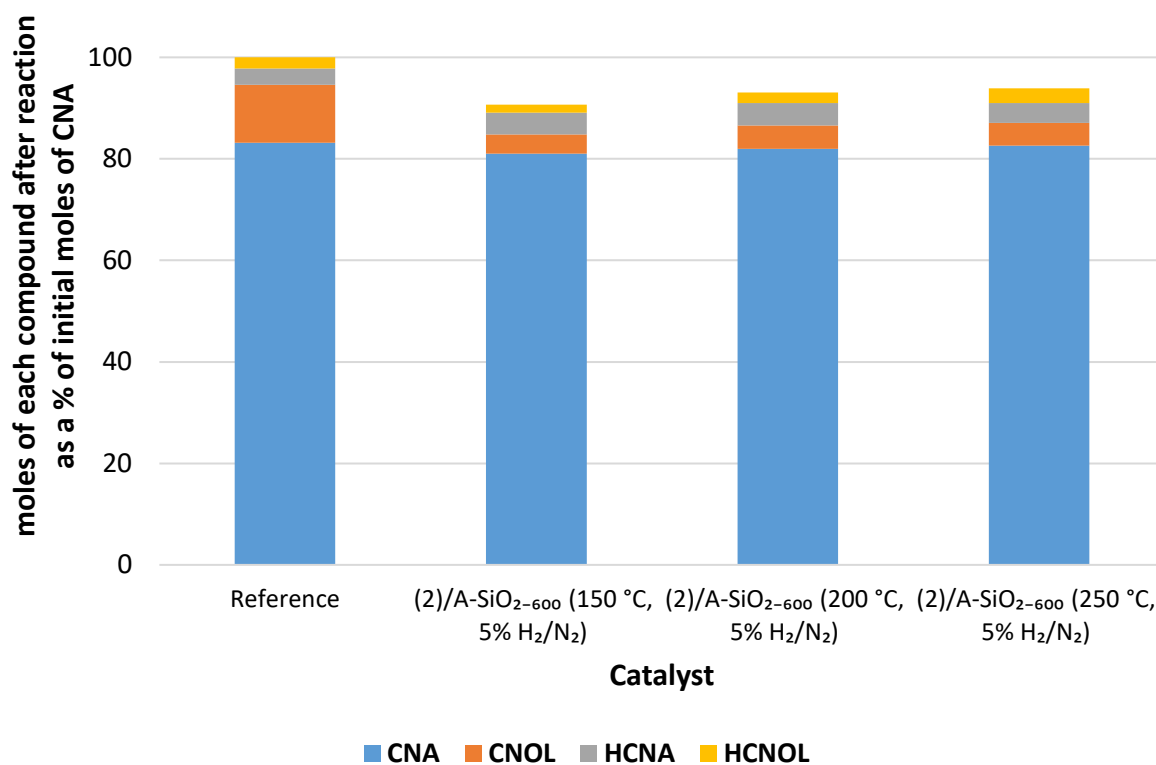


Figure 5.2. Product distribution from the catalytic hydrogenation of CNA using $(2)/\text{A-SiO}_{2-600}$ (T °C, 5% H_2/N_2) where $T = 150, 200, \text{ and } 250$ °C; reaction conditions: 9 h, 150 °C, $20 \text{ mL min}^{-1} \text{ H}_2$, stirring speed: 250 rpm
Errors: ± 2 % for CNA; ± 1 % for CNOL; ± 1 % for HCNA; ± 1 % for HCNOL

5.1.1.1.1 Origin of the Poor Mass Balance Measured for the Hydrogenation of CNA

To probe the poor substrate/product mass balance measured for the hydrogenation of CNA using $(2)/\text{A-SiO}_{2-600}$ (T °C, 5% H_2/N_2), where $T = 150, 200, \text{ and } 250$ °C, the GC-FID chromatogram from each reaction was examined further. On closer inspection, the GC-FID analysis of the reaction mixture obtained following hydrogenation of CNA with each of the these three catalysts revealed a small quantity of product with a retention time of 14.5 minutes and a group of 13 more side products with retention times above 16 mins (present in very small amounts), which do not appear in the GC-FID of the CNA hydrogenation using the reference catalyst $\text{Co}(\text{NO}_3)_2/\text{SiO}_2$. To aid in the observation of these side products, catalytic hydrogenation of CNA using $(2)/\text{A-SiO}_{2-600}$ (150 °C, N_2 , then H_2 , vacuum) (catalyst discussed in Section 5.1.1.5), reaction conditions: 33 h, 150 °C, $20 \text{ mL min}^{-1} \text{ H}_2$, stirring speed: 250 rpm, was performed. After 33 h, comparatively small quantities of one side-product with

retention time 14.5 mins and 16 side-products with retention times between 16 – 25 mins were observed (Figure 5.3).

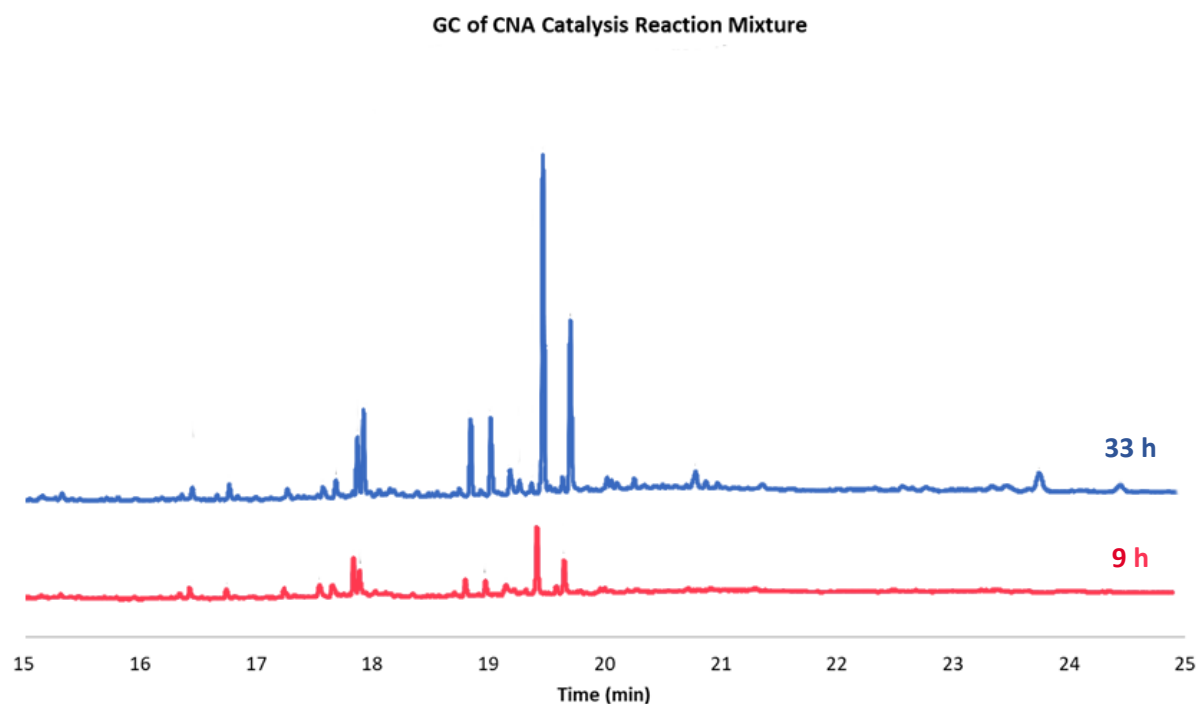


Figure 5.3. GC analysis of products formed during the catalytic hydrogenation of CNA using **(2)/A-SiO₂₋₆₀₀** (150 °C, N₂, then H₂, vacuum), reaction conditions: 150 °C, 20 mL min⁻¹ H₂, monitored after 9 and 33 h of reaction time.

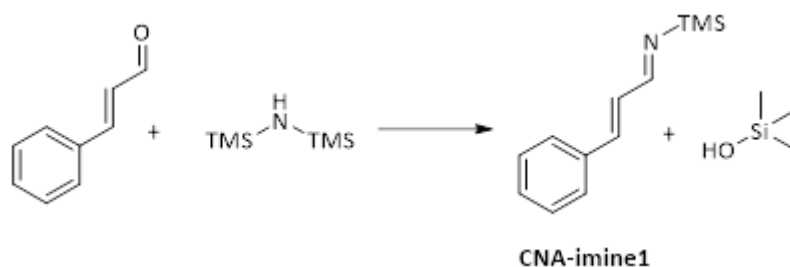
5.1.2.1 Formation and Characterisation of Side-products Formed During Hydrogenation of CNA

5.1.2.1.1 Formation and Characterisation of Side-product: CNA-Imine1

Given that the catalysts **(2)/A-SiO₂₋₆₀₀** (T °C, 5% H₂/N₂) [T = 150, 200, and 250 °C] are all likely to have *bis*(trimethylsilyl)amine[‡] on their surfaces, while the reference catalyst **Co(NO₃)₂/SiO₂** doesn't, it was suspected that HN(TMS)₂ was reacting with the CNA to form (1*E*,2*E*)-3-phenyl-*N*-(trimethylsilyl)-2-propen-1-imine (denoted as CNA-imine1) (Scheme 5.2).

It was determined in Section 4.1.3.2.2 that the -NSiMe₃ tethered to the cobalt was lost during the synthesis of **(2)/A-SiO₂₋₆₀₀** (150 °C, 5% H₂/N₂). SS-NMR analysis has not been performed on **(2)/A-SiO₂₋₆₀₀** (200 °C, 5% H₂/N₂) and **(2)/A-SiO₂₋₆₀₀** (250 °C, 5% H₂/N₂), but it can be assumed that the cobalt-tethered -NSiMe₃ was also lost in these materials, as they were heated to higher temperatures than **(2)/A-SiO₂₋₆₀₀** (150 °C, 5% H₂/N₂), and the loss of the HDMS occurs at temperatures under 150 °C.

[‡] It is known from ¹H SS-NMR analysis of **(2)/A-SiO₂₋₆₀₀** (150 °C, 5% H₂/N₂) (Section 4.1.3.2) that *bis*(trimethylsilyl)amine is released from the cobalt centre.



Scheme 5.2. CNA and HMDS reacting to give (1E,2E)-3-Phenyl-N-(trimethylsilyl)-2-propen-1-imine side-product (denoted as CNA-imine1)

To fully verify that the poor substrate/product mass balance was indeed a result of *bis*(trimethylsilyl)amine reacting with CNA to form CNA-imine1, a solution of *bis*(trimethylsilyl)amine and CNA was heated at 150 °C without any catalyst present for a period of 6 days. Over the reaction period the yellow solution turned dark red, and a colourless liquid condensed on the walls of the reaction flask. Vacuum distillation of the reaction mixture afforded a dark red oil, which gave a single signal by GC-FID with a retention time of 14.5 minutes consistent with this red oil being CNA-imine1, something confirmed by multinuclear NMR spectroscopy. Together, this reactivity and associated formation of the imine helps to account for 37 - 44 % of the observed discrepancy in substrate/product mass balance determined for the catalytic transformations described in Section 5.1.1.1. The inclusion of CNA-imine in the selectivities of reactions using **(2)/A-SiO₂₋₆₀₀ (T °C, 5% H₂/N₂)**, where T = 150, 200, and 250 °C is shown in Figure 5.4.

It is important to note that the amount of CNA-imine1 that can be formed during the catalysis reaction is restricted by the amount of amine that is present in the reaction mixture. Since the cobalt centre on **(2)/A-SiO₂₋₆₀₀** is mono-grafted with one -N(TMS)₂ ligand (see Section 3.1.2), the maximum amount of CNA-imine1 that can form during the hydrogenation reaction is 0.044 mmol, equating to 6% of the starting CNA. Examination of the GC-FID data from the catalyst test reactions with reactions using **(2)/A-SiO₂₋₆₀₀ (T °C, 5% H₂/N₂)**, where T = 150, 200, and 250 °C, it was found that 3 – 4 % of CNA was indeed converted to CNA-imine1 over a reaction period of 9 hours, which accounts for up to 44% of the missing mass balance. Notably after 33 h, in the catalyst test reaction mediated by **(2)/A-SiO₂₋₆₀₀ (150 °C, N₂, then H₂, vacuum)** (catalyst from Section 5.1.1.5), reaction conditions: 33h, 150 °C, 20 mL min⁻¹ H₂, stirring speed: 250 rpm), the formation of CNA-imine1 is 6%, which is in line with the predicted maximum.

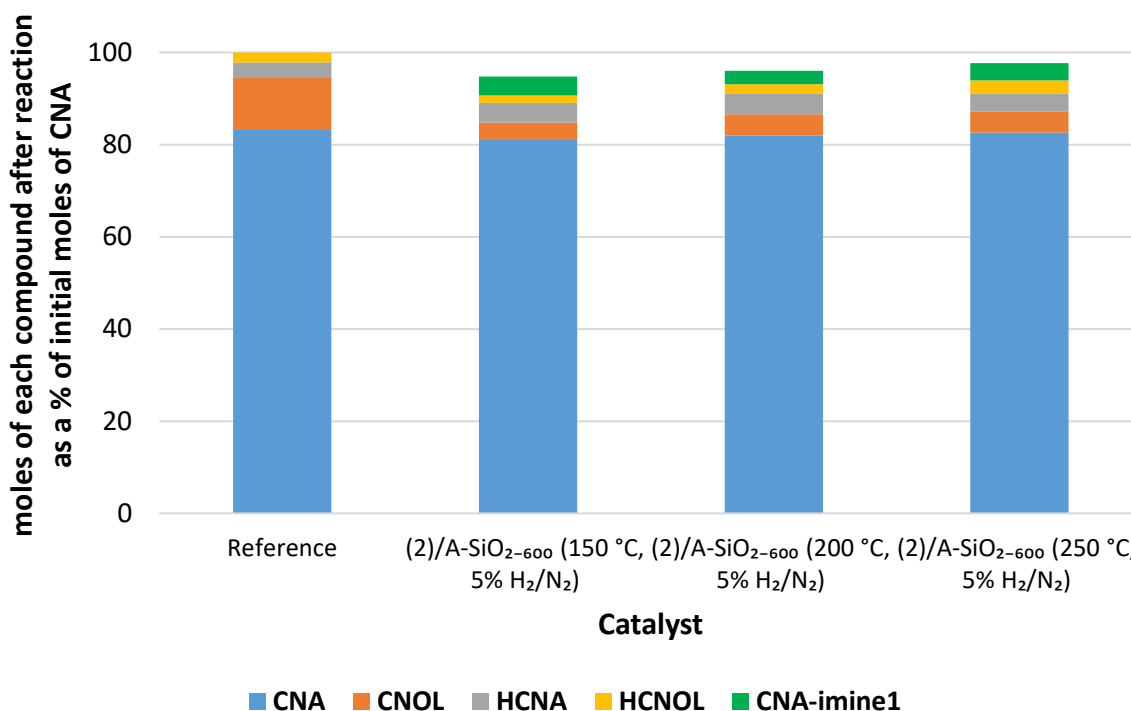


Figure 5.4. Product distribution from the catalytic hydrogenation of CNA using (2)/A-SiO₂₋₆₀₀ (T °C, 5% H₂/N₂) where T = 150, 200, and 250 °C, including CNA-imine1; reaction conditions: 9 h, 150 °C, 20 mL min⁻¹ H₂, stirring speed: 250 rpm
Errors: ±2 % for CNA; ±1 % for CNOL; ±1% for HCNA; ±1 % for HCNOL; ±2 % for CNA-imine1

5.1.2.1.2 The Formation of Other Side-Products

Taking the formation of CNA-imine1 into account during the catalytic hydrogenation of CNA using (2)/A-SiO₂₋₆₀₀ (150 °C, N₂, then H₂, vacuum) {reaction conditions: 33h, 150 °C, 20 mL min⁻¹ H₂, stirring speed: 250 rpm}, there is still an additional 10% of the mass balance that is not accounted for by CNA, CNOL, HCNA, HCNOL, or CNA-imine1 formation after 33 h. The remaining poor substrate/product mass balance is due to 16 unknown side products as observed by GC-FID (Section 5.1.1.1.1), with retention times between 16 – 25 minutes (Figure 5.3). These side-products are not formed from HMDS, as all of the HMDS has been converted into CNA-imine1. These 16 unknown side-products are also less volatile, “heavier” (retention times: 16 – 25 mins), and possibly more polar than CNA and its hydrogenation products (retention times: 10 – 12 minutes). Notably, none of these “heavy” products are formed during hydrogenation of CNA mediated by the reference catalyst.[§]

A possible origin of these 16 “heavy” side-products is that they are formed from CNA (and its derivatives) reacting with themselves in the presence of cobalt. According to Chirieac *et al.*, cobalt-based catalysts are known to catalyse the formation of CNOL from CNA, but cobalt can also be an active catalyst for other reactions, such as intramolecular cyclization of cinnamyl derivatives,

[§] Reference catalyst: Aeroperl 300/30 silica impregnated with an aqueous solution of Co(NO₃)₂·6H₂O via incipient wetness (2.3% w.t Co loading), calcined at 120 °C, then reduced under H₂ at 500 °C

alkoxylation, and ester exchange by acting as a base, something that has been previously seen for “uncalcined layered double hydroxides”.¹² Similar reactions may be occurring, giving rise to the 16 side-products seen by GC-FID. A possible example is the compound in Figure 5.5, CNA-ester1. It can be derived from cinnamaldehyde through the Tischenko reaction;¹³ once formed this could be followed by further intramolecular Diels-Alder reactions,¹⁴ leading to cyclisation (Scheme 5.3). Note, due to time constraints, no GC-MS data could be obtained to probe the nature of the unknown side products with GC-FID retention times 16 – 25 minutes.

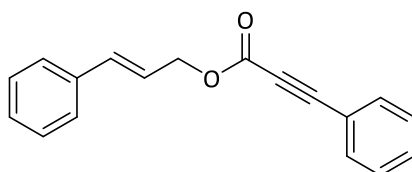
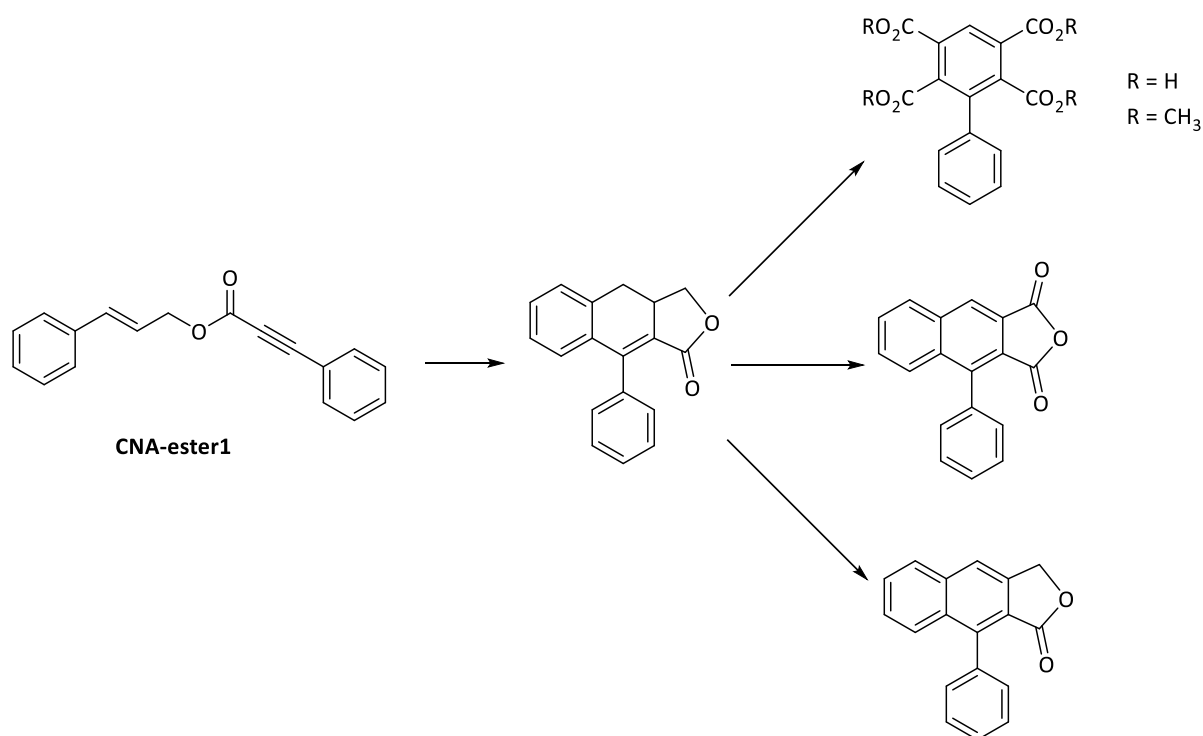


Figure 5.5. A possible side product derived from trans-cinnamyl alcohol, denoted as CNA-ester1



Scheme 5.3. Further intramolecular Diels-Alder reactions of CNA-ester1¹⁵

A graphical representation of the formation of the various products from the hydrogenation of CNA by **(2)/A-SiO₂₋₆₀₀ (150 °C, N₂, then H₂, vacuum)** as a function of time is given in Figure 5.6. Of note, compounds “Unknowns” 9, 11, and 14 appear after 3, 6, and 8 h, respectively, of reaction time, while “Unknowns” 10, 15, and 16 do not appear until after 9 h. “Unknowns” 4 and 5 show a possible decrease in concentration over time after they have formed. This possible decrease in concentration of these side-products after they have formed indicates that “Unknowns” 4 and 5 may continue to

react further. This would be in line with the proposal above that compounds similar to CNA-ester1 are forming from CNOL, and then undergo further transformations such as cyclisation.

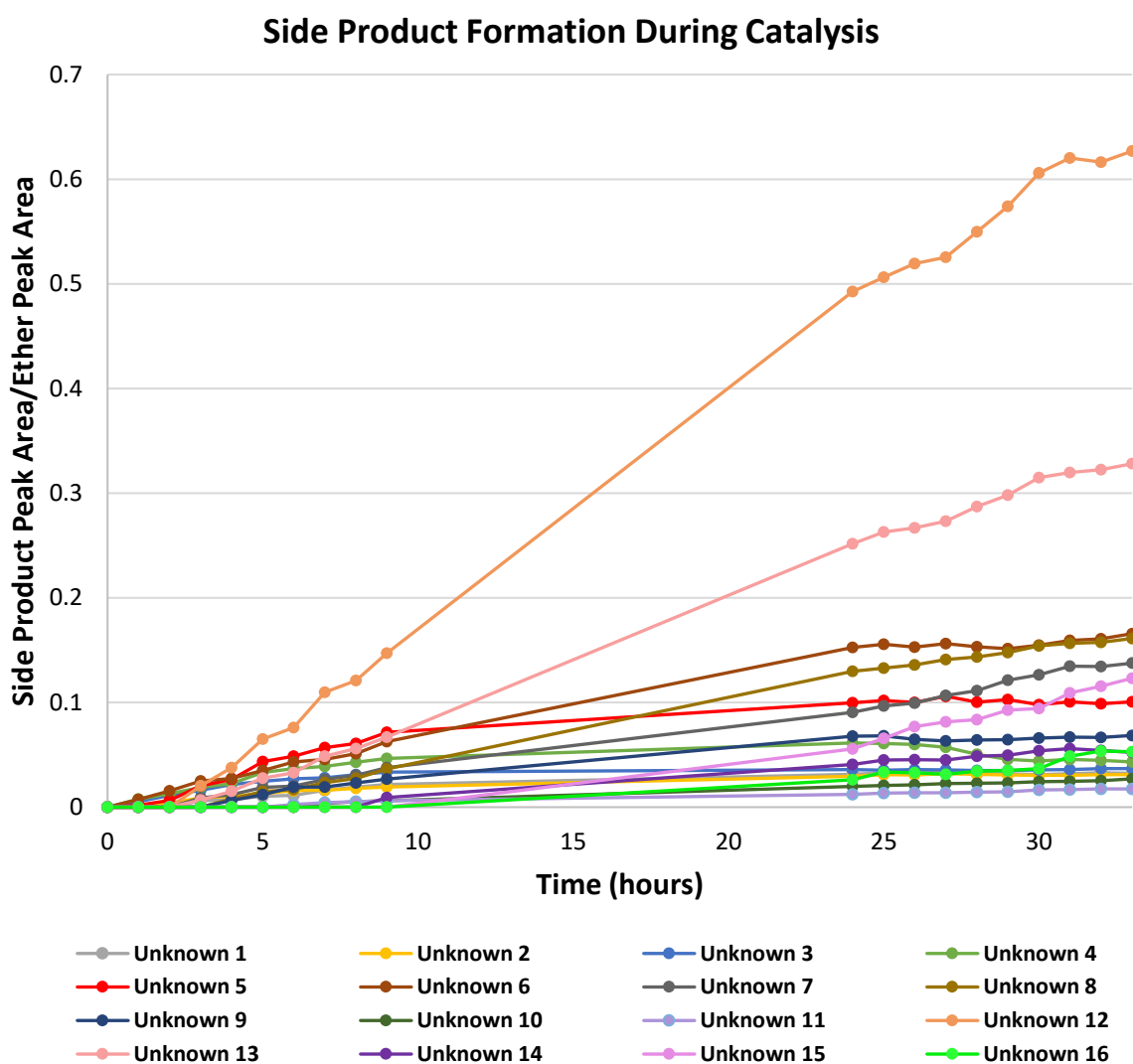


Figure 5.6. The formation of the side-production as a function of time from the catalytic hydrogenation of CNA over 33 h mediated by (2)/A-SiO₂₋₆₀₀ (150 °C, N₂, then H₂, vacuum); reaction conditions: 150 °C, 20 mL min⁻¹ H₂, 33 h, stirring speed: 250 rpm.

5.1.1.3 Reducing the Amount of Surface Amine on Catalysts via Heating Under Vacuum or Pentane Wash

As discussed in Section 5.1.1.1.1, the formation of CNA-imine1 and potential the other unwanted side-products that have been observed in the GC-FID analysis of the post-catalysis hydrogenation reactions have, in part, been attributed to the presence of bis(trimethylsilyl)amine on the surface of (2)/A-SiO₂₋₆₀₀ (T °C, 5% H₂/N₂) [T = 150, 200, and 250 °C]. Consequently, to reduce the formation of side-products during catalysis, surface-bound amine must be removed from the catalysts prior to their use. This has been attempted in two different ways after the reduction was performed: i) heating the catalyst under vacuum and ii) more extensive washing of the catalyst with pentane.

To this end, **(2)/A-SiO₂₋₆₀₀ (150 °C, 5% H₂/N₂)** was treated post-reduction by either heating at 150 °C under vacuum or by washing several times with dry pentane, to produce **(2)/A-SiO₂₋₆₀₀ (150 °C, 5% H₂/N₂, vacuum)** and **(2)/A-SiO₂₋₆₀₀ (150 °C, 5% H₂/N₂, pentane-wash)**, respectively. Subsequently, the performance of both materials was explored for the hydrogenation of CNA under the same reaction conditions that were described in Section 5.1.1.

The product distributions achieved for CNA hydrogenation using **(2)/A-SiO₂₋₆₀₀ (150 °C, 5% H₂/N₂, vacuum)** and **(2)/A-SiO₂₋₆₀₀ (150 °C, 5% H₂/N₂, pentane-wash)** are summarised in comparison to the as-prepared material **(2)/A-SiO₂₋₆₀₀ (150 °C, 5% H₂/N₂)** in Figure 5.7. Compared to the performance of the as-prepared material **(2)/A-SiO₂₋₆₀₀ (150 °C, 5% H₂/N₂)**, use of both **(2)/A-SiO₂₋₆₀₀ (150 °C, 5% H₂/N₂, vacuum)** and **(2)/A-SiO₂₋₆₀₀ (150 °C, 5% H₂/N₂, pentane-wash)** results in better substrate/product mass balance. This has been attributed to lower amounts of CNA-imine1 being formed with these latter two catalysts following removal of surface amine. The best substrate/product mass balance obtained (96%) is with **(2)/A-SiO₂₋₆₀₀ (150 °C, 5% H₂/N₂, vacuum)**.

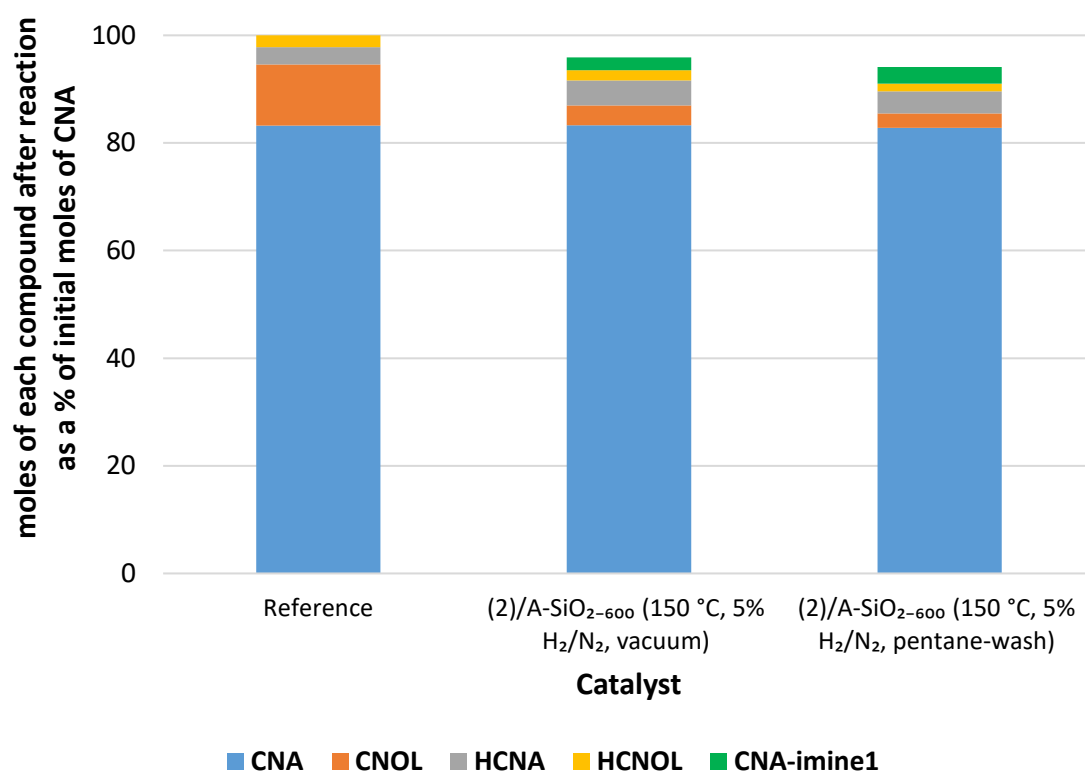


Figure 5.7. Product distribution from the catalytic hydrogenation of CNA using **(2)/A-SiO₂₋₆₀₀ (150 °C, 5% H₂/N₂, vacuum)** and **(2)/A-SiO₂₋₆₀₀ (150 °C, 5% H₂/N₂, pentane-wash)**; reaction conditions: 9 h, 150 °C, 20 mL min⁻¹ H₂, stirring speed: 250 rpm

Errors: ±2 % for CNA; ±1 % for CNOL; ±1% for HCNA; ±1 % for HCNOL; ±2 % for CNA-imine1

5.1.1.4 Thermal Treatment of (2)/A-SiO₂₋₆₀₀ In Absence of Hydrogen

As described in Chapter 4, heating **(2)/A-SiO₂₋₆₀₀** under hydrogen and under nitrogen produces different surface species. Consequently, two catalysts were prepared by heating **(2)/A-SiO₂₋₆₀₀** under a flow of nitrogen (50 mL min⁻¹) at 150 and 250 °C, giving **(2)/A-SiO₂₋₆₀₀ (150 °C, N₂, vacuum)** and **(2)/A-SiO₂₋₆₀₀ (250 °C, N₂, vacuum)**, respectively, without exposure to hydrogen gas.

Subsequently, the hydrogenation of CNA mediated by **(2)/A-SiO₂₋₆₀₀ (150 °C, N₂, vacuum)** and **(2)/A-SiO₂₋₆₀₀ (250 °C, N₂, vacuum)** was explored; results are summarised in Figure 5.8. Notably, both **(2)/A-SiO₂₋₆₀₀ (150 °C, N₂, vacuum)** and **(2)/A-SiO₂₋₆₀₀ (250 °C, N₂, vacuum)** are catalytically active, with a significant selectivity towards HCNA (11-16±1%). The overall selectivity change to HCNA is accompanied by increased overall consumption of CNA (26 – 28±1% *cf.* 17- 19 %), with similar yields of CNOL and HCNOL being obtained as for previously studied **(2)/A-SiO₂₋₆₀₀**-derived catalysts (Sections 5.1.1.1 & 5.1.1.3). These differences are in agreement with the generation of different surface structures according to the conditions used for their preparation (either heating under hydrogen or under nitrogen). Similarly, these observations are consistent with the differences between the materials indicated by TEM imaging (Section 4.1.3.6), where those heated under hydrogen show indistinct particles (0.5 – 3 nm) and those heated under nitrogen show bright, defined particles (2 – 3 nm).

The selectivity of both **(2)/A-SiO₂₋₆₀₀ (150 °C, N₂, vacuum)** and **(2)/A-SiO₂₋₆₀₀ (250 °C, N₂, vacuum)** towards HCNA rather than CNOL is unexpected as it has been reported in the literature that cobalt is particularly suitable for selective hydrogenation to the unsaturated alcohol.^{3, 4, 5, 7} Indeed, it is known that the addition of cobalt to a Pt-based nanoparticle improves the selectivity towards CNOL,¹⁴ *e.g.* Pt-Co/SBA-15 enhances the yield of cinnamyl alcohol compared with Pt/SBA-15, as reported by Zheng *et al.*¹⁶ Elemental cobalt is also known to improve selectivity and conversion towards CNOL for cobalt oxide particles used for CNA hydrogenation.⁵

Currently, it remains unclear why a different product selectivity results from the hydrogenation of CNA with **(2)/A-SiO₂₋₆₀₀ (150 °C, N₂, vacuum)** and **(2)/A-SiO₂₋₆₀₀ (250 °C, N₂, vacuum)** compared with the reference catalyst and the catalysts prepared by heating under hydrogen. However, it is suggested tentatively that the changes in selectivity towards the saturated aldehyde HCNA are due to the size of the cobalt-containing particles produced under the different conditions. It has been reported previously that relatively “large sizes of Co crystallites” are required for the selectivity towards CNOL,¹⁷ and the cobalt structures on **(2)/A-SiO₂₋₆₀₀ (150 °C, N₂, vacuum)** and **(2)/A-SiO₂₋₆₀₀ (250 °C, N₂, vacuum)** appear to be small (2 - 3 nm in TEM imaging, Section 4.1.3.6), and may be the origin of the switch in selectivity to HCNA.

It should be noted that use of both the materials **(2)/A-SiO₂₋₆₀₀ (150 °C, N₂, vacuum)** and **(2)/A-SiO₂₋₆₀₀ (250 °C, N₂, vacuum)** still lead to the formation of imine (CNA-imine1), consistent with an incomplete surface amine removal through simple mild thermal methods alone. **(2)/A-SiO₂₋₆₀₀ (250 °C, N₂, vacuum)** produces less CNA-imine1 as a side-product than **(2)/A-SiO₂₋₆₀₀ (150 °C, N₂, vacuum)**: 2±1 vs 4±1% CNA-imine1, respectively. This is likely to be because **(2)/A-SiO₂₋₆₀₀ (250 °C, N₂, vacuum)** has been heated to a higher temperature, which has resulted in more silyl amine having been removed from the surface.

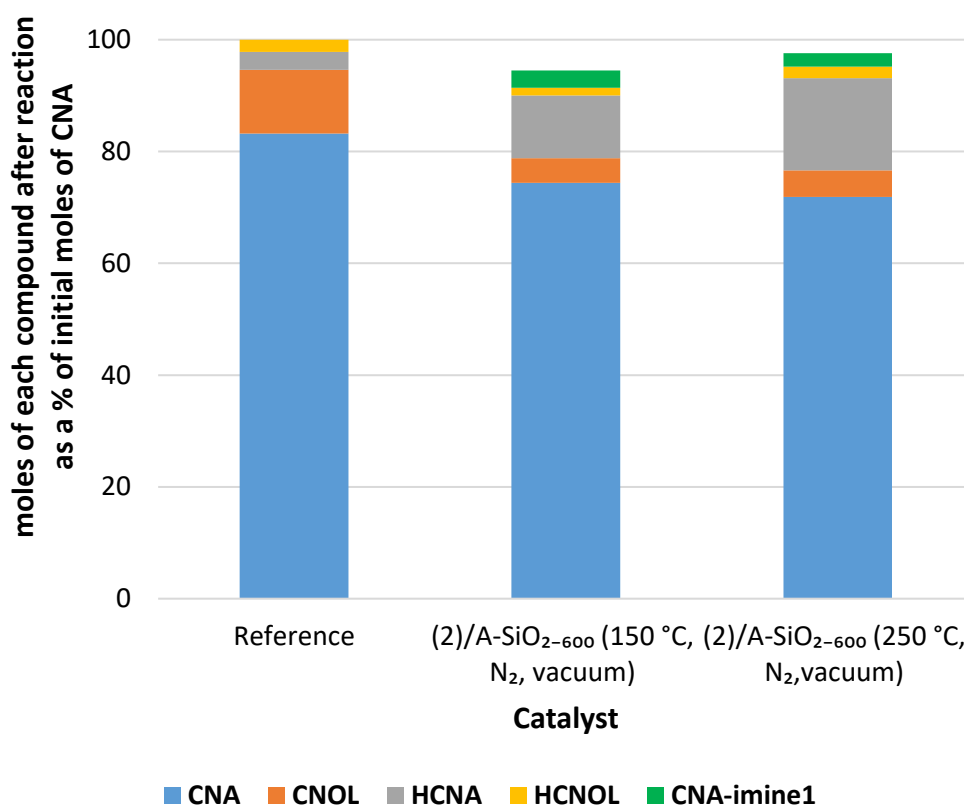


Figure 5.8. Product distribution from the catalytic hydrogenation of CNA using **(2)/A-SiO₂₋₆₀₀ (150 °C, N₂, vacuum)** and **(2)/A-SiO₂₋₆₀₀ (250 °C, N₂, vacuum)**; reaction conditions: 9 h, 150 °C, 20 mL min⁻¹ H₂, stirring speed: 250 rpm
Errors: ±2 % for CNA; ±1 % for CNOL; ±1% for HCNA; ±1 % for HCNOL; ±2 % for CNA-imine1

5.1.1.5 Thermal Treatment of **(2)/A-SiO₂₋₆₀₀** Prior to Reduction Under Hydrogen

To determine whether **(2)/A-SiO₂₋₆₀₀ (150 °C, N₂, vacuum)** and **(2)/A-SiO₂₋₆₀₀ (250 °C, N₂, vacuum)** are active for CNA hydrogenation following reduction under hydrogen, **(2)/A-SiO₂₋₆₀₀ (150 °C, N₂, then H₂, vacuum)** was prepared by first heating a sample of **(2)/A-SiO₂₋₆₀₀** at 150 °C until it was a uniformly black-coloured material (60 mins, by eye), then reduced at 150 °C under a flow of neat hydrogen (50 mL min⁻¹). In a related fashion, **(2)/A-SiO₂₋₆₀₀ (150 °C, N₂, then 5% H₂/N₂, vacuum)** was prepared by heating at 150 °C until it was also a uniformly black in appearance and then reduced under 5% H₂/N₂ at 150 °C.

Following their formation, both **(2)/A-SiO₂₋₆₀₀ (150 °C, N₂, then H₂, vacuum)** and **(2)/A-SiO₂₋₆₀₀ (150 °C, N₂, then 5% H₂/N₂, vacuum)** were tested for the hydrogenation of CNA; a summary of catalyst results is presented in Figure 5.9. Like the catalysts produced through heating under nitrogen only (Section 5.1.1.4), both **(2)/A-SiO₂₋₆₀₀ (150 °C, N₂, then H₂, vacuum)** and **(2)/A-SiO₂₋₆₀₀ (150 °C, N₂, then 5% H₂/N₂, vacuum)** are catalytically active with selectivity towards HCNA. This is likely due to having similar cobalt species on the silica surface, which are produced through the initial heating of **(2)/A-SiO₂₋₆₀₀** under nitrogen, namely small cobalt-containing nanoparticles (2-3 nm) (Section 4.1.3.6.2). Despite different concentrations of hydrogen being used during the reduction step of their preparation, little difference in their CNA hydrogenation performance is observed, although both **(2)/A-SiO₂₋₆₀₀ (150 °C, N₂, then H₂, vacuum)** and **(2)/A-SiO₂₋₆₀₀ (150 °C, N₂, then 5% H₂/N₂, vacuum)** are slightly more catalytically active than catalysts that had been produced without a hydrogen reduction step, *i.e.* **(2)/A-SiO₂₋₆₀₀ (150 °C, N₂, vacuum)** and **(2)/A-SiO₂₋₆₀₀ (250 °C, N₂, vacuum)**.

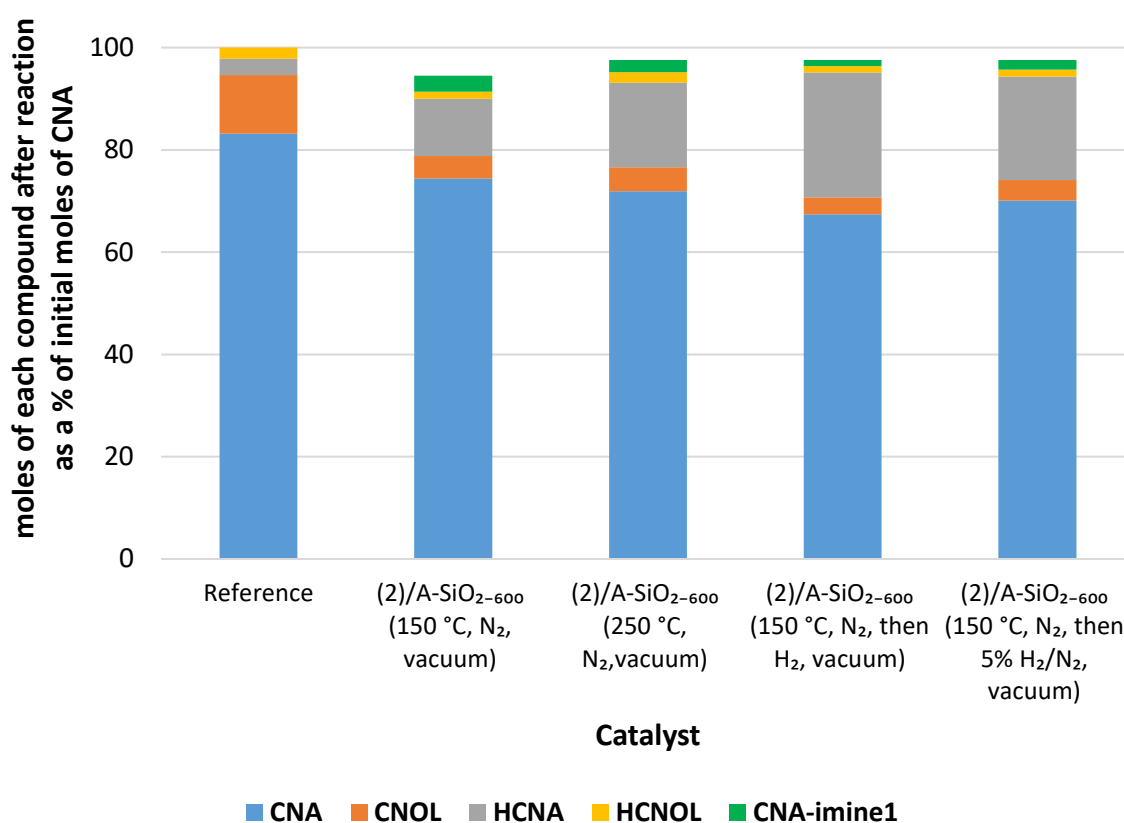


Figure 5.9. Comparison of the product distribution from the catalytic hydrogenation of CNA using **(2)/A-SiO₂₋₆₀₀ (150 °C, N₂, vacuum)**, **(2)/A-SiO₂₋₆₀₀ (250 °C, N₂, vacuum)**, **(2)/A-SiO₂₋₆₀₀ (150 °C, N₂, then H₂, vacuum)** and **(2)/A-SiO₂₋₆₀₀ (150 °C, N₂, then 5% H₂/N₂, vacuum)**; reaction conditions: 9 h, 150 °C, 20 mL min⁻¹ H₂, stirring speed: 250 rpm
Errors: ±2 % for CNA; ±1 % for CNOL; ±1% for HCNA; ±3% for HCNOL; ±1% for CNA-imine1

5.1.1.6 Probing the Effects of Air Exposure on Reduced (2)/A-SiO₂₋₆₀₀ Catalysts

The general assumption throughout the majority of this project was that both the catalyst precursor **(2)/A-SiO₂₋₆₀₀** and the resulting catalysts were air-sensitive and, as a result, they were handled in order to avoid exposure to air and/or moisture, *i.e.* storing the catalysts/precursor in a nitrogen-filled glovebox, loading the catalysts and reagents into pre-dried glassware using Schlenk techniques, and performing the catalysis without exposure to air. However, for both ease of use and for general application of the various catalysts it was of interest to determine the effects of air-exposure. Consequently, variants of the catalysts exposed to air at different stages in their preparation (see synthesis Section 5.1.1.4) were tested for CNA hydrogenation under reaction conditions identical to those above (Section 5.1.1); test results are summarised in Figure 5.10 (a).

The three catalysts, **air-exposed (2)/A-SiO₂₋₆₀₀**, **(2)/A-SiO₂₋₆₀₀ (air-exposed, 150 °C, H₂, vacuum)**, and **air-exposed (2)/A-SiO₂₋₆₀₀ (150 °C, N₂, then H₂, vacuum)**, all gave rise to similar CNA hydrogenation performance to the catalysts prepared by reduction under hydrogen as described in Sections 5.1.1.1 and 5.1.1.2. When comparing **(2)/A-SiO₂₋₆₀₀ (air-exposed, 150 °C, H₂, vacuum)** to its equivalent non-air-exposed catalyst, the catalysts give similar CNA hydrogenation product distribution profiles (Figure 5.10 (b)). In contrast, when **air-exposed (2)/A-SiO₂₋₆₀₀ (150 °C, N₂, then H₂, vacuum)** is compared its equivalent catalyst **(2)/A-SiO₂₋₆₀₀ (150 °C, N₂, then H₂, vacuum)**, which is made by heating under nitrogen, there is a difference in performance, with the non-air-exposed catalyst showing significantly more activity towards HCNA (2 vs. 24%). This shows that exposure to air shuts down the pathway that is responsible for the production of HCNA in the catalysts produced by heating under nitrogen (Section 5.1.1.4 and 5.1.1.5). In addition, when comparing the air-exposed catalysts to non-air-exposed catalysts, the extent of production of CNA-imine1 is greater for catalysts that have been exposed to air (yield = 4-6±2% CNA-imine1) than the catalysts that hadn't been exposed to atmosphere discussed previously in this chapter (yield = 1-4±1% CNA-imine1), and that there is a larger amount of "missing" mass balance, suggesting that more side products have formed. It is proposed that this small increase in formation of CNA-imine1 from catalysts that have been exposed to air may be due to water on the catalyst surface (from air exposure) providing Brønsted acidity, which promotes imine formation. Water is known to be on the surface of **(2)/A-SiO₂₋₆₀₀**-derived catalysts after air-exposure, as ¹H SS-NMR spectroscopy shows that the surface becomes rehydroxylated (Section 4.1.3.2).

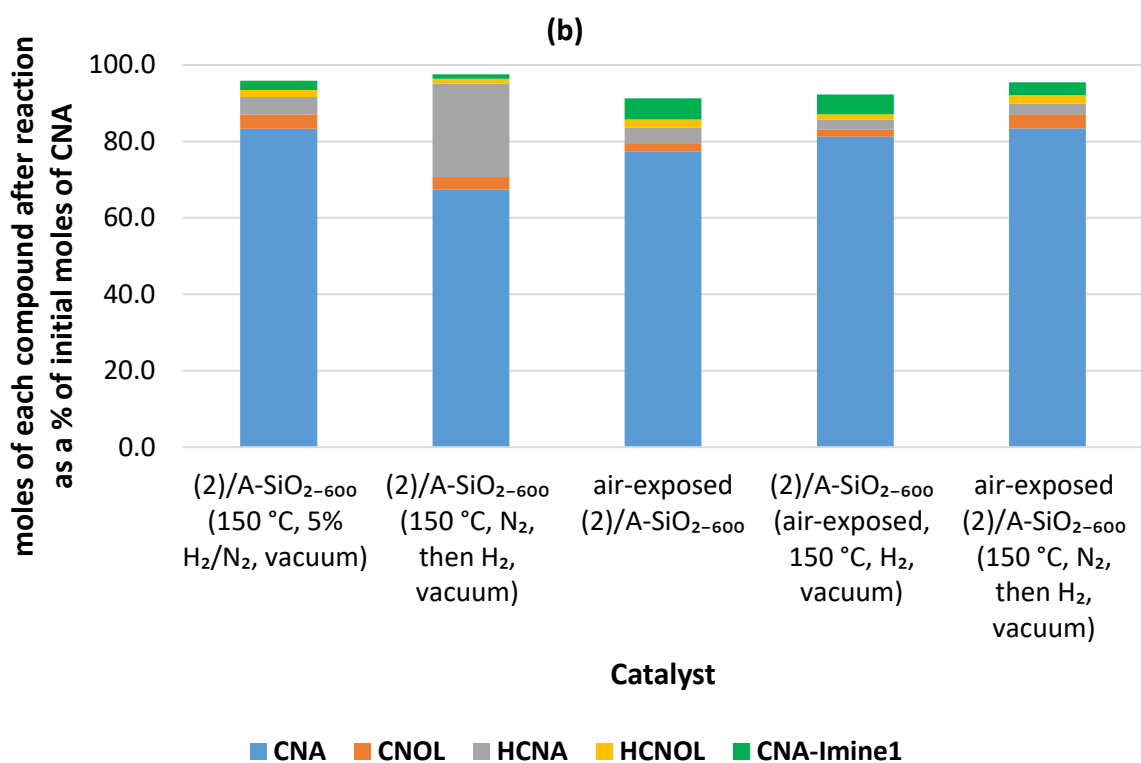
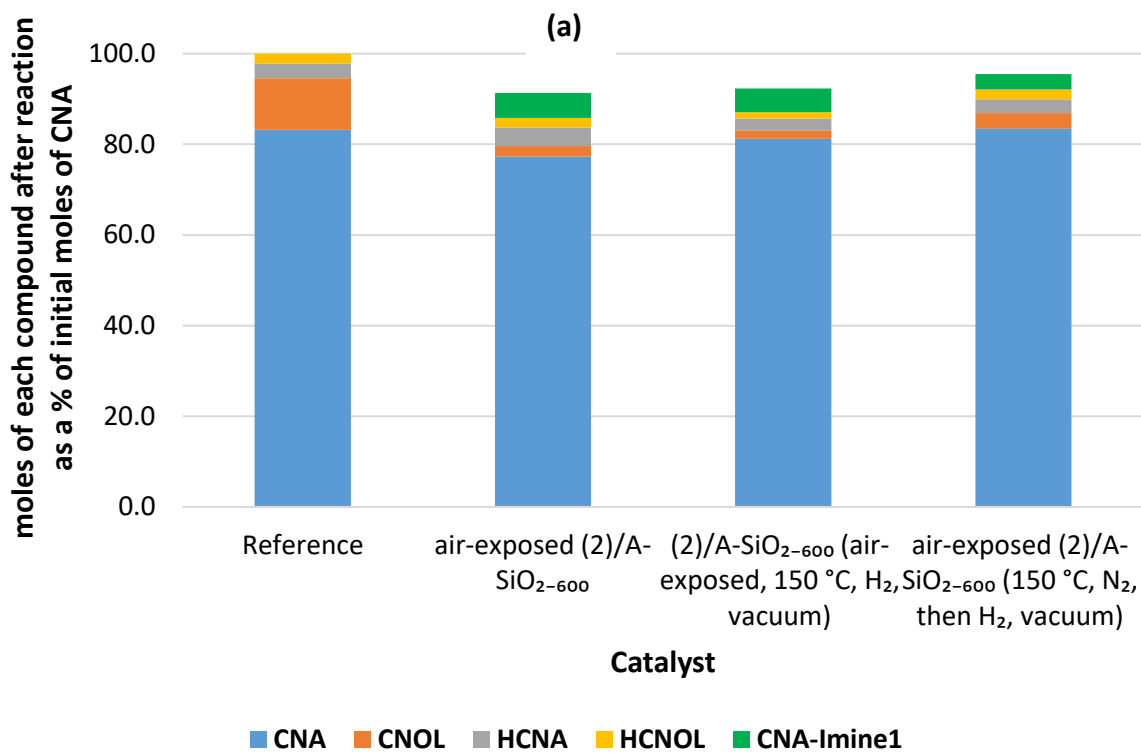


Figure 5.10. a) Product distribution from the catalytic hydrogenation of CNA using *air-exposed* (2)/A-SiO₂₋₆₀₀, (2)/A-SiO₂₋₆₀₀ (*air-exposed*, 150 °C, H₂, vacuum) and *air-exposed* (2)/A-SiO₂₋₆₀₀ (250 °C, N₂, then H₂ vacuum); b) Comparison of product distribution from the catalytic hydrogenation of CNA using catalysts exposed to air and catalysts no exposed to air;
reaction conditions: 9 h, 150 °C, 20 mL min⁻¹ H₂, stirring speed: 250 rpm
Errors: ±2% for CNA; ±1% for CNOL; ±1% for HCNA; ±1% for HCNOL; ±2% for CNA-imine1

5.1.2 Analysis of the Activity and Selectivity of (2)/A-SiO₂₋₆₀₀ (150 °C, N₂, then H₂, vacuum) For Hydrogenation of CNA

To further explore the mode of action of the CNA hydrogenation catalysts, a time course study using **(2)/A-SiO₂₋₆₀₀ (150 °C, N₂, then H₂, vacuum)** (chosen since it shows the highest yield and selectivity) was undertaken. To this end, a CNA hydrogenation reaction using **(2)/A-SiO₂₋₆₀₀ (150 °C, N₂, then H₂, vacuum)** was undertaken and aliquots of the reaction mixture were taken and analysed every hour over the reaction period, with yields of CNA to the CNOL, HCNA, HCNOL, and CNA-imine1 being recorded (Figure 5.11). Consumption of CNA is seen to be non-linear over time, something paralleled by the formation of HCNA. The reaction is slower at the start of the reaction, with a slight rate increase occurring after approximately 2 h, something that has been attributed tentatively to the result of an induction period, possibly because of further catalyst reduction *in situ* or to displacement of (TMS)₂NH from the catalyst prior to imine formation.

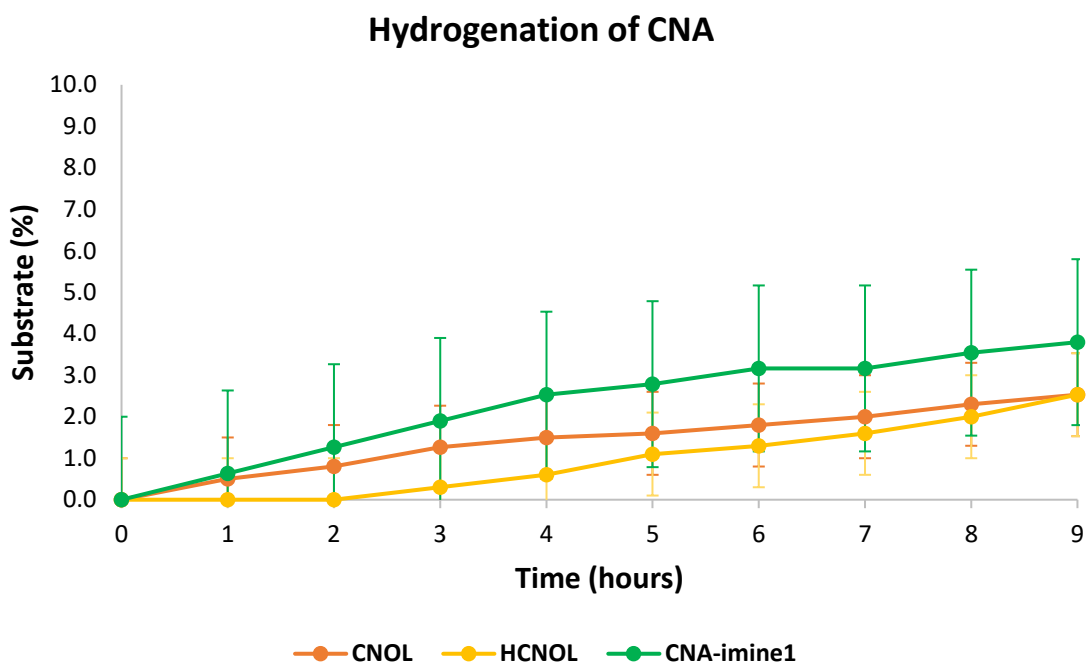
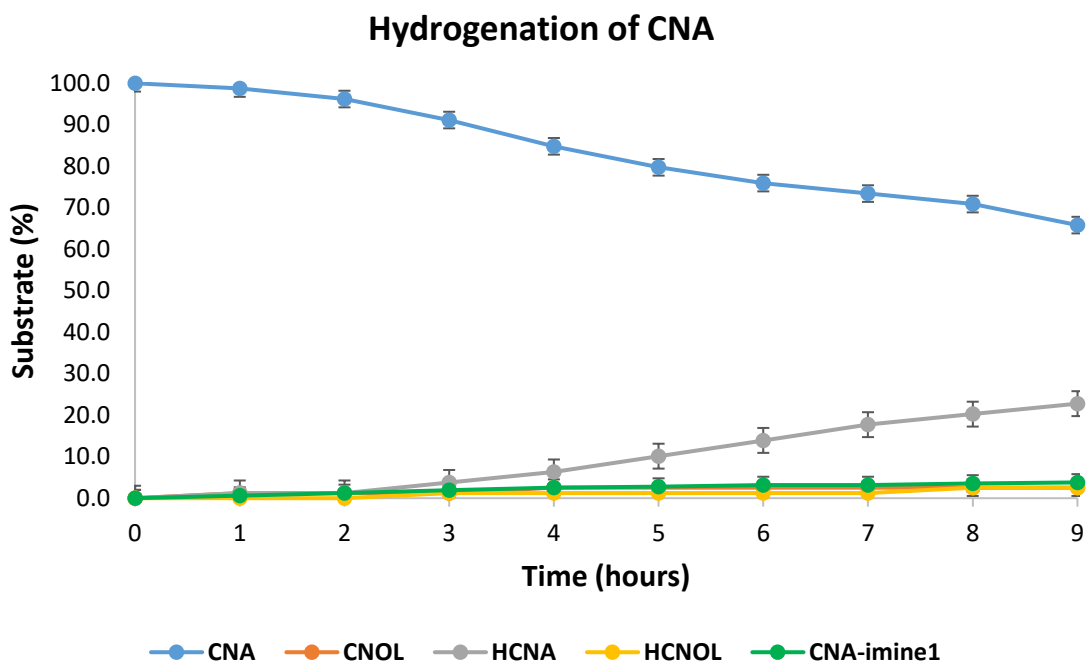


Figure 5.11. Catalytic performance of **(2)/A-SiO₂₋₆₀₀** (150 °C, N₂, then H₂, vacuum); reaction conditions: 9 h, 150 °C, 20 mL min⁻¹ H₂, stirring speed: 250 rpm

To probe the catalyst's lifetime towards hydrogenation catalysis by **(2)/A-SiO₂₋₆₀₀** (150 °C, N₂, then H₂, vacuum) of CNA hydrogenation was probed over a 33 h period; the reaction outcomes for hydrogenation of CNA are summarised in Figure 5.12. After 14 h, the catalytic activity decreases as indicated by a slowing in the rate of CNA consumption, mirrored in the corresponding rate of HCNA production. Throughout the 33 h reaction time, the colour of the reaction mixture visibly changes from

colourless to an increasingly intense yellow (Figure 5.13). The yellow colour change has been attributed to the production of side-products, such as CNA-imine1 and the 16 unknown side-products, as the reactants and products (CNA, CNOL, HCNA, and HCNOL) are not strongly coloured. At hour 33, ~16% of the mass-balance is unaccounted for by the calculated yields of CNA, CNOL, HCNA, and HCNOL. This 16% of the reaction mass is attributed to side products (observed by GC-FID, with retention times of 16 – 25 minutes), which includes CNA-imine1 as discussed in Section 5.1.1.2.

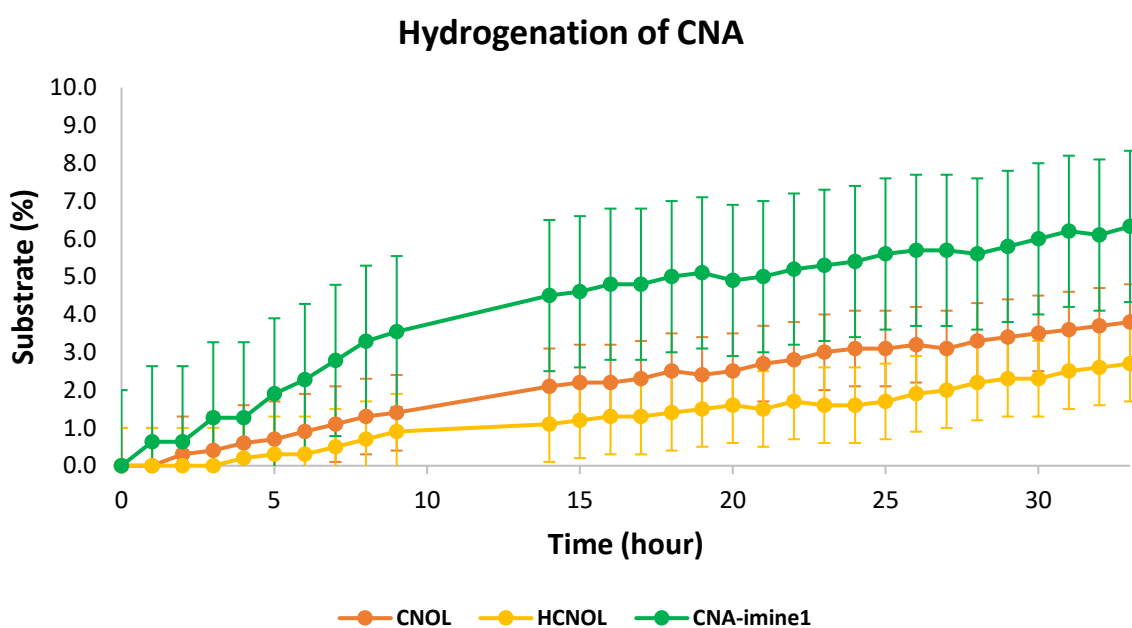
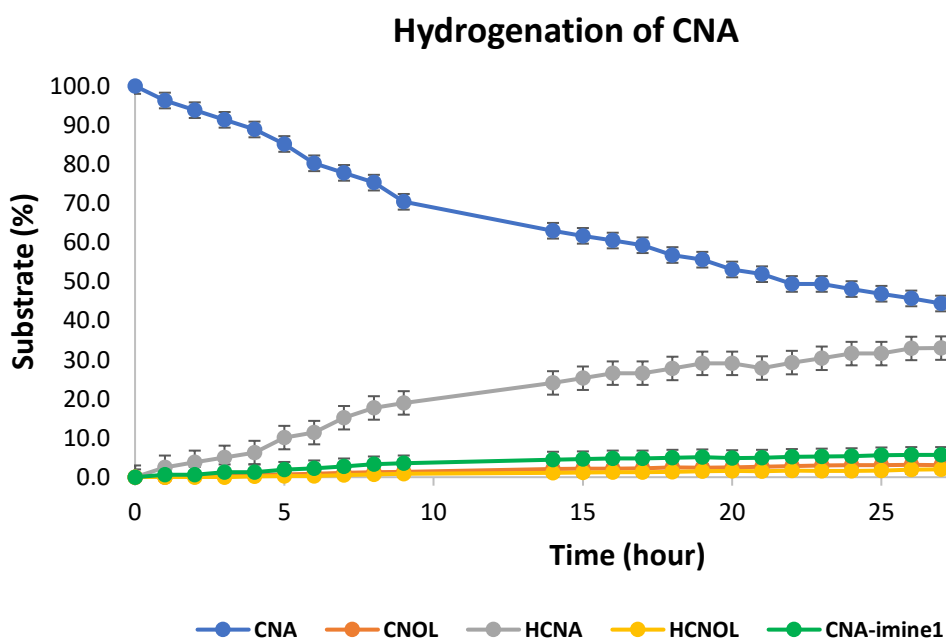


Figure 5.12. Catalytic performance for the hydrogenation of CNA mediated by (2)/A-SiO₂₋₆₀₀ (150 °C, N₂, then H₂, vacuum); reaction conditions: 33 h, 150 °C, 20 mL min⁻¹ H₂, stirring speed: 250 rpm



Figure 5.13. The colour change of the reaction mixture obtained during the catalytic hydrogenation of CNA using **(2)/A-SiO₂₋₆₀₀ (150 °C, N₂, then H₂, vacuum)**, over 33 h. The numbers on the vials refer to the time in hours when the aliquot was taken from the reaction mixture.

5.1.3 Summary and Discussion of Catalysts Synthesised from Precursor **(2)/A-SiO₂₋₆₀₀** and their Catalytic Selectivity for the Reaction of CNA

The various catalysts derived from **(2)/A-SiO₂₋₆₀₀** and their methods of preparation are summarised in Table 5.1; data resulting from use of these catalysts for the hydrogenation of CNA are summarised in Table 5.2 and in Figures 5.14 and 5.15. Out of the twelve catalysts tested in this project, four (**(2)/A-SiO₂₋₆₀₀ (150 °C, N₂, then H₂, vacuum)**, **(2)/A-SiO₂₋₆₀₀ (150 °C, N₂, then 5% H₂/N₂, vacuum)**, **(2)/A-SiO₂₋₆₀₀ (150 °C, N₂, vacuum)**, and **(2)/A-SiO₂₋₆₀₀ (250 °C, N₂, vacuum)**) were catalytically active for the hydrogenation of CNA (conversion of 11- 24%). Their increased activity compared to other **(2)/A-SiO₂₋₆₀₀**-derived catalysts is attributed to additional HCNA being produced rather than other reaction pathways being displaced. In comparison, the reference catalyst, **Co(NO₃)₂/SiO₂**, was active and selective towards the formation of the alcohol, HCNOL, with a CNA conversion of 11%.

The formation of side products (not observed with the reference catalyst **Co(NO₃)₂/SiO₂**), in addition to CNA, CNOL, HCNA, and HCNOL, is summarised in Table 5.2. From a comparison of the catalytic performance (Table 5.2) and catalyst preparation methods (Table 5.1), it is clear that the method of catalyst preparation affects not just the formation of the target products (*i.e.* CNOL, HCNA, and HCNOL), but also the formation of side products (*e.g.* CNA-imine1). Notably, use of **air-exposed (2)/A-SiO₂₋₆₀₀** and **(2)/A-SiO₂₋₆₀₀ (air-exposed, 150 °C, H₂, vacuum)** leads to the formation of the greatest amount of side-product CNA-imine1. Both **air-exposed (2)/A-SiO₂₋₆₀₀** and **(2)/A-SiO₂₋₆₀₀ (air-exposed, 150 °C, H₂, vacuum)** were synthesised with a step that exposed their common precursor **(2)/A-SiO₂₋₆₀₀** to air. It is therefore proposed that water from air-exposure on the catalyst surface promotes faster formation of CNA-imine1 because of the presence of a great number of surface Brønsted acid sites, which catalyse imine formation. In contrast, **(2)/A-SiO₂₋₆₀₀ (250 °C, N₂, vacuum)**, which was heated to the highest temperature under vacuum, without exposure to air during any step of its synthesis, produced the least amount of CNA-imine1. Together, this emphasises the importance of keeping the catalysts synthesised from the precursor **(2)/A-SiO₂₋₆₀₀** under a dry, inert atmosphere at all times.

Table 5.1. A summary of the syntheses of catalysts studied in this project

Catalyst name	Catalyst Precursor	Reduction Treatment		Post-Treatment	Catalyst Colour
		Temperature (°C)	Gas		
<i>Co(NO₃)₂/SiO₂ Reference</i>	Co(NO ₃) ₂ /A-SiO ₂	500	5% H ₂ /N ₂	-	black
<i>(2)/A-SiO₂₋₆₀₀ (150 °C, 5% H₂/N₂)</i>	(2)/A-SiO ₂₋₆₀₀	150	5% H ₂ /N ₂	-	blue
<i>(2)/A-SiO₂₋₆₀₀ (200 °C, 5% H₂/N₂)</i>	(2)/A-SiO ₂₋₆₀₀	200	5% H ₂ /N ₂	-	blue/black
<i>(2)/A-SiO₂₋₆₀₀ (250 °C, 5% H₂/N₂)</i>	(2)/A-SiO ₂₋₆₀₀	250	5% H ₂ /N ₂	-	blue/black
<i>(2)/A-SiO₂₋₆₀₀ (150 °C, 5% H₂/N₂, vacuum)</i>	(2)/A-SiO ₂₋₆₀₀	150	5% H ₂ /N ₂	heat at 150 °C <i>in vacuo</i>	blue
<i>(2)/A-SiO₂₋₆₀₀ (150 °C, 5% H₂/N₂, pentane-wash)</i>	(2)/A-SiO ₂₋₆₀₀	150	5% H ₂ /N ₂	pentane-wash	blue
<i>(2)/A-SiO₂₋₆₀₀ (150 °C, N₂, then H₂, vacuum)</i>	(2)/A-SiO ₂₋₆₀₀	150	heated then exposed to H ₂	heat at 150 °C <i>in vacuo</i>	black
<i>(2)/A-SiO₂₋₆₀₀ (150 °C, N₂, then 5% H₂/N₂, vacuum)</i>	(2)/A-SiO ₂₋₆₀₀	150	heated then exposed to 5% H ₂ /N ₂	heat at 150 °C <i>in vacuo</i>	black
<i>(2)/A-SiO₂₋₆₀₀ (150 °C, N₂, vacuum)</i>	(2)/A-SiO ₂₋₆₀₀	150	N ₂	heat at 150 °C <i>in vacuo</i>	black
<i>(2)/A-SiO₂₋₆₀₀ (250 °C, N₂, vacuum)</i>	(2)/A-SiO ₂₋₆₀₀	250	N ₂	heat at 250 °C <i>in vacuo</i>	black
<i>air-exposed (2)/A-SiO₂₋₆₀₀</i>	air-exposed (2)/A-SiO ₂₋₆₀₀		-	-	blue
<i>(2)/A-SiO₂₋₆₀₀ (air-exposed, 150 °C, H₂, vacuum)</i>	air-exposed (2)/A-SiO ₂₋₆₀₀	150	H ₂	heat at 150 °C <i>in vacuo</i>	blue
<i>air-exposed (2)/A-SiO₂₋₆₀₀ (150 °C, N₂, then H₂, vacuum)</i>	(2)/A-SiO ₂₋₆₀₀	150	heated then exposed to H ₂	heat at 150 °C <i>in vacuo</i> then exposed to air	blue

Table 5.2. Yield and product selectivity for the hydrogenation of CNA by various silica-supported cobalt catalysts studied in this project; reaction conditions: 113 mg 2.4 w.t% Co catalyst, 9 h, 150 °C, 20 mL min⁻¹ H₂

Catalyst	CNA average converted%	Std. Dev.	CNOL average % yield	Std. Dev.	HCNA average % yield	Std. Dev.	HCNOL average % yield	Std. Dev.	Total CNA + CNOL + HCNA + HCNOL %
Co(NO₃)₂/SiO₂ Reference *	16	2	11	1	3	0	2	1	100
A-SiO₂₋₆₀₀	4	1	1	0	2	1	1	0	100
(2)/A-SiO₂₋₆₀₀ (150 °C, 5% H₂/N₂)	19	2	4	1	4	1	2	0	91
(2)/A-SiO₂₋₆₀₀ (200 °C, 5% H₂/N₂)	18	2	5	1	4	1	2	1	93
(2)/A-SiO₂₋₆₀₀ (250 °C, 5% H₂/N₂)	17	1	5	1	4	1	3	1	94
(2)/A-SiO₂₋₆₀₀ (150 °C, 5% H₂/N₂, vacuum)	17	2	4	0	5	1	2	0	94
(2)/A-SiO₂₋₆₀₀ (150 °C, 5% H₂/N₂, pentane-wash)	17	1	3	1	4	0	1	0	91
(2)/A-SiO₂₋₆₀₀ (150 °C, N₂, then H₂, vacuum)	33	2	3	1	24	3	1	0	96
(2)/A-SiO₂₋₆₀₀ (150 °C, N₂, then 5% H₂/N₂, vacuum)	30	2	4	0	20	2	1	1	95
(2)/A-SiO₂₋₆₀₀ (150 °C, N₂, vacuum)	26	2	4	1	11	2	1	0	91
(2)/A-SiO₂₋₆₀₀ (250 °C, N₂, vacuum)	28	1	5	0	17	3	2	0	97
air-exposed (2)/A-SiO₂₋₆₀₀	23	-	2	-	4	-	2	-	86
(2)/A-SiO₂₋₆₀₀ (air-exposed, 150 °C, H₂, vacuum)	19	-	2	-	3	-	1	-	87
air-exposed (2)/A-SiO₂₋₆₀₀ (150 °C, N₂, then H₂, vacuum)	17	-	4	-	3	-	2	-	92

* Aeroperl 300/30 silica impregnated with an aqueous solution of Co(NO₃)₂.6H₂O *via* incipient wetness (2.3% w.t Co loading), calcined at 120 °C, then reduced under H₂ at 500 °C

In all cases, the catalytic activity and product selectivities associated with the hydrogenation of CNA are undoubtedly attributable to cobalt surface species present on the silica, since blank silica does not exhibit any catalytic activity (Table 5.2). The materials **(2)/A-SiO₂₋₆₀₀ (150 °C, N₂, then H₂, vacuum)**, **(2)/A-SiO₂₋₆₀₀ (150 °C, N₂, then 5% H₂/N₂, vacuum)**, **(2)/A-SiO₂₋₆₀₀ (150 °C, N₂, vacuum)**, and **(2)/A-SiO₂₋₆₀₀ (250 °C, N₂, vacuum)** all have a suspected cobalt-containing nanoparticle surface species, as suggested by the bright, well defined features in the TEM images of each of these materials (Section 4.1.3.5). The surface species of other catalyst materials, **(2)/A-SiO₂₋₆₀₀ (T °C, 5% H₂/N₂)**, where T = 150, 200, and 250 °C, **(2)/A-SiO₂₋₆₀₀ (150 °C, 5% H₂/N₂, vacuum)**, and **(2)/A-SiO₂₋₆₀₀ (150 °C, 5% H₂/N₂, pentane-wash)** also have cobalt-containing particles, however these particles in the TEM images are less defined and difficult to differentiate from the silica support. Together, this suggests that selectivity for the formation of HCNA is dictated by the structure of the cobalt nanoparticles present on the silica as proposed at the start of this project.

The summaries of data presented in Figures 5.14 and 5.15 show the reactions and yields of CNA to CNOL, HCNA, and HCNOL and highlights differences in catalytic activity between catalysts exposed to hydrogen prior to catalysis and catalysts that were not exposed to hydrogen prior to catalysis, with the former being more catalytically active. This difference in performance has been attributed to **(2)/A-SiO₂₋₆₀₀ (150 °C, N₂, then H₂, vacuum)** and **(2)/A-SiO₂₋₆₀₀ (150 °C, N₂, then 5% H₂/N₂, vacuum)** having been reduced under hydrogen prior to the catalysis reaction. The fact that **(2)/A-SiO₂₋₆₀₀ (150 °C, N₂, vacuum)** and **(2)/A-SiO₂₋₆₀₀ (250 °C, N₂, vacuum)** both show hydrogenation activity is attributed to *in situ* reduction that occurs during the catalytic hydrogenation reaction itself, something that is likely to correspond to the induction period (0 – 3 h, observed by GC-FID analysis of the reaction mixture as a function of time, Figures 5.8 and 5.9) at the start of the catalysis reaction. This induction period lowers catalytic activity of **(2)/A-SiO₂₋₆₀₀ (150 °C, N₂, vacuum)** and **(2)/A-SiO₂₋₆₀₀ (250 °C, N₂, vacuum)**, and shows the importance of heating the catalysts under hydrogen prior to catalysis, to optimise the catalytic activity of catalysts derived from **(2)/A-SiO₂₋₆₀₀**.

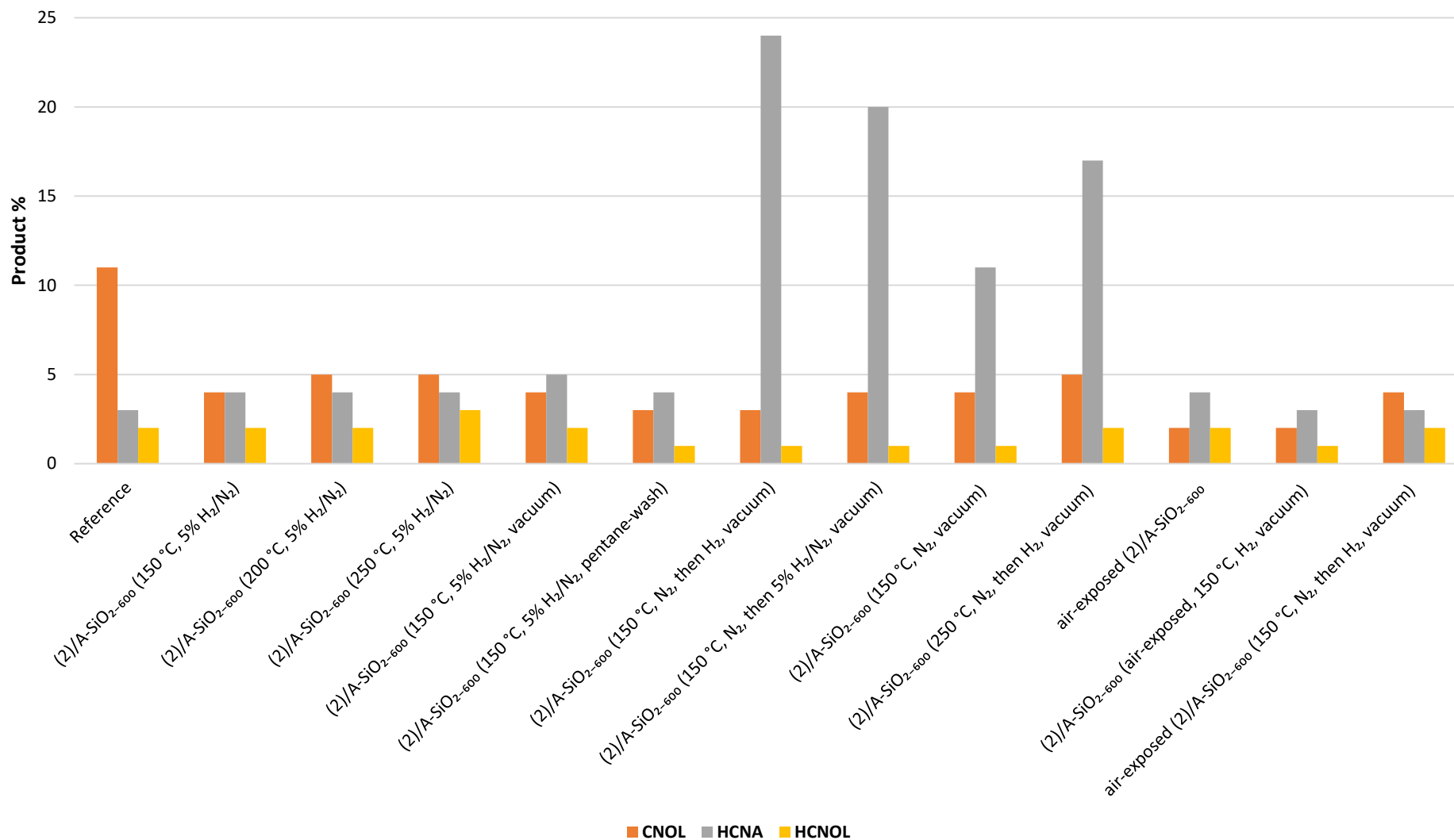


Figure 5.14. Comparison of product distributions for the hydrogenation of CNA using catalysts studied in this project ; reaction conditions: 113 mg 2.4 w.t% Co catalyst, 9 h, 150 °C, 20 mL min⁻¹ H₂, stirring speed: 250 rpm

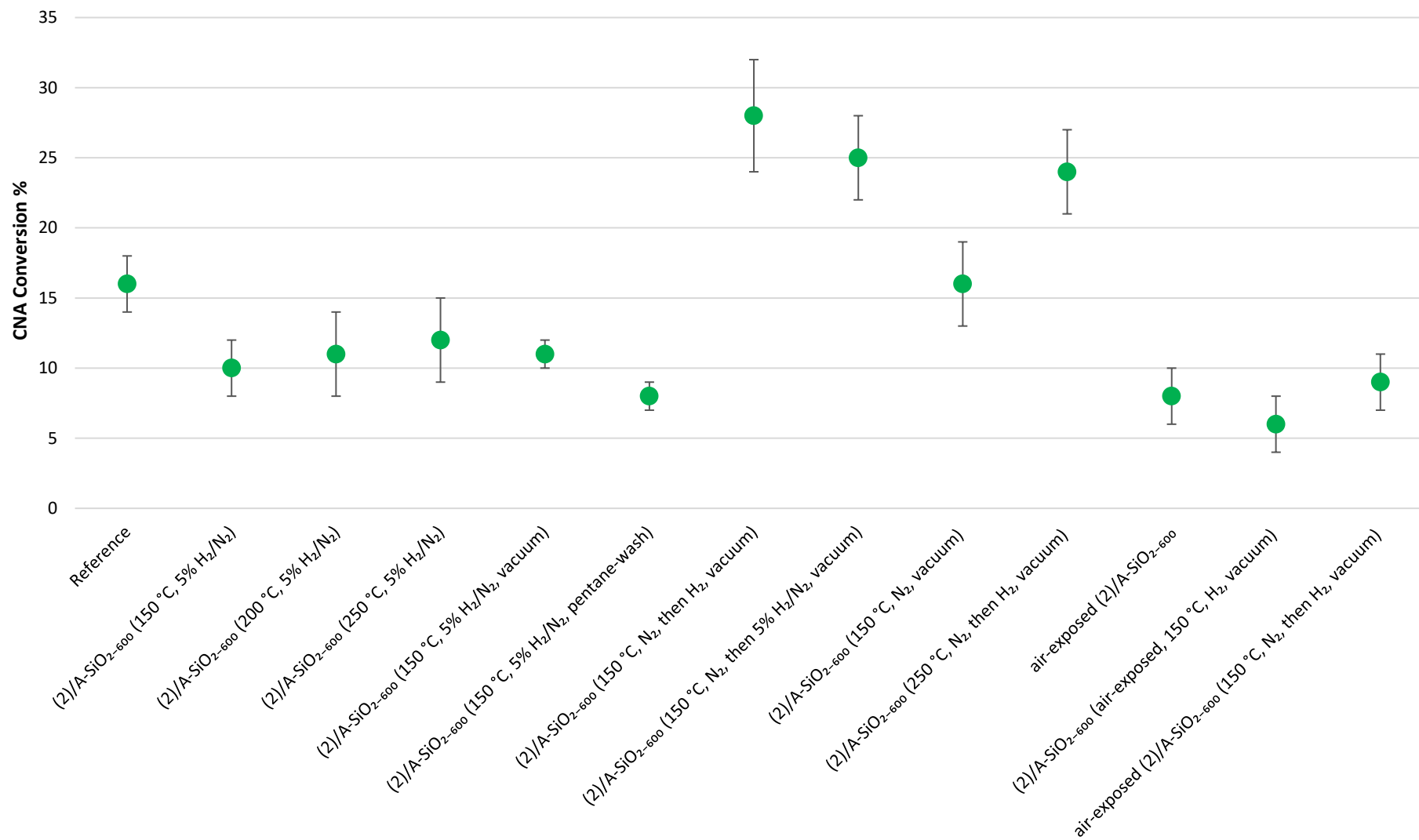


Figure 5.15. Yields of CNOL + HCNA + HCNO combined, via catalytic hydrogenation of CNA using Catalysts Derived from (2)/A-SiO₂₋₆₀₀

5.2 Conclusions

A series of catalysts were prepared based on the materials synthesised from the reduction of **(2)/A-SiO₂₋₆₀₀** described in Chapter 4. Four of the catalysts, **(2)/A-SiO₂₋₆₀₀ (150 °C, N₂, then H₂, vacuum)**, **(2)/A-SiO₂₋₆₀₀ (150 °C, N₂, then 5% H₂/N₂, vacuum)**, **(2)/A-SiO₂₋₆₀₀ (150 °C, N₂, vacuum)**, and **(2)/A-SiO₂₋₆₀₀ (250 °C, N₂, vacuum)**, showed moderate catalytic activity in the hydrogenation of CNA, giving rise to various levels of formation of HCNA mediated by cobalt-containing particles on the surface of silica. The catalytic activity of the catalysts changes over 33 hours, reducing in effectiveness; for example, **(2)/A-SiO₂₋₆₀₀ (150 °C, N₂, then H₂, vacuum)** reduces in effectiveness for synthesis of HCNA from 0.02 mmol hour⁻¹ during 0 – 9 h, to 0.004 mmol hour⁻¹ during 24 – 33 h (Figure 5.9). In comparison to **(2)/A-SiO₂₋₆₀₀ (150 °C, N₂, then H₂, vacuum)**, **(2)/A-SiO₂₋₆₀₀ (150 °C, N₂, then 5% H₂/N₂, vacuum)**, **(2)/A-SiO₂₋₆₀₀ (150 °C, N₂, vacuum)**, which show selectivity towards HCNA (11-24 %), the reference catalyst, **Co(NO₃)₂/SiO₂**, is selective towards CNOL (11 %).

All twelve catalysts prepared from **(2)/A-SiO₂₋₆₀₀** also produce side-products during the catalytic hydrogenation reaction of CNA, one of which has been identified as the imine formed (CNA-imine1) from reaction of CNA and HMDS, which results from deposition of HN(TMS)₂ on the surface and/or formation of SiO-N(TMS)₂ both from reaction of the [Co(N(TMS)₂)₂(THF)] precursor employed in catalyst synthesis. The formation of CNA-imine1 formation can be reduced by removing amine from the catalyst prior to catalysis through washing with pentane or by heating under vacuum. It has been shown that heating the catalyst under vacuum prior to catalysis is more effective in reducing the formation of CNA-imine1 than washing with pentane. While steps have been taken to reduce the amount of amine on the catalyst surface, and therefore reduce side-product formation, side-reactions have not been completely prevented as other side-products form during the hydrogenation of CNA when using catalysts derived from **(2)/A-SiO₂₋₆₀₀**. It has also been proven that it is important to prevent the catalysts from being exposed to air at any step during their synthesis, as it reduces catalytic activity and increases the production of CNA-imine1.

5.3 References

1. H. X. Li, X. F. Chen, M. H. Wang and Y. P. Xu, *Appl. Catal. A: General*, 2002, **225**, 117.
2. P. Gallezot and D. Richard, *Catal. Rev. Sci. Eng.*, 1998, **40**, 81 - 126.
3. Y. Yang, D. Rao, Y. Chen, S. Dong, B. Wang, X. Zhang and M. Wei, *ACS Catal.*, 2018, **8**, 11749 - 11760.
4. Z. Wu, J. Zhao, M. Zhang, W. Li and K. Tao, *Catal. Commun.*, 2010, **11**, 973 -976.
5. T. M. Bustamante, M. A. Fraga, J. L. G. Fierro, C. H. Campos and G. Pecchi, *Catalysis Today*, 2020, **356**, 330 - 338.

6. P. Mente, V. Mashindi, A. Magubane, T. N. Phaahlamohlaka, P. M. Gangatharan, R. P. Forbes, and N. J. Coville, *Can. J. Chem.*, 2021, **100**, 114 - 122.
7. D. Yi, Y. Min, B. Muzzi, A. Marty, I. Romana, P-F. Fazzini, T. Blon, G. Viau, P. Serp and K. Soulantica, *ACS Appl. Nano Mater.*, 2022, **5**, 4, 5498 – 5507
8. T. Elangovan and B. Viswanathan, *Catal. Lett.* , 2012, **142**, 1, 87 - 94
9. B. Dragoi, A. Ungureanu, C. Ciotonea, A. Chirieac, S. Petit, S. Royer and E. Dumitriu, *Microporous Mesoporous Mater.*, 2016, **224**, 176-189.
10. B. M. Bhanage, Y. Ikushima, M. Shirai and M. Arai, *Studies in Surface Science and Catalysis*, 2001, **132**, 1079 - 1082.
11. L. Romaka, V. V. Romaka, N. Melnychenko, Y. Stadnyk, L. Bohun and A. Horyn, *J. Alloys Compd.*, 2018, **739**, 771-779.
12. A. Chirieac, B. Dragoi, A. Ungureanu, A. M. Corcodel, C. Rudolf, A. Sasu and E. Dumitriu, *Environ. Eng. Manag. J.*, 2012, **11**, 47 - 54.
13. B. Jiang, Y. Lin, M-L. Wang, D-S Liu, B-H Xu and S. Zhang, *Org. Chem. Front.*, 2019, **6**, 801 - 807
14. B. Liu, L. Lu, T. Cai and K. Iwatani, *Appl. Catal. A, General*, 1999, **180**, 105 - 111.
15. L. H. Klemm, D. H. Lee, K. W. Gopinath and C. E. Klopfenstein, *J. Org. Chem.*, 1966, **31**, 2376 - 2380.
16. Q. Zheng, D. Wang, F. Yuan, Q. Han, Y. Dong and Y. Liu, *Catalysis Letters*, 2016, **146**, 1535 - 1543.
17. Y. Nitta, Y. Hiramatsu and T. Imanaka, *J. Catal.*, 1990, **126**, 235-245.

Chapter 6: Experimental

6.0 Experimental

6.0.1 General Considerations

Manipulations of air-/moisture-sensitive materials were carried out under an atmosphere of dry nitrogen using standard Schlenk-line and glove box (*Innovative Technologies*) techniques. All solvents, excluding THF and *n*-pentane, were dried using an *Innovative Technologies Solvent Purification System* facility. THF was dried by distillation from sodium benzophenone. Propanal and benzaldehyde were dried by distillation from CaCl_2 . *n*-Pentane was dried by distillation from CaH_2 . All solvents were degassed prior to use using freeze-pump-thaw techniques. Chemicals were purchased from *Sigma Aldrich* or *Fisher Scientific*, and used without further purification with the following exceptions: *n*-butyllithium in hexanes was titrated against *N*-benzylbenzamide to determine accurate concentration;¹ 2-bromomesitylene was dried and stored over activated 3 Å molecular sieves; and trimethylsilyl amine was fractionally distilled under nitrogen into an ampule and degassed using the freeze-pump-thaw technique. Deuterated chloroform (CDCl_3) and deuterated benzene (C_6D_6) were dried by distillation from calcium hydride, degassed and stored under nitrogen. Aqua regia was prepared by mixing concentrated nitric acid (70 %) and concentrated hydrochloric acid (35 %) in a molar ratio of 1:3.

BET experiments were carried out on a Micromeritics ASAP 2420 Physisorption Analyser. Samples were analysed using nitrogen at liquid nitrogen temperature. BET surface areas were measured in accordance with ASTM Method D 3663-03, "Standard Test Method for Surface Area of Catalysts and Catalyst Carriers". The adsorption and desorption isotherms were measured according to ASTM Method D4222-03, "Standard Test Method for Determination of Nitrogen Adsorption and Desorption Isotherms of Catalysts and Catalyst Carriers by Static Volumetric Measurements". The Hg intrusion experiments were carried out using a Micromeritics 9600 AutoPore V 9600 instrument in accordance with ASTM D4284, "Standard Test Method for Determining Pore Volume Distribution of Catalysts and Catalyst Carriers by Mercury Intrusion Porosimetry". The data are derived using the Washburn Equation employing a contact angle of 140° .

Solid-state nuclear magnetic resonance (NMR) spectroscopic analyses were performed on a *Varian VNMRS-400* with samples packed into an airtight rotor inside a nitrogen-filled glove box and sealed under an inert atmosphere. Solution-state NMR spectroscopic analyses were performed on *Bruker Avance III - 400 MHz* instrument. Gas chromatographic (GC) analyses were run on a *Bruker Scion 456-GC* instrument equipped with a *Stabilwax-DA* column (0.25 mm ID, 0.20 μm df) and an FID detector, in split-less injection mode, using the following temperature program: hold 30°C for 10 min, ramp $10^\circ\text{C min}^{-1}$ to 100°C , ramp $20^\circ\text{C min}^{-1}$ to 260°C , hold 260°C for 10 min (total: 35 min). Sample elution

times were as follows: DCM: 0.85 min, heptane: 1.8 min, toluene: 2.7 min, nonane: 8.4 min, propanal 15.7 min. Gas chromatography-mass spectrometry (GC-MS) analyses were performed on a *Thermo TRACE GC* instrument. ICP-OES analyses were conducted using Jobin Yvon Horiba Ultima 2 instrument equipped with the following features: sequential monochromator, radial torch, cyclonic spray chamber, concentric nebulizer. Air-sensitive PXRD samples were analysed using a *Bruker AXS D8 Advance GX000713* diffractometer fitted with a Mo source and Ge(111) monochromator, using an Oxford Cryosystems cobra system that allows measurements on capillary samples. Non-air-sensitive PXRD samples were run on a *Bruker AXS D8 Advance GX003410* with a Cu source. CHN measurements were obtained with the *Exeter Analytical CE-440* elemental analyser. Magnetic moment measurements were measured on a JME (Johnson Matthey Equipment Limited) Gouy balance. Transmission electron microscopy (TEM) studies were conducted using a *JEOL 2100F FEG* transmission electron microscope with a Schottky field emitter operating at 200 kV. A resolution of 2.3 Å (1 Å information limit) was used for TEM imaging.

6.0.2 Methodology of Analytical Techniques

6.0.2.1 BET and Hg intrusion Analyses

BET and Hg intrusion analyses were performed by Johnson Matthey. BET samples were supplied to Johnson Matthey sealed in a glass vial under a dry nitrogen atmosphere, with the vials being further sealed using PVC electrical tape to limit contamination during delivery. Hg intrusion samples were supplied to Johnson Matthey sealed in U-shaped BET tubes under a dry nitrogen atmosphere, stoppered and sealed further using PVC electrical tape to limit contamination during delivery.

6.0.2.2 Oxide Support Hydroxyl Density Determination via Grignard Titration

Silica (~0.2g) was accurately weighed into a Schlenk flask. Dry hexane (10 mmol) was added and the suspension was cooled to 0 °C. *o*-Tolylmagnesium bromide (1.8 mL, 2M, 3.6 mmol) was slowly added *via* a syringe, and the reaction then allowed to warm to room temperature before subsequently stirring for 1 hour. The mixture was cooled to 0 °C and propanal (5 mL, 69.7 mmol) slowly added *via* syringe over a period of 10 min. The reaction was then allowed to warm to room temperature, and stirred overnight, forming an off-white solid. Nonane (1.0 mL) was added as an internal GC standard, before the solution was filtered through a glass wool plug. An aliquot (~0.1 mL) of the filtrate was removed and diluted in DCM (~2 mL) prior to GC analysis.

6.0.2.3 Solid State NMR Spectroscopy

Both cross polarisation (CP) and direction excitation (DE) ²⁹Si SS-NMR spectroscopic techniques were used. REAPDOR experiments were performed to identify C-H coupling. Silica samples were transferred into a nitrogen-filled glove box after a period of 48 h under vacuum, and were prepared within the glovebox. Analysis by solid-state NMR spectroscopy was undertaken by packing portions of

each of the variously-treated silicas into a wide bore sample rotor [4 mm] to maximise sample amount and thus maximise signal-to-noise. Using the MestReNova software package (version: x64 24/01/18), the spectral baseline was corrected by “zero fill and LP” options using a Toeplitz method with a coefficient of 8, and then phase correction was applied. The baseline was further corrected with a polynomial fit. Using the Origin software package (version: 01/06/2018), the inbuilt baseline algorithm was used to correct the baseline.

6.0.2.4 ICP-OES Analysis: Sample Preparation

Pyrex boiling tubes were washed out three times with *aqua regia* and three times with distilled water prior to use. Each sample of Co/SiO₂ was accurately weighed into a boiling tube, and *aqua regia* (3 mL) added. The boiling tubes containing the sample and *aqua regia* were heated to 80 °C using a stirrer hotplate fitted with an aluminium heating block for 1 hour to ensure full digestion of the metal from the surface of silica; the tubes were then allowed to cool to room temperature. The contents of the boiling tubes were washed into volumetric flasks (pre-washed three times with *aqua regia* and three times with distilled water) and the solutions made up to the mark with distilled water. The resulting solution was filtered through a glass wool plug to remove any residual silica, and the prepared solutions were submitted to the Durham University ICP-OES service for analysis. Sample digestion was repeated in duplicate. Each ICP-OES Co determination was undertaken alongside a Co standard (Co(NO₃)₂·6H₂O) with a known concentration of cobalt. The ICP-OES results were returned in mg/L and the cobalt % w.t. loading of the materials were calculated subsequently.

6.0.2.5 GC Analysis of Reaction Solvent to Quantify Ligand Released during Impregnation

A sample of **A-SiO₂₋₆₀₀** (0.5 g) was loaded into an ampule (fitted with a Young’s tap and side-arm and ground glass connector) along with the chosen cobalt complex (0.42 mmol, assuming that there is 0.83 mmol g⁻¹ of OH species available to react). Dry pentane (10 mL) was added and the reaction was stirred at room temperature for 2 hours. The ampule was attached to one side of a glass vacuum transfer arm and a clean empty ampule to the other; the arm and second ampule were evacuated. The ampule containing the sample was degassed using three freeze-pump-thaw cycles. Subsequently, all volatile components, including solvent and released ligand, were transferred to the clean ampule *via* a vacuum transfer process using liquid N₂ as refrigerant. The system was allowed to warm to room temperature and cautiously back filled with nitrogen to atmospheric pressure. An internal standard of nonane was added to the mixture of volatile components in the second ampule, stirred for 5 min, and an aliquot (~0.1 mL) removed for analysis by GC.

6.0.2.6 PXRD Sample Preparation

Air-sensitive samples for PXRD analysis were prepared in a nitrogen-filled glovebox by charging a 1 mm diameter glass capillary tube with the sample and sealing it with plasticine. The capillary was removed

from the glovebox, and the end sealed with plasticine was flame-sealed. The sample was submitted to the Durham PXRD service for analysis.

Non-air-sensitive samples for PXRD analysis were prepared by applying a thin layer of Vaseline to a PXRD disc. The sample was sprinkled on top of the Vaseline on the PXRD disc, with excess powder being tapped off, leaving a thin layer of flat sample stuck to the plate. The sample was submitted to the PXRD service for analysis.

6.0.2.7 CHN Sample Preparation

Non-air-sensitive samples for CHN were submitted to the Durham University CHN service as a powder in a vial. Air-sensitive samples for CHN were prepared in a nitrogen-filled glovebox, by sealing the sample in a pre-weighed tin capsule with a press, and then submitting the sealed tin capsules in a sealed vial under nitrogen, in order to limit exposure to atmosphere. A 'blank' tin capsule was also prepared alongside each sample, with the tin capsule being sealed in the same manner to enclose the same glovebox nitrogen atmosphere. The blank tin capsule was used to standardise the end results of the air-sensitive CHN sample analyses.

6.0.2.7.1 Calculations for Expected CHN of blank $A\text{-SiO}_{2-600}$ and (2)/ $A\text{-SiO}_{2-600}$

The expected CHN analysis of blank $A\text{-SiO}_{2-600}$ was calculated using the hydroxyl density that was determined in Section 2.2.2 (0.83 mmol g^{-1}). The calculation for the percentage of hydrogen present in $A\text{-SiO}_{2-600}$ is shown in Figure 6.1. The carbon and nitrogen contents were not calculated, as none are present in the blank silica. The expected CHN of $A\text{-SiO}_{2-600}$ is C 0%; H 0.08%; N 0%.

$$\begin{aligned}
 0.83 \text{ OH mmol g}^{-1} &= 0.83 \text{ H mmol g}^{-1} \\
 \text{H mmol g}^{-1} \times \frac{\text{H molecular weight (g mol}^{-1}\text{)}}{1000} & \\
 0.83 \text{ mmol g}^{-1} \times \frac{1.001 \text{ g mol}^{-1}}{1000} &= 0.00083 \text{ g} \\
 \frac{\text{weight of hydrogen}}{\text{weight of total}} \times 100 & \\
 \frac{0.00083 \text{ g}}{1 \text{ g}} \times 100 &= 0.083 \%
 \end{aligned}$$

Figure 6.1. Calculations using the hydroxyl density derived from titration with *o*-tolyl-MgBr to determine the expected hydrogen content of $A\text{-SiO}_{2-600}$ for CHN analysis

The calculation for the determination of the expected CHN analyses of (2)/ $A\text{-SiO}_{2-600}$ is similar to that described in Figure 6.1, however, the calculation needs to include the ligands on the cobalt centre,

the remaining unreacted silanols, and other surface species such as $-\text{SiMe}_3$. It is assumed that all tethered cobalt species are mono-grafted, losing one silyl-amine ligand to form $-\text{Co-N}(\text{TMS})_2(\text{THF})$. As the cobalt density of **(2)/A-SiO₂₋₆₀₀** is known to be 0.39 mmol g^{-1} (see Section 3.1.2.1), the surface densities of the $-\text{N}(\text{TMS})_2$ ligand and coordinated THF can also be derived. The number of unreacted silanols ($0.332 \text{ mmol g}^{-1}$) and the number of surface $-\text{SiMe}_3$ species ($0.108 \text{ mmol g}^{-1}$) is known (see Section 3.1.2.4). The calculation for the expected hydrogen content of **(2)/A-SiO₂₋₆₀₀** is given in Figure 6.2. Similar calculations were done for the expected carbon and nitrogen content. The expected CHN analyses are C 5.12%; H 1.16%; N 0.6%.

$$\begin{aligned}
 0.39 \text{ mmol g}^{-1} \text{ of } -\text{CoN}(\text{TMS})_2 &= 10.1 \text{ H mmol g}^{-1} \\
 0.108 \text{ mmol g}^{-1} \text{ of } -\text{SiMe}_3 &= 0.972 \text{ H mmol g}^{-1} \\
 0.385 \text{ OH mmol g}^{-1} &= 0.385 \text{ H mmol g}^{-1} \\
 \text{H mmol g}^{-1} \times \frac{\text{H molecular weight (g mol}^{-1}\text{)}}{1000} & \\
 \left(10.1 \text{ mmol g}^{-1} \times \frac{1.001 \text{ g mol}^{-1}}{1000} \right) + \left(0.972 \text{ mmol g}^{-1} \times \frac{1.001 \text{ g mol}^{-1}}{1000} \right) & \\
 + \left(0.332 \text{ mmol g}^{-1} \times \frac{1.001 \text{ g mol}^{-1}}{1000} \right) &= 0.011 \text{ g} \\
 \frac{\text{weight of hydrogen}}{\text{weight of total}} \times 100 & \\
 \frac{0.008 \text{ g}}{1 \text{ g}} \times 100 &= 1.1 \%
 \end{aligned}$$

Figure 6.2. Calculation for determining the expected hydrogen content of **(2)/A-SiO₂₋₆₀₀** for CHN analysis.

6.0.2.8 Temperature Programmed Reduction (TPR)

The general set-up for the Temperature Programmed Reduction (TPR) of materials is shown in Figure 6.3. The material to be analysed was accurately weighed ($\sim 100 - 150 \text{ mg}$) inside a nitrogen-filled glovebox and loaded into a quartz tube (i.d. = 0.25 mm) between two acid-washed quartz wool plugs. Before removing from the glove box, the ends of the quartz tube were fitted with metal ball valves connected to the tube using UltraTor fittings to enable transfer of the tube to the horizontal furnace and TPR set-up without exposing the sample material to atmosphere. The quartz tube was connected to a Schlenk line through one of the taps, and after application of a vacuum/nitrogen cycle, the tap was then opened to the nitrogen line. The quartz tube was inserted into the horizontal furnace. The Mass-Flow Controller and gas delivery line were purged for 10 minutes under a flow of nitrogen (50 mL min^{-1}). While the quartz tube is under a flow of nitrogen, the seal on the end of quartz tube was removed and connected to the Mass-Flow Controller. Then, the quartz tube was disconnected from

the Schlenk line and connected to the CaCl_2 drying column and TCD detector. Once the quartz tube was fully connected to the TPR set-up, the gas flow was changed to a flow of N_2 (40 mL min^{-1}) and H_2 (10 mL min^{-1}). The sample was heated to $500 \text{ }^\circ\text{C}$ at a rate of $10 \text{ }^\circ\text{C min}^{-1}$, before being held at this temperature for 30 minutes. The sample was allowed to cool, then transferred to a nitrogen-filled glovebox without exposure to atmosphere using the reverse of the procedure described above. Samples were stored in the glovebox until used.

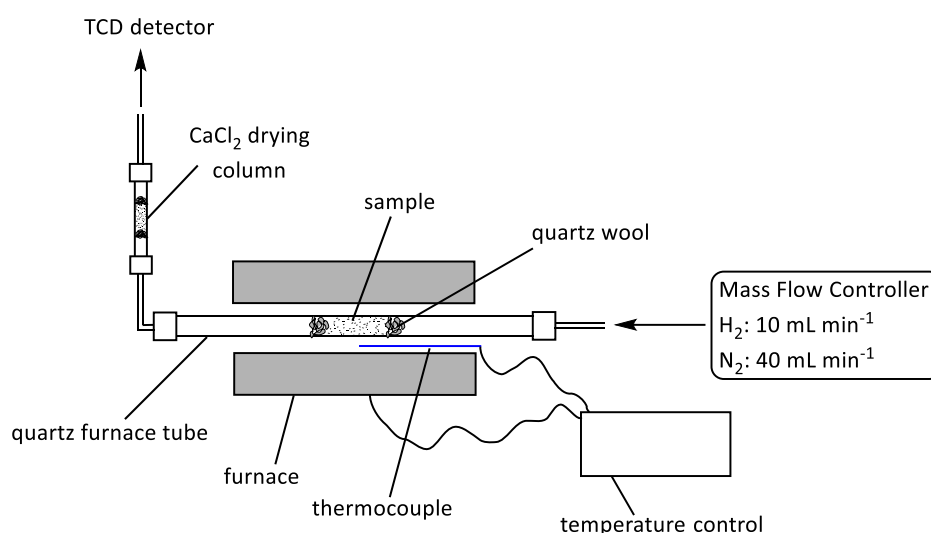


Figure 6.3. General set-up for TPR analysis

6.0.2.9 Magnetic Moment Measurement using a Gouy (JME) Balance

All samples and the standard $(\text{NH}_4)_2\text{Fe}(\text{SO}_4)_2 \cdot 6\text{H}_2\text{O}$ were ground to a uniform powder before analysis. A custom made Gouy tube fitted with a Youngs tap was carefully loaded with ground $(\text{NH}_4)_2\text{Fe}(\text{SO}_4)_2 \cdot 6\text{H}_2\text{O}$, ensuring that the packing was homogenous, until the sample length was ~ 3.5 cm. The length of the sample and its weight were accurately measured. The Gouy tube was inserted into the Gouy balance and the reading and temperature were recorded. The calibration constant of the Gouy balance was calculated using the standard $(\text{NH}_4)_2\text{Fe}(\text{SO}_4)_2 \cdot 6\text{H}_2\text{O}$, assuming that the mass susceptibility of $(\text{NH}_4)_2\text{Fe}(\text{SO}_4)_2 \cdot 6\text{H}_2\text{O}$ was: χ_g at $20 \text{ }^\circ\text{C} = 4.059 \times 10^{-7} \text{ m}^3\text{kg}^{-1}$. The same Gouy tube was used for analysis of all samples. Air-sensitive samples were loaded into the Gouy tube inside a nitrogen-filled glovebox, and sealed with the Youngs tap to maintain an inert atmosphere.

6.0.2.10 Transmission Electron Microscopy (TEM) Imaging

Samples for non-air-sensitive TEM analysis were prepared by dispersing a small amount of each reduced material in 2-propanol (Fisher Scientific, laboratory reagent grade) using an ultrasonic bath. Two drops of the suspension were then added dropwise onto a holey carbon film, (EM Resolutions, 300 mesh, copper) and dried at room temperature. The average Co particle sizes and the size

distribution histograms were typically determined from TEM images by counting 50 particles from at least three different regions of the film.

Air-sensitive TEM samples were analysed by Johnson Matthey. The samples were supplied to Johnson Matthey sealed in a screw-cap glass vial under a dry nitrogen atmosphere, with the vials being further sealed using PVC electrical tape to limit contamination during delivery.

6.0.2.11 Approximation of the Diameter of Complex 2, 4, and 7

Using the Scigress software package (*version: 3.5 20/08/22*), the structures of the complexes were drawn, and corrected with the software's 'beautify' method. The distance between the two furthest atoms were measured. This process was repeated until the widest diameter was found and then this value used as the diameter of the complex.

6.0.3 Synthetic Methods

6.0.3.1 Synthesis of SBA-15

SBA-15 was prepared according to a literature procedure.² Pluronic-123 (8.097 g, 1.42 mmol), HCl (2M, 240 mL) and distilled water (60 mL) were placed in a 500 mL polypropylene bottle. The mixture was heated to 45 °C in a water bath and stirred with a Teflon-coated stirrer bar for 4 hours or until the solution became clear/homogeneous. Tetraethyl orthosilicate (TEOS) (17.034 g, 82.2 mmol) was added, and the reaction was stirred at 45 °C for 20 hours, forming a fine white solid. The bottle was removed from the water bath, sealed, and placed in an oven at 100 °C (with no stirring) to age for 24 hours. The resulting white solid was isolated by hot filtration with a glass frit and washed with ethanol (3 × 75 mL) and water (3 × 75 mL). The silica was allowed to air-dry overnight, before being calcined in a furnace at a ramp rate of 1 °C min⁻¹ to 550 °C and maintained at 550 °C for 4 hours, before being allowed to cool to RT over a period of 12 hours. Yield: 4.825 g; PXRD data are consistent with prior literature.²

6.0.3.2 Synthesis of KIT-6

KIT-6 was prepared according to a literature procedure.³ Pluronic-123 (8.097 g, 1.42 mmol), HCl (37 %, 6.7 mL, 13 mmol) and distilled water (144 mL) were placed in a 500 mL polypropylene bottle. The mixture was heated at 35 °C in a water bath and stirred with a Teflon-covered stirrer bar for 2 hours or until the solution became clear/homogeneous. *n*-Butanol (4.068 g, 43.1 mmol) was added and the mixture stirred at 35 °C for 1 hour. Tetraethyl orthosilicate (TEOS) (8.634 g, 42.17 mmol) was added, and the reaction mixture was stirred at 35 °C for 24 hours, during which time the clear colourless solution formed a fine white solid. The bottle was removed from the water bath, sealed, and placed in an oven at 100 °C with no stirring action to age for 24 hours. The resulting white solid was isolated by hot filtration with a glass frit and washed with 2 M HCl (3 × 50 mL) and ethanol (3 × 75 mL). The silica was allowed to air-dry for 3 days, before being calcined in a furnace at a rate of 1 °C min⁻¹ to

550 °C and maintained at 550 °C for 6 hours, before being allowed to cool to RT over a period of 12 hours. Yield: 2.455 g; PXRD data are consistent with prior literature.³

6.0.3.3 Calcination of Aeroperl 300/30 Silica (A-SiO_{2-700/600/400/200})

The general experimental set-up used for the calcination of the various oxide supports comprises a vertically-set quartz furnace tube, located within a furnace (Figure 6.4). A quartz tube (20 mm i.d.) was charged with an acid-treated quartz wool plug and Aeroperl 30/300 silica (~5 g) and placed vertically in a tube furnace. The silica was placed under a downward flow of nitrogen (flow rate of 1 bubble.s⁻¹) exiting the reactor *via* an oil bubbler (to ensure efficient removal of the released water) and heated to 600 °C at a rate of 10 °C min⁻¹ and held at this temperature for 24 hours. The silica was allowed to cool under a flow of nitrogen before being transferred to a Schlenk flask without exposure to the atmosphere. The silica was stored in a nitrogen-filled glove box until its use. An identical process was used for the preparation of A-SiO₂₋₇₀₀, A-SiO₂₋₄₀₀ and A-SiO₂₋₂₀₀ at calcination temperatures of 700, 400, and 200 °C, respectively.

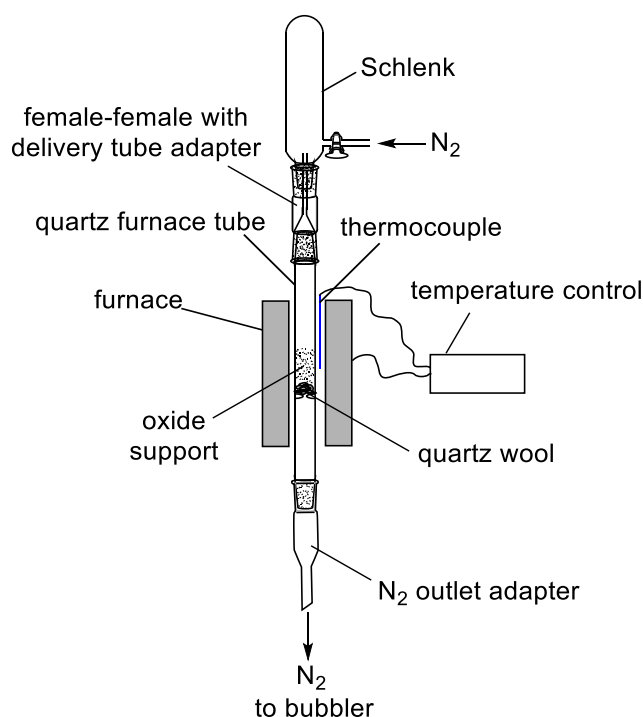


Figure 6.4. Experimental set-up for the calcination of oxide supports

6.0.3.4 Synthesis of Li(N(TMS)₂)(THF)

The title compound was prepared according to a literature procedure.⁴ A solution of *n*-BuLi (2.3 M in hexane, 19 mL, 44.9 mmol) in dry THF (30 mL) was cooled to -78 °C in a dry-ice/acetone bath, and HN(TMS)₂ (8.4 mL, 40.1 mmol) was subsequently added dropwise over 30 min. The reaction was stirred at -78 °C for 1 hour. A white precipitate formed in a pale yellow solution. The reaction was allowed to warm to room temperature and all volatiles were removed *in vacuo*, leaving a pale yellow

solid. The solid was washed with cold dry pentane at $-78\text{ }^{\circ}\text{C}$ to yield $\text{Li}(\text{N}(\text{TMS})_2)(\text{THF})$ as a white powder. The solid was dried *in vacuo*, then stored in a nitrogen-filled glovebox until needed. Yield: 8.76 g, 36.6 mmol, 91%; ^1H NMR (400 MHz, C_6D_6) δ 3.74 – 3.56 (m, 4H; CH_2O , THF), 1.26 – 1.21 (m, 4H; CH_2 , THF), 0.37 (d, $J = 0.8\text{ Hz}$, 18H; CH_3 , TMS); ^{13}C NMR (101 MHz, C_6D_6) δ 68.93 (s; CH_2O , THF), 25.39 (s; CH_2 , THF), 6.39 (s; CH_3 , TMS); ^6Li NMR (155 MHz, C_6D_6) δ 1.14 (s, 1Li). The ^1H , ^{13}C , and ^6Li NMR spectral data are consistent with prior literature.⁴

6.0.3.5 Synthesis of $[\text{Co}(\text{N}(\text{TMS})_2)_2(\text{THF})]$ (**2**)

The title compound was prepared using a modified literature procedure.⁴ $\text{Li}(\text{N}(\text{TMS})_2)(\text{THF})$ (8.76g, 36.6 mmol) was dissolved in dry THF (40 mL). The solution was transferred *via* a cannula to a round bottom flask charged with CoCl_3 (2.16 g, 16.6 mmol), keeping the flask cooled at $0\text{ }^{\circ}\text{C}$. The reaction was allowed to warm to room temperature and heated for 2 hours at reflux. The solution colour changed from blue to dark green. All volatile components were then removed *in vacuo*, leaving a dark green solid. The solid was extracted with dry pentane ($5 \times 20\text{ mL}$) to give a dark green solution. All volatile components were removed *in vacuo*, leaving $[\text{Co}(\text{N}(\text{TMS})_2)_2(\text{THF})]$ (**2**) as a bright green solid and used without further purification. Yield: 4.65 g, 10.3 mmol, 62 %; CHN (Expect: C, 42.53 %; H 9.82 %; N, 6.15 %; Found: C, 42.44 %; H 10.01 %; N, 6.20 %)

6.0.3.6 Synthesis of dimesitylphenyl iodine (dmp-I)

The title compound was prepared according to a literature procedure.⁵ Dry 1,3-dichlorobenzene (4.6 ml, 40 mmol) and dry THF (100 mL) were cooled to $-78\text{ }^{\circ}\text{C}$. *n*-BuLi (2.3 M in hexane, 19.1 mL, 44 mmol) was added over 30 min. The reaction was stirred for 150 min, maintaining the temperature at $-78\text{ }^{\circ}\text{C}$. The solution changed from clear and colourless, to a white suspension, to a black solution. A solution of Mes-MgBr in THF (1M in THF, 100 mL, 50 mmol) was added over 120 min at $-78\text{ }^{\circ}\text{C}$. The reaction mixture was then allowed to warm to room temperature and stirred for 18 h, then heated for a further 2 hours at reflux. The reaction was cooled to $0\text{ }^{\circ}\text{C}$ and a THF solution (100 mL) of I_2 (25.4 g, 100 mmol) was added over 30 min. The reaction mixture was allowed to return to room temperature and stirred for 20 hours. The reaction was quenched by addition of a saturated aqueous sodium thiosulfate (400 mL) solution and separated. The aqueous layer was further washed with diethyl ether ($5 \times 100\text{ mL}$). The organic layers were combined and dried with MgSO_4 ; subsequently all volatile components were removed to give a pale yellow solid. The crude product was recrystallized from ethanol (800 mL) to give dimesitylphenyl iodine as a white crystalline solid, following isolation by filtration. ^1H -NMR spectroscopy confirmed the compound's structure as dmp-I. Yield: 7.214 g, 16.382 mmol, 41 %; ^1H NMR (400 MHz, chloroform-*d*) δ 7.48 (t, $J = 7.5\text{ Hz}$, 1H; *p*- C_6H_3), 7.10 (d, $J = 7.5\text{ Hz}$, 2H; *m*- C_6H_3), 6.99 (s, 4H; *m*-MesH), 2.38 (s, 6H; *p*- ArCH_3), 2.01 (s, 12H; *o*- ArCH_3). The ^1H NMR spectral data are consistent with prior literature.⁵

6.0.3.7 Synthesis of dimesitylphenyl lithium (dmp-Li)

The title compound was prepared according to a literature procedure.⁵ A dry toluene (38 mL)/hexane (32 mL) solution of dmp-I (7.214 g, 16.4 mmol) was cooled to 0 °C and *n*-BuLi (1.9 M in hexane, 10 mL, 17.2 mmol) was added dropwise. The reaction was stirred for 30 min then removed from the cold bath and stirred for a further 2 hours at room temperature. The solution changed from pale yellow to bright yellow with formation of a white suspension. The reaction was filtered, and all volatile components subsequently removed *in vacuo* from the filtrate to give a bright yellow solid. The solid was washed with dry hexane at –78 °C until the solid was a clean white powder. Dimesitylphenyl lithium, as a white powder, was dried *in vacuo* and stored in a nitrogen glovebox until needed. Yield: 3.93g, 12.3 mmol, 75%; ¹H NMR (400 MHz, chloroform-*d*) δ 7.24 (t, *J* = 7.5 Hz, 1H; *p*-C₆H₃), 6.84 (m, 6H; *m*-C₆H₃, *m*-MesH), 2.17 (s, 6H; *p*-ArCH₃), 1.83 (s, 12H; *o*-ArCH₃); ⁶Li NMR (400 MHz, chloroform-*d*) δ 1.41 (s, 1 Li). The ¹H NMR and ⁶Li NMR spectral data are consistent with literature data.⁵ Reliable CHN analyses could not be obtained due to how air-sensitive the compound was.

6.0.3.8 Synthesis of Co(dmp)₂ (4)

The title complex was prepared according to a literature procedure.⁵ Anhydrous CoBr₂(DME) (0.89 g, 2.88 mmol) and dmp-Li (2.045 g, 6.38 mmol) were dissolved in dry toluene (30 mL), giving an opaque brown slurry after two min. Dry THF (2 mL) was then added and the solution instantly turned a clear blue colour. The reaction mixture was stirred for 19 hours at room temperature, during which time the solution colour changed to a dark red. All volatile components were removed *in vacuo* to give a dark red solid. The solid was extracted with hexane (3 × 20 mL) to give a dark red solution. The solution was concentrated *in vacuo* and cooled to –25 °C to induce crystallisation. The red crystals of Co(dmp)₂ were isolated by filtration and dried *in vacuo*. Yield: 0.878 g, 1.28 mmol, 44 %; CHN (Expected: C, 84.06 %; H 7.35 %; N, 0 %; Found: C, 85.01 %; H 7.36 %; N, 0.07 %).

6.0.3.9 Synthesis of CoCp(CO)₂ (5)

The title complex was prepared according to a literature procedure.⁶ Dicyclopentadiene was degassed using the freeze-pump-thaw technique before cracking into cyclopentadiene monomer, which was isolated *via* reactive distillation at 42-43 °C. The cyclopentadiene monomer was stored in the dark under nitrogen at 0 °C until needed. Co₂(CO)₈ (2.098 g, 6.13 mmol) was dissolved in DCM (20 mL) in the dark and cyclopentadiene monomer (2.5 mL, 30.4 mmol) added *via* syringe. The reaction was heated under reflux at 45 °C, with the exclusion of light, for 48 h. The reaction was allowed to cool, then the DCM was removed by distillation at 40-42 °C. The CoCp(CO)₂ was isolated from the reaction mixture *via* a vacuum transfer as a dark red oil. The CoCp(CO)₂ product was stored under nitrogen, excluded from the light, at –25 °C. Yield: 0.684 g, 3.8 mmol, 62 %; FTIR (cm⁻¹): 2015 (C-O stretch), 1960 (C-O stretch). The FTIR spectroscopic data are consistent with data in the literature.⁶

6.0.3.10 Synthesis of $\text{Co}(\text{C}_8\text{H}_{12})(\text{C}_8\text{H}_{13})$ (7)

The title complex was prepared according to a literature procedure.^{7,8} Anhydrous CoCl_2 (0.478 g, 3.68 mmol) was dissolved in dry THF (40 mL), and pyridine (1.6 mL, 19.86 mmol) and then COD (1.6 mL, 13.04 mmol) were added sequentially. The mixture was stirred for 90 min. The pale blue suspension turned to a pale violet purple. The mixture was added to sodium (0.169 g, 7.35 mmol), and quickly cooled to -8°C . The reaction was stirred for 48 hours at -8°C . The reaction turned black with a dark precipitate. The reaction was filtered under nitrogen *via* a frit, to give a dark solution. All volatile components were removed under vacuum to give a dark brown solid. The solid was redissolved in pentane (20 mL), cooled to -8°C and filtered through a frit. The solution was concentrated *in vacuo* and cooled to -25°C to induce crystallisation. The shiny black crystals of $\text{Co}(\text{C}_8\text{H}_{12})(\text{C}_8\text{H}_{13})$ were isolated by filtration, dried *in vacuo* and stored in a nitrogen glovebox until needed. Yield: 0.188 g, 0.68 mmol, 18.5%. CHN (Expected: C, 69.55 %; H 9.12 %; N, 0 %; Found: C, 71.43 %; H 8.86 %; N, 0.04 %) Due to air-sensitivity of title complex, CHN analysis was difficult and CHN results are slightly off from their expected values.

6.0.3.11 Tethering Cobalt Complexes 2-5, 7, and 8 to Silica

The chosen cobalt complex was dissolved in dry pentane (20 mL) at room temperature. The amount of cobalt used was calculated using the hydroxyl density of the silica previously determined by titration. Silica was loaded into a Schlenk flask and the Co-complex/pentane solution was transferred *in via* cannula to the SiO_2 , and the mixture was stirred for up to 4 hours at room temperature. During this time, the solution lost some colour, while the white silica became coloured. The pentane/pentane-soluble materials were removed by filtration and the residual solid was washed with dry pentane (3×10 mL). The solid was carefully dried *in vacuo*, leaving a coloured solid. The solid was stored in the glove box for further use.

6.0.3.12 Addition of $\text{Co}_2(\text{CO})_8$ (6) to Silica

$\text{Co}_2(\text{CO})_8$, **6**, (0.042 g, 0.242 mmol, 1.13 Co wt. %) was dissolved in dry pentane (10 mL) at 0°C . Aeroperl 30/300 Silica (**A-SiO₂₋₆₀₀**) (1.028 g) was loaded into a Schlenk flask. The $\text{Co}_2(\text{CO})_8$ /pentane solution was transferred *via* cannula onto the sample of **A-SiO₂₋₆₀₀**, and the mixture was stirred for 15 min at 0°C . All volatile components were carefully removed under a partial vacuum, leaving a pale brown solid. The solid was stored in the dark, under nitrogen, at -17°C .

6.0.3.13 Reduction of (2)/**A-SiO₂₋₆₀₀**

Freshly prepared **(2)/A-SiO₂₋₆₀₀** (1 g) was loaded and sealed into the reduction set-up shown in Figure 6.5 in a nitrogen-filled glovebox. The set-up was attached to a Schlenk line and opened to the nitrogen line after application of a vacuum/nitrogen cycle. A pre-mixed 5% H_2/N_2 supply (BOC) was connected *via* a gas flow meter and all the tubing was purged with H_2/N_2 gas for 5 minutes to remove oxygen and

moisture. Under a flow of nitrogen from the Schlenk line and a flow of H₂/N₂ from the cylinder, the cylinder was connected to the reduction set up. The set-up was disconnected from the Schlenk line and attached to an oil bubbler. The gas flow of H₂/N₂ (50 mL min⁻¹) was controlled by the flow meter. The set-up was lowered into a pre-heated oil bath (150 °C) as shown in Figure 6.5, so that all of the sample was below the oil. The sample was heated for 3 hours to ensure complete reduction. A colour change from green to blue was observed. When the reduction was finished, the set-up was allowed to cool to room temperature. The resulting material was stored in a nitrogen-filled glovebox until used. This method was used for all gases and all temperatures.

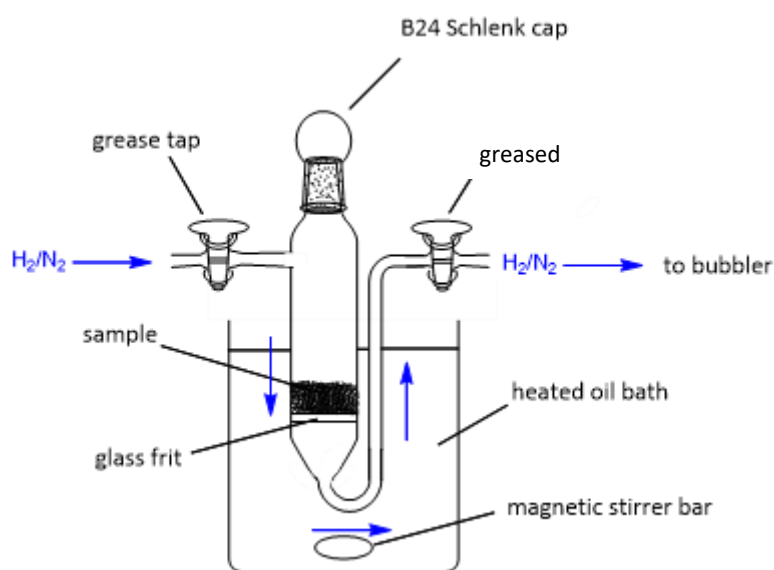


Figure 6.5. General set-up for the reduction of (2)/A-SiO₂₋₆₀₀

6.0.3.14 Sublimation of Residual Complex 3 from (3)/A-SiO₂₋₆₀₀

(3)/A-SiO₂₋₆₀₀ (0.5 g) was loaded into a Schlenk flask inside a nitrogen-filled glovebox. The Schlenk flask was fitted with a cold finger and placed under vacuum. The cold finger was cooled to -78 °C with dry ice/acetone. The bottom of the Schlenk was gently heated to 60 °C with an oil bath while under a static vacuum. The sample of (3)/A-SiO₂₋₆₀₀ showed no colour change, and no solid appeared on the cold finger. The temperature was slowly raised 10 °C every 15 minutes until 100 °C when a colour change was observed, the sample of (3)/A-SiO₂₋₆₀₀ changing colour from purple to black. A dark purple crystalline solid appeared on the cold finger and was subsequently isolated and determined to be cobaltocene by CHN.

6.0.3.15 Synthesis of Co(NO₃)₂/SiO₂

Co(NO₃)₂·6H₂O (0.3421 g, 1.175 mmol, 2.3% w.t. Co) was dissolved in deionised water (5.5 mL). A vial was charged with calcined Aeroperl 300/30 silica, A-SiO₂₋₆₀₀, (3.009 g), and the Co(NO₃)₂·6H₂O solution was added dropwise. The resulting material was mixed using a vortex mixer, and then the material was calcined in an oven at 120 °C for 24 h. The colour of the material changed from pink to black. The

material was then charged into a quartz tube and reduced under a flow of H_2/N_2 (10 mL/40 mL) while heating to 500 °C at a rate of 10 °C min^{-1} , before being held at this temperature for 30 min. The sample was allowed to cool, then transferred to a nitrogen-filled glovebox without exposure to atmosphere. $\text{Co}(\text{NO}_3)_2/\text{SiO}_2$ was stored in the glovebox until used.

6.0.3.16 Catalytic Hydrogenation of CNA

A three-neck 50 mL round bottom flask was charged with the chosen catalyst (113 mg, 2.4 w.t% Co) inside a nitrogen-filled glovebox, and fitted with a water condenser, a gas adaptor tap, and two glass stoppers (see Figure 6.6). The flask was connected to the Schlenk line through the gas adaptor tap and opened to nitrogen following a vacuum/nitrogen cycle. Under a slow flow of N_2 (5 mL min^{-1}), the glass stopper on top of the water condenser was replaced with a three-way gas adaptor tap, connected to the nitrogen line and vented to an oil bubbler, under a flow of nitrogen. A solution of cinnamaldehyde (0.1 mL, 0.79 mmol) in propylene carbonate (20 mL) was added to the flask. A fritted gas inlet dip tube, connected to a hydrogen gas cylinder, was attached to the flask, and the fritted gas inlet dip tube was lowered until the frit was below the surface of the solution. The H_2 gas flow was set to 20 mL min^{-1} using a rotameter, and the reaction was heated to 150 °C for 9 hours while stirring. The reaction was allowed to cool completely, *n*-butyl ether was then added to the reaction mixture as an internal standard, and the organic solution was isolated by filtration through a celite plug. An aliquot (~0.1 mL) of this solution was removed for analysis by GC.

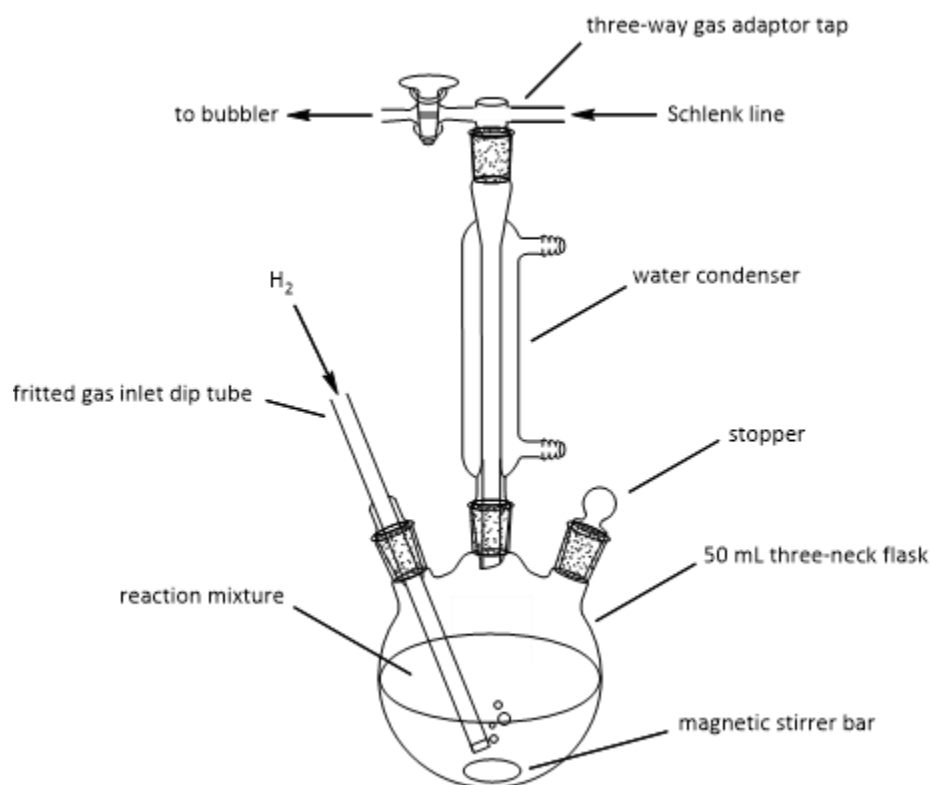


Figure 6.6. General set-up for the hydrogenation of CNA

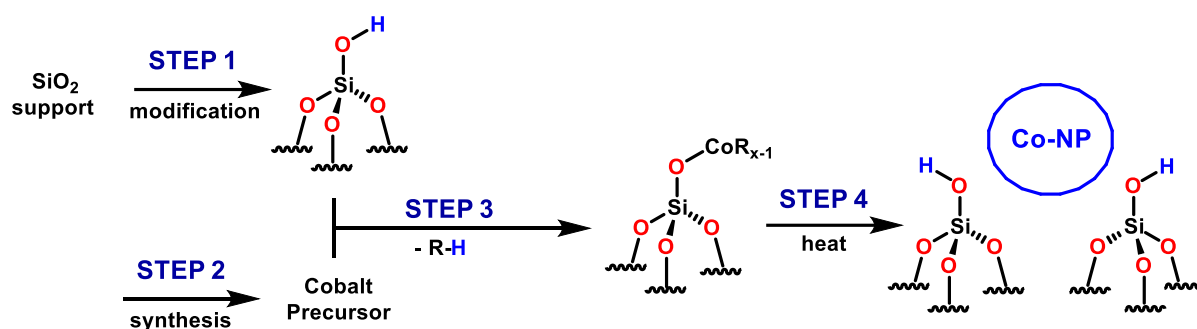
6.1 References

1. A. F. Burchat, J. M. Chong and N. Nielsen, *J. Org. Chem.*, 1997, **542**, 281-283.
2. V. V. Pushkarev, K. An, S. Alayoglu, S. K. Beaumont and G. A. Somorjai, *J. Catal.*, 2012, **292**, 64-72.
3. F. Kleitz, S. H. Choi and R. Ryoo, *Chem. Commun.*, 2003, 2136-2137.
4. D. C. Bradley, R. G. Copperthwaite, M. W. Extine, W. W. Reichert and M. H. Chisholm, in *Inorg. Synth.*, ed. B. E. Douglas, Hoboken, New Jersey, 2007, vol. Volume XVIII, pp. 112 - 119.
5. D. L. Kays and A. R. Cowley, *Chem. Commun.*, 2007, 1053-1055.
6. T. S. Piper, F. A. Coyron and G. Wilkinson, *J. Inorganic and Nuclear Chemistry*, 1955, **1**, 165-174.
7. D. Zitoun, C. Amiens and B. Chaudret, *J. Phys. Chem. B*, 2003, **107**, 6997-7005.
8. T. O. Ely, C. Pan, C. Amiens and B. Chaudret, *J. Phys. Chem. B*, 2000, **104**, 695-702.

Chapter 7: Summary and Future Work

7.0 Summary

This project set out with the aim of synthesising sub-nanosized supported cobalt particles through a new synthetic route (Scheme 7.1), as part of a broader study into developing routes to sub-nanosized particles for catalysis. A secondary project aim was to investigate the catalytic properties of the prepared nanoparticles and correlate their formation and their resulting size to their catalytic activity/selectivity.

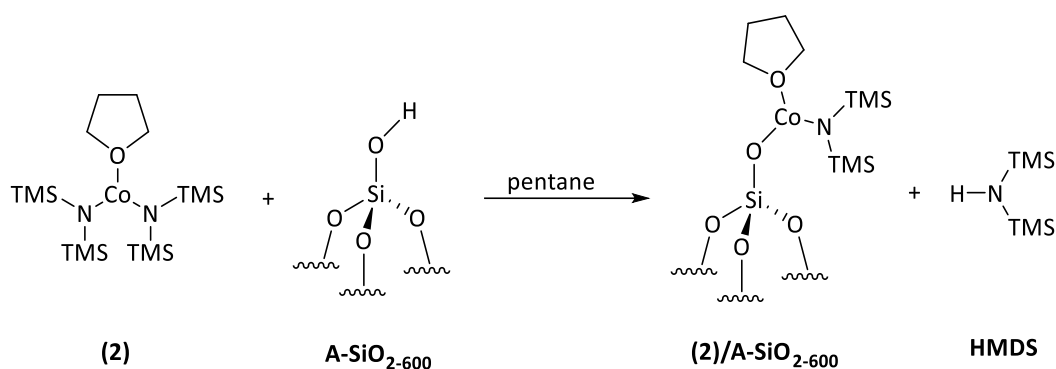


Scheme 7.1. The four-step method simplified for the synthesis of bound nanoparticles.

Early in the project, it was identified that a key component for controlling the size and formation of cobalt nanoparticles was the oxide support, here silica, something related to the oxide's modification/preparation. While silica supports are already well-documented in literature,¹⁻⁴ this project looked at SBA-15, KIT-6, and Aeroperl 300/30 silicas with a larger focus on the silanol density on the silica surface than usually seen in literature, and how the silanol density may be varied through use of different calcination temperatures. It has been shown successfully that both ¹H SS-NMR spectroscopy and chemical titration methods using *o*-tolylmagnesium chloride, when used in conjunction with BET surface analysis, can be used to determine the silanol density on the silica surface and give results that are in good agreement. As anticipated, it was confirmed that silicas' silanol density decreases with an increase in calcination temperature (200 – 700 °C). ²⁹Si SS-NMR spectroscopy was found to be useful method for identifying the different types of silanol groups present on the oxide. Aeroperl 300/30 silica was found to be the best support for this project's goals due to its consistent silanol density after calcination and thermal stability up to 700 °C and, based on previous work with the group,⁵ calcination under a flow of N₂ at 600 °C for 24 h was chosen as the pre-treatment (the resulting material denoted as **A-SiO₂₋₆₀₀**).

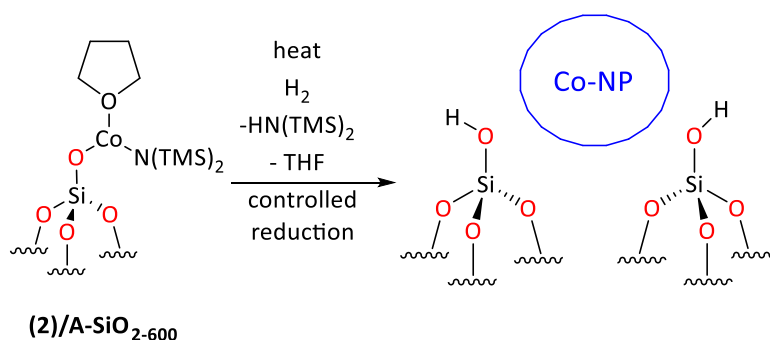
[Co(N(TMS)₂)₂(THF)] was chosen as a nanoparticle precursor due to prior work by Oakton *et al.* who explored the generation of silver nanoparticles on silica through a silver silylamide precursor.⁶ [Co(N(TMS)₂)₂(THF)], denoted as complex **2**, became the main focus of the project after it was successfully tethered to **A-SiO₂₋₆₀₀**, the resulting material characterised, and identified as possessing a

mono-grafted cobalt surface species, **(2)/A-SiO₂₋₆₀₀** (Scheme 7.2). A paramagnetic Co²⁺ species is present in **(2)/A-SiO₂₋₆₀₀**, so analysis by SS-NMR spectroscopy was limited; though two surface species, -Co(NSiMe₃) and -OSiMe₃, were tentatively identified by ¹H SS-NMR analysis. ICP-OES analysis confirmed the degree of loading of complex **2** to **A-SiO₂₋₆₀₀** (2.2% w.t. Co), and a %CHN determination was used to identify that one HMDS ligand was attached to the cobalt metal centre. BET analysis showed the decrease in pore size as functionalisation (a combination of metalation and silylation) of the silica surface occurred during impregnation. The material **(2)/A-SiO₂₋₆₀₀** was determined to be a promising precursor to small cobalt nanoparticles due to how reactive it was.



*Scheme 7.2. Reaction of complex **2** and **A-SiO₂₋₆₀₀** to form **(2)/A-SiO₂₋₆₀₀** and concomitant release of a molecule of HMDS*

The reduction of **(2)/A-SiO₂₋₆₀₀** (Scheme 7.3) was probed by TPR methods, with the material being found to undergo a reaction with hydrogen at 150 °C. Subsequently, **(2)/A-SiO₂₋₆₀₀** was reduced under a number of different conditions, using a range of temperatures (150, 200, 250 °C) and gas compositions (5% H₂/N₂, H₂, N₂) to form **(2)/A-SiO₂₋₆₀₀ (T °C, gas)**. Subsequent SS-NMR spectroscopic studies of the reduced **(2)/SiO₂₋₆₀₀** materials indicated that -OSiMe₃ surface species are present. A TEM investigation of a range of **(2)/A-SiO₂₋₆₀₀ (T °C, gas)** materials was undertaken using non-air sensitive and air-sensitive techniques. Subsequent TEM imaging of **(2)/A-SiO₂₋₆₀₀ (150 °C, H₂)**, air-exposed **(2)/A-SiO₂₋₆₀₀**, and **(2)/A-SiO₂₋₆₀₀ (air-exposed, 150 °C, H₂)** showed the presence of small cobalt particles (0.5 - 3 nm). TEM images of **(2)/A-SiO₂₋₆₀₀ (150 °C, N₂)** achieved without exposure of the materials to air/moisture indicated that there are cobalt particles on the surface (2 – 3 nm), while TEM images of **(2)/A-SiO₂₋₆₀₀ (150 °C, N₂)** obtained following sample exposure to air, showed crystal lattice lines with a d-spacing that matches cubic CoO (NaCl, Fm-3m).⁷ Analysis of the magnetic properties of the various cobalt-modified silicas under inert atmosphere conditions were inclusive, and it could not be determined whether the particles were cobalt(II) oxide or metallic Co⁰. The nature of the cobalt surface species could not be determined due to their air-sensitivity.



Scheme 7.3. The proposed reduction of (2)/A-SiO₂₋₆₀₀ into cobalt nanoparticles

Subsequent work described in this thesis probed the use of **(2)/A-SiO₂₋₆₀₀**-derived materials as hydrogenation catalysts. Since α,β -unsaturated aldehydes offer two sites for reduction (hydrogenation of the C=C or the C=O bond), the hydrogenation of cinnamaldehyde (CNA) was chosen as a test reaction to explore catalytic selectivity as well as activity. While it is noted in the literature that cobalt-based catalysts are particularly selective towards the formation of unsaturated alcohol (CNOL),^{8, 9} it was found that four catalysts, **(2)/A-SiO₂₋₆₀₀ (150 °C, N₂, then H₂, vacuum)**, **(2)/A-SiO₂₋₆₀₀ (150 °C, N₂, then 5% H₂/N₂, vacuum)**, **(2)/A-SiO₂₋₆₀₀ (150 °C, N₂, vacuum)**, and **(2)/A-SiO₂₋₆₀₀ (250 °C, N₂, vacuum)**, showed catalytic activity towards the formation of the saturated aldehyde, HCNA. Catalysts derived from **(2)/A-SiO₂₋₆₀₀** show a different hydrogenation selectivity than the reference catalyst **(A-SiO₂₋₆₀₀ impregnated with Co(NO₃)₂·6H₂O, denoted here as Co(NO₃)₂/SiO₂)**, which was selective towards the formation of CNOL. It is thought that the catalysis of CNA to HCNA is due to the cobalt particles (2-3 nm) on the surface of silica. It is currently unknown why the selectivity of these catalysts is towards HCNA rather than CNOL.

The catalytic activity of **(2)/A-SiO₂₋₆₀₀ (150 °C, N₂, then H₂, vacuum)** changed over time, reducing in effectiveness across a period of 33 hours. This loss of performance coincided with the production of several unwanted side-products, including (1E,2E)-3-Phenyl-N-(trimethylsilyl)-2-propen-1-imine (denoted as CNA-imine1) which formed from the reaction between CNA and trace HMDS remaining on the catalyst surface. Treatment to remove physisorbed HDMS (heating under vacuum and washing with pentane) would truncate the production of CNA-imine1 and other unwanted side-products. While successful hydrogenation cobalt catalysts were synthesised, which demonstrated a selectivity towards HCNA, the formation of unwanted side-products could not be completely prevented.

To briefly summarise, studies done in this project have shown that **(2)/A-SiO₂₋₆₀₀**, when heated under hydrogen at relatively low temperatures (150 - 250 °C), is a good precursor to nanosized cobalt particles (0.5 - 3 nm) tethered to a silica support. Heating the **(2)/A-SiO₂₋₆₀₀** precursor at 150 – 250 °C in the absence of hydrogen will produce cobalt particles (2-3 nm) on the silica surface instead. These

cobalt particles are capable of catalytic hydrogenation of CNA to HCNA, contrary to the usual selectivity that cobalt catalysts have towards CNOL that is reported in the literature.^{8,9}

This synthetic route to supported cobalt particles (Scheme 7.1) studied by this thesis is a promising method and, so far, capable of producing very small Co nanoparticles on silica. While there are highly unstable intermediates that require handling under strict conditions to prevent contact with air and/or moisture, and can make characterisation difficult, the route shows several promising aspects. These aspects include a high degree of control over the metal loading, through precisely controlling the hydroxyl density of the silica support by calcination, and activation of catalysts at relatively low temperatures (150 °C).

7.1 Future Work

As the oxide support is considered to have an important role in the formation of the nanoparticle and in the resulting supported nanoparticle catalyst's behaviour,¹⁰⁻¹² further research into different oxide supports is imperative. While silica was the focus of this thesis, alumina is another common oxide often used as a support in industrial heterogeneously-catalysed reactions. Alumina and silica share many desirable traits with one another - durability and stability in harsh conditions such as high temperatures (up to 973 K for γ -alumina) and pressures. However, catalysts deposited on alumina often show different behaviour from catalysts prepared using silica, something attributed to 'support effects', where a catalyst's behaviour or formation is altered by the molecular environment of the support, as reported by Somorjai *et al.*'s study, which compares silica and alumina, as well as other supports (TiO_2 , Nb_2O_5 , Ta_2O_5 , and ZrO_2).¹³ Other oxide support that are potentially beneficial to study due to potential support effects on this thesis's synthesis towards sub-nanosized particles include silica-alumina, titania, and zirconia. Silica-alumina offers an interesting comparison to both silica and alumina separately, as it has been suggested in literature that it may be better to consider silica-alumina as silica with discrete patches of alumina within the structure.¹⁴ Titania also promises to be an interesting oxide support, as it is unique among other oxide supports due to the presence of SMSI effects.¹⁵ It may also be valuable to study as an oxide support for this synthetic route to sub-nanosized particles due to its acid-base properties,¹⁶ which makes it an interesting comparison to more typically acidic oxide supports like silica and silica-alumina. For a more stable catalyst support, zirconia can be employed due to its high chemical inertness compared to that of other oxide supports such as silica and alumina.¹⁷ Monoclinic zirconia has excellent thermodynamic stability below 1170 °C, is chemically stable, has good mechanical strength and can have high accessible surface area.¹⁷ Zirconia could offer an new perspective on an oxide support calcined at temperatures above 800 °C, without the risk of pore structure collapse and loss of surface area.

Following the analysis into different support effects from different oxide supports, pre-treatment of the oxide support should be examined further, such as the effects of the temperature of calcination on nanoparticle formation. While silica supports calcined at 600 °C were studied more deeply than other calcination temperatures in this thesis, it is valuable to consider the effects of raising or lowering the calcination temperature on any resulting nanoparticles. A higher oxide support pre-calcination temperature will decrease the loading of cobalt (as a result of a lower silanol density) and therefore potentially resulting in smaller nanoparticles on the support's surface, but there is a possibility of pore structure collapse as was seen for KIT-6 in Section 2.2.1.3. A lower calcination temperature will result in a higher cobalt species loading, and is something likely to form bipodal cobalt surface-bound species, as discussed in Section 1.0.6.1,¹⁸ which side-effects on the formation of nanoparticles is currently unknown.

Following on from the results described in Chapter 3 and 4, other precursors, such as complex **4** (Co(dmp)₂), should be further examined as precursors to sub-nanosized cobalt particles. Complexes **4** – **8** (from Chapter 3) were chosen and synthesised in this project due to the anticipation that they would reduce to small nanoparticles, but due to time constraints, they were not fully characterised when tethered to the surface of silica, nor were their reductions to nanoparticles explored. Thus, further study into the cobalt precursor should be considered high importance, as the precursor choice has a profound effect on the formation of the nanoparticles.

In order to improve understanding of the reduced material derived from **(2)/A-SiO₂₋₆₀₀**, it is imperative that a broader range of analytic techniques is explored, such as Mössbauer spectroscopy to probe the nature of the cobalt cations present in the nanoparticles or STEM to analyse the 3D morphology of the nanoparticles. The development of more air-sensitive techniques is also necessary, to allow better characterisation of the surface species of materials derived from **(2)/A-SiO₂₋₆₀₀**.

A deeper investigation into the hydrogenation of CNA *via* silica-supported cobalt species is required to explore the cause of the selectivity towards HCNA when using catalysts derived from heating **(2)/A-SiO₂₋₆₀₀** in the absence of hydrogen. It is currently unknown why the selectivity of these catalysts (**(2)/A-SiO₂₋₆₀₀** (150 °C, N₂, then H₂, vacuum), **(2)/A-SiO₂₋₆₀₀** (150 °C, N₂, then 5% H₂/N₂, vacuum), **(2)/A-SiO₂₋₆₀₀** (150 °C, N₂, vacuum), and **(2)/A-SiO₂₋₆₀₀** (250 °C, N₂, vacuum)) is towards HCNA rather than CNOL, but it has been proposed by this project that the selectivity towards the saturated aldehyde is due to the presence of small cobalt particles on the silica surface. Further investigation is required in order to understand the differences in selectivity and structure of the catalysts.

As alluded to in Section 1.0.8.1, it would be valuable to probe other catalytic hydrogenation reactions, such as the hydrogenation of nitrobenzene to aniline,¹⁹ which has industrial interests due to the commercial significance of aniline and its derivatives.²⁰ Although nitrobenzene is considered to have one available site for hydrogenation (ignoring the possibility of hydrogenating the aromatic ring), the NO₂ group, the reaction has been shown to proceed through a complex reaction pathway, with several intermediates and possible side-products.²¹ However, in the literature, this reduction is often explored in terms of catalytic activity rather than selectivity,²⁰ making the reaction of nitrobenzene to aniline a good probe for the activity of the catalysts synthesised in this thesis. There remains a significant scope for interesting development and optimisation of this route to supported cobalt nanoparticles, as well as their potential in heterogeneous hydrogenation.

7.2 References

1. L. T. Zhuravlev, *Langmuir*, 1987, **3**, 316-318.
2. A. P. Legrand, *The Surface Properties of Silicas*, John Wiley, Chichester, 1998.
3. E. F. Vansant, P. V. D. Voort and K. C. Vrancken, *Characterisation and Chemical Modification of the Silica Surface*, Elsevier, Wilrijk, Belgium, 1995.
4. J. T. Marta Szekeres, Imre Dékány, *Langmuir*, 2002, **18**, 2678-2685.
5. M. J. Lamb, D. C. Apperley, M. J. Watson and P. W. Dyer, *Top. Catal.*, 2018, **61**, 213-224.
6. E. Oakton, G. Vilé, D. S. Levine, E. Zocher, D. Baudouin, J. Pérez-Ramírez and C. Copéret, *Dalton Trans.*, 2014, **43**, 15138-15142.
7. S. Sasaki, K. Fujino and Y. Takéuchi, *Proc. Japan Acad.*, 1979, **55**, 43 - 48.
8. Y. Yang, D. Rao, Y. Chen, S. Dong, B. Wang, X. Zhang and M. Wei, *ACS Catal.*, 2018, **8**, 11749 - 11760.
9. Z. Wu, J. Zhao, M. Zhang, W. Li and K. Tao, *Catal. Commun.*, 2010, **11**, 973 -976.
10. F. Rascón, R. Wischert and C. Copéret, *Chem. Sci.*, 2011, **2**, 1449-1456.
11. P. Denton, A. Giroir-Fendler, H. Praliaud and M. Primet, *J. Catal.*, 2000, **189**, 410-420.
12. J. Handzlik, J. Ogonowski, J. Stoch, M. Mikołajczyk and P. Michorczyk, *Appl. Catal., A: General*, 2006, **312**, 213-219.
13. K. An, S. Alayoglu, N. Musselwhite, K. Na and G. A. Somorjai, *J. Am. Chem. Soc.*, 2014, **136**, 6830-6833.
14. E. J. M. Hensen, D. G. Poduval, V. Degirmenci, D. A. J. M. Ligthart, W. Chen, F. o. Maugé, M. S. Rigutto and J. A. R. v. Veen, *J. Phys. Chem.*, 2012, **116**, 21416-21429.
15. M. A. Vannice, S.-Y. Wang and S. H. Moon, *J. Catal.*, 1981, **71**, 152-166.
16. D. Stošić, S. Bennici, J.-L. Couturier, J.-L. Dubois and A. Auroux, *Catal. Commun.*, 2012, **17**, 23-28.

17. P. D. L. Mercera, J. G. v. Ommen, E. B. M. Doesburg, A. J. Burggraaf and J. R. H. Ross, *Appl. Catal.*, 1991, **71**, 363-391.
18. C. Copéret, A. Comas-Vives, M. P. Conley, D. P. Estes, A. Fedorov, V. Mougel, H. Nagae, F. Núñez-Zarur and P. A. Zhizhko, *Chem. Rev.*, 2016, **116**, 324-421.
19. Q. Zhang, J. Bu, J. Wang, C. Sun, D. Zhao, G. Sheng, X. Xie, M. Sun and L. Yu, *ACS Catal.*, 2020, **10**, 10350-10363.
20. Y. Cao, K. Liu, C. Wu, H. Zhang and Q. Zhang, *Appl. Catal. A, General*, 2020, **592**, 1-9.
21. E. A. Gelder, S. D. Jackson and C. M. Lok, *Chem. Commun.*, 2005, 522-524.

Appendices

Appendix A: Calibration of Nonane against Toluene

This appendix consists of the calibration curve (Figure A.1) used to identify the number of moles of toluene produced during the determination of the hydroxyl density on the surfaces of silica supports (Aeroperl 300/30, SBA-15, and KIT-6). Nonane is used as an internal standard. The areas of the peaks in the GC-FID spectrum were used to calculate the datapoints. Figure A.1 was fitted with a linear trendline with the intercept set to zero.

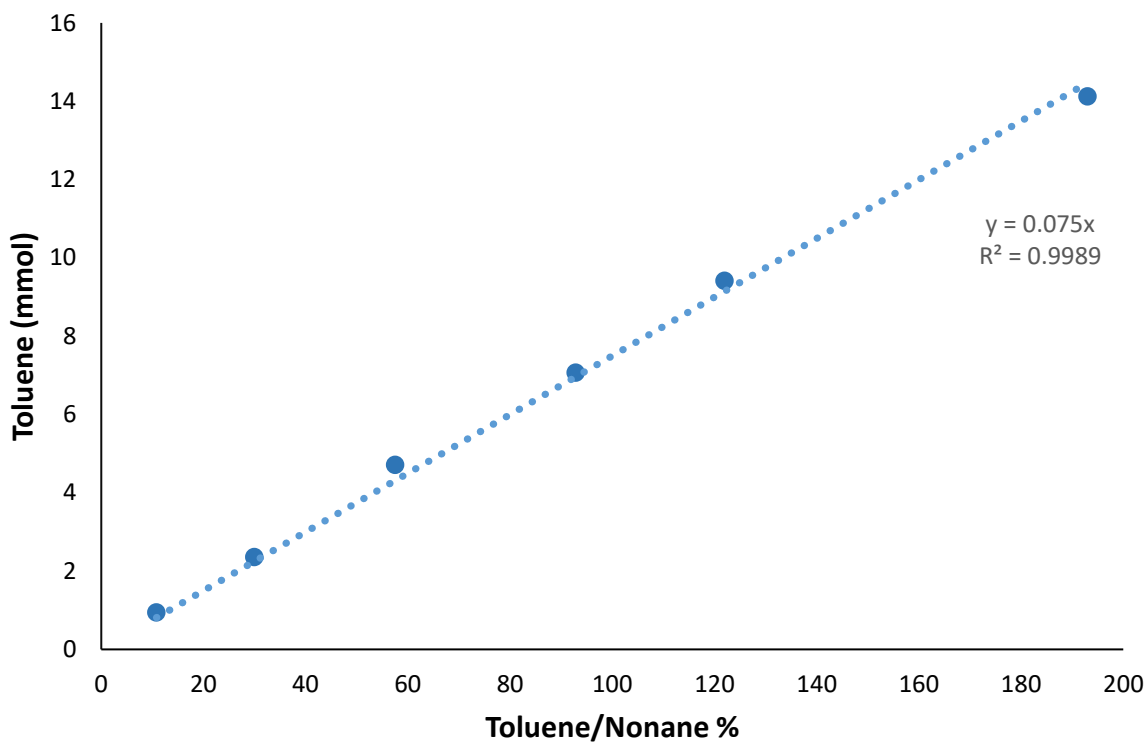


Figure A.1. Nonane vs. toluene calibration curve

Appendix B: Brunauer-Emmett-Teller (BET) Analysis

BET analysis is often used to probe the surface area of porous and non-porous materials such as catalyst supports. The BET theory follows on from the Langmuir theory, which describes the behaviour of monolayer adsorption. BET extends the Langmuir theory to multilayer adsorption by making three important assumptions:¹

1. gas molecules physically adsorb on a solid in layers infinitely,
2. there is no interaction between each adsorption layer,
3. the Langmuir theory can be applied to each layer.

BET analysis of a solid material typically is performed with an unreactive gas such as nitrogen and at low temperatures (*ca.* ~ 77 K, *a.k.a* – the boiling point of liquid nitrogen) to increase the interaction between the gas and the solid material. The pressure of the adsorbing gas is increased, maintaining the same temperatures, and more molecules are adsorbed onto the surface to form a mono-layer. From the volume of adsorbed molecules on the material surface, the surface area can be calculated from the BET equation (Equation A.1), which links the number of gas molecules adsorbed at a given relative pressure (P/P_0), where C , the BET constant, is a second parameter related to the heat of adsorption.¹ C is expressed as Equation A.2.¹

$$\frac{1}{v[(P_0/P) - 1]} = \frac{C - 1}{v_m C} \left(\frac{P}{P_0}\right) + \frac{1}{v_m C}$$

Equation A.1. The BET equation ¹

v = amount of gas adsorbed

v_m = monolayer capacity

(P/P_0) = relative pressure

C = BET constant

$$C = \exp\left(\frac{K_1 - K_L}{RT}\right)$$

Equation A.2. The C value, calculated from the intercept and intercept of the isotherm, and related to the heat of adsorption on the surface.¹

K_1 = heat of adsorption for the first layer

K_L = heat of adsorption for second layer and higher (is equal to the heat of vaporisation)

R = gas constant

T = temperature

Appendix C: ^1H SS-NMR Spectroscopy of Complex **2**

An ^1H SS-NMR spectrum of complex **2** was obtained, to compare it to **(2)/A-SiO₂₋₆₀₀** and identify any changes that the complex undergoes when tethered to the silica. Complex **2** is expected to exhibit 3 peaks in the ^1H NMR spectrum: 2 resonances representing the coordinated THF and 1 resonance correlated to the HMDS ligands. The ^1H NMR spectrum recorded at a spin of 40 kHz (Figure A.2) shows very narrow lines, and peaks at an unusually high chemical shift. It also exhibits a strong NOE (Nuclear Overhauser Effect) enhancement, as shown by significantly more signal with a short (1 s) recycle delay than a longer recycle delay (10 s).

A slower spin spectrum (spinning at 30 kHz) was recorded to confirm that the lines at 65.9 ppm and 114 ppm are centre bands (Figure A.3). The 30 kHz spectrum shows broader lines than that recorded at 40 kHz (Figure A.2). This is most likely the effect of complex **2** heating under MAS, melting slightly within the rotor, as the sample can be around 60 °C when spin at a faster spin rate (40 kHz).² Complex **2** has a melting point of 73 - 73 °C.³ In the 30 kHz spectrum, side bands appear at the spin-rate x2. This is unusual as there are no side bands at spin-rate x1, where they would be expected to be, nor any sidebands evident beyond spin-rate x2. It is suspected that the signals may be shifted due to the paramagnetic Co^{II} in complex **2**.

The ^1H spectrum for complex **2** (Figure A.2) and **(2)/A-SiO₂₋₆₀₀** (Figure 3.5, Section 3.1.2.3) are very different. As the ^1H spectrum for complex **2** is unusual and the peaks were not identified, it is difficult to compare it to **(2)/A-SiO₂₋₆₀₀** (Figure 3.5, Section 3.1.2.3).

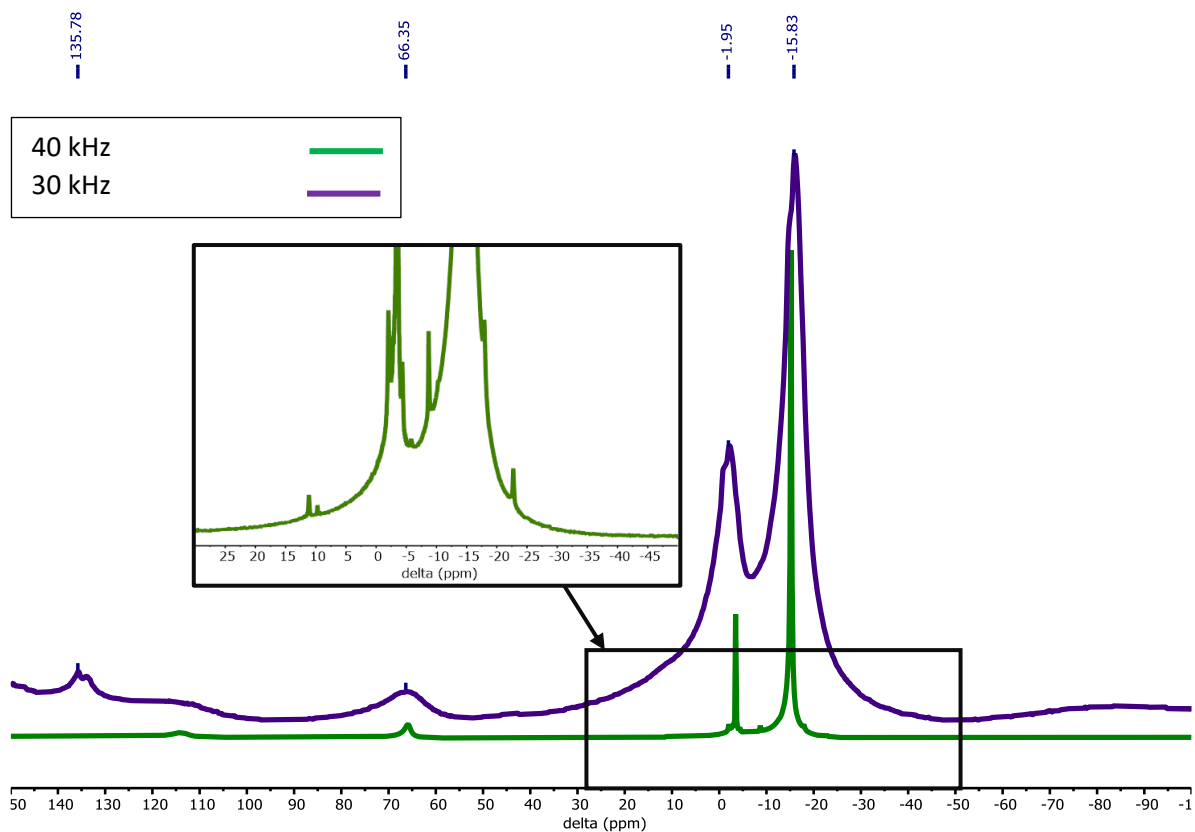


Figure A.2. Comparison of 40 kHz and 30 kHz ^1H SS-NMR spectra of complex **2**, Frequency 400.17 MHz

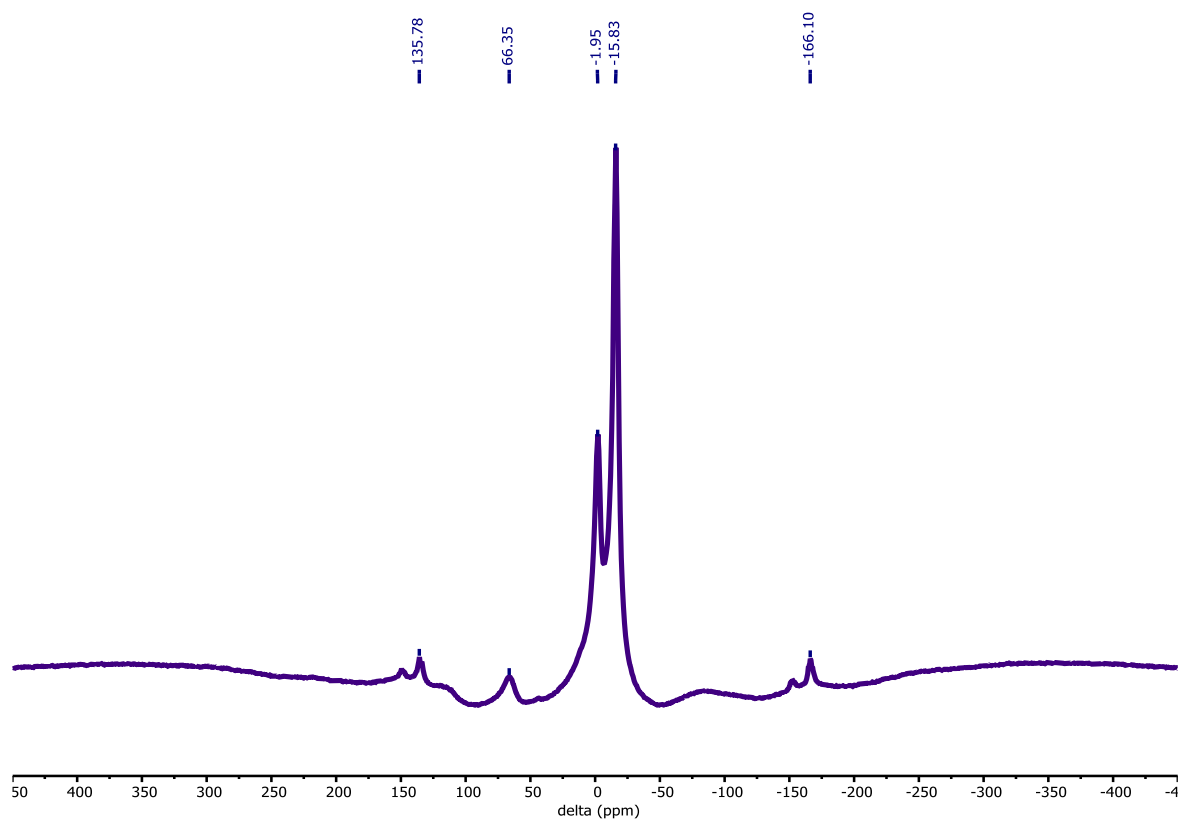


Figure A.3. A wider field of 30 kHz ^1H SS-NMR of complex **2**. Resonances at -2.0 and -15.3 ppm can be clearly identified with satellites. A third peak can be seen at 66.4 ppm, Frequency 400.17 MHz, Spin-rate 30 kHz

Appendix D: REAPDOR SS-NMR Spectroscopy of (3)/A-SiO₂₋₆₀₀

The paramagnetic cobalt in the system is likely to interfere with the cross-polarisation process, particularly with any protons near the Co. This interference would leave only SiOH groups remote from the Co available for participation in the cross-polarisation process. Therefore, a REAPDOR (Rotational Echo Adiabatic Passage Double Resonance) experiment was performed on a sample of the (3)/A-SiO₂₋₆₀₀ material. In a REAPDOR experiment, the proton signal was observed while recoupling any dipolar coupling with the cobalt (the magic-angle spinning removes this interaction so it has to be reintroduced). However, despite application of this method the resulting spectrum showed no evidence for such a Co···H interaction. The REAPDOR spectrum (Figure A.4) showed two signals: one at 1.8 ppm that was attributed to SiOH species with the other narrow signal near 0 ppm most likely being residual silicone grease picked up during the synthesis. There was no evidence for the protons in the hydrogen-containing ligands on the Co species. This indicates that either the cobalt was having a disruptive effect on the NMR or both Cp rings have been lost.

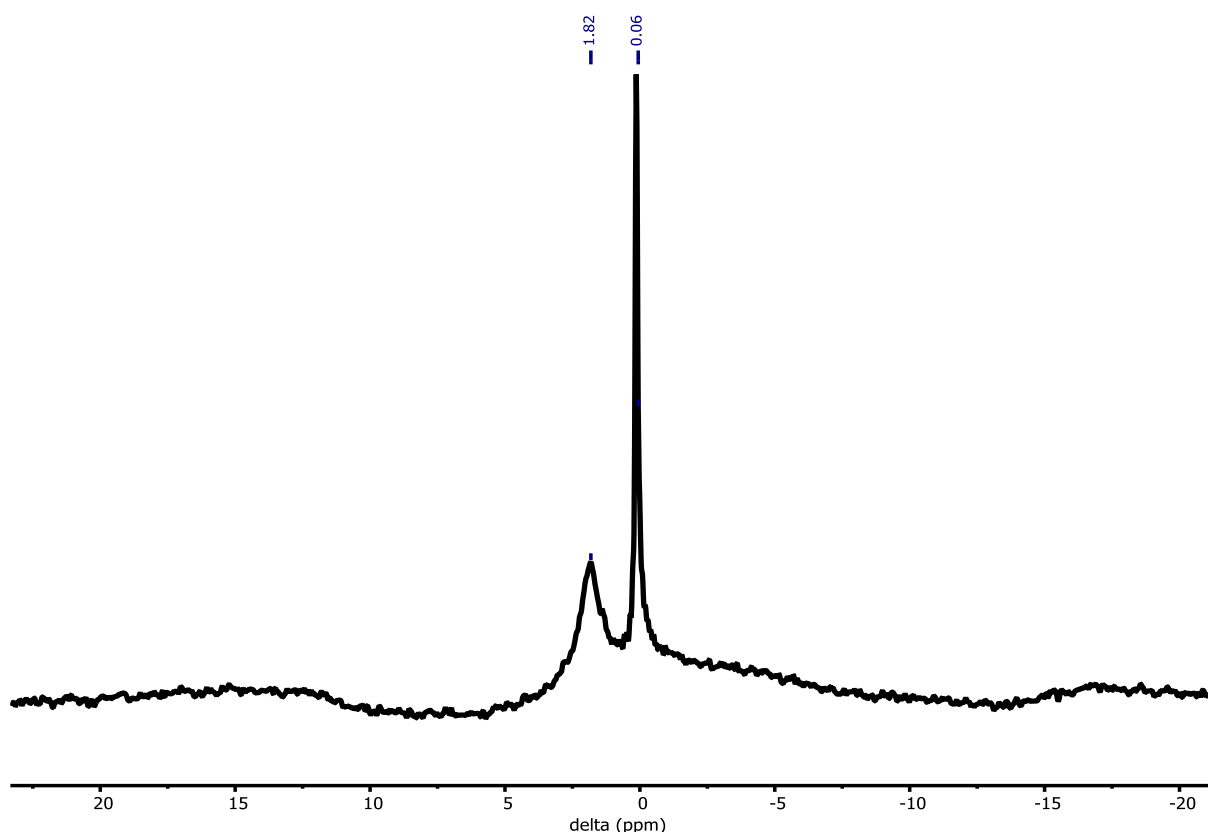


Figure A.4. ²⁹Si REAPDOR SS-NMR spectrum of (3)/A-SiO₂₋₆₀₀

Appendix E: Initial Attempts at TPR Analysis of (2)/A-SiO₂₋₆₀₀

While the high reactivity of (2)/A-SiO₂₋₆₀₀ makes it a promising precursor for small nanoparticles, this presented problems when attempting TPR analyses. While there were signals in the TPR, indicating that hydrogen was consumed and a reduction was occurring, the signals were broad (Figure A.5). The broad signal between 95 and 220 °C is suspected to be multiple signals that were very close together as a result of multiple reduction processes occurring. The resulting material from the reduction was not uniformly coloured, instead the bed of material closest to the gas outlet was dark blue, while the rest of the material was black (Figure A.6). It was suspected that this mix of blue and black material was due to partial oxidation from atmosphere during the TPR, as (2)/A-SiO₂₋₆₀₀ turns blue on exposure to atmosphere.

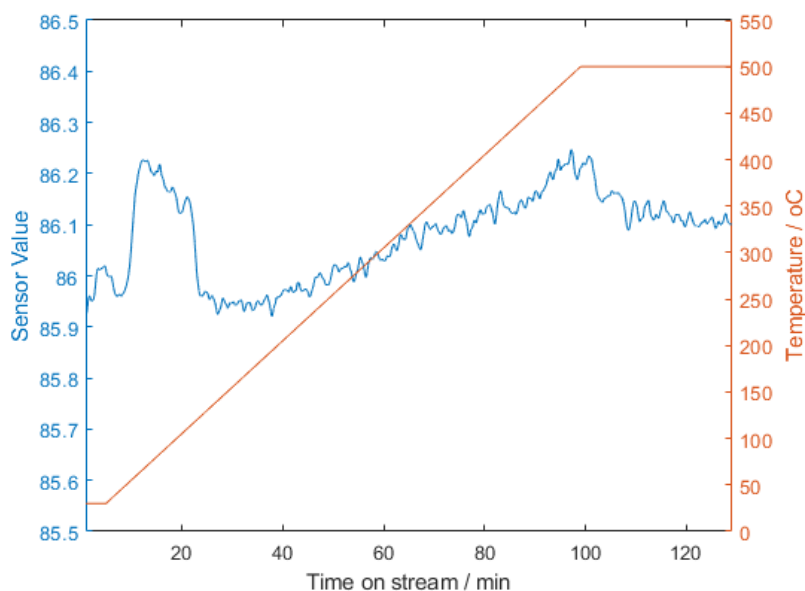


Figure A.5. Initial TPR Analysis of (2)/A-SiO₂₋₆₀₀

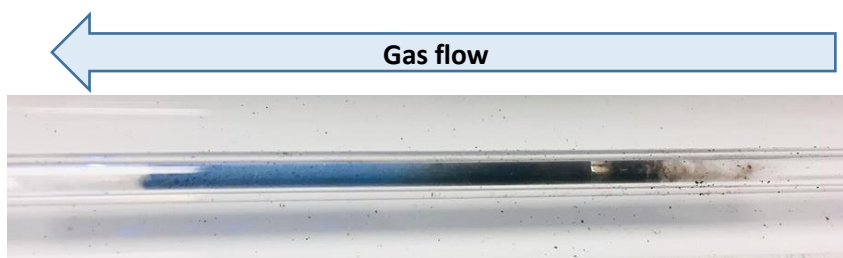


Figure A.6. The resulting colour of the (2)/A-SiO₂₋₆₀₀ post TPR analysis (TPR in Figure A.5), with the direction of gas flow shown

A second attempt at TPR analysis is shown in Figure A.7. The attempt gave a broad detector response between 50 – 150 °C. The resulting material from the TPR analysis from Figure A.7 showed different colours (grey or blue) in different parts of the sample.

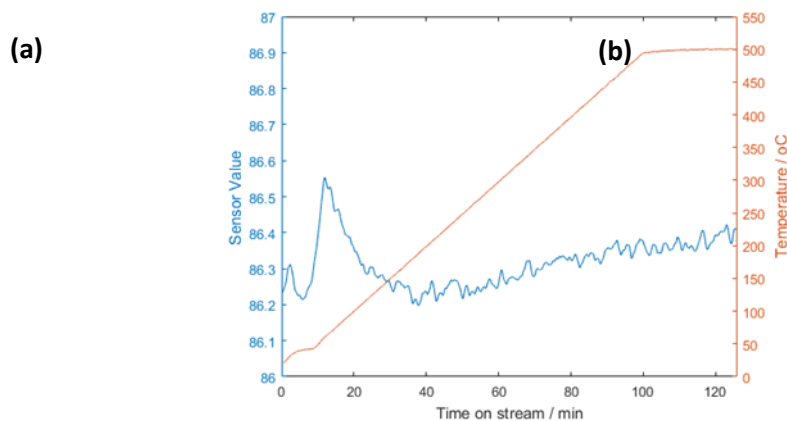


Figure A.7. TPR analysis of (2)/A-SiO₂₋₆₀₀ showing broad and noisy signals

Another attempt at the TPR analysis of (2)/A-SiO₂₋₆₀₀, seen in Figure A.8, has two overlapping signals names Peak 1 and Peak 2. The resulting material of the TPR analysis can be seen in Figure A.9, with two distinct colours, grey and blue, in different areas of the sample. The reduction occurs between 90 – 230 °C. As Figure A.8 appears to be two separate signals that overlap, it was decided that deconvolution should be employed to determine each individual peak area.

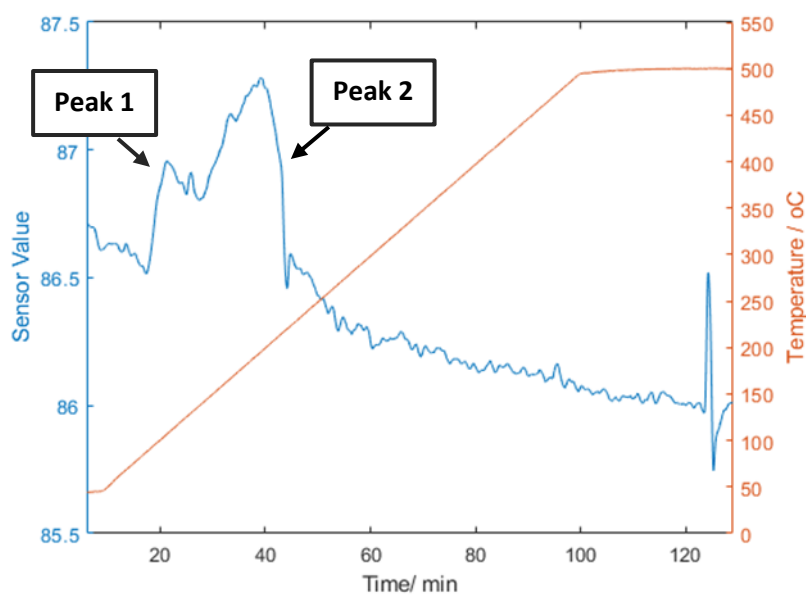


Figure A.8. TPR Analysis of (2)/A-SiO₂₋₆₀₀ showing two possible overlapping signals between 90 and 230 °C *

* The sharper peak at 125 to 130 minutes is due to a disruption in the hydrogen supply caused by other equipment in the laboratory.



Figure A.9. The resulting colour of the TPR analysis of **(2)/A-SiO₂₋₆₀₀** seen in FIGURE

Deconvolution of the Initial Attempts at TPR of **(2)/A-SiO₂₋₆₀₀**

As the TPR analysis of **(2)/A-SiO₂₋₆₀₀** seen in Figure A.8 has two signals, Signal 1 and Signal 2, deconvolution was attempted. The baseline of the TPR GC trace of **(2)/A-SiO₂₋₆₀₀** (Figure A.8) is slanted and noisy, so it was processed according to the method in Section 6.0.2.3. However, there is a feature near the baseline to the high temperature side Signal 2, labelled as Feature 3 in Figure A.10. It is not known if this feature is part of Signal 2, a third signal, or part of the baseline. As baseline adjustment is performed according to the immediate region on either side of the signal in question, Feature 3 will have an effect on baseline correction. Several attempts at deconvolution were done, with including and excluding Feature 3 from the baseline adjustment. The results of the deconvolutions of the TPR analysis of **(2)/A-SiO₂₋₆₀₀** (Figure A.10) are given in Table A.1. Hydrogen consumption ranges from 0.24 to 0.28 mmol. The hydrogen consumption was calculated with Feature 3 included and excluded from the adjusted baseline. The calculated hydrogen consumption varies depending on the inclusion of Feature 3 as part of the baseline. When Feature 3 is included in the baseline adjustment, the hydrogen consumption is calculated to be higher; the hydrogen consumption when Feature 3 is excluded is on average lower (0.25 mmol) than when Feature 3 included in the baseline adjustment (0.27 mmol). Feature 3 was also fitted as a possible third signal, that had a similar area to Signal 1.

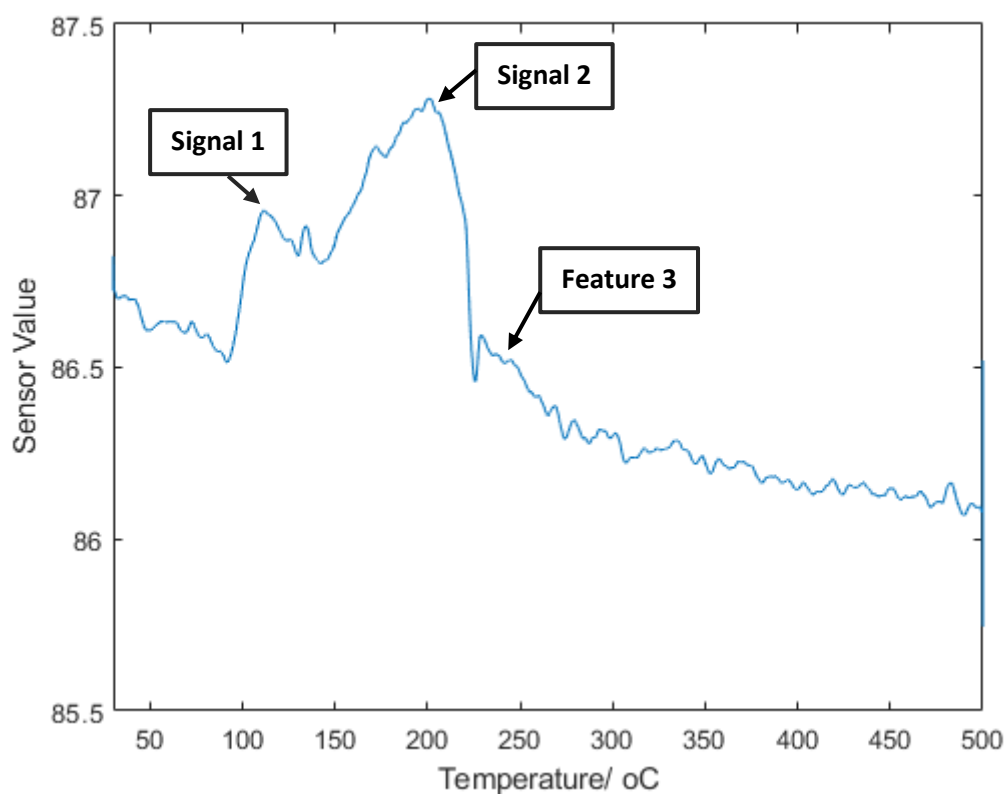


Figure A.10. TPR Analysis of (2)/A-SiO₂₋₆₀₀

There appears to be two distinctive peaks (Peak 1 and Peak 2) and a third feature (Feature 3) near the baseline.

Table A.1. The hydrogen consumption of (2)/A-SiO₂₋₆₀₀, calculated from the possible deconvolutions of the TPR analysis (Figure A.10). The baseline was adjusted depending on whether Feature 3 was considered part of the baseline or not.

Baseline	Peak Type	Signal 1 H ₂ consumption (mmol)	Signal 2 H ₂ consumption (mmol)	Feature 3 H ₂ consumption (mmol)
Feature 3 excluded	Gaussian	0.05	0.19	x
Feature 3 excluded	Lorentzian	0.04	0.21	x
Feature 3 included	Gaussian	0.07	0.21	x
Feature 3 included	Lorentzian	0.06	0.22	x
Feature 3 excluded	Gaussian	0.05	0.18	0.04
Feature 3 included	Gaussian	0.05	0.15	0.05

Appendix F: Scherrer Equation for PXRD analysis of

The Scherrer equation (Equation A.3) relates crystallite size to broadening of the reflection observed in PXRD.⁴ While the Scherrer equation is often mistaken as a formula for particle size, it can offer some insight on the size of nanoparticles present in a sample as particles can be considered agglomerations of crystallites. The crystallite size is equal or less than nanoparticle size.

$$\tau = \frac{K\lambda}{\beta \cos\theta}$$

Equation A.3. The Scherrer equation⁴

τ = mean size of crystallite

K = shape factor

λ = X-Ray wavelength

β = full width at half maximum of reflection

θ = Bragg angle

Appendix G: Testing for Cobalt in CNA Catalysis Reaction Mixture

A step in the analysis of the catalytic hydrogenation of CNA used in this project is the separation of the catalyst from the CNA hydrogenation reaction mixture prior to GC-FID analysis. This is done for two reasons: to prevent small particles from blocking the GC column and to stop any further reaction from being catalysed by any remaining cobalt catalyst. The method used to separate the catalysts from the CNA hydrogenation reaction mixture in this project is two filtrations through a celite and glass wool plug.

To ensure that no catalyst remained in the CNA hydrogenation reaction solution, a qualitative test for the presence of cobalt was performed using ether and ammonium thiocyanate. In small vials, a mixture of ether and ammonium thiocyanate (ca. ~ 5 mg) was prepared (Figure A.11). In vial (a), cobalt nitrate was added; in vial (b), two drops of unfiltered CNA hydrogenation reaction mixture was added; in vial (c), two drops of CNA hydrogenation reaction mixture filtered through one celite and glass wool plug; and in vial (d), two drops of CNA hydrogenation reaction mixture filtered through two celite and glass wool plugs. If cobalt is present in the filtered reaction mixture, cobalt thiocyanate, a bright blue compound, will form and a colour change from colourless to blue will be observed. This is observed in vial (a), where the cobalt nitrate was added so the colour change from colourless to blue could be observed and compared to the other vials. Vials (b) and (c) also underwent a colour change to partially blue, indicating that cobalt was present in the unfiltered CNA hydrogenation reaction mixture and the CNA hydrogenation reaction mixture that had been filtered once. There was no colour change in vial (d), showing that no cobalt was present and that two filtrations was enough to remove all the catalyst from the CNA hydrogenation reaction mixture. This also showed that no cobalt leeching from the silica surface had occurred, as removal of the solid catalyst removed all cobalt from the reaction mixture.

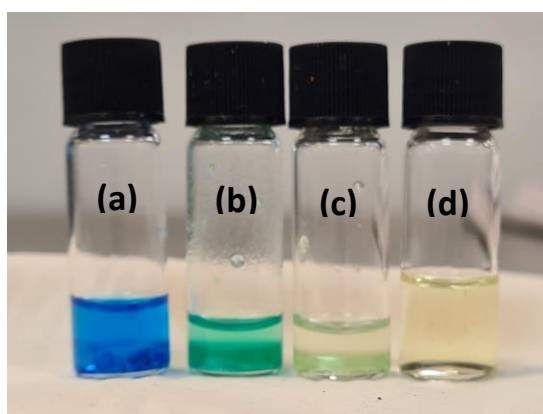


Figure A.11. Qualitative test for the presence of cobalt using a mixture of ether and ammonium thiocyanate (a) cobalt nitrate; (b) unfiltered CNA hydrogenation reaction mixture; (c) CNA hydrogenation reaction mixture filtered once through a celite and glass wool plug; (d) CNA hydrogenation reaction mixture filtered through two celite and glass wool plugs

Appendix H: Calibration Curves For CNA, CNOL, HCNA, HCNOL in the Hydrogenation of CNA

This appendix consists of the calibration curves used to identify the number of moles of CNA (Figure A.12), CNOL (Figure A.13), HCNA (Figure A.14), and HCNOL (Figure A.15) produced during the hydrogenation of CNA. *n*-butyl ether is used as an internal standard. The areas of the peaks in the GC-FID spectrum were used to calculate the datapoints. Figures A.12 - A.15 were fitted with a linear trendline with the intercept set to zero.

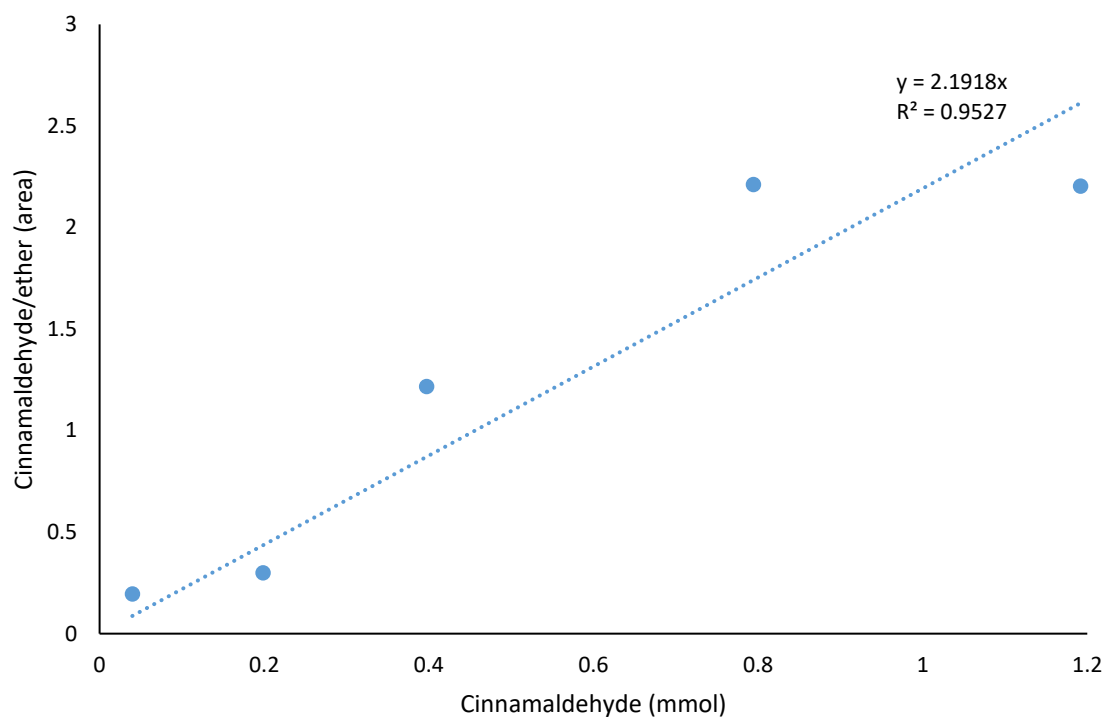


Figure A.12. *n*-butyl ether vs. cinnamaldehyde calibration curve

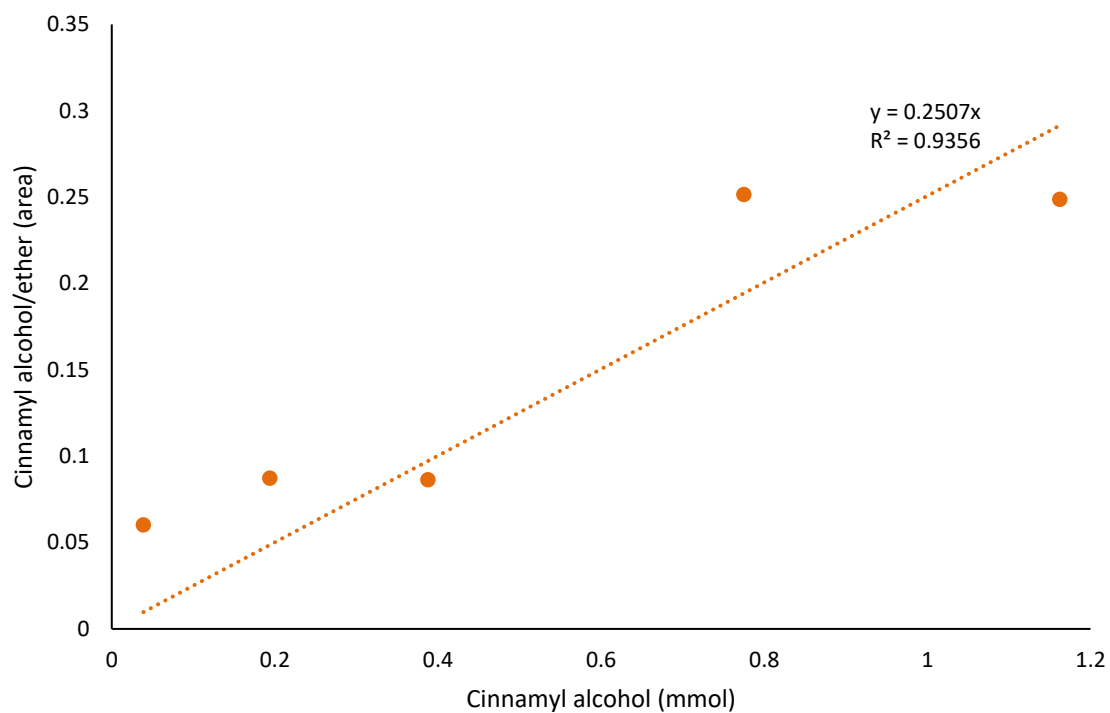


Figure A.13. *n*-butyl ether vs. cinnamalcohol calibration curve

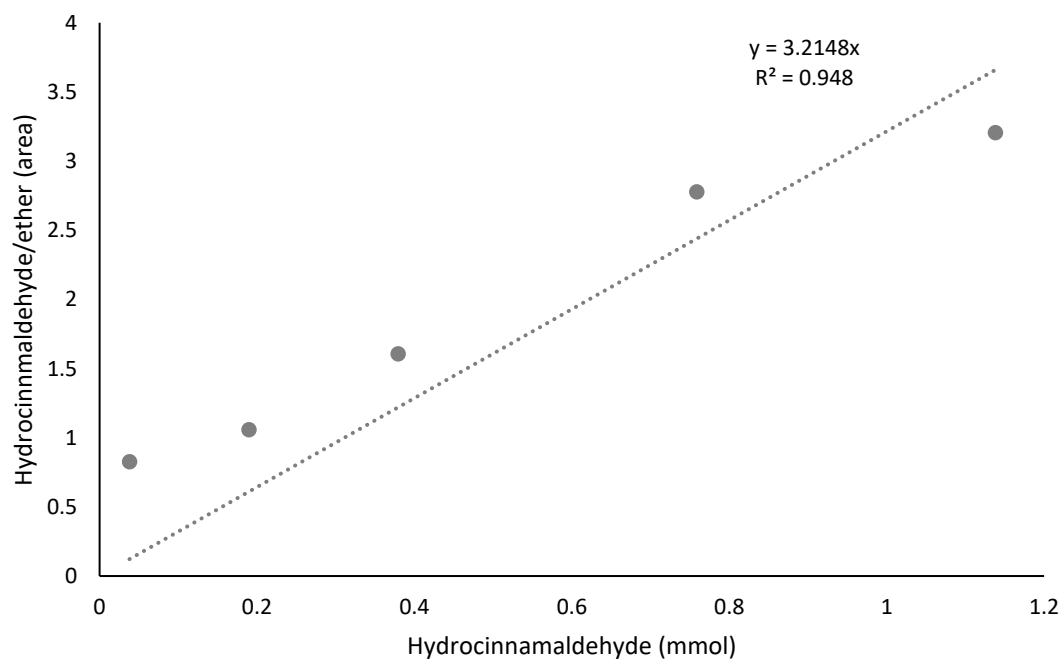


Figure A.14. *n*-butyl ether vs. hydrocinnamaldehyde calibration curve

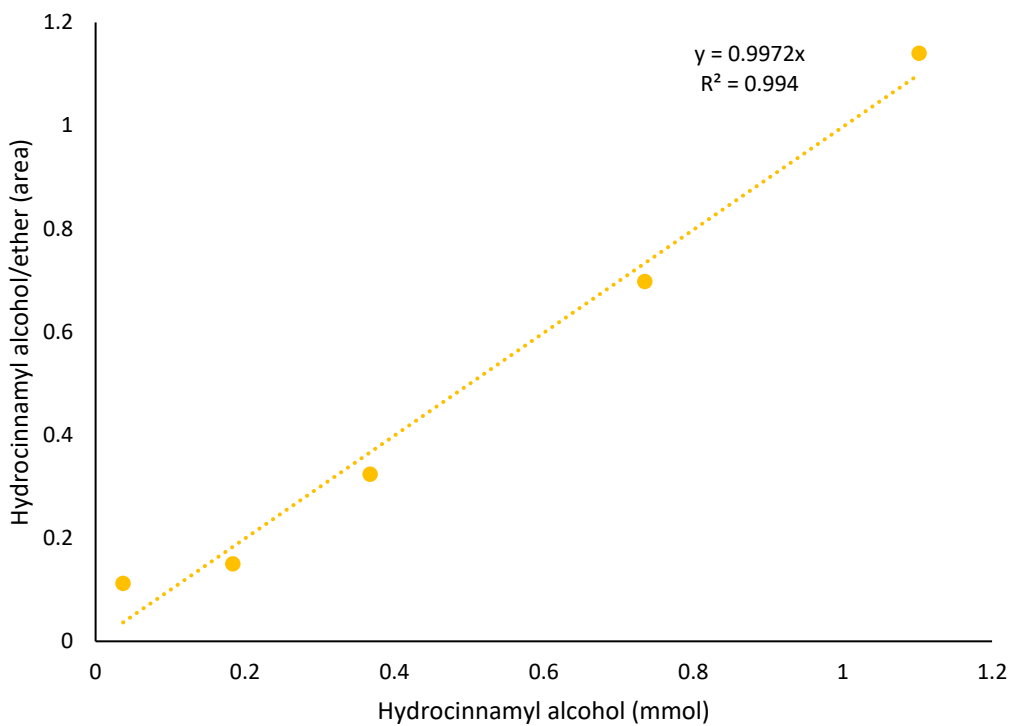


Figure A.15. *n*-butyl ether vs. hydrocinnamyl alcohol calibration curve

Appendix References

1. S. Brunauer, P. H. Emmet and E. Teller, *J. Am. Chem. Soc.*, 1938, **60**, 309-319.
2. F. Aguilar-Parrila, B. Wehrle, H. Braunling and H.-H. Limbach, *J. Magn. Reson.*, 1969, **87**, 592 - 597.
3. H. Bürger and U. Wannagat, *Monatshefte für Chemie*, 1963, **94**, 1007 - 1012.
4. A. L. Patterson, *Phys. Rev.*, 1939, **56**, 978 - 982.